

ASTRONOMICAL INSTITUTE
SLOVAK ACADEMY OF SCIENCES

PROCEEDINGS OF THE CONFERENCE
INTEGRAL AND BART
WORKSHOP 2023

May 22 – 26, 2023, Karlovy Vary, Czech Republic

CONTRIBUTIONS
OF THE ASTRONOMICAL OBSERVATORY
SKALNATÉ PLESO

• VOLUME LIII •

Number 4



December 2023

Editorial Board

Editor-in-Chief

Augustín Skopal, *Tatranská Lomnica, The Slovak Republic*

Managing Editor

Richard Komžík, *Tatranská Lomnica, The Slovak Republic*

Editors

Július Koza, *Tatranská Lomnica, The Slovak Republic*

Aleš Kučera, *Tatranská Lomnica, The Slovak Republic*

Luboš Neslušan, *Tatranská Lomnica, The Slovak Republic*

Vladimír Porubčan, *Bratislava, The Slovak Republic*

Theodor Pribulla, *Tatranská Lomnica, The Slovak Republic*

Advisory Board

Bernhard Fleck, *Greenbelt, USA*

Arnold Hanslmeier, *Graz, Austria*

Marian Karlický, *Ondřejov, The Czech Republic*

Jan Vondrák, *Prague, The Czech Republic*

©

Astronomical Institute of the Slovak Academy of Sciences
2023

ISSN: 1336-0337 (on-line version)

CODEN: CAOPF8

Editorial Office: Astronomical Institute of the Slovak Academy of Sciences
SK-059 60 Tatranská Lomnica, The Slovak Republic

CONTENTS

List of participants	11
Preface	13

SESSION A: GAMMA-RAY BURSTS AND ROBOTIC TELESCOPES

F. Giovannelli: The contribution of robotic telescopes to the knowledge of our Universe	15
J. Štrobl, M. Jelínek, C. Polášek, R. Hudec: D50: Autonomous robotic telescope in Ondřejov	49
P. Kroll: Proposal of optical sky monitoring with subsecond cadence	62
S. Karpov, J. Peloton: The rate of satellite glints in ZTF and LSST sky surveys	69
R. Hudec, M. Jelínek, J. Štrobl: Long term follow-up coverage of Gaia photometric alert sources by Ondřejov robotic telescopes	81
S. Pinter, L.G. Balazs, Z. Bagoly, I. Horvath: Gamma-Ray Bursts' redshift distribution's dependence on their duration	93
I.I. Racz: Estimating GRBs' cosmological distances	100
I.I. Racz, L.G. Balazs, I. Horvath: Redshift dependence of GRBs' observed parameters	115
M. Jelínek: Photometric pipeline for robotic telescopes	127

SESSION B: HIGH ENERGY ASTRONOMY

R. Hudec, V. Šimon, A. Read: X-ray astrophysics as secondary science with ESA/China SMILE satellite	136
R. Hudec: Comparison of Gaia BP/RP spectra with LDS (Low Dispersion Spectroscopy) photographic sky surveys	144
B. Koncz, A.P. Joó, S. Pintér: Investigating star formation in Illustris TNG galaxy mergers	153
A. P. Joó, B. Koncz, E. Pichler: Investigating star formation in nearby interacting galaxies	164
V. Karas, K. Klimovičová, D. Lančová, M. Štolc, J. Svoboda, G. Török, M. Matuszková, E. Šrámková, R. Šprňa, M. Urbanec: Timing of accreting neutron stars with future X-ray instruments: towards new constraints on dense matter equation of state	175
V. Šimon, R. Hudec: Development of an operation plan for observing the Galactic center region with the lobster-eye monitor	191

SESSION C: SMALL SATELLITES FOR ASTROPHYSICS

V. Tichý, M. Míka, R. Hudec: **Preliminary optical tests of lobster eye X-ray optics prototype for nano-satellite missions based on new technology** 198

V. Tichý, R. Hudec: **Overview of LOPSIMUL software, quick ray-tracing simulator of multi-foil reflective optical system** . . . 206

The Contributions of the Astronomical Observatory Skalnaté Pleso
are available in a full version
in the frame of ADS Abstract Service
and can be downloaded in a usual way from the URL address:

<https://ui.adsabs.harvard.edu/>

as well as from the web-site of
the Astronomical Institute of the Slovak Academy of Sciences
on the URL address:

<https://www.astro.sk/caosp/caosp.php>

The journal is covered/indexed by:

Web of Science (WoS)

WoS Core Collection: Science Citation Index Expanded

SCOPUS

Index Copernicus International

PROCEEDINGS OF THE CONFERENCE

**INTEGRAL AND BART
WORKSHOP 2023**

Edited by:

Martin Jelínek & Marianna Dafčíková

May 22 – 26, 2023, Karlovy Vary, Czech Republic

Astronomical Institute, Academy of Sciences of the Czech Republic, Ondřejov,
Czech Republic

Dept. of Theoretical Physics and Astrophysics, Faculty of Science, Masaryk
University, Brno, Czech Republic

<https://www.ibws.cz/>

Scientific Organizing Committee

Zsolt Bagoly (Hungary)
Thorsten Dohring (Germany)
Franco Giovannelli (Italy)
René Hudec (Czech Republic)
Martin Jelínek (Czech Republic)
Vladimír Karas (Czech Republic)
Karl Mannheim (Germany)
Klaus Schilling (Germany)
Norbert Werner (Czech Republic)
Joern Wilms (Germany)

Local Organizing Committee

René Hudec (Czech Republic)
Veronika Maršíková (Czech Republic)
Ondřej Nentvich (Czech Republic)
Miroslav Spurný (Czech Republic)
Martin Urban (Czech Republic)





LIST OF PARTICIPANTS

Katrin Berger	Dr. Karl Remeis Sternwarte Bamberg & Erlangen Center for Astroparticle Physics, FAU
Enrico Bozzo	University of Geneva
Asen Christov	Institute of Physics, Czech Academy of Sciences
Ronan Cunniffe	Institute of Physics, Czech Academy of Sciences
Marianna Dafčíková	Masaryk University
Vladimír Dániel	Czech Aerospace Research Centre
Robert Filgas	IEAP Czech Technical University in Prague
Peter Friedrich	Max Planck Institute for Extraterrestrial Physics
Franco Giovannelli	INAF-Istituto di Astrofisica e Planetologia Spaziali
Rene Hudec	Astronomical Institute, Czech Academy of Sciences & Czech Technical University in Prague
Adolf Inneman	Rigaku Innovative Technologies Europe s.r.o.
Martin Jelínek	Astronomical Institute, Czech Academy of Sciences
Jakub Jon	Výzkumný a zkušební letecký ústav, a.s.
Amy Joyce	Dr. Karl Remeis Sternwarte Bamberg and Erlangen Center for Astroparticle Physics (ECAP), FAU
Vladimír Karas	Astronomical Institute, Czech Academy of Sciences
Sergey Karpov	Institute of Physics, Czech Academy of Sciences
Kateřina Klimovičová	Institute of Physics, Silesian university in Opava
Bendegúz Koncz	Eötvös Loránd University
Peter Kroll	Sonneberg Observatory
Debora Lančová	Institute of Physics, Silesian University in Opava
Karl Mannheim	Universität Würzburg
Ezequiel J. Marchesini	OAS-INAF Bologna
Veronika Maršíková	Rigaku Innovative Technologies Europe s.r.o.
Monika Matuszková	Institute of Physics, Silesian University in Opava
Filip Münz	Masaryk University, Faculty of Science
Lorenzo Natalucci	INAF/Istituto di Astrofisica e Planetologia Spaziali
Ondřej Nentvich	Czech Technical University in Prague
Richard Pavlica	5M s.r.o.
Sandor Pinter	University of Public Service
Ladislav Pína	Rigaku Innovative Technologies Europe s.r.o.
Istvan Racz	University of Public Service
Maryam Raouph Lashkami	Philipps-University Marburg
Jakub Řípa	Masaryk University, Faculty of Science, Department of Theoretical Physics and Astrophysics
Wladislaw Schulga	Institut für Theoretische Physik und Astrophysik Universität Würzburg
Ladislav Sieger	Czech Technical University in Prague

Veronika Stieglitz
Vladimír Tichý
Gabriel Török
Martin Urban
Pavel Vančura

Norbert Werner
Nicolas Zalot

Berenika Čermáková
Vojtěch Šimon
René Šprňa
Eva Šrámková
Jan Štrobl
Vratislav Šálený

Max Planck Institute for Extraterrestrial Physics
Czech Technical University in Prague
Institute of Physics, Silesian university in Opava
Czech Technical University in Prague
Faculty of Nuclear Sciences and Physical Engineering
Masaryk University
Friedrich-Alexander-Universität Erlangen-Nürnberg
Universität Würzburg
Astronomical Institute, Czech Academy of Sciences
Institute of Physics, Silesian university in Opava
Institute of Physics, Silesian university in Opava
Astronomical Institute, Czech Academy of Sciences
Brno University of Technology

PREFACE

IBWS (INTEGRAL/BART workshop) is a series of successful international workshops dedicated to all aspects of high energy astrophysics and supporting ground-based experiments (e.g. robotic telescopes). Within these frameworks, the detailed program reflects the scientific interests of participants as we do not have invited talks but the contributions are submitted by the conference participants.

Originally, the IBWS (INTEGRAL/BART) workshops focused on the work of High energy astrophysics group (at that time dominated by young research fellows and students) in Astronomical Institute of the Academy of Sciences of the Czech Republic and relevant national and international collaborators from the field, with intensive student participation. During the early years, these activities were focused on the ESA INTEGRAL satellite and on the related ground-based robotic telescopes, e.g. the small robotic BART telescope at the Ondrejov Observatory.

Nowadays, the IBWS workshops promote regional collaboration in galactic and extragalactic high-energy astrophysics, both experimental as well as theoretical, with an emphasis on the interface between satellite projects and ground-based experiments (e.g. robotic telescopes). We continue our emphasis on wide participation and presentations of students and young research fellows.

The 17th of a series of INTEGRAL / BART Workshop was held in Karlovy Vary from 22 to 26 May 2023. This conference was a place for a meeting of the scientist, researchers, research fellow, professors and students from several countries, institutions and research areas.

The INTEGRAL/BART Workshop was organized by the High Energy Astrophysics Group of the Stellar Department of the Astronomical Institute of the Academy of Sciences of the Czech Republic together with the Czech Technical University in Prague (Czech Republic), the Friedrich Alexander University Astronomical Institute Observatory in Bamberg (Germany), the University of Wurzburg (Germany) and the Karlovy Vary Observatory. These institutions have also contributed their active participation on the contributions of presentations and expert discussions.

49 participants from 5 countries (Germany, Hungary, Switzerland, Italy, and the Czech Republic) attended this year's edition of this European regional conference.

The conference topics included astrophysical session covering both theoretical as well as observational aspects of high energy and very high energy astrophysics, both galactic and extragalactic, as well as gamma-ray bursts. The experimental session focused on small satellites for astrophysics, CubeSats and high-energy satellites with related ground-based instrumentation with data analyses.

The official conference program was divided into three sections:

- High energy astrophysics

- Gamma-Ray Bursts and Robotic Telescopes
- Small satellites for astrophysics & Instrumental session

Nevertheless, the conference was held in the idea of finding common bridges between these areas instead of their separation.

The program of the conference included 56 contributions from all fields. They were focused on high-energy satellite astrophysics, research of high energy cosmic sources, astrophysical applications of very small satellites, and also the use of robotic telescopes and the preparation of future space missions and experiments. For example, the results from the first Czech nanosatellite VZLUSAT-1 which was launched in June 2017, Slovak's CubeSat skCUBE and the introducing of new ESA satellite projects such as SMILE and THESEUS were discussed. The satellite designs for future astrophysical applications of small satellites (CubeSats), involving experts from the Czech Republic as well as the introduction of new projects and progresses by CubeSats experts from Germany and Hungary were presented.

The conference also featured the active participation of numerous university students.

René Hudec, SOC Chair

Ondřejov, November 2023

The contribution of robotic telescopes to the knowledge of our Universe

F. Giovannelli

*INAF - Istituto di Astrofisica e Planetologia Spaziali (E-mail:
franco.giovannelli@iaps.inaf.it)*

Received: June 25, 2023; Accepted: September 6, 2023

Abstract. In this review I will discuss the importance of small telescopes for the advancement of knowledge of our Universe. The use of robotic telescopes scattered all over the world is fundamental. The results obtained complement those obtained with medium and large telescopes and with both small and large space experiments. Due to the limited space and my limited knowledge I will be forced to discuss some topics, important in my opinion, but which obviously do not pretend to permeate the entire field of astrophysics.

Key words: GRBs – SNe – Optical Transients – HE-Astrophysics – Exoplanets

1. Introduction

One of the most important problems in modern astrophysics is that of the long surveys of different kind of cosmic sources. For this purpose the medium and large telescopes are practically unuseful since their allocated time is restricted by the numerous excellent programs that allow only to short periods of scheduling. Thanks to the modern CCD cameras placed in the focus of small telescopes, not subject to limited scheduled time, it is possible to operate for long term surveys up to ~ 21 - 22 mag. Of course a limitation is coming from the lack of observers that for different reasons cannot operate continuously. Thus, the winner idea of using robotic telescopes was used starting from about three decades ago.

Robotic telescopes have many advantages. Removing humans from the observing process allows faster observation response times. Robotic telescopes can also respond quickly to alert broadcasts from satellites and begin observing within seconds. Particularly in the field of gamma ray bursts, very early observations have led to significant advances in astronomers understanding of these events. Automation in a telescopes observing program eliminates the need for an observer to be constantly present at a telescope. This makes observations more efficient and less costly. Many telescopes operate in remote and extreme environments such as mountain tops, deserts, and even Antarctica. Under difficult conditions like these, a robotic telescope is usually cheaper, more reliable and more efficient than an equivalent non-robotic telescope.

However, the main disadvantage of a robotic system is that automation requires work. The more sophisticated the degree of autonomy the telescope has, the greater the amount of work required to enable that functionality. Scheduling systems usually combine a number of different variables (visibility, priority, weather conditions and many more) in order to decide the best course of action for a telescope at any given time (based on work by Eric Saunders, Las Cumbres Observatory: <https://lco.global/spacebook/telescopes/robotic-telescopes/>).

Among the many fields of astrophysics that can be explored with the aid of small telescopes, there is one particularly important: the detection of exoplanets. For this purpose there are different methods for their detection, namely: (i) Radial velocities method (Wright, 2018); (ii) Transit photometry method (Deeg & Roi, 2018); (iii) Gravitational microlensing method (Batista, 2018); (iv) Astrometry method (Malbet & Sozzetti, 2018); (v) Direct imaging method (Pueyo, 2018); (vi) Timing method (pulsars and stellar pulsations) (Kramer, 2018 and Hermes, 2018, respectively); (vii) Radio observations method (Lazio, 2018).

Bennett et al. (2019) in "*Astro2020 Science White Paper*" summarize current and planned exoplanet detection programs using a variety of methods.

Yee et al. (2018) in "*White Paper: Exoplanetary Microlensing from the Ground in the 2020s*" discussed on Microlensing that can access planet populations that no other method can probe: cold wide-orbit planets beyond the snow line^(*), planets in both the Galactic bulge and disk, and free floating planets (FFPs). The demographics of each population will provide unique constraints on planet formation.

It is important to mention the PhD thesis of Clément Ranc (2015a) "*Exoplanets and brown dwarfs detections through gravitational microlensing. Study of interferometric observations*". He discussed the gravitational microlensing effect that has become a unique tool to detect and characterise exoplanets. A microlensing effect occurs when a foreground star (the microlens) and a background star (the source) are aligned with the Earth on the same line of sight. The light from the furthest star, usually in the Galactic bulge, is deflected by the microlens located on the disk. During this phenomenon, multiple images of the source are created by the lens, bigger than the source that consequently seems amplified. When one of these images are located in the vicinity of an exoplanet, a short amplification jump occurs revealing its presence. After a quick overview of the exoplanets field of research, he highlighted the specificities of microlensing comparing to the other planets detection techniques.

^(*) Snow line or ice line or frost line, is the particular distance in the solar nebula from the central protostar where it is cold enough for volatile compounds such as water, ammonia, methane, carbon dioxide, and carbon monoxide to condense into solid ice grains (i.e., for the water, it is the minimum radius from the Sun at which water ice could have condensed, at about 150 K (-190 °F, -120 °C) (e.g. Liu, Yao & Ding (2017)).

2. A summary of the robotic experiments

In this short excursion about the tools necessary for an advance of our knowledge of the physics of the Universe, we cannot omit the extreme importance of small experiments, like those Space-based: small-, mini-, micro-, nano-, and cube-satellites, and those Ground-based: small-telescope, and Robotic-telescopes.

Castro-Tirado (2010a) in his review "*Robotic Autonomous Observatories: A Historical Perspective*" presented a historical introduction to the field of Robotic Astronomy, discussing the basic definitions, the differing telescope control operating systems, observatory managers, as well as a few current scientific applications in that time.

The number of automatic astronomical facilities worldwide continues to grow, and the level of robotisation, autonomy, and networking is increasing as well. This has a strong impact in many astrophysical fields, like the search for extrasolar planets, the monitoring of variable stars in our Galaxy, the study of active galactic nuclei, the detection and monitoring of supernovae, and the immediate followup of high-energy transients such as gamma-ray bursts (Castro-Tirado, 2008, 2010b).

The number of Robotic Autonomous Observatories (RAOs) has rapidly grown. Figure 1 shows the location of more than 100 RAOs worldwide (Castro Cerón, 2011). They are providing excellent results which should be impossible to obtain with the larger telescopes subject to strict scheduling, and in any case not available for long term runs of observations.

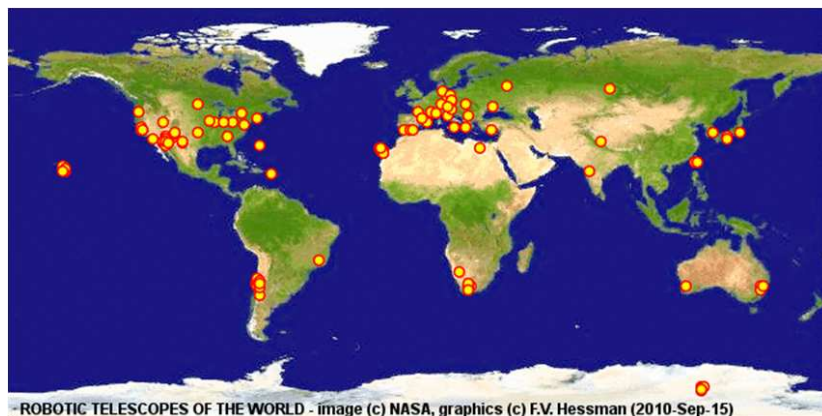


Figure 1. The Robotic Autonomous Observatories worldwide (adopted from Castro Cerón (2011), after Hessman (2001a,b)).

Just for giving to the reader a short panorama about the many small ground- and space-based experiments, not necessarily autonomous, we list the following:

a) **MITSuME (Multicolor Imaging Telescope for Survey and Monstrous Explosions)** has been built to perform Multi-color photometry of NIR /optical afterglow covering the wavebands from K_s to g' allowing the photometric redshift measurements up to $z \sim 10$. Two 50 cm optical telescopes are built at Akeno, Yamanashi in eastern Japan, and at OAO, Okayama in western Japan. Each telescope has a Tricolor Camera, which allows us to take simultaneous images in g' , R_c , and I_c bands. These telescopes respond automatically to GCN alerts and start taking series of tricolor images, which are immediately processed through the analysis pipeline on site. The pipeline consists of source finding, catalog matching, sky coordinates mapping to the image pixels, and photometry of the found sources. An automated search for an optical counterpart is performed. While waiting for GRBs, the MITSuME Telescopes automatically patrol pre-selected interesting objects such as AGNs and galactic transients for multiwavelength studies with Fermi (GLAST) and MAXI (Shimokawabe et al., 2009).

b) **The CHASE (CHilean Automatic Supernova sEarch)** project began in 2007 (Pignata et al., 2009) with the goal to discover young, nearby southern supernovae in order to i) better understand the physics of exploding stars and their progenitors, and ii) refine the methods to derive extra-galactic distances. During the first four years of operation, CHASE has produced more than 130 supernovae, being the most successful project of its type in the southern hemisphere (Hamuy et al., 2012).

c) **PLANET (the Probing Lensing Anomalies NETwork)** is an international collaboration - since 1995 - searching for extrasolar planets via microlensing effects. They work closely with the OGLE, MOA, LCOGT and KMTNet teams forming a global Worldwide consortium, sharing their resources, observations and models real time (Albrow et al., 1995).

d) **RoboNet-II** uses a global network of robotic telescopes to perform follow-up observations of microlensing events in the Galactic Bulge. The current network consists of three 2 m telescopes located in Hawaii and Australia (owned by Las Cumbres Observatory) and the Canary Islands (owned by Liverpool John Moores University). In future years the network will be expanded by deploying clusters of 1 m telescopes in other suitable locations. A principal scientific aim of the RoboNet-II project is the detection of cool extra-solar planets by the method of gravitational microlensing. RoboNet-II acts in coordination with the PLANET microlensing follow-up network and uses an optimization algorithm (web-PLOP) to select the targets and a distributed scheduling paradigm (eSTAR) to execute the observations. Continuous automated assessment of the observations and anomaly detection is provided by the ARTEMiS system (Tsapras et al., 2009).

e) **LCOGT (the Las Cumbres Observatory Global Telescope Network)** is a research organisation in the process of designing and building a network of robotic telescopes to be used for research in time-domain astrophysics and ed-

ucation. The network will have complete latitude coverage in both hemispheres to allow continuous observations of any target (Hidas et al., 2008).

The LCOGT comprises nine 1-meter and two 2-meter telescopes, all robotic and dynamically scheduled, at five sites spanning the globe (Boroson et al., 2014). This first of LCOGT's 1-m telescopes have been deployed, and the result is a young organization dedicated to time-domain observations at optical and (potentially) near-IR wavelengths. To this end, LCOGT is constructing a world-wide network of telescopes, including the two 2m Faulkes telescopes, as many as 17×1 m telescopes, and as many as 23×40 cm telescopes (Brown et al., 2013).

f) **The eSTAR Project** uses intelligent agent technologies to carry out resource discovery, submit observation requests and analyze the reduced data returned from a meta-network of robotic telescopes (Allan et al., 2004; Allan, Naylor & Saunders, 2006). In 2009 the project lost funding and was shuttered.

g) **OGLE (the Optical Gravitational Lensing Experiment)**, led by Andrzej Udalski of Warsaw University, found the first 3 planets ever detected through microlensing. The international project makes use of the 1.3-meter Warsaw telescope at Las Campanas, Chile, to search for microlensing events. Every night the telescope is pointed toward the same dense field of 100 million stars in the vicinity of the galactic bulge, while the telescope's complex CCD cameras note any change in brightness of any point in the starfield. Every year OGLE detects about 500 microlensing events, but planet detections are extremely rare. As of February 2020, it had found 49 exoplanets.

h) **MOA (Microlensing Observations in Astrophysics)**, led by Yasushi Muraki of Nagoya University, is a Japanese-New Zealand collaboration that uses a 1.8-meter telescope in New Zealand. As of February 2020 it had yielded 24 exoplanets.

i) **KMTNet (the Korea Microlensing Telescope Network)** runs CCD-equipped, 2-meter telescopes at 3 southern observatories. As of February 2020 it had discovered 10 exoplanets.

j) **ROTSE (Robotic Optical Transient Search Experiment)** has developed a next-generation instrument, ROTSE-III, for continuing the search for fast optical transients. The entire system was designed as an economical robotic facility to be installed at remote sites throughout the world (Akerlof et al., 2003).

k) **The (B)urst (O)bserver and (O)ptical (T)ransient (E)xploring (S)ystem (BOOTES)**, a set of instruments that was conceived in 1995 and has contributed significantly to the understanding of astrophysical transients and other high-energy phenomena in the Universe (Castro-Tirado et al., 2012).

l) **The Russian global network of telescopes robot MASTER** (Lipunov et al., 2010). MASTER is very fast positioning alert, follow up and survey twin telescopes Global network with own real-time auto-detection software. MASTER

goal is One Sky in One Night up to 20-21 mag. The network is spread along the whole world. In the following are reported the MASTER Net Sites:

- MASTER-Amur: Russia, near Blagoveschensk. Collaboration with the Blagoveschensk State Pedagogic University. It started in October 2009.
- MASTER-Tunka: Russia, near Irkutsk. Collaboration with the Applied Physics Institute, Irkutsk State University. It started in November 2009.
- MASTER-Ural: Russia, near Ekaterinburg. Collaboration with the Kourovka Astronomical Observatory, Ural State University. It started in December 2008.
- MASTER-Kislovodsk: Russia, Near Kislovodsk, north Caucasus. Kislovodsk Solar Station of the Pulkovo Observatory, and Lomonosov Moscow State University Mountain Observatory (KGO SAI). It started in July 2007.
- MASTER-SAAO: South Africa, Sutherland. Collaboration with the South African Astronomical Observatory (SAAO). It started in December 2014.
- MASTER-IAC: Spain, Canary Islands. Collaboration with the Instituto de Astrofísica de Canarias (IAC). It started in June 2015.
- MASTER-OAFA: Argentina. Collaboration with the Observatorio Astronómico Felix Aguilar (OAFA), Instituto de Ciencias Astronómicas de la Tierra y del Espacio (ICATE), National University of San Juan. It started in February 2012.
- MASTER-Progenitor: Russia, Moscow. Collaboration with the Alexander Krylov Observatory. It started in 2002.
- MASTER-Mexican (MASTER-OAGH - Guillermo Haro Astrophysics Observatory) in Cananea, Sonora, Mexico. Collaboration with the National Institute for Astrophysics, Optics and Electronics (INAOE). It started in December 2021.

m) **Very small satellites for multifrequency astrophysics** have been discussed by Hudec et al. (2017). About the small satellites we can assist to a strong competition (typically for ESA missions, 60 proposals for 1 satellite), and moreover all the system is affected by funding problems.

The development of the Pico (Cube) and Nanosatellites is running at many Universities, mostly with involvement of students for evident goals of education.

The standard size for a CubeSat is 1 Liter Volume, i.e. $10 \times 10 \times 10 \text{ cm}^3$ and typically a weight of $\sim 1.3 \text{ kg}$. Multiple modules are possible, i.e. 3 Units = 3 modules/units, i.e. $10 \times 10 \times 30 \text{ cm}^3$, typically up to 12 Units.

The range of weight of Picosatellites is 0.1-1 kg, Femtosatellites 10-100 g, Nanosatellites 1-10 kg, Microsatellites 10-100 kg.

Recent technological progress allows their use in any field of astrophysics.

Undoubtedly MASTER contributions to transient alerts in Astronomer's telegrams is fundamental. For instance in the period 2013-2014, MASTER contribution is of order 25% of the total as shown in Fig. 2 (after Buckley, 2015).

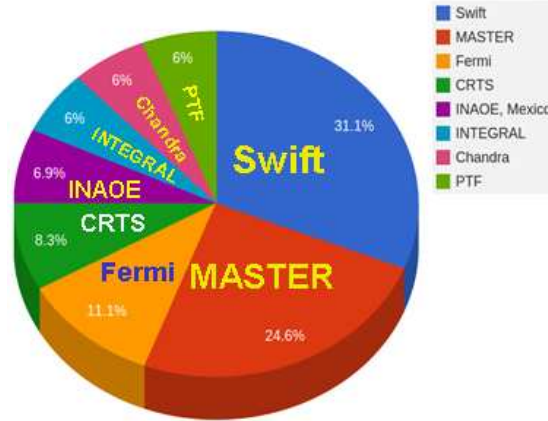


Figure 2. Contribution of different space- and ground-based experiments to the transient alerts in Astronomer's telegrams in the period 2013-2014 (after Buckley, 2015).

Though I have not shown a complete list of small experiments both space- and ground-based, I am able to affirm that small telescopes are unreplaceable tools complementary to larger telescopes and to bigger ground- and space-based multifrequency experiments. In the following section I will present a summary of the selected main results coming from "small" robotic experiments.

3. A summary of the selected results from robotic experiments

The most important news about the many scientific results obtained with the RAOs can be found in the proceedings of the series of Workshops on Robotic Autonomous Observatories (Bloom, Castro-Tirado, Hanlon & Kotani, 2010; Guziy, Pandey, Tello & Castro-Tirado, 2012; Tello, Riva, Hiriart & Castro-Tirado, 2014; Caballero-García, Pandey, Hiriart & Castro-Tirado, 2016a; Caballero-García, Pandey & Castro-Tirado, 2019; Castro-Tirado, Pandey & Caballero-García, 2021).

In the following I will try to report the selected results obtained with the small experiments listed in the previous section, without any pretension to be

exhaustive because the limited space available for this review, and for my limited knowledge.

3.1. MITSuME (Multicolor Imaging Telescope for Survey and Monstrous Explosions)

MITSuME gave a huge amount of information about GRBs. Tens of GNC have been published and can be found for instance looking at the ADS-NASA under the name of Tachibana Yutaro from 2013 to 2019.

Tachibana, Kawai & Pike (2015) presented the long-term light curve data of 3C 454.3 in three energy bands i.e. optical (R-band), X-ray (2-4 keV), and γ -ray (0.1-300 GeV) provided by MITSuME and SMARTS, MAXI/GSC, and Fermi/LAT, and reveal several time variability properties using the optical and the γ -ray flux data. The remarkable result in this research is the finding of a sign of change in the plateau magnitude. The physical parameter of the accretion disk or the relativistic electron in the jet might have changed gradually and significantly.

Fujiwara et al. (2017) report the observations of early GRB afterglows carried out with Akeno 50 cm Telescope from 2008 to 2016. In this period, fourteen GRB afterglows were detected within 1000 seconds after the detections of the prompt emission. They show the optical light curves of the GRB afterglows to discuss timing properties of the external shock. Then, they compare the light curves with the forward/reverse shock models. They discuss the number ratios of the different light-curve types based on the simulation by Gao et al. (2015). Finally, the ratio of magnetic equipartition parameters in the reverse and forward shocks are evaluated as 10-100.

One of the most important results coming from MITSuME was the detection of the outburst on June 15, 2015 after 26 years of quiescence of the black hole binary V404 Cygni (= GS 2023+338). Tachibana et al. (2017) report on the multi-color optical observation (g', RC, and IC) of this object at the beginning of its outburst performed by the MITSuME 50 cm telescope in Akeno, Yamanashi, and the MURIKABUSHI 105 cm telescope at Ishigakijima Astronomical Observatory. The observed SED (Spectral Energy Distribution) from optical to ultraviolet can be expressed by a model consisting of a power-law component and an irradiated disk component.

The long gamma-ray burst GRB 161017A was detected by Fermi and Swift, and its afterglow was observed by the MITSuME 50 cm optical telescope promptly, about 50 s after the burst (Tachibana et al., 2018). They found that the central engine released more energy as jets with a lower photon-emission efficiency in the X-ray flare activity. This qualitative change in the activity may provide us with a hint to understand the mechanisms of jet formation and prompt/X-ray flare emission.

3.2. The CHASE (CHilean Automatic Supernova sEarch)

CHASE is one of the most important hunters of supernovae (SNe). Indeed if we look at the Central Bureau Electronic Telegrams with the name Pignata, P. et al. since 2007 it is possible to see the detection of ~ 188 SNe.

In 2007 the CHilean Automatic Supernova sEarch (CHASE) program started (Pignata et al. 2009) in order to discover young and nearby SNe for which they could directly identify their progenitors in pre-explosion images, or through the fingerprints left by the progenitor in the early phases of evolution of the SN. Intensive spectroscopic and photometric follow-up studies of selected CHASE SNe also allow to test explosion models and learn about the complex physics involved in such phenomena. Last but not least, the CHASE SNe have constituted an important source of targets for the Carnegie Supernova Program (Hamuy et al. 2006) in order to calibrate the SN luminosities and refine methods to determine accurate and precise extragalactic distances. On average CHASE program observes ~ 250 galaxies per night and takes one 80-sec exposures of each galaxy. During the first four years of operation, CHASE has produced more than 130 supernovae, being the most successful project of its type in the southern hemisphere (Hamuy et al., 2012).

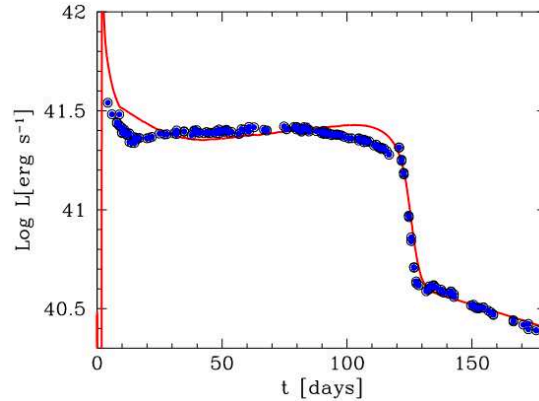


Figure 3. Bolometric light curve of SN 2008bk (blue circles) and hydrodynamic model (red line). The horizontal axis shows the time since explosion (adopted from Hamuy et al., 2012).

Just to show the goodness of CHASE program Fig. 3 shows the bolometric light curve of SN 2008bk in NGC 7793, most likely a low-luminosity SN II-P, which was discovered by Monard (2008) and independently confirmed by CHASE. Hydrodynamic models yield very good fits to CHASE observations, from which it was possible to derive the following parameters: explosion en-

ergy of $E_{\text{exp}} = 0.25 \times 10^{51}$ ergs, progenitor mass $M_{\text{pr}} = 12 M_{\odot}$, initial radius $R_{\text{in}} = 500 R_{\odot}$, and only $0.009 M_{\odot}$ of freshly synthesized radioactive ^{56}Ni . An independent study by Van Dyk et al. (2012) of previously recorded images of the host galaxy taken with the Very Large Telescope and Gemini-South instruments, allowed them to identify the progenitor star and infer a ZAMS mass of $12 M_{\odot}$, in agreement with the hydrodynamic model.

3.3. PLANET (the Probing Lensing Anomalies NETwork)

Gravitational microlensing occurs when a massive compact object (such as a star) passes very near the line-of-sight to a background luminous source (such as another star). The gravitational field of the foreground "lens" bends the light rays from the background "light bulb", resulting in more light reaching the observer's telescope. Significant lensing requires precise source-lens alignment, comparable to the angular radius of the so-called Einstein ring, defined as $\Theta_E = [4GM(1-x)/(c^2D_L)]^{1/2}$, where $x = D_L/D_S$, and M , D_L , and D_S are the lens mass, lens distance, and source star distance, respectively. For typical Galactic microlensing, $\Theta_E \sim 1$ mas, corresponding to separations of 1-5 AU at the position of the lenses. Thus, when these rare precise alignments occur, planetary orbits comparable in size to those of Earth and Jupiter are detectable (Sackett et al., 2003).

Gaudi et al. (2002) analyzed 5 years of PLANET photometry of microlensing events toward the Galactic bulge to search for the short-duration deviations from single-lens light curves that are indicative of the presence of planetary companions to the primary microlenses.

They concluded that less than 33% of M dwarfs in the Galactic bulge have Jupiter-mass companions between 1.5 and 4 AU, and less than 45% have $3M_J$ companions between 1 and 7 AU. These are the first significant limits on planetary companions to M dwarfs.

With generous time allocations at the observatories, PLANET (Probing Lensing Anomalies NETwork) obtained a dense round-the-clock coverage (Albrow et al., 1998) of galactic bulge microlensing events in I with additional observations in R and V with its current network of 1m-class telescopes formed by SAAO 1.0m (South Africa), Danish 1.54m at ESO La Silla (Chile), Canopus 1.0m (Tasmania), and Perth 0.6m (Western Australia), and also with Dutch 0.9m and 2.2m at ESO La Silla, 0.9m and Yale 1.0m at CTIO (Chile), and MSO 50" (Australia). PLANET experiment constrains the abundance and can yield the discovery of planets down to the mass of earth around galactic disk and bulge stars. Data taken until 1999 imply that less than 1/3 of bulge M-dwarfs are surrounded by Jupiter-mass companions at orbital radii between 1 and 4 AU. The current rate of microlensing alerts allows 15-25 Jupiters and 1-3 Earths to be probed per year (Dominik et al., 2004).

Important result has been found by Ranc et al. (2015b) by analysing MOA-2007-BLG-197Lb, the first brown dwarf companion to a Sun-like star detected through gravitational microlensing.

3.4. RoboNet-II

RoboNet-II has developed a complete architecture and supporting software to implement that architecture for the automated detection and characterization of exoplanets detected via the microlensing technique. The RoboNet-1.0 pilot programme in previous seasons has returned promising results and contributed to almost all of the microlensing planetary discoveries to 2009. Current efforts are directed in further automation and restructuring of the scheduling, data acquisition and image processing, improving the alerting system and responses, as well as significant upgrades to the telescope engineering. These involve the deployment of new instruments and electrical safety and performance reliability upgrades. LCOGT is in the process of expanding the robotic network of telescopes. Current plans are for 18 new 1m and 240 .4m telescopes which are expected to be fully integrated and in operation by 2011. The microlensing search for planets, and in particular the method pioneered by the RoboNet project which can potentially make full use of the facilities in an automated way, is a science objective that can be efficiently realized with this network.

3.5. LCOGT (the Las Cumbres Observatory Global Telescope Network)

The LCOGT network V1.0 began full science operations in 2014. It is being used in novel ways to undertake investigations related to supernovae, microlensing events, solar system objects, and exoplanets. The network's user base includes a number of partners, who are providing resources to the collaboration (Borison et al., 2014).

Valenti et al. (2015) presented the first results from the LCOGT Network's Active Galactic Nuclei (AGNs) Key Project, a large program devoted to using the robotic resources of LCOGT to perform time domain studies of active galaxies. They monitored the Seyfert 1 galaxy Arp 151 (Mrk 40) for ~ 200 days with robotic imagers and with the FLOYDS robotic spectrograph at Faulkes Telescope North. Arp 151 was highly variable during this campaign, with V-band light curve variations of ~ 0.3 mag and H_β flux changing by a factor of ~ 3 . They measured robust time lags between the V-band continuum and the H_α , H_β , and H_γ emission lines. The lag for the $\text{He II } \lambda 4686$ emission line is unresolved. They estimated a black hole mass of $M_{\text{BH}} = 6.2_{-1.2}^{+1.4} \times 10^6 M_\odot$.

These results represent the first step to demonstrate the powerful robotic capabilities of LCOGT for long-term AGN time domain campaigns that human intensive programs cannot easily accomplish. Arp 151 is now one of just a few

AGNs where the virial product is known to remain constant against substantial changes in H_β lag and luminosity.

One important result coming from a collaboration among the LCOGT, SMARTS telescopes, HST and XMM-Newton is that about the young (7 Myr) $1.5 M_\odot$ T Tauri star T Cha (Brown et al., 2018). This star shows high variability. The optical extinction varies by at least 3 magnitudes on few hour time-scales. The obscuration is produced by material at the inner edge of the circumstellar disk and therefore characterizing the absorbing material can reveal important clues regarding the transport of gas and dust within such disks. The inner disk of T Cha is particularly interesting, because T Cha has a transitional disk with a large gap at 0.2 – 15 AU in the dust disk and allows study of the gas and dust structure in the terrestrial planet formation zone during this important rapid phase of protoplanetary disk evolution. They examine which spectral features in the different spectral regions (FUV/NUV/optical/X-ray) change and by how much, and thereby determine the location of different emitting regions within the complex stellar/inner disk system relative to the absorbers along the line-of-sight to the stellar photosphere. Understanding these contributions is vital for estimating the properties of the absorbing gas and dust.

Important results are coming from the collaboration among All-Sky Automated Survey for SuperNovae (ASAS-SN, the LCOGT and the TESS, as well as archival data from other missions. Bredall et al.(2020) reported about T Tauri-like "dipper" stars. These stars vary due to transient partial occultation by circumstellar dust, and observations of this phenomenon inform us of conditions in the planet-forming zones close to these stars. They identified 11 dipper stars in the Lupus star forming region. All 11 stars lie above or redward of the zero-age main sequence and have infrared excesses indicating the presence of full circumstellar disks. They obtained reddening-extinction relations for the variability of 7 stars using their combined ASAS-SN-TESS and LCOGT photometry. In all cases the slopes are below the ISM value, suggesting larger grains, and they found a tentative relation between the slope (grain size) and the $Ks - [22 \mu m]$ infrared color regarded as a proxy for disk evolutionary state.

Accretion outbursts are key elements in star formation. ASASSN-13db is a M5-type star with a protoplanetary disk, the lowest-mass star known to experience accretion outbursts. Since its discovery in 2013, it has experienced two outbursts, the second of which started in November 2014 and lasted until February 2017. Sicilia-Aguilar et al. (2017) used high- and low-resolution spectroscopy and time-resolved photometry from the ASAS-SN survey, the LCOGT and the Beacon Observatory to study the light curve of ASASSN-13db and the dynamical and physical properties of the accretion flow. Photometrically and spectroscopically, the 2014-2017 event displays an intermediate behavior between EXors and FUors. The properties of ASASSN-13db suggest that temperatures lower than those for solar-type stars are needed for modeling accretion in very-low-mass systems.

One of the most important contribution of the LCOGT is that of the survey of supernovae (SNe). Indeed, for instance, a multifilter follow-up campaign started on 2015 March 12, when the ASASSN-15ed was already past-maximum, and lasted over two months. It was performed using several telescopes available to the collaboration, including the 1.82-m Copernico Telescope at Mt Ekar (Asiago, Italy), equipped with AFOSC, the LCOGT 1.0-m telescope at McDonald Observatory (Texas, USA) equipped with an SBIG camera, the 10.4-m Gran Telescopio Canarias (GTC) equipped with OSIRIS, the 3.58-m Telescopio Nazionale Galileo (TNG) equipped with DOLORES (LRS), the 2.5-m Nordic Optical Telescope (NOT) with ALFOSC and the 2.0-m Liverpool Telescope (LT) with the IO:O camera, all sited at La Palma (Canary Islands, Spain)(Pastorello et al., 2019).

Another example of the contribution to the knowledge of SNe is the early photometric and spectroscopic observations of SN 2013ej (Valenti et al., 2014), a bright Type IIP supernova (SN) in M 74. SN 2013ej is one of the closest SNe ever discovered. The available archive images and the early discovery help to constrain the nature of its progenitor. The earliest detection of this explosion was on 2013 July 24.125 UT and their spectroscopic monitoring with the FLOYDS spectrographs began on July 27.7 UT, continuing almost daily for two weeks. Daily optical photometric monitoring was achieved with the 1 m telescopes of the LCOGT network, and was complemented by UV data from Swift and near-infrared spectra from Public ESO Spectroscopic Survey of Transient Objects and Infrared Telescope Facility.

Edwards et al. (2021) report photometric follow-up observations of thirteen exoplanets (HATS-1 b, HATS-2 b, HATS-3 b, HAT-P-18 b, HAT-P-27 b, HAT-P-30 b, HAT-P-55 b, KELT-4A b, WASP-25 b, WASP-42 b, WASP-57 b, WASP-61 b and WASP-123 b), as part of the Original Research By Young Twinkle Students (ORBYTS) programme. All these planets are potentially viable targets for atmospheric characterisation and their data, which were taken using the LCOGT network of ground-based telescopes, will be combined with observations from other users of ExoClock^(*) to ensure that the transit times of these planets continue to be well-known, far into the future. These exoplanets will be potential targets for the missions Ariel and JWST that will be able to observe the whole sky, while Twinkle's field of regard is limited to planets within $\pm 40^\circ$ of the ecliptic plane, meaning HAT-P-18 b, HAT-P-55 b and WASP-61 b cannot be studied by this mission.

(*) The ExoClock project, an open, integrated and interactive platform with the purpose of producing a confirmed list of ephemerides for the planets that will be observed by Ariel (Kokori et al., 2021).

3.6. The eSTAR Project

The eSTAR project was a multi-agent system that aimed to implement a heterogeneous network of robotic telescopes for automated observing, and ground-based follow-up to transient events (Allan et al., 2004). By 2007 the eSTAR Project was "live" supporting two real-time observing projects.

One of the most important project was the automated follow-up observations of gamma-ray bursts (GRBs) performed using the 3.8 m United Kingdom Infrared Telescope (UKIRT) operated by Joint Astronomy Centre in Hawaii (JACH). The first ground based observations of GRB 090423 were triggered via the eSTAR Project, with initial observations by the Swift GRB Mission automatically followed by UKIRT just a few minutes after the initial observation by the SWIFT satellite. The observations autonomously triggered by the eSTAR software were reported in Tanvir et al. (2009). This GRB was, at the time of discovery, the most distant object then known in the Universe. GRB090423 lies at a redshift of $z \sim 8.2$, implying that massive stars were being produced and dying as GRBs ~ 630 Myr after the Big Bang. The burst also pinpoints the location of its host galaxy.

Another important program was the search for extra-solar planets by placing observations on the RoboNet system of telescopes on behalf of the PLANET collaboration. The technique of gravitational microlensing is used to monitor large numbers of stars in the galactic bulge looking for the tell-tale signature of cool planets orbiting those stars. The project also operated the heaviest used of the initial generation of Virtual Observatory VOEvent brokers, exposing its real-time alert system to other collaborators, like the TALONS (White et al., 2004).

Unfortunately in 2009 the project lost funding and was shuttered.

3.7. OGLE (the Optical Gravitational Lensing Experiment)

The OGLE collaboration, together with others span in detecting exoplanets from brown dwarfs to Earth and super-Earth-mass planets, to sub-Saturn-mass planets, to Jupiter and super-Jupiter-mass planets, to neutron stars and low mass black holes.

Skowron et al. (2015) reported the discovery of a Jupiter-mass planet orbiting an M-dwarf star that gave rise to the microlensing event OGLE-2011-BLG-0265. Such a system is very rare among known planetary systems and thus the discovery is important for theoretical studies of planetary formation and evolution. High-cadence temporal coverage of the planetary signal, combined with extended observations throughout the event, allows them to accurately model the observed light curve. However, the final microlensing solution remains degenerate, yielding two possible configurations of the planet and the host star. In the case of the preferred solution, the mass of the planet is $M_{\text{planet}} = 0.9 \pm 0.3 M_{\text{J}}$, and the planet is orbiting a star with a mass $M = 0.22 \pm 0.06 M_{\odot}$. The

second possible configuration (2σ away) consists of a planet with $M_{\text{planet}} = 0.6 \pm 0.3 M_{\text{J}}$ and host star with $M = 0.14 \pm 0.06 M_{\odot}$. The system is located in the Galactic disk 3-4 kpc toward the Galactic bulge. In both cases, with an orbit size of 1.5-2.0 AU, the planet is a "cold Jupiter" – located well beyond the "snow line" of the host star.

Bond et al. (2017) reported the discovery of the lowest mass ratio exoplanet to be found by the microlensing method in the light curve of the event OGLE 2016-BLG-1195. This planet revealed itself as a small deviation from a microlensing single lens profile from an examination of the survey data. The duration of the planetary signal is ~ 2.5 h. The measured ratio of the planet mass to its host star is $q = (4.2 \pm 0.7) \times 10^{-5}$. They further estimate that the lens system is likely to comprise a cold ~ 3 Earth mass planet in an ~ 2 AU wide orbit around a 0.2 Solar mass star at an overall distance of 7.1 kpc.

The discovery and analysis of a Saturn-mass planet in the microlensing event OGLE-2017-BLG-0406, which was observed both from the ground and by the Spitzer satellite in a solar orbit have been reported by Hirao et al. (2020). At high magnification, the anomaly in the light curve was densely observed by ground-based-survey and follow-up groups, and it was found to be explained by a planetary lens with a planet/host mass ratio of $q = 7.0 \times 10^{-4}$ from the light-curve modeling. The ground-only and Spitzer-"only" data each provide very strong one-dimensional (1D) constraints on the 2D microlens parallax vector π_{E} . When combined, these yield a precise measurement of π_{E} and of the masses of the host $M_{\text{host}} = 0.56 \pm 0.07 M_{\odot}$ and planet $M_{\text{planet}} = 0.41 \pm 0.05 M_{\text{J}}$. The system lies at a distance $D_{\text{L}} = 5.2 \pm 0.5$ kpc from the Sun toward the Galactic bulge, and the host is more likely to be a disk population star according to the kinematics of the lens. The projected separation of the planet from the host is $a_{\perp} = 3.5 \pm 0.3$ AU (i.e., just over twice the snow line).

Zang et al. (2020) reported the discovery and analysis of a sub-Saturn-mass planet in the microlensing event OGLE-2018-BLG-0799. The planetary signal was observed by several ground-based telescopes, and the planet-host mass ratio is $q = (2.65 \pm 0.16) \times 10^{-3}$. The ground-based observations yield a constraint on the angular Einstein radius Θ_{E} , and the microlens parallax π_{E} is measured from the joint analysis of the Spitzer and ground-based observations, which suggests that the host star is most likely to be a very low-mass dwarf. A full Bayesian analysis using a Galactic model indicates that the planetary system is composed of an $M_{\text{planet}} = 0.22_{-0.06}^{+0.19} M_{\text{J}}$ planet orbiting an $M_{\text{host}} = 0.080_{-0.020}^{+0.080} M_{\odot}$, at a distance of $D_{\text{L}} = 4.42_{-1.23}^{+1.73}$ kpc. The projected planet-host separation is $r_{\perp} = 1.27_{-0.29}^{+0.45}$ AU, implying that the planet is located beyond the snow line of the host star. However, because of systematics in the Spitzer photometry, there is ambiguity in the parallax measurement, so the system could be more massive and farther away.

Zang et al. (2021a) report the discovery of KMT-2020-BLG-0414Lb, with a planet-to-host mass ratio = $3\text{-}4 M_{\oplus}$ at 1σ , which is the lowest mass-ratio mi-

cro lensing planet to date. The detection of this planet, despite the considerable difficulties imposed by COVID-19 (two KMT sites and OGLE were shut down), illustrates the potential utility of this program.

With a mass ratio of $q \sim 1.27 \pm 0.07$ or $\sim 1.45 \pm 0.15 \times 10^{-5}$, OGLE-2019-BLG-0960Lb is the smallest mass-ratio microlensing planet ever found (Yee et al., 2021). The annual parallax effect combined with the finite source effect indicate the host star is an M-dwarf at $D_L \leq 1$ kpc with a super-Earth planet orbiting between 1 and 2 AU. Indeed, the mass of the host star ($M_L = 0.3 - 0.6 M_\odot$), the mass of its planet ($m_p = 1.4-3.1 M_\oplus$), the projected separation between the host and planet ($a_\perp = 1.2-2.3$ AU), and the distance to the lens system ($D_L = 0.6-1.2$ kpc).

By using measurements with OGLE, MOA, HST, and Gaia, Lam et al. (2022) presented the analysis of five black hole (BH) candidates identified from gravitational microlensing surveys. One of the five targets (OGLE-2011-BLG-0462/MOA-2011-BLG-191 or OB110462 for short) is the first definitive discovery of a compact object through astrometric microlensing and it is most likely either a neutron star or a low-mass black hole (its mass ranging from 1.6 to 4.2 M_\odot). This compact object lens is relatively nearby (690-1370 pc) and has a slow transverse motion of < 25 km/s. For the remaining four candidates, the lens masses are $< 2 M_\odot$ and they are unlikely to be black holes; but two of the four are likely white dwarfs or neutron stars.

Another important result is that reported by Shin et al. (2022). OGLE-2016-BLG-1093 is a planetary microlensing event that is part of the statistical Spitzer microlens parallax sample. The precise measurement of the microlens parallax effect for this event, combined with the measurement of finite source effects, leads to a direct measurement of the lens masses and system distance: $M_{\text{host}} = 0.38-0.57 M_\odot$, $m_p = 0.59-0.87 M_J$, and the system is located at the Galactic bulge ($D_L \sim 8.1$ kpc).

The transition objects between stars and planets are very probably brown dwarfs. But this transition is poorly understood. Mass measurements are generally difficult for isolated objects but also for brown dwarfs orbiting low-mass stars, which are often too faint for spectroscopic follow-up. Herald et al. (2022) analyse the microlensing event OGLE-2019-BLG-0033/MOA-2019-BLG-035, which is due to a binary system composed of a brown dwarf orbiting a red dwarf. The result obtained – thanks to Spitzer and extensive ground observations – is an accurate estimates of all microlensing parameters, including parallax, source radius and orbital motion of the binary lens. After accurate modeling, they find that the lens is composed of a red dwarf with mass $M_1 = 0.149 \pm 0.010 M_\odot$ and a brown dwarf with mass $M_2 = 0.0463 \pm 0.0031 M_\odot$, at a projected separation of $a_\perp = 0.585$ AU. The system has a peculiar velocity that is typical of old metal-poor populations in the thick disk.

3.8. MOA (Microlensing Observations in Astrophysics)

In a collaboration between MOA and OGLE, Hirao et al. (2017) reported the discovery and the analysis of the planetary microlensing event, OGLE-2013-BLG-1761. The lens system is located $D_L = 6.9_{-1.2}^{+1.0}$ kpc away from us and the host star is an M/K dwarf with a mass of $M_L = 0.33_{-0.19}^{+0.32} M_\odot$ orbited by a super-Jupiter mass planet with a mass of $m_P = 2.7_{-1.5}^{+2.5} M_J$ at the projected separation of $a_\perp = 1.8_{-0.5}^{+0.5}$ AU.

Blackman et al. (2021) reported the non-detection of a main-sequence lens star in the microlensing event MOA-2010-BLG-477Lb12 using near-infrared observations from the Keck Observatory. They determined that this system contains a $0.53 \pm 0.11 M_\odot$ white-dwarf host orbited by a 1.4 ± 0.3 Jupiter-mass planet with a separation on the plane of the sky of 2.8 ± 0.5 AU, which implies a semi-major axis larger than this. This system is evidence that planets around white dwarfs can survive the giant and asymptotic giant phases of their host's evolution, and supports the prediction that more than half of white dwarfs have Jovian planetary companions (Schreiber et al., 2019). Located at approximately 2.0 kpc towards the centre of our Galaxy, it is likely to represent an analogue to the end stages of the Sun and Jupiter in our own Solar System.

As part of a systematic modelling effort in the context of a > 10 -yr retrospective analysis of MOA's survey observations to build an extended MOA statistical sample, Ranc et al. (2021) analysed the light curve of the planetary microlensing event MOA-2014-BLG-472. This event provides weak constraints on the physical parameters of the lens, as a result of a planetary anomaly occurring at low magnification in the light curve. They used a Bayesian analysis to estimate the properties of the planet, based on a refined Galactic model and the assumption that all Milky Way's stars have an equal planet-hosting probability. They found that a lens consisting of a $1.9_{-1.2}^{+2.2} M_J$ giant planet orbiting a $0.31_{-0.19}^{+0.36} M_\odot$ host at a projected separation of 0.75 ± 0.24 AU is consistent with the observations and is most likely, based on the Galactic priors. The lens most probably lies in the Galactic bulge, at $7.2_{-1.7}^{+0.6}$ kpc from Earth.

3.9. KMTNet (the Korea Microlensing Telescope Network)

Jung et al. (2020a) reported the discovery of a planet in the microlensing event OGLE-2018-BLG-1269 with a planet-host mass ratio $q \sim 6 \times 10^{-4}$, i.e., 0.6 times smaller than the Jupiter/Sun mass ratio. Combined with the Gaia parallax and proper motion, a strong one-dimensional constraint on the microlens parallax vector allows them to significantly reduce the uncertainties of lens physical parameters. A Bayesian analysis that ignores any information about light from the host yields that the planet is a cold giant ($M_2 = 0.69_{-0.22}^{+0.44} M_J$) orbiting a Sun-like star ($M_1 = 1.13_{-0.35}^{+0.72} M_\odot$) at a distance of $D_L = 2.56_{-0.62}^{+0.92}$ kpc. The projected planet-host separation is $a_\perp = 4.61_{-1.17}^{+1.70}$ AU.

Jung et al. (2020b) – with large collaboration among KMTNet, OGLE, and MOA – found that KMT-2019-BLG-0842Lb is a cold planet located beyond the snow line of its host, and the planet/host mass ratio is $q = (4.09 \pm 0.27) \times 10^{-5}$, which is similar to the ratio of Uranus/Sun in the solar system. The discovery of the planetary system, together with similar systems previously discovered, provides evidence that such planets are not rare. Nevertheless, further discoveries will be necessary to estimate the frequency and characterize the distribution of such planets.

In order to exhume the buried signatures of "missing planetary caustics" in Korea Microlensing Telescope Network (KMTNet) data, Zang et al. (2021b) conducted a systematic anomaly search of the residuals from point-source point-lens fits, based on a modified version of the KMTNet EventFinder algorithm. This search revealed the lowest-mass-ratio planetary caustic to date in the microlensing event OGLE-2019-BLG-1053, for which the planetary signal had not been noticed before. The planetary system has a planet-host mass ratio of $q = (1.25 \pm 0.13) \times 10^{-5}$. A Bayesian analysis yielded estimates of the mass of the host star, $M_{\text{host}} = 0.61_{-0.24}^{+0.29} M_{\odot}$, the mass of its planet, $M_{\text{planet}} = 2.48_{-0.98}^{+1.19} M_{\oplus}$, the projected planet-host separation, $a_{\perp} = 3.4_{-0.5}^{+0.5}$ AU, and the lens distance, $D_L = 6.8_{-0.9}^{+0.6}$ kpc. The discovery of this very-low-mass-ratio planet illustrates the utility of their method and opens a new window for a large and homogeneous sample to study the microlensing planet-host mass ratio function down to $q \sim 10^{-5}$.

3.10. ROTSE (Robotic Optical Transient Search Experiment)

Following the results from ROTSE-I instrument described by Woźniak et al. (2004) it is possible to understand the importance of such instrument. They presented the Northern Sky Variability Survey (NSVS), the most extensive temporal record of the sky on large spatial scales, updated to 2004. All of the survey data is available to the astronomical community and can be searched efficiently using the public SkyDOT database. The database contains a total of 3.35 billion measurements for approximately 14 million objects in the 8-15.5 mag range. Time sampling over 1 full year is between twice per night and once every four nights, on average. The ROTSE-I instrument has achieved a complete spatial coverage of the northern hemisphere and a large fraction of the southern sky using remarkably low cost hardware. These two factors pose limits to the level of detail at which variability of the sky was recorded: low spatial resolution, spatial sensitivity variations, a nonstandard filter, and complicated systematics near the Galactic plane. Despite its limitations, the NSVS is a truly rich source of information on stellar variability. Among stars in the Galaxy, the fraction of variables with amplitudes detectable by the NSVS is about $\sim 1\%$ (Eyer, 1999; Eyer & Cuipers 2000). Based on that and on preliminary results in Akерlof et al. (2000), one can expect that tens of thousands of new variable stars with good uniform quality light curves are present in the data set. Current

database schema needs to be expanded along the lines described in Woźniak et al. (2002) to accommodate various types of variables and provide classification capability. The NSVS combined with astrometric catalogs providing distances and motions, as well as multicolor surveys (2MASS, or even SDSS in a narrow magnitude range) will enable a comprehensive look at the Galaxy as traced by variable stars. The NSVS objects are bright and therefore the preferred targets for detailed spectroscopic and astrometric work. The spatial resolution of the survey is not far from that of high-energy sky catalogs like the ROSAT All Sky Survey (Voges et al., 1999) or the XMM Catalog of Serendipitous Sources (Watson, 2003), and therefore it is well suited for cross-correlations. Perhaps the most exciting questions to be attacked using the NSVS are regarding rare, hard to find objects. The astronomical literature provides numerous unexplained reports of variability events on normal stars (e.g., Schaefer, King, & Deliyannis 2000 and references therein). Photometric monitoring data for active galactic nuclei (AGNs) providing diagnostics of accretion flows is valuable, but limited. Only a few bright AGNs are within the magnitude limit of the NSVS, so the real contribution to AGN physics will require deeper flux limits and better resolution in future projects. A major but low cost improvement in data usability would be the use of a set of standard filters before starting deeper surveys with more frequent time sampling. Small robotic telescopes with automated data-processing pipelines are the best candidates for closing the gap in the current level of temporal monitoring of the sky. The computing power to perform on-line photometry is available. Experiments like RAPTOR (Vestrand et al., 2002) are starting to tackle the problem of real-time detection and immediate follow-up of short timescale phenomena. One can envision a monitoring system capable of partial interpretation of various events occurring on a variety of timescales and notifying subscribers about interesting changes of objects in their scientific problem domain. The main challenge is making the immense data stream comprehensible by putting enough smarts into the software. The sky itself is the ultimate astronomical database that should be mined continuously and in real time.

ROTSE-II was a set of twin 0.45 m aperture, f/1.9 telescopes to be operated in stereo mode. The optical design was performed by Mel Kreitzer (1976) and Jacob Moskovich (1978) at OPCON Associates, Inc. Each telescope covers a field of view of $1.9^\circ \times 1.9^\circ$ and was expected to achieve a limiting magnitude of $m_v \simeq 18$ for a 10-second exposure. By scanning around the most probable burst location, a $16^\circ \times 16^\circ$ error box can be searched in 16 minutes. More accurate initial coordinates will permit faster scans or deeper images (Marshall et al., 1997). By co-adding frames, both ROTSE-I and ROTSE-II was to be able to detect objects considerably fainter than the limits quoted above. In particular, ROTSE-II was able to find optical transients at the levels discovered for GRB 970228 and GRB 970508.

The observation of a prompt optical flash from GRB 990123 convincingly demonstrated the value of autonomous robotic telescope systems. Pursuing a

program of rapid follow-up observations of GRBs. For this reason ROTSE developed a next-generation instrument, ROTSE-III, that continues the search for fast optical transients. The entire system was designed as an economical robotic facility to be installed at remote sites throughout the world. There are seven major system components: optics, optical tube assembly, CCD camera, telescope mount, enclosure, environmental sensing and protection, and data acquisition. Each is described in turn in the hope that the techniques developed will be useful in similar contexts elsewhere (Akerlof et al., 2003). ROTSE-III is a homogeneous worldwide array of 4 robotic telescopes. They were designed to provide optical observations of GRB afterglows as close as possible to the start of γ -ray emission. ROTSE-III is fulfilling its potential for GRB science, and provides optical observations for a variety of astrophysical sources in the interim between GRB events (Yost et al., 2006).

Ruiz-Velasco et al. (2007) report on follow-up observations of the GRB 060927 using the robotic ROTSE-IIIa telescope and a suite of larger aperture ground-based telescopes. They discuss the implications of this work for the use of GRBs as probes of the end of the dark ages and draw three main conclusions: (1) GRB afterglows originating from $z > 6$ should be relatively easy to detect from the ground, but rapid near-infrared monitoring is necessary to ensure that they are found; (2) the presence of large H_I column densities in some GRB host galaxies at $z > 5$ makes the use of GRBs to probe the reionization epoch via spectroscopy of the red damping wing challenging; and (3) GRBs appear crucial to locate typical star-forming galaxies at $z > 5$, and therefore the type of galaxies responsible for the reionization of the universe.

Quinby et al. (2012) presented a sample of 23 spectroscopically confirmed Type Ia supernovae (SNe Ia) that were discovered in the background of galaxy clusters targeted by ROTSE-IIIb and use up to 18 of these to determine the local ($\bar{z} = 0.05$) volumetric rate. They found that the total SNe Ia rate may be higher than the canonical value.

One more interesting result coming from ROTSE-III is relative to the Luminosity Function (LF) of GRBs. Indeed, Cui et al. (2014) estimated, from a uniform sample of 58 GRBs from observations with the ROTSE-III, the cumulative distribution of optical emission at 100 s, well described by an exponential rise and power-law decay, a broken power law, and Schechter LFs^(*). A single power-law (SPL) LF, on the other hand, is ruled out with high confidence.

(*) The Schechter luminosity function provides a parametric description of the space density of galaxies as a function of their luminosity.

3.11. The (B)urst (O)bserver and (O)ptical (T)ransient (E)xploring (S)ystem (BOOTES)

The Burst Observer and Optical Transient Exploring System (BOOTES) was considered as a part of the preparations for ESA's INTEGRAL satellite, and

was developed in Spain, as a Spanish-Czech collaboration, devoted to study optical emissions from GRBs. It makes use of two sets of wide-field cameras, 240 km apart, and two robotic 0.3-m telescopes. The first observing station (BOOTES-1) was located at the Estación de Sondeos Atmosféricos in Centro de Experimentación de El Arenosillo, a dark-sky site near Mazagón (Huelva), center owned by the Instituto Nacional de Técnica Aeroespacial (INTA).

The first light was obtained in July 1998. During the test phase, it has provided rapid follow-up observations with the wide-field cameras for 19 GRBs detected by BATSE aboard CGRO, and narrow-field imaging for 6 bursts. Limiting magnitudes for any GRB optical afterglow are $I \sim 13$ and $R \sim 16.5$, a few minutes after the events (Castro-Tirado et al., 1999, 2000).

The second observing station was opened in 2001 and it was located at the Estación Experimental de La Mayora (dubbed BOOTES-2), 240 km apart. The latter is run by the Consejo Superior de Investigaciones Científicas (CSIC). BOOTES-2 has been equipped with COLORES (Compact Low Resolution Spectrograph) (Rabaza et al., 2013). It is a spectrograph designed to be lightweight enough to be carried by the high-speed robotic telescope 60 cm (BOOTES-2). It works in the wavelength range of (3800 - 11500) Å and has a spectral resolution of (15 - 60) Å. The primary scientific target of the spectrograph is a prompt GRB follow-up, particularly the estimation of redshift.

In 2009 BOOTES started to expand abroad, adding stations BOOTES-3 in Lauder (South Island, New Zealand), BOOTES-4 (2011, Lijiang Astronomical Observatory in Yunnan, China, Guziy et al., 2013), BOOTES-5 (2013, San Pedro Martir, Mexico), BOOTES-6 (2021, Boyden Observatory, South Africa) and eventually finishing the world-wide coverage by BOOTES-7 (2023, San Pedro de Atacama, Chile).

Since the first light on 1998, more than a hundred of GRBs have been observed with BOOTES, some of them only ≈ 30 s after the onset of the γ -ray event. More in general BOOTES has been used for the follow-up of optical transient, such as the X-ray/Be system A0535+26/HDE245770 and the accreting black hole SS 433 (e.g. Caballero-García et al., 2014). Interesting results from BOOTES-2 and COLORES are those of the DG Canum Venaticorum (DG CVn). This is a very fast rotating star and this fact has been associated to the youth of the star: 30 Myr (Caballero-García et al., 2016b and the references therein). This star experienced a big flare that can be explained by the presence of (a) large active region(s) on the surface of the star. Such activity is similar to the most extreme solar flaring events. This points towards a plausible extrapolation between the behaviour from the most active red-dwarf stars and the processes occurring in the Sun (Caballero-García et al., 2015).

A contribution of BOOTES-2/COLORES has been given during the sub-second optical flaring in V404 Cyg during the 2015 outburst peak (Gandhi et al., 2016). Indeed, the most prominent optical emission line in the case of V404 Cyg is H_{α} , which falls in the r' band. They estimated the relative flux contribution of H_{α} , being the emission line strength relative to continuum strongly variable.

One of the most significant result of this investigation is the following: under the compact jet scenario, it is possible to place limits on the magnetic field strength at the synchrotron emission zone of $B \leq 2 \times 10^5$ G, and a zone size $R \geq 140 R_G$. If the fastest flares arise within this zone, the variability time-scale of the unresolved flares of < 24 ms implies $R \leq 500 R_G$, being R_G the gravitational radius.

An important contribution of BOOTES to the knowledge of GRBs is coming from ~ 70 GNC (GRB Coordinates Network, Circular Service) publications where optical observations of different GRBs have been reported. They can be found in the NASA-ADS under the name Caballero-Garcia, M.D. from 2016 to 2022 (March 17th).

3.12. The Russian global network of telescopes robot MASTER

The Russian global network of telescopes robot MASTER has the fundamental advantage that the observations are performed with identical telescopes equipped with identical photometers. No other network of telescopes can boast such a feature.

I will discuss in the following some of the numerous important results obtained with the MASTER Robotic Net.

On 2015 June 15, the Swift space observatory discovered that the Galactic black hole candidate V 404 Cyg was undergoing another active X-ray phase, after 25 years of inactivity. The 12 telescopes of the MASTER Global Robotic Net located at six sites across four continents were the first ground-based observatories to start optical monitoring of the microquasar after its gamma-ray wake up at 18h 34m 09s U.T. on 2015 June 15 (Lipunov et al., 2016a). The discovery of variable optical linear polarization, changing by 4%-6% over a timescale of ~ 1 hr, on two different epochs, allows to conclude that the additional variable polarization arises from the relativistic jet generated by the black hole in V 404 Cyg. The polarization variability correlates with optical brightness changes, increasing when the flux decreases. The relativistic jet generated by the black hole was only observed until 2015 June 15 in nonthermal radio and hard X-ray emission.

Gorbovskey et al. (2016) reported early optical linear polarization observations of two GRBs made with the MASTER Robotic Net. They found the minimum polarization for GRB 150301B to be 8% at the beginning of the initial stage, whereas they detected no polarization for GRB 150413A either at the rising branch or after the burst reached the power-law afterglow stage. This is the earliest measurement of the polarization (in cosmological rest frame) of GRBs. By the way, they reported the discovery of the optical counterpart of one of the two bursts: GRB 150413A. This GRB was detected by BAT instrument of Swift observatory (Markwardt et al. 2015), and soon after was associated to an optical transient by the telescope of MASTER Robotic Net located at Tunka astrophysical centre near Baikal lake.

Important contribution of the MASTER Robotic Net was the early discovery of the optical afterglow of the GRB 140801A in the 137 deg^2 3σ error-box of the Fermi Gamma-ray Burst Monitor (GBM) (Lipunov et al., 2016b). Indeed, MASTER is the only observatory that automatically reacts to all Fermi alerts. GRB 140801A is one of the few GRBs whose optical counterpart was discovered solely from its GBM localization. The optical afterglow of GRB 140801A was found by MASTER Global Robotic Net 53 s after receiving the alert, making it the fastest optical detection of a GRB from a GBM error-box. Spectroscopy obtained with the 10.4-m Gran Telescopio Canarias and the 6-m Big Telescope Alt-azimuth of the Special Astrophysical Observatory of the Russian Academy of Sciences reveals a redshift $z = 1.32$. The rest-frame bolometric isotropic energy release and peak energy of the burst are $E_{\text{iso}} = 5.54_{-0.24}^{+0.26} \times 10^{52}$ erg and $E_{\text{p,rest}} \simeq 280$ keV, respectively, which is consistent with Amati's relation.

Lipunov et al. (2017a) presented the discovery of the rare explosive star MASTER OTJ004207.99+405501.1 – a luminous red nova (LRN) – in the Andromeda galaxy M31 N2015-01a, and long-term observations of its light curve with the MASTER network of robotic telescopes. Monitoring has been carried out for 72 d after the discovery of this LRN. They found that the multicolour passband light curves of the LRN are consistent with an initial common envelope radius of $10 R_{\odot}$, a merger mass of $3 M_{\odot}$ and an explosion energy of 3×10^{48} erg. As a result, the phenomenon of novae consists of two classes: classical nuclear novae and more rare events (red novae) connected with the loss of compact common envelopes.

One of the most important results obtained with the Global MASTER Robotic Net has been reported by Lipunov et al. (2017b). They received the GW 150914 alert message with the error region just over a day after the GW-event, on 2015 September 16. All telescopes in the MASTER network began observing different parts of the GW 150914 error region when the corresponding areas became visible. The first images in response to the GW 150914 alert were taken at the MASTER-SAAO observatory at 2015 September 16 20:18:11 UT, and the follow-up was extended until September 22. The results obtained with this campaign of observations are consistent with the conclusion that GWs from GW 150914 were produced in a binary black hole merger. The detection of this event was predicted in 1997 on the basis of the Scenario Machine population synthesis calculations, as discussed in Lipunov et al. (2017c and in the references therein).

During this campaign of observations eight optical transient (OTs) were detected. Among them there are: (1) MASTER OT J040938.68-541316.9 (a possible SN discovery); (2) MASTER OT J070747.72-672205.6 (a possible U Gem type (dwarf nova outburst) detection); (3) MASTER OT J042822.91-604158.3 discovery (possible dwarf nova outburst). The data cannot exclude that MASTER OT J040938.68-541316.9 exploded on 2015 September 14.

On 2017 August 17 the merger of two compact objects with masses consistent with two neutron stars was discovered through gravitational-wave (GW170817),

γ -ray (GRB 170817A), and optical (SSS17a/AT2017gfo) observations. The optical source was associated with the early-type galaxy NGC 4993 at a distance of just ~ 40 Mpc, consistent with the gravitational-wave measurement, and the merger was localized to be at a projected distance of ~ 2 kpc away from the galaxy's center (Abbott et al., 2017a,b).

Lipunov et al. (1995) predicted the NS-NS merger at a distance of ≤ 50 Mpc and the possibility of detecting GWs!

This prediction was born by the "Scenario Machine" that describes the evolution of gravimagnetic rotators (Lipunov, 1987; Lipunov, & Postnov, 1988), and commented by Giovannelli (2016).

The MASTER Global Robotic Net telescopes obtained the first image of the NGC 4993 host galaxy. An optical transient, MASTER OTJ130948.10-232253.3/SSS17a was later found, which appears to be a kilonova resulting from the merger of two neutron stars (NSs) (Lipunov et al., 2017d). They described this independent detection and photometry of the kilonova made in white light, and in B, V, and R filters. They noted that the luminosity of this kilonova in NGC 4993 is very close to those measured for other kilonovae possibly associated with GRB 130603 and GRB 080503. The agreement between the observed absolute magnitudes and characteristic luminosities evoke the old idea about viewing GRBs as standard candles (Lipunov, Postnov & Prokhorov, 2001). However, we are now dealing with kilonovae that accompany short GRB events. Here there is rather an analogy with Type Ia SNe. Both kinds of event may represent collisions of compact stars: binary white dwarfs and binary NSs in the case of supernovae and kilonovae, respectively.

GRB 161017A was first detected at γ -ray wavelengths by the Lomonosov and Swift instruments. Following the Swift's transmission of a GCN alert, the MASTER robotic telescopes were automatically directed to the preliminary GRB source coordinates to begin their optical observations (Sadovnichy et al., 2018). Following the MASTER automatic observation, the analysis software reported the detection of a GRB optical emission and signaled the world's largest optical telescope, the 10.4 m Gran Telescopio Canarias (GTC) located in the Canary Islands, which recorded the burst and from the redshift value determined the host galaxy to be about 10 billion light years away.

Its γ -ray emission measured up to 0.5 MeV. At a redshift $z = 2.0127$, the most recent findings are $H_0 = 67.3 \text{ km s}^{-1} \text{ Mpc}^{-1}$, $\Omega_\Lambda = 0.685$, $\Omega_M = 0.315$ (Planck Collaboration et al., 2016), $E_{\text{iso}} \simeq 10^{53} \text{ erg}$ (for a GRB fluence of $3 \times 10^{-6} \text{ erg s}^{-1}$ and a luminosity distance of $D_L = 16.081 \text{ Gpc}$). There is no apparent forward shock emission in the optical light curve, and only an afterglow emission component is visible, peaking at around 100 s. If we interpret these observations according to the correlation provided by Liang et al. (2010), it is possible to infer the initial Lorentz factor to be $\Gamma_0 \sim 300$.

MASTER Robotic Net is useful also for the study of SNe. Indeed, for example, MASTER OT J120451.50+265946.6 (M 12045), discovered by the MASTER Global Robotic Net, is a Type Ib supernova (SN) that exploded in NGC

4080. Singh et al. (2019) presented the BVRI photometric and spectroscopic observations up to ~ 250 days since B_{\max} . At the time of discovery the SN was a few weeks past maximum light and their observations capture the linearly declining light curve phase. M 12045 declined faster as compared to SNe 1999dn and 2009jf at comparable epochs. Rigorous spectroscopic monitoring revealed that M 12045 is a normal Type Ib SN. The analysis of the nebular phase spectra indicated that $\sim 0.90 M_{\odot}$ of O is ejected in the explosion. The line ratio of $[O\text{I}]$ and $[\text{CaII}]$ in the nebular phase supports a massive WR progenitor with main sequence mass of $\sim 20 M_{\odot}$.

Important efforts have been performed in searching for the High-Energy (HE) neutrino progenitor. Lipunov et al. (2020) presented the earliest astronomical observation of a HE neutrino error box of which the variability was discovered after HE-neutrino detection. The one robotic telescope of the MASTER global international networks automatically imaged the error box of the very HE-neutrino event IceCube-170922A. Observations were carried out in minutes after the detection of the IceCube-170922A neutrino event, obtained by the IceCube observatory at the South Pole. MASTER found the blazar TXS 0506+056 to be in the off-state after one minute and then switched to the on-state no later than two hours after the event. The effect is observed at a 50σ significance level.

The event that they discovered, namely the decrease of the brightness of the TXS 0506+056 blazar near the neutrino detection time, provides complementary and very compelling evidence for the link between the blazar and the IceCube-170922 neutrino event. They analyzed also archival data (MASTER unique 518 photometry data for 16 yr), which they found to be consistent with this fact. They also proposed a hypothesis explaining the anticorrelation of the optical and neutrino flux. An increase in neutrino flux means that up to half of the protons disappear. If one assumes that these protons produce synchrotron optical radiation, then any increase in neutrino luminosity will lead to a decrease in the optical brightness of the blazar.

Interesting results are coming from polarimetric measurements obtained with the RINGO3 (Słowikowska et al., 2016) and MASTER II (Lipunov et al., 2010) polarimeters on GRB 190114C (Jordana-Mitjans et al., 2020). They report multicolor optical imaging and polarimetry observations of the afterglow of the first TeV-detected GRB, GRB 190114C. Observations began 31 s after the onset of the GRB and continue until ~ 7000 s postburst. The unexpectedly low intrinsic polarization degree in GRB 190114C can be explained if largescale jet magnetic fields are distorted on timescales prior to reverse shock emission.

Buckley et al. (2021) reported on results of spectropolarimetry of the afterglow of the long GRB 191221B, obtained with SALT/RSS and VLT/FORS2, as well as photometry from two telescopes in the MASTER Global Robotic Net, at the MASTER-SAAO (South Africa) and MASTER-OAFA (Argentina) stations. Prompt optical emission was detected by MASTER-SAAO 38 s after the alert, which dimmed from a magnitude (white-light) of ~ 10 to 16.2 mag over a period of ~ 10 ks, followed by a plateau phase lasting ~ 10 ks and then a decline to \sim

18 mag after 80 ks. They concluded that the GRB 191221B optical afterglow is powered by slow-cooling synchrotron emission, ruling out a reverse-shock origin.

3.13. Very small satellites for multifrequency astrophysics

I do not want to enter in a discussion about small (and very small) satellites. However, I suggest to the reader to see the fundamental paper "*Small satellites for space science: A COSPAR scientific roadmap*" by Millan et al. (2019) in which there are the recommendations to: (i) the science community; (ii) the space industry; (iii) the space agencies; (iv) the policy makers; (v) the COSPAR.

A fundamental paper about "*Global Trends in Small Satellites*" discussed about the future of small satellites (smallsats) starting about their definition. Indeed, there is no universally accepted definition of a small satellite. Various groups and reports have classified smallsats according to their mass, volume, cost, capabilities, or some combination thereof. A reasonable compromise defines smallsats as satellites with masses < 200 kg. However, some exceptions are possible (Lal et al., 2017).

The global consultancy Euroconsult predicts that, whereas fewer than 700 smallsats were launched from 2006-2015, up to 3,600 smallsats are likely to be launched in the coming decade for a variety of missions. This number could reach well over 10,000 if even a fraction of the planned broadband constellations are deployed. This fact pose a problem about the overcrowding and debris concerns, especially for the Low Earth Orbits (LEO). This renders unsafe satellite operation in LEO orbits. In this scenario, as a result of the growing number of smallsats in LEO and one or more high debris-causing collisions, it is unsafe to operate satellites in orbits between 500 and 1,200 km without risking collision. As a consequence, LEO is no longer viable for widespread commercialization without government reimbursement. Further, smallsats are larger and more expensive for operation in different orbits. Smallsats operating in higher orbits have an increased cost to manufacture, given the need for radiation and higher power, and are more costly to launch and operate (Behrens & Lal, 2019).

About the use in astronomy of very small satellites see the presentation *CubeSats in astronomy and astrophysics* by Cahoy (2015), where a panorama of the potential use of these Cubesats for enhancing the knowledge of many problems in different fields of astrophysics is discussed.

An interesting paper critically discuss the opportunities for astrophysics of using smallsats, from Radio-, to Infrared- to HE-astronomy until the hunt to exoplanets and the "mystery" of solar system, by studying the astrobiology involved in (Serjeant, Elvis & Tinetti, 2020). The potential science questions are indeed both biological and chemical. And finally smallsats are often used to increase the Technology Readiness Level (TRL) of a satellite component by demonstrating capability in an operational environment. All these future possibilities are becoming real as the cost and technical barriers to smallsat-astronomy are reduced, one possible overarching consequence of increasing the numbers of PI-led

missions is the impact on and from Open Science. Observatory missions typically have raw data proprietary lifetimes of 6-12 months, while PI missions and instruments sometimes have much more restrictive policies. Initiatives such as the European Open Science Cloud (Ayrís et al., 2016) aim to make all data FAIR (Findable, Accessible, Interoperable, Reusable), which in astronomy usually involves, among other things, the integration of products into the Virtual Observatory (Pasian et al., 2016). Meanwhile, data management and deposition plans are increasingly being required by funding bodies. Commissioning novel instrumentation can sometimes be a sound justification for extended proprietary lifetimes, but existing software, data standards and data repositories can still represent a significant cost saving to a small mission. The future smallsat-astronomy community could therefore do well to maintain the open data culture from observatories, not just for exploiting existing standards and repositories, but also for teams to be eligible for follow-on funding in the current climate of open data.

4. Conclusions

I believe this review article is helpful in illustrating the impact of using robotic telescopes on advancing knowledge about our Universe. In fact, their contribution ranges from the various fields of "classical" astrophysics to the discovery of exoplanets which constitutes one of the most fascinating themes of current research. Undoubtedly, the advantages of robotic telescopes are much greater than the technical difficulties of their use. Indeed, with networks of robotic telescopes spread across the globe at all longitudes and latitudes, surveys of cosmic sources can be made seamlessly. This implies a deeper understanding of the physical phenomena occurring in the target sources.

Because of a reasonable length of this paper, I have been obliged to make a strong selection of the arguments discussed, that however are, in my opinion, sufficient to demonstrate the importance of the results obtained with different networks of robotic telescopes.

Acknowledgments. This research has made use of The NASA's Astrophysics Data System.

References

- Abbott, B.P. et al. (LIGO Scientific Coll. and Virgo Coll.): 2017a, PhRvL 119, Issue 16, id. 161101
- Abbott, B.P. et al. (LIGO Scientific Collaboration and Virgo Collaboration, Fermi GBM, INTEGRAL, IceCube Collaboration, AstroSat Cadmium Zinc

Telluride Imager Team, IPN Collaboration, The Insight-HXMT Collaboration, ANTARES Collaboration, The Swift Collaboration, AGILE Team, The 1M2H Team, The Dark Energy Camera GW-EM Collaboration and the DES Collaboration, The DLT40 Collaboration, GRAWITA: GRAvitational Wave Inaf TeAm, The Fermi Large Area Telescope Collaboration, ATCA: Australia Telescope Compact Array, ASKAP: Australian SKA Pathfinder, Las Cumbres Observatory Group, OzGrav, DWF (Deeper, Wider, Faster Program), AST3, and CAASTRO Collaborations, The VINROUGE Collaboration, MASTER Collaboration, J-GEM, GROWTH, JAGWAR, Caltech-NRAO, TTU-NRAO, and NuSTAR Collaborations, Pan-STARRS, The MAXI Team, TZAC Consortium, KU Collaboration, Nordic Optical Telescope, ePESSTO, GROND, Texas Tech University, SALT Group, TOROS: Transient Robotic Observatory of the South Collaboration, The BOOTES Collaboration, MWA: Murchison Widefield Array, The CALET Collaboration, IKI-GW Follow-up Collaboration, H.E.S.S. Collaboration, LOFAR Collaboration, LWA: Long Wavelength Array, HAWC Collaboration, The Pierre Auger Collaboration, ALMA Collaboration, Euro VLBI Team, Pi of the Sky Collaboration, The Chandra Team at McGill University, DFN: Desert Fireball Network, ATLAS, High Time Resolution Universe Survey, RIMAS and RATIR, and SKA South Africa/MeerKAT): 2017b, ApJL 848, Issue 2, article id. L12, 59 pp.

Akerlof, C. et al.: 2000, AJ 119, Issue 4, 1901-1913.

Akerlof, C.W. et al.: 2003, PASP 115, Issue 803, 132-140. .

Albrow, M. et al.: 1996, in *Astrophysical applications of gravitational lensing*, C.S. Kochanek & Jacqueline N. Hewitt (Eds.), IAU Symp. 173, Kluwer Academic Publishers; Dordrecht, pp. 227-228.

Albrow, M. et al.: 1998, ApJ 509, Issue 2, 687-702.

Allan, A. et al.: 2004, in *Advanced Software, Control, and Communication Systems for Astronomy*. Lewis, Hilton, Raffi, Gianni (Eds.), Proc. of the SPIE 5496, 313-322.

Allan, A., Naylor, T., Saunders, E.S.: 2006, Astron. Nach. 327, Issue 8, p.767

Ayris, P. et al.: 2016, *Realising the European Open Science Cloud*, Publ. Office of the European Union, Luxembourg.

Batista, V.: 2018, in *Handbook of Exoplanets*, ISBN 978-3-319-55332-0. Springer International Publishing AG, part of Springer Nature, 2018, id. 120.

Behrens, J.R., Lal, B.: 2019, New Space 7, issue 3, 126-136.

Bennett, D. et al.: 2019, in *Astro2020: Decadal Survey on Astronomy and Astrophysics*, science white papers, no. 505; Bulletin of the AAS 51, Issue 3, id. 505.

Blackman, J.W et al.: 2021, Nature 598, Issue 7880, 272-275.

- Bloom, J., Castro-Tirado, A.J., Hanlon, L., Kotani, T. (Eds.): 2010, *I Workshop on Robotic Autonomous Observatories*, Advances in Astronomy, Vol. 2010.
- Bond, I.A. et al.: 2017, MNRAS 469, Issue 2, 2434-2440.
- Boroson, T. et al.: 2014, Proc. of the SPIE 9149, id. 91491E, 10 pp.
- Bredall, J.W. et al.: 2020, MNRAS 496, Issue 3, 3257-3269.
- Brown, T.M. et al.: 2013, PASP, 125, Issue 931, 1031-1090.
- Brown, A. et al.: 2018, in *The 20th Cambridge Workshop on Cool Stars, Stellar Systems and the Sun*, Online at <http://coolstars20.cfa.harvard.edu/>, cs20, id. 28.
- Buckley, D., 2015, talk at the Palermo Workshop on " *The Golden Age of Cataclysmic Variables and Related Objects - III* " .
- Buckley, D.A.H. et al.: 2021, MNRAS 506, Issue 3, 4621-4631.
- Caballero-García, M.D. et al.: 2014, in *10 Years of Discovery (SWIFT 10)*, Online at <http://pos.sissa.it/cgi-bin/reader/conf.cgi?confid=233>, id. 126.
- Caballero-García, M.D. et al.: 2015, MNRAS 452, Issue 4, 4195-4202.
- Caballero-García, M.D., Pandey, S.B., Hiriart & Castro-Tirado, A.J. (Eds.): 2016, *IV Workshop on Robotic Autonomous Observatories*, RMxAC Vol. 48.
- Caballero-García, M.D. et al.: 2016, in *IV Workshop on Robotic Autonomous Observatories*, María Dolores Caballero-García, Shasi B. Pandey, David Hiriart & Alberto J. Castro-Tirado (Eds.), Rev. Mex. A&A, (Serie de Conferencias) Vol. 48, 59-63.
- Caballero-García, M.D., Pandey, S.B. & Castro-Tirado, A.J. (Eds.): 2019, *V Workshop on Robotic Autonomous Observatories*, RMxAC Vol. 51.
- Cahoy, K.: 2015, Presentation at the SSB CubeSat Symposium, Irvine, CA, 2 September 2015. Online at http://sites.nationalacademies.org/cs/groups/ssbsite/documents/webpage/ssb_167819.pdf
- Castro-Tirado, A.J. et al.: 1999, A&A Suppl. Ser. 138, 583-585.
- Castro-Tirado, A.J. et al.: 2000, in *Gamma-Ray Bursts*, AIP Conf. Proc. 526, 260-264.
- Castro Cerón, J.M.: 2011, talk at the Frascati Workshop 2011 on " *Multifrequency Behaviour of High Energy Cosmic Sources* " .
- Castro-Tirado, A.J.: 2008, in *3rd Symposium of the Astrophysics Group of the Spanish Royal Physical Society (RSEF)*, A. Ulla & M. Manteiga (Eds.), Lecture Notes and Essays in Astrophysics 3, 131.
- Castro-Tirado, A.J.: 2010a, Adv. Astron. 2010, Article ID 570489, 8 pp.
- Castro-Tirado, A.J.: 2010b, Adv. Astron. Vol. 2010, Article ID 824731, 1 p.

- Castro-Tirado, A.J. et al.: 2012, in *Second Workshop on Robotic Autonomous Observatories*, Sergey Guziy, Shashi B. Pandey, Juan C. Tello & Alberto J. Castro-Tirado (Eds.), ASI Conf. Ser. 7, 313-320.
- Castro-Tirado, A.J. Pandey, S.B. & Caballero-García (Eds.): 2021, *VI Workshop on Robotic Autonomous Observatories*, RMxAC Vol. 53.
- Cui, X.H. et al.: 2014, ApJ 795, Issue 2, article id. 103, 6 pp.
- Deeg, H.J., Alonso, R.: 2018, in *Handbook of Exoplanets*, ISBN 978-3-319-55332-0. Springer International Publishing AG, part of Springer Nature, 2018, id. 117.
- Dominik, M. et al.: 2004, in *Extrasolar planets: Today and Tomorrow*, J.-P. Beaulieu, A. Lecavelier des Etangs, & C. Terquem (Eds.), ASP Conf. Ser. 321, 121-122.
- Edwards, B. et al.: 2021, Astron. Theory, Observ. and Meth. J. 1, No. 1, 1-12. Also arXiv:2111.10350.
- Eyer, L.: 1999, Baltic Astron. 8, 321-324.
- Eyer, L., Cuypers, J.: 2000, in *The Impact of Large-Scale Surveys on Pulsating Star Research*, L. Szabados & D. Kurtz (Eds.), ASP Conf. Ser. 203, 71-72.
- Fujiwara, T. et al.: 2017, in *7 years of MAXI: monitoring X-ray Transients*, held 5-7 December 2016 at RIKEN. Online at <https://indico2.riken.jp/indico/conferenceDisplay.py?confId=2357>, p. 277.
- Gandhi, P. et al.: 2016, MNRAS 459, Issue 1, 554-572.
- Gao, H. et al.: 2015. ApJ 810, Issue 2, article id. 160, 13 pp.
- Gaudi, B.S et al.: 2002, ApJ 566, Issue 1, 463-499.
- Giovannelli, F.: 2016, in *Proceedings of the 4th Ann. Conf. on High Energy Astrophysics in Southern Africa (HEASA 2016)*. Online at <http://pos.sissa.it/cgi-bin/reader/conf.cgi?confid=275>, id. 31.
- Gorbovskoy, E.S. et al.: 2016, MNRAS 455, 3312-3318.
- Guziy, S., Pandey, S.B., Tello, J.C. & Castro-Tirado, A.J. (Eds.): 2012, *II Workshop on Robotic Autonomous Observatories*, Astron. Soc. of India Conf. Ser., Vol. 7.
- Guziy, S. et al.: 2013, in *Gamma-ray Bursts: 15 Years of GRB Afterglows*. A.J. Castro-Tirado, J. Gorosabel & I.H. Park (Eds.), EAS Publ. Ser. 61, 251-254.
- Hamuy, M. et al.: 2006, PASP 118, Issue 839, 2-20.
- Hamuy, M. et al.: 2012, Mem. S.A.It. Vol. 83, 388.
- Herald, A. et al. (OGLE Coll.; MOA Coll.; The Spitzer Team; The MiNDSTEP Consortium; The LCO & μ FUN Coll.): 2022, arXiv:2203.04034.




- Hermes, J.J.: 2018, in *Handbook of Exoplanets*, ISBN 978-3-319-55332-0. Springer International Publishing AG, part of Springer Nature, 2018, id. 6.
- Hessman, F.V.: 2001a, in *Small Telescope Astronomy on Global Scales*, Bohdan Paczynski, Wen-Ping Chen & Claudia Lemme (Eds.), ASP Conf. Ser. 246, 13.
- Hessman, F.V.: 2001b, in *Small Telescope Astronomy on Global Scales*, Bohdan Paczynski, Wen-Ping Chen & Claudia Lemme (Eds.), ASP Conf. Ser. 246, 357.
- Hidas, M.G. et al.: 2008, *Astron. Nach.* 329, Issue 3, 269-270.
- Hirao, Y. et al. (The MOA Coll.; The OGLE Coll.): 2017, *AJ* 154, Issue 1, article id. 1, 8 pp.
- Hirao, Y. et al. (The OGLE Coll.; The KMTNet Coll.; The Spitzer Team; The LCO and μ FUN Follow-up Teams; The MindSTeP Coll.; The IRSF Team): 2020, *AJ* 160, Issue 2, id. 74.
- Hudec, R. et al.: 2017, talk at the Frascati Workshop 2017 on *Multifrequency Behaviour of High Energy Cosmic Sources - XII*, Mondello, Palermo, Italy, 12-17 June.
- Jordana-Mitjans, N. et al.: 2020, *ApJ* 892, Issue 2, id. 97, 17 pp.
- Jung, Y.K. et al.: 2020a, *AJ* 160, Issue 3, id. 148, 18 pp.
- Jung, Y.K. et al.: 2020b, *AJ* 160, Issue 6, id. 255, 11 pp.
- Kokori, A. et al.: 2021, *Experimental Astronomy*, Online First at <https://doi.org/10.1007/s10686-020-09696-3>.
- Kreitzer, M.H.: 1976, *Image Quality Criteria for Aberrated Systems*, PhD Thesis, The University of Arizona (USA), Source: Dissertation Abstracts International, Volume: 37-09, Section: B, page: 4538.
- Kramer, M.: 2018, in *Handbook of Exoplanets*, ISBN 978-3-319-55332-0. Springer International Publishing AG, part of Springer Nature, 2018, id. 5.
- Lal, B. et al.: 2017, IDA SCIENCE & TECHNOLOGY POLICY INSTITUTE, Paper P-8638; Log: H 17-000435.
- Lam, C.Y. et al.: 2022, arXiv:2202.01903.
- Lazio, T.J.W.: 2018, in *Handbook of Exoplanets*, ISBN 978-3-319-55332-0. Springer International Publishing AG, part of Springer Nature, 2018, id. 9.
- Liang, En-Wei et al.: 2010, *ApJ* 725, Issue 2, 2209-2224.
- Lipunov, V.M.: 1987, *Ap&SS* 132, no. 1, 1-51.
- Lipunov, V.M.: 1995, in *Frontier Objects in Astrophysics and Particle Physics*, F. Giovannelli & G. Mannocchi (Eds.), SIF, Bologna, Italy, 47, 61-76.

- Lipunov, V.M., Postnov, K.A., Prokhorov, M.E.: 2001, ARep 45, Issue 3, 236-240.
- Lipunov, V.M., Postnov, K.A.: 1988, Ap&SS 145, no. 1, 1-45.
- Lipunov, V., Kornilov, V. et al.: 2010, Adv. Astron. article id. 349171, 6 pp.
- Lipunov, V.M. et al.: 2016a, ApJ 833, Issue 2, article id. 198, 12 pp.
- Lipunov, V.M. et al.: 2016b, MNRAS 455, 712-724.
- Lipunov, V.M. et al.: 2017a, MNRAS 470, 2339-2350.
- Lipunov, V.M. et al.: 2017b, MNRAS 465, 3656-3667.
- Lipunov, V.M. et al.: 2017c, New Astron. 51, 122-127.
- Lipunov, V.M. et al.: 2017d, ApJL 850, Issue 1, article id. L1, 9 pp.
- Lipunov, V.M. et al.: 202, ApJL 896, Issue 2, id. L19, 5 pp.
- Liu, C-J., Zhen Yao, Z., Ding, W-B.: 2017, Res. Astron. Astrophys. 17, No. 8, 78 (10 pp).
- Malbet, F., Sozzetti, A.: 2018, in *Handbook of Exoplanets*, ISBN 978-3-319-55332-0. Springer International Publishing AG, part of Springer Nature, 2018, id. 196.
- Markwardt C.B. et al.: 2015, GRC Circ., 17688, 1.
- Marshall, S. et al.: 1997, AAS 191st AAS Meeting, id. 48.15; Bulletin of the AAS Vol. 29, p. 1290.
- Millan, R.M. et al.: 2019, Adv. Spa. Sci. 64, Issue 8, 1466-1517.
- Monard, L.A.G.: 2008, CBET 1315.
- Moskovich, J.: 1978, in *Computer-Aided Optical Design*, R.E. Fischer. Bellingham, WA (Eds.), SPIE Proc. Vol. 147. Society for Photo-Optical Instrumentation Engineers, p. 149.
- Pasian, F. et al.: 2016, *ASTERICS: Addressing Cross-Cutting Synergies and Common Challenges for the Next Decade Astronomy Facilities*, in *Astronomical Data Analysis Software and Systems XXV* 512, 57-60.
- Pastorello, A. et al.: 2019, VizieR On-line Data Catalog: J/MNRAS/453/3649. Originally published in: 2015MNRAS.453.3649P.
- Pignata, G. et al.: 2009, AIPC, 1111, 551.
- Planck Collaboration; Ade, P.A.R. et al.: 2016, A&A 594, id. A13, 63 pp.
- Pueyo, L.: 2018, in *Handbook of Exoplanets*, ISBN 978-3-319-55332-0. Springer International Publishing AG, part of Springer Nature, 2018, id. 10.
- Quimby, R.M. et al.: 2012, AJ 144, Issue 6, article id. 177, 16 pp.
- Rabaza, O. et al.: Rev. Sci. Instr. 84, Issue 11, id. 114501-114501-9.

- Ranc, C.: 2015a, Ph.D. Thesis, Institut d'Astrophysique de Paris, Université Pierre et Marie Curie - Paris VI, 326 pages.
- Ranc, C. et al.: 2015b, *A&A* 580, id. A125, 16 pp.
- Ranc, C. et al.: 2021, *MNRAS* 506, Issue 1, 1498-1506.
- Ruiz-Velasco, A.E. et al.: 2007, *ApJ* 669, Issue 1, 1-9.
- Sackett, P.N. et al.: 2003, in *Bioastronomy 2002: Life Among the Stars*, R. Norris, C. Oliver & F. Stootman (Eds.), IAU Symp. 213, ASP Conf. Ser. TBD, 1-5.
- V. A. Sadovnichy, V.A. et al.: 2018, *ApJ*, 861, Issue 1, article id. 48, 12 pp.
- Schaefer, B.E., King, J.R., Deliyannis, C.P.: 2000, *ApJ* 529, Issue 2, 1026-1030.
- Schreiber, M.R. et al.: 2019, *ApJL* 887, Issue 1, article id. L4, 8 pp.
- Serjeant, S., Elvis, M., Tinetti, G.: 2020, *Nature Astron.* 4, 1031-1038.
- Shimokawabe, T. et al.: 2009, *AIPC* 1133, 79.
- Shin, In-Gu et al.: 2022, *arXiv:2201.04312*.
- Sicilia-Aguilar, A. et al.: 2017, *A&A* 607, id. A127, 27 pp.
- Singh, M. et al.: 2019, *MNRAS* 485, Issue 4, 5438-5452.
- Skowron, J. et al. (The OGLE Coll.; The MOA Coll.; The Wise group; The μ FUN Coll.; The PLANET Coll.; The RoboNet Coll.; The MiNDSTEp consortium): 2015, *ApJ* 804, Issue 1, article id. 33, 12 pp.
- Ślowikowska, A., et al.: 2016, *MNRAS* 458, Issue 1, 759-771.
- Tachibana, Y., Kawai, N., Pike, S. (for the MAXI team and the MITSuME team): 2015, in *5th Fermi Symposium Proc.: Nagoya, Japan: 20-24 Oct, 2014*, *arXiv:1502.03610*.
- Tachibana, Y. et al.: 2017, *PASJ* 69, Issue 4, id. 63.
- Tachibana, Y. et al.: 2018, *PASJ* 70, Issue 5, id. 92.
- Tanvir, N.R. et al.: 2009, *Nature* 461, Issue 7268, 1254-1257.
- Tello, J.C., Riva, A., Hiriart, D. & Castro-Tirado, A.J. (Eds.): 2014, *III Workshop on Robotic Autonomous Observatories*, RMxAC, Vol. 45.
- Tsapras, Y. et al.: 2009, *Astron. Nachr.* 330, No. 1, 4-11.
- Valenti, S. et al.: 2014, *MNRAS* 438L, Issue 1, L101-L105.
- Valenti, S. et al.: 2015, *ApJL* 813, Issue 2, article id. L36, 5 pp.
- Van Dyk, S.D. et al.: 2012, *AJ* 143, Issue 1, article id. 19, 12 pp.
- Vestrand, W.T. et al.: 2002, in *Advanced Global Communications Technologies for Astronomy II*, Kibrick, Robert I (Ed.), Proc. of the SPIE 4845, 126-136.
- Voges, W. et al.: *A&A* 349, 389-405.

- Watson, M.G.: 2003, in *Astronomical Data Analysis Software and Systems XII*, H.E. Payne, R.I. Jedrzejewski & R.N. Hook (Eds.), ASP Conf. Ser. 295, 107-116.
- White, R.R. et al.: 2004, in *Advanced Software, Control, and Communication Systems for Astronomy*. Lewis, H., Raffi, G. (Eds.), Proc. of the SPIE, Vol. 5496, 302-312.
- Woźniak, P.R. et al.: 2002, in *Virtual Observatories*, Szalay, Alexander S (Ed.), Proc. of the SPIE 4846, 147-157.
- Woźniak, P.R. et al.: 2004, AJ 127, Issue 4, 2436-2449.
- Wright, J.T.: 2018, in *Handbook of Exoplanets*, ISBN 978-3-319-55332-0. Springer International Publishing AG, part of Springer Nature, 2018, id. 4.
- Yee, J.C. et al.: 2018, arXiv:1803.07921.
- Yee, J.C. et al.: 2021, AJ 162, Issue 5, id. 180, 22 pp.
- Yost, S.A. et al.: 2006, Astron. Nach. 327, Issue 8, p. 803.
- Zang, W. et al.: 2020, arXiv:2010.08732.
- Zang, W. et al.: 2021a, AJ 162, Issue 4, id. 163, 18 pp.
- Zang, W. et al.: 2021b, Res. A&A 21, Issue 9, id. 239, 19 pp.

D50: Autonomous robotic telescope in Ondřejov

J. Štrobl¹ , M. Jelínek¹ , C. Polášek¹ and R. Hudec^{1,2} 

¹ *Astronomical Institute of the Czech Academy of Sciences, Ondřejov, Czech Republic*

² *Czech Technical University in Prague, Prague, Czech Republic*

Received: August 21, 2023; Accepted: November 2, 2023

Abstract. The D50 is an autonomous robotic telescope, located at the Ondřejov observatory in the Czech Republic. Completed in 2007, the telescope's primary purpose was and is to respond to gamma-ray burst detections. After several years of use, some parts of the telescope have been redesigned to be more reliable and better suited to its primary purpose. In addition, the telescope serves as a testbed for development and student projects, so it is continuously being improved in hardware and software. We present the current status and parameters of the telescope as well as the level of data processing automation we have achieved.

Key words: gamma rays: bursts – instrumentation: miscellaneous – telescopes

1. Introduction

The D50 telescope is located at the Ondřejov observatory in the Czech Republic, at coordinates 49.909376N 14.781358E, at an altitude of 527 m above sea level.

In 1996 we started to develop and use a new small robotic telescope BART (Štrobl et al., 2019), primarily for the observation of optical counterparts of gamma-ray bursts (GRBs). Due to the relatively low accuracy of the localization of GRBs, the telescope was equipped with a wide-field camera, and the automatic control software allowed for a prompt response to the detection transmitted by the GCN network (Barthelmy, 2008).

Long before the discovery of the first optical detection of GRBs (GRB 970228, van Paradijs et al. 1997), many scientists expected for various reasons GRBs to be accompanied by low-energy emissions, including optical light. The scientists at the High Energy Astrophysics Group of Astronomical Institute CAS in Ondřejov were involved in various projects searching for these optical emissions, both using historical records as well as follow-up coverage by photographic telescopes without obvious success (Hudec, 1995; Greiner et al., 1995), probably due to both the low accuracy of old GRB localizations and to improper expectations about GRB recurrences.

The BART telescope was one of the first robotic instruments devoted to automatic alert observations of GRBs. Its early stages were related to the work of

Martin Jelínek and Petr Kubánek (Jelínek, 2002; Kubánek, 2003). The BART concept and idea were later adopted in an international collaboration with the Spanish team of the BOOTES project (Jelínek et al., 2016; Castro-Tirado, 2011) that began with RT installations in Spain and later extended worldwide (Castro-Tirado et al., 1999). The development and operation of the BART RT represented one of the key projects of the HEA group in Ondřejov, in addition to investigations of galactic and extragalactic high-energy sources and participation in various space projects.

A few years later, thanks to the new generation of GRB-detecting satellites (INTEGRAL, Swift) that could localize bursts much more precisely, ground-based follow up no longer needed the wide field-of-view that favoured smaller instruments. At the same time, there turned out to be very few bright GRBs, so something much bigger was obviously needed.

We used a funding opportunity for revitalizing the older, unused observatory equipment to build a new instrument. The older components (dome and mount) were refurbished and robotized. The body of the main telescope was built new (on order by an external supplier), and the primary mirror was made at the observatory by Cyril Polášek.

As a result, we got a new, suitable telescope for a very reasonable price. The first light of the D50 telescope was achieved in 2007, and regular observing followed (Nekola et al., 2010).

Operating experience soon showed reliability problems and inadequate performance (including the movement speed of the mount, but other parameters also). Most of these problems were eliminated during an additional reconstruction in 2012. Even since then, however, the configuration has never remained stable for long - the telescope has been gradually changed and improved, as it functions as a test facility for both hardware and software development, often carried out by students.

The telescope is cost-effective, yet progressive and inventive. Although it is based on old components and related technologies, it uses unconventional solutions and approaches.

2. Physical specifications

2.1. Optics and CCD

The optical design of the telescope is a Newtonian reflector with a field corrector. The primary mirror has a diameter of $D = 500$ mm and a focal length of $f = 1975$ mm. The flat secondary mirror has a diameter (i.e. the minor axis the ellipse) of 100 mm. The optical system further comprises a field corrector Tele Vue Paracorr PSB-1100, which extends the focal length of the whole system to $f_{eff} = 2277$ mm.

As a camera we use Andor iXon Ultra 888, model DU-888U3-CS0-BVF. It has a back-illuminated EMCCD chip with 1024×1024 pixels, and a pixel size



Figure 1. Photos showing the initial (left) and current (right) state of the D50 telescope.

of $13 \times 13 \mu\text{m}$. This setup provides a field of view of $20' \times 20'$ and a resolution of 1.18 arcsec per pixel. The chip has a visual-light optimized coating and also uses "Fringe Suppression" technology to reduce fringing. In addition to excellent parameters (cooling 95°C below ambient, low readout noise, high quantum efficiency $QE_{MAX} \approx 95\%$), the camera can also use unique readout modes enabled by electron-multiplying (EM) technology. For normal observations we usually use the non-EM amplifier with 1 MHz readout rate, 16-bit, which gives gain of $0.81 e^-$ per A/D count and single pixel noise of $4.63 e^-$.

2.2. Focuser and filter wheel

We use a modified digital filter wheel from Moravian Instruments, containing SDSS g' , r' , i' , z' filters. One position is left empty for unfiltered observations.

For focusing the telescope, we use a custom-made digital focuser, to bear the camera's considerable weight. The assembly also includes an additional dew-protection cover for the camera.

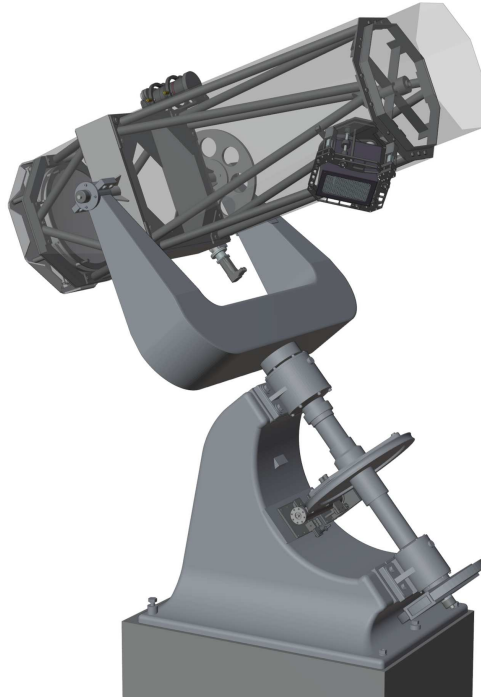


Figure 2. The internal arrangements of the D50 telescope, with the duralumin covers shown translucent. The covers of the worm drives of both axes are omitted.

2.3. OTA and mount

The telescope tube is a steel truss structure composed of tubes and profiles. It is relatively heavy but rigid, its shape is optimized to minimize flexure. The design and initial construction was carried out by AstroLab, a small consortium of specialists. Optical shielding is provided by covers made of duralumin sheets.

The mount is the telescope's oldest component, made in the 50's to carry the large wide-field Richter-Slevogt camera similar to one still in use at the Crimean Observatory ([Terebizh, 2011](#)). This camera was later damaged and replaced by another instrument for solar observations, then around 2000 the mount became available and was used (on the same site) for the construction of the D50 telescope.

The mount is a massive wide fork mount, made of steel. Each axis is driven by a servo motor through a worm drive and gearbox. The servos have an internal resolver, which is used for feedback positioning. Specifically, we use TGT2-0060-30-24/T1KX-2M 24 V AC synchronous motors, driven by TGA-24-9/20-04 servo

Table 1. Mechanical and performance parameters of both axes.

axis	gear ratio	v_{\max}	acceleration	deceleration
RA	1:2304	$10.0\text{ }^{\circ}\text{s}^{-1}$	$0.8\text{ }^{\circ}\text{s}^{-2}$	$0.8\text{ }^{\circ}\text{s}^{-2}$
Dec	1:4000	$5.5\text{ }^{\circ}\text{s}^{-1}$	$1.8\text{ }^{\circ}\text{s}^{-2}$	$0.9\text{ }^{\circ}\text{s}^{-2}$

controllers (both produced by TG Drives).

The goal was to achieve the highest possible speeds of movement, and the selection of motor and gear ratio was adapted to this. In order to reduce gear wear at higher speeds in the RA axis, we use electromagnetically driven pressure control of the worm.

As a result, we achieve a movement speed of up to $10\text{ }^{\circ}\text{s}^{-1}$ in the RA axis ($5.5\text{ }^{\circ}\text{s}^{-1}$ in the Dec axis respectively, more detailed values are given in Tab. 1), which can be considered satisfactory for this mechanical setup and such a massive construction. These speeds are used only for GRBs observations, when slewing time must be reduced as much as possible. For normal operations we use a less demanding max. speed of $5.0\text{ }^{\circ}\text{s}^{-1}$.

This wide range of required speeds led to insufficiently subtle control at slow speeds (e.g. during sidereal tracking). We solved the problem by switching the servo controller to its "stepper motor" mode, driven by pulses provided externally. In addition to this mode change, we also dynamically change the controller's PID feedback parameters as needed - looser when moving fast, tighter when tracking.

During the reconstruction in 2012 we paid great attention to reducing the periodic error in the RA axis. Despite a considerable improvement thanks to the new brushed worm, it still remains significant: a peak to peak amplitude of ≈ 7 arcsec, over a period of 3 minutes.

To ensure reliability, both axes are equipped with independent, on-axis optical position encoders, specifically ARC 425 13PA (produced by LARM), which are 13 bit resolution devices, providing 2.6 arcmin accuracy. These provide independent confirmation of the actual mount position, used by high level software checking.

The assembly further uses REMOTES drive units (Jakubec et al., 2012). This is a unique, sophisticated and tailor-made solution for controlling the entire observatory with a complex system of fail-safe mechanisms. Currently only the low-level functions of the system are deployed, to control the worm pressure, to generate the pulses for the RA servo in its stepper motor mode, and to read the position encoders. All its parameters can be changed dynamically, which is mainly used for changes in tracking speed when autoguiding is in progress.

2.4. Auxiliary devices

To enable long exposures, an autoguider was necessary, and for this we mounted a separate external instrument, based around an MC Rubinar 500 mm f/ 5.6 photographic mirror lens, $D \approx 10$ cm, $f = 500$ mm, an MI (Moravian Instruments) C1-5000 camera and a FLI digital focuser. Since the camera lacks a shutter, we provide a custom-built external shutter, whose electronics also provide information about temperature and humidity inside and outside of the main telescope.

2.5. Dome

The dome is another old and refurbished component, wooden with a steel sliding roof. The roof mechanism is now motorized, controlled from the driving PC. This configuration is very cramped when closed - the telescope must be parked before the roof can close - and unfortunately the open roof also partially restricts the movement of the telescope in the northern parts of the sky. This is why we are considering replacing the dome with a new, less restrictive solution in the future.

2.6. Enviromental sensors

We use set of meteorological sensors, shared by both the D50 and BART telescopes: an anemometer, a thermometer-and-hygrometer, rain sensors and cloud detectors. The anemometer and the rain sensors are professional products (made by Meteoservis and MIRES CONTROL), while the remaining sensors, especially two different versions of the cloud detectors are the result of an experimental open-hardware project MLAB (Horkel et al., 2003). In addition to these shared sensors, the D50 has local sensors measuring temperature and humidity in the dome and also inside the telescope.

Usage of the sensor values is simple - there are distinct threshold values for good and bad weather, and a delay interval for the transition from bad to good weather to prevent oscillation. The telescope will only observe if all sensors show fair weather.

3. Software equipment

3.1. Observatory control system

The entire autonomous observatory is driven by the RTS2 (Kubánek, 2010) robotic observatory control system, running on an ordinary PC. Originally written for the BART telescope, it is now used by various telescopes around the world, but the Ondřejov telescopes still serve as its primary development environment.

The RTS2 system is designed in a very general way to allow modifications according to the requirements of a specific telescope. For the D50 telescope we use a number of locally specific features. The mount driver is particularly

advanced - for example, before any movement, we search for a safe path between the current and new position, so as not to enter the forbidden zones defined by the proximity of the dome and its roof (taking into account its state, so the telescope can be safely manipulated even when the dome is closed). The movement is planned and implemented with respect to the properties of the RTS2 system - using a sequence of successively changed target positions for individual servos so that the duration of the movement is as short as possible and yet everything is safe, i.e. no collision occurs even in case of any postponement in the sequence. We call this the "Successive Safe Points" method.

The mount-driver uses the TPoint system (Wallace, 1994) to improve pointing accuracy. And we use the standard Debian Linux distribution as an operating system.

3.2. Automated data processing

Images are automatically matched to the catalogue immediately, as part of RTS2's acquisition process, so that the detected position can be used as feedback for the mount position. This step is carried out using a script to control the Astrometry.net (Barron et al., 2008) software package. As a result, we can normally assume all our images have correctly filled WCS data in their FITS headers.

The next stage of automatic processing follows within minutes: after the application of the basic calibrations (master versions of dark frame and flat-field), all stars are found and photometrically measured in each image. The photometric calibration is then performed by fitting according to the catalogue and all photometric measurements (of all stars in the image) are then stored in the database. The automated image-processing pipeline is written in Python and uses the IRAF (Tody, 1993) and SExtractor (Bertin & Arnouts, 1996) software packages.

4. Observational plan

4.1. General considerations and strategies

As mentioned before, the primary mission of the telescope is to promptly react to GRB detections and to try to observe their optical counterparts in both their early and later phases. However, as GRBs are not very frequent, most of the observational time is spent observing other targets, typically cataclysmic variable stars (CVs), blazars/AGNs and others. The telescope also functions as a ground segment for INTEGRAL and Gaia space missions, which implies occasional simultaneous/campaign observation, as well as subsequent observation and long-term monitoring of objects of interest.

4.2. Per-night target selections and scheduling

The RTS2 system currently allows two internally defined approaches - either automatically select a target from the database according to the simple internal priority system (based on interval since last observation, zenith distance, etc.) and bonus ratings, along with per-target boundary conditions for observation. Or alternatively, to use a system of priority queues, where after the highest queue has been emptied of observable targets, the next queue is approached for observation, and so on.

At the D50 telescope, we use the latter approach - the system of queues, which are automatically filled by a daily script launched by the Unix system cron service. We use this to maintain a group of objects to be observed once per night (and removed from the queue after observation), and a group that is renewed once every 10 days. In addition, there are bottom queues, containing targets for repeated observations, where targets are not removed after observation, and so get observed repeatedly until some object from a higher queue becomes available. At the top of the queue hierarchy there are the queues for recent GRBs and for manual or campaign observations. This approach provides natural control matching what we want to do, and ensures the telescope is always doing something useful.

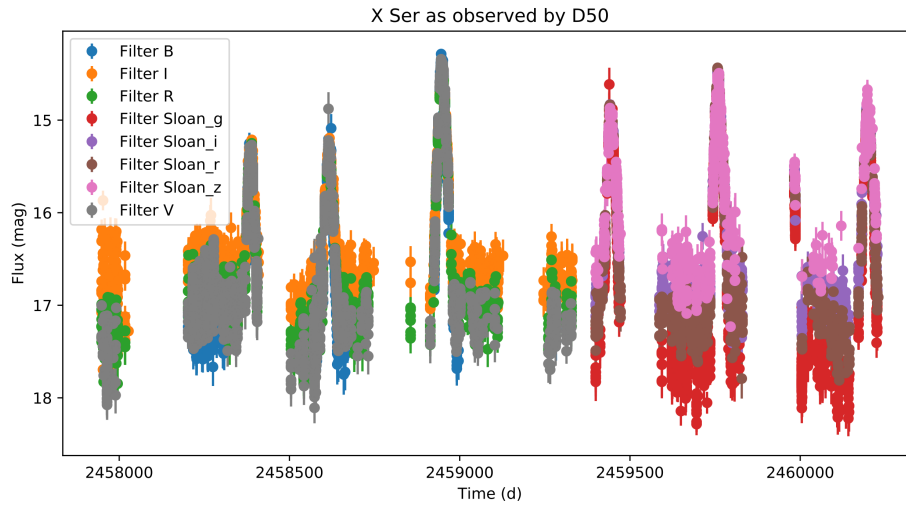


Figure 3. The light curve of the variable star X Ser, observed with the D50 telescope, generated via a web interface from a database of automatically processed data.

5. Results

5.1. Direct results

So far, we have been lucky to observe multiple GRBs, including several really interesting ones. For example, the very bright GRB 210619B with prominent reverse-shock (Oganesyan et al., 2023) or GRB 190919B with an unusual light curve, which we suspect is the result of a combination of two peaks (Jelínek et al., 2022).

We have also observed several very interesting secondary targets. For example, the blazar OJ 287, a supermassive black hole (SBH) binary, where brightenings are caused by the interference of the secondary SBH with the accretion disc around the primary SBH (Valtonen et al., 2023). Another example is the gravitational microlensing event Gaia16aye, discovered by the Gaia space mission, where the the complicated light curve variations with five brightening events was explained as a gravitational lensing of a bright single star, lensed by much closer and fainter, randomly passing binary star system (Wyrzykowski et al., 2020). Often, the value of this kind of studies arises from long-term monitoring, one of the main strengths of robotic observatories.

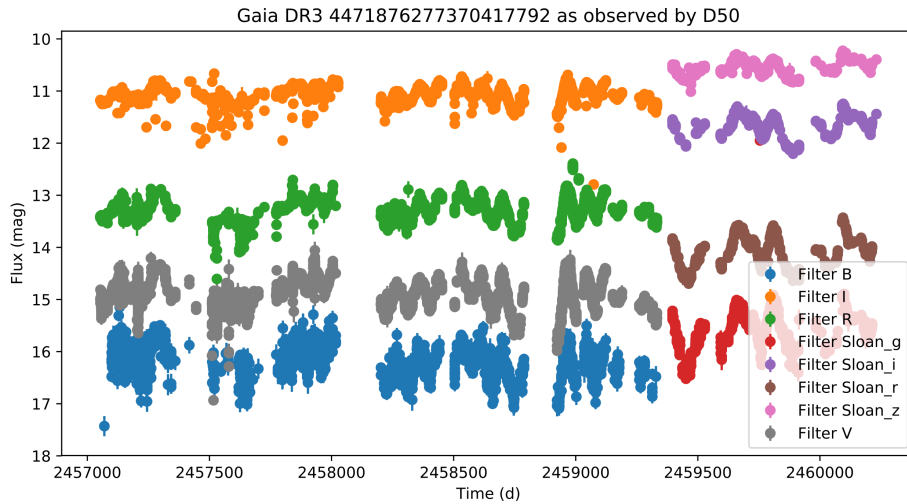


Figure 4. Light curve of the variable star CzeV1266, discovered in the D50 telescope data. The object was in the field of another object observed. The graph was generated via a web interface to a database of automatically processed data.

5.2. Archive

Every object, in every image that the D50 has ever taken since first light, was measured, photometrically calibrated and stored in the database. Thanks to this, we now have (as of 24/11/2022) a total of 845 859 396 photometric measurements in the database - all automatically generated.

Any target can be examined using our web interface (currently not publicly available), providing quick access to measured data. For example, Fig. 3 shows a light-curve of X Ser (which is one of our observational long-term targets) and Fig. 4 which shows CzeV1266 (Gaia DR3 4471876277370417792), a newly discovered variable star that happened to lie in the field of view of a different object we regularly observe. CzeV1266 was one of the variable objects discovered in the initial period of our photometric database, as a result of a search for new variables in our data, an assignment for one of our high school student internships.

6. Recent status and future plans

The telescope has been observing every clear night since its opening, with the exception of a few technological breaks required for rebuilding, configuration adjustments and solving technical problems. Observation statistics can be seen in the graph of the number of images in a given month (Fig. 5).

In the future, in addition to the aforementioned reconstruction of the dome, we are considering adding the possibility of capturing low-dispersion spectra with the help of a rotating secondary mirror and an independent telescope exit, equipped with the new low-dispersion spectrograph. A student internship is currently underway to verify the basic considerations and create an initial trial version of the spectrograph.

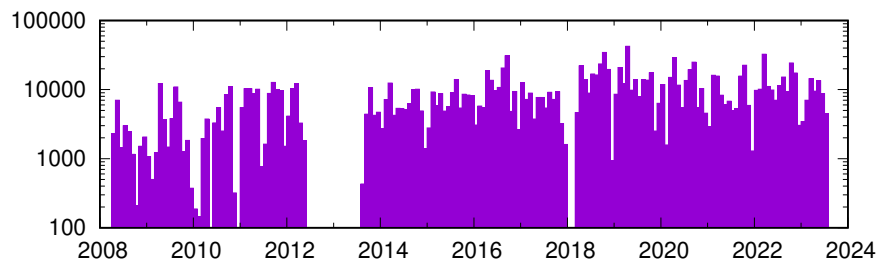


Figure 5. The number of images the D50 has taken in a given month. Includes only high quality images of the sky that have passed the automated data processing.

7. Conclusion

The aim of this paper was to give a report on the actual state and properties of the autonomous robotic telescope D50. The telescope is rather small, however the autonomous robotic mode that it operates in gives it valuable abilities and also makes it very cost-effective.

The importance of observing GRBs is obvious, but even secondary science leads to meaningful results. Thanks to automatic processing, it is possible to obtain reasonable and photometrically calibrated data easily and quickly after it's acquisition.

The telescope is being continuously improved, largely with the help of students, and is thus also valuable for educational purposes. One of the philosophies of the telescope is to make meaningful use of old things for modern science, thus reducing costs while being environmentally friendly.

Acknowledgements. Support by the project RVO:67985815 is acknowledged. This research made use of data provided by Astrometry.net. We sincerely thank a number of students and other people, especially Michal Jakubec, who contributed greatly to the design and implementation of the telescope modifications. We thank also to Ronan Cunniffe for several improvements to the telescope and for proofreading this paper.

References

- Barron, J. T., Stumm, C., Hogg, D. W., Lang, D., & Roweis, S., Cleaning the USno-B Catalog Through Automatic Detection of Optical Artifacts. 2008, *Astronomical Journal*, **135**, 414, DOI: 10.1088/0004-6256/135/1/414
- Barthelmy, S., GCN and VOEvent: A status report. 2008, *Astronomische Nachrichten*, **329**, 340, DOI: 10.1002/asna.200710954
- Bertin, E. & Arnouts, S., SExtractor: Software for source extraction. 1996, *Astronomy and Astrophysics, Supplement*, **117**, 393, DOI: 10.1051/aas:1996164
- Castro-Tirado, A. J., Robotic Astronomy and the BOOTES Network of Robotic Telescopes. 2011, *Acta Polytechnica*, **51**, 16
- Castro-Tirado, A. J., Soldán, J., Bernas, M., et al., The Burst Observer and Optical Transient Exploring System (BOOTES). 1999, *Astronomy and Astrophysics, Supplement*, **138**, 583, DOI: 10.1051/aas:1999362
- Greiner, J., Wenzel, W., Hudec, R., et al., Simultaneous Optical/Gamma-ray Observations of GRBs. in , *IAU Colloq. 151: Flares and Flashes*, ed. J. Greiner, H. W. Duerbeck, & R. E. Gershberg, Vol. **454**, 381
- Horkel, M., Kákona, J., Kákona, M., et al. 2003, MLAB: Open-Hardware Modular Laboratory, <https://www.mlab.cz/>
- Hudec, R., Search for GRB Counterparts in the Optical. 1995, *Astrophysics and Space Science*, **231**, 239, DOI: 10.1007/BF00658624

- Jakubec, M., Skala, P., Sedlacek, M., et al., REMOTES: reliable and modular telescope solution for seamless operation and monitoring of various observation facilities. 2012, in Society of Photo-Optical Instrumentation Engineers (SPIE) Conference Series, Vol. **8451**, *Software and Cyberinfrastructure for Astronomy II*, ed. N. M. Radziwill & G. Chiozzi, 84511I
- Jelínek, M. 2002, Detection of bursting sources of gamma-ray radiations using instruments with CCD detection., Master's thesis, Charles University, Prague, Praha, CZ
- Jelínek, M., Castro-Tirado, A. J., Cunniffe, R., et al., A Decade of GRB Follow-Up by BOOTES in Spain (2003-2013). 2016, *Advances in Astronomy*, **2016**, 192846, DOI: 10.1155/2016/1928465
- Jelínek, M., Topinka, M., Karpov, S., et al., GRB 190919B: Rapid optical rise explained as a flaring activity. 2022, *Astronomy and Astrophysics*, **662**, A126, DOI: 10.1051/0004-6361/202143010
- Kubánek, P. 2003, Improvement of the observation software for telescope BART, Master's thesis, Charles University, Prague, Praha, CZ
- Kubánek, P., RTS2—The Remote Telescope System. 2010, *Advances in Astronomy*, **2010**, 902484, DOI: 10.1155/2010/902484
- Nekola, M., Hudec, R., Jelínek, M., et al., Robotic telescopes for high energy astrophysics in Ondřejov. 2010, *Experimental Astronomy*, **28**, 79, DOI: 10.1007/s10686-010-9190-5
- Oganesyan, G., Karpov, S., Salafia, O. S., et al., Exceptionally bright optical emission from a rare and distant gamma-ray burst. 2023, *Nature Astronomy*, DOI: 10.1038/s41550-023-01972-4
- Terebizh, V. Y., New designs of survey telescopes. 2011, *Astronomische Nachrichten*, **332**, 714, DOI: 10.1002/asna.201111576
- Tody, D., IRAF in the Nineties. 1993, in Astronomical Society of the Pacific Conference Series, Vol. **52**, *Astronomical Data Analysis Software and Systems II*, ed. R. J. Hanisch, R. J. V. Brissenden, & J. Barnes, 173
- Valtonen, M. J., Zola, S., Gopakumar, A., et al., Refining the OJ 287 2022 impact flare arrival epoch. 2023, *Monthly Notices of the RAS*, **521**, 6143, DOI: 10.1093/mnras/stad922
- van Paradijs, J., Groot, P. J., Galama, T., et al., Transient optical emission from the error box of the γ -ray burst of 28 February 1997. 1997, *Nature*, **386**, 686, DOI: 10.1038/386686a0
- Štrobl, J., Jelínek, M., & Hudec, R., Small Binocular Telescope: The new epoch of Burst Alert Robotic Telescope. 2019, *Astronomische Nachrichten*, **340**, 633, DOI: 10.1002/asna.201913668
- Wallace, P. T., TPOINT – Telescope Pointing Analysis System. 1994, *Starlink User Note*, **100**

Wyrzykowski, L., Mróz, P., Rybicki, K. A., et al., Full orbital solution for the binary system in the northern Galactic disc microlensing event Gaia16aye. 2020, *Astronomy and Astrophysics*, **633**, A98, DOI: 10.1051/0004-6361/201935097

Proposal of optical sky monitoring with subsecond cadence

P. Kroll 

Sonneberg Observatory (E-mail: pk@4pisysteme.de), Germany

Received: June 30, 2023; Accepted: October 31, 2023

Abstract. Sky monitoring needs to trade-off time resolution against limiting magnitude, usually leading to exposure times of some seconds or tens of seconds. Consequently, photometric information in the range below seconds remains largely undetected. We propose a scheme of sky monitoring using CMOS cameras to improve cadence aiming at exploring the sky in the subsecond region without relinquishing fainter stars. Optical systems could even be operated without any mechanical drives reducing costs and processed in a way similar to TDI mode. Data handling would be a challenge of processing and storage. We sketch the benefits of such a monitoring from meteors to high energy events.

Key words: Surveys – Stars: variables – Meteors – Gamma-ray burst: general – Techniques: photometric – Techniques: image processing

1. Introduction

Sky monitoring aims at detecting the unexpected, such as meteors, Cherenkov flashes or optical transients from gamma-rays bursts (GRBs) or fast radio bursts (FRBs), flaring stars, cataclysmic events and others. As these events happen to appear at any position on the sky at any time, sky monitoring requires either large-field-of-view optical systems or batteries of telescopes to cover as much sky area as possible.

The approach to permanent sky monitoring is not new, mostly driven by searches for optical transients of possibly different astrophysical origins. It was unknown for many years if bursts detected in the gamma-ray region of the electromagnetic spectrum would have optical counterparts at all or if there are optical flashes without high-energy counterpart, see e.g. [Schaefer et al. \(1987\)](#). Since a couple of years fast radio bursts propose a similar conundrum, in this case at the weaker side of the electromagnetic spectrum ([Tingay, 2020](#); [Tingay & Joubert, 2021](#)).

The motivation is high to detect transient events in the optical as instruments and detectors are available at comparably low costs. As we see later, detectors of CMOS type are exceptionally suitable for this task owing to their high sensitivity and low noise even for subsecond exposure times. They have therefore been used since a couple of years in different projects ([Biryukov et al., 2015](#); [Beskin et al., 2017](#); [Sako et al., 2018](#); [Arimatsu et al., 2021](#)).

Table 1. Some large currently active or coming digital sky monitoring programme.

Program	Site(s)	Cadence	Reference
OGLE	Las Campanas	20 min	OGLE (2023)
ASAS-SN	World-wide network	1 day	ASAS-SN (2023)
Las Cumbres O.	world-wide network	5 min	LCO (2023)
Argus Pathfinder	PARI	1 s – 30 s	AP (2023)
NGTS	Cerro Paranal	13 s	NGTS (2023)
ODNet, eVScope		0.2 – 0.3 s	Cazeneuve et al. 2023

2. Classical photographic sky patrol

Historically, sky monitoring started by means of photographic plates at different places in the world roughly one hundred years ago. Resulting from the relatively poor sensitivity of the emulsions of those days, typical exposure times were in the order of several hours. Exposures of the same field on the sky could be repeated only within days or weeks between them. Also, covering the whole sky was virtually impossible.

With the improvement of sensitivity of photographic emulsions the exposure time could be reduced reaching the same limiting magnitude, and thus the cadence of repeated exposures could be shortened to hours. Batteries of short-focal telescopes allowed to cover large areas on the sky simultaneously, such as the Sky Patrol installation at Sonneberg Observatory with 14 cameras of 55/250 mm lenses operated in parallel in the red-yellow (photovisual) and blue (photographic) color band between 1950ies and 2010.

Photographic plates of different monitoring programs are stored at several places in the world. A comprehensive overview about plate archives is given by [Hudec \(2019\)](#).

Generally speaking, the cadence of photographic monitoring is in the order of days to years, at best some hours.

3. Digital sky monitoring

The invention of digital solid state detectors such as CCDs (charge-coupled devices) improved sky monitoring in manifold ways. While the quantum efficiency of photographic plates is in the order of a very few percent, back-side illuminated CCDs are sensitive of up to 95% or even better. This feature allowed to dramatically reduce exposure time and, in combination with comparably short download times, improves the cadence of monitoring down to minutes or seconds.

Table 1 lists a representative but non-exhaustive subset of large currently active or coming digital sky monitoring programme.

4. Digital meteor monitoring

In the recent years a number of automatic meteor surveillance networks have emerged, such as [FRIPON \(2023\)](#) and [AllSky7 \(2023\)](#), see also [Hankey et al. \(2020\)](#), to mention a few, with impressive results of several thousands of meteor detections annually and frequent fireball registrations. In case of AllSky7 network, seven CMOS (complementary metal-oxide-semiconductor) sensors of SONY STARVIS IMX291 type are used in combination with 4 mm f/1.0 lenses. All cameras are 24/7 operated and read-out with 25 images per seconds in HD (high definition) and SD (standard definition) streams in parallel.

Although the image analysis software of AllSky7 is optimised to detect meteors, the images do also show stars down to magnitude 4.5 roughly, which is amazing with respect to the very short exposure time of 40 milliseconds and the small aperture.

This very feature of AllSky7 network cameras led us to the idea of this paper's subject, namely to exploit CMOS detectors with short exposure times, thus high cadence, to explore any other celestial events of subsecond duration or photometric variations shorter than seconds which are completely or partly missed by traditional monitoring programme like those listed in [table 1](#).

5. Proposal: high-cadence optical sky monitoring

5.1. Scientific goals

High-cadence sky monitoring may follow two different strategies: follow-up observations of optical events, and detection of transient events by chance by means of continuously scanning large portions of the sky.

5.1.1. Follow-up observations

High-cadence observations are important for the following targets, which are possibly detected beforehand by other monitoring programme:

- Flare events of red dwarf stars.
- Outbursts of dwarf novae, novae, and supernovae.
- Optical transients of GRBs. Such counterparts of GRBs were detected in past, of which the brightest event GRB 080319B flared up to an optical magnitude of 5.7 ([Bloom et al., 2009](#); [Beskin et al., 2010](#)). Although this particular GRB was observed with 0.13 seconds exposures, which is of comparably high cadence, it is unknown if bursts in general show structures at even shorter timescales or might be brighter for a very short period of time in some cases.

- Optical transients of FRBs. Optical counterparts are unknown so far. As the duration of radio bursts is in the order of a few milliseconds, one might expect similar time scales in the optical.

5.1.2. Detection by chance

Astronomical events on short time scales may appear at any position on the sky at any time. Therefore, permanent monitoring large field of views – virtually the whole sky –, promise to reveal lots of hitherto undetected objects:

- All types of events already listed in the previous sub section of follow-up observations.
- Transits of extrasolar planets and moons.
- Occultation events of asteroidal and cometary bodies in the main and Kuiper belts and the Oort cloud. These events may not only reveal the bodies themselves but also moons or rings around them.
- Meteors of solar system origin.
- Sub-relativistic meteors. The existence of this interesting phenomenon was proposed by Siraj and Loeb, 2020. It is unknown, if such type of meteors exist, but they could be detected by monitoring in the milli-second and micro-second range.

As a byproduct of sub-second cadence monitoring, tens of thousands of artificial satellites are monitored and need to be distinguished from real astronomical events. As these objects also flare, they cause lots of false events. Surveillance of satellite fleets and space debris, which both will grow in future dramatically, might become important also for other branches of observational astronomy. In this way, the proposed type of sky monitoring is able to yield data for different aims in parallel.

5.2. Instrumentation

In principle, any telescope can be used for monitoring, just by pointing it to the sky, equipping it with a camera and repeating readout.

For follow-up observations, slow optics (focal ratios 1:5 or less) can be used, as the target is already known.

In contrast, to cover large fields fast short-focal instruments (focal ratios 1:0 . . . 1:5) are preferable for monitoring to detect events of all types mentioned above.

In combination with the advantages of CMOS cameras, which is sketched in the next section, an interesting and simple approach emerges. As optical transients and other events occur non-predictable at any time and everywhere

on the sky, it is equal where to look at. This offers the use of pure OTAs (optical tube assembly) without any astronomical mounting. The OTA has only to be mechanically fixed for stable pointing upwards. A battery of such OTAs may scan the sky by simply passing the stars through the field of view (scan mode). As CMOS cameras can be exposed and read out very quickly within milliseconds the effect of Earth's rotation is negligible. In this way, a sky monitoring program can be set up for moderate prices and may be very robust and reliable as no mechanical components are involved (except dome or movable roof).

This approach offers also a new life for old, non-computerized telescopes. These instruments are available at many places in the world, but they are frequently not used any more as mechanical parts are broken or got stuck, or it is too expensive to upgrade the mounting to modern GOTO-functionality. Mostly, the pure optical system is still working (possibly needs some cleaning) and thus ready for monitoring in the proposed way.

5.3. Camera and hardware and software requirements

To achieve sub-second cadence cameras with CMOS detector type are recommended. Exposure time can be very short and even for chips with tens of millions of pixels the read-out times are below seconds. By binning technique read-out time can be further reduced. In this way, very short-living astronomical events can be detected in single images and in series of consecutive images which were lost or too faint to be detected in long-time exposures.

Another advantage of CMOS detectors is the very low read-out signal and noise. This offers the possibility of adding up images to increase limiting magnitude, of course at the expense of temporal resolution.

For the case of fixed OTAs as proposed in the previous section, adding up images is more complicated as the drift speed of all objects across the chip decreases from equator to the poles. However, as long as the exposure time of a single image is short enough that stars appear as points, the declination dependent adding-up of images can be processed by software by separating parts of the images. In a certain sense this mode resembles the TDI (time delayed integration) mode of CCD cameras, which would here completely be made by software.

It is obvious that, by operating CMOS cameras in the proposed way a lot of data will be produced even for short operation times. This requires powerful computer hardware for storing the data stream from camera to disk, and also for analysing all the images. There are efficient software packages available today for astronomical image processing such as [Astropy \(2023\)](#) in Python language to set up a complete processing pipeline from raw images to object databases. Nevertheless, it remains a challenging task.

Other open questions concern networking with many stations world-wide, setting-up a kind of central database or making the software publicly available.

6. Concluding remarks



Apart from adaptive optics techniques for large telescopes or lucky imaging methods to compensate the influence of atmospheric turbulences, until now sub-second optical astronomy is poorly studied. Entering unexplored terrain usually leads to unexpected results and discoveries, or as Hermann Bondi with respect to short-time constant astronomy mentioned in 1970: "... but I think it is sometimes overlooked that perhaps we are missing a whole continent."

References

- AllSky7. 2023, <https://allsky7.net/>
- AP. 2023, <https://evrscope.astro.unc.edu/>
- Arimatsu, K., Tsumura, K., Usui, F., Ootsubo, T., & Watanabe, J.-i., Detectability of Optical Transients with Timescales of Subseconds. 2021, *Astronomical Journal*, **161**, 135, DOI: 10.3847/1538-3881/abd94d
- ASAS-SN. 2023, <https://www.astronomy.ohio-state.edu/asasn/>
- Astropy. 2023, <https://www.astropy.org/>
- Beskin, G., Karpov, S., Bondar, S., et al., Fast Optical Variability of a Naked-eye Burst—Manifestation of the Periodic Activity of an Internal Engine. 2010, *Astrophysical Journal, Letters*, **719**, L10, DOI: 10.1088/2041-8205/719/1/L10
- Beskin, G. M., Karpov, S. V., Biryukov, A. V., et al., Wide-field optical monitoring with Mini-MegaTORTORA (MMT-9) multichannel high temporal resolution telescope. 2017, *Astrophysical Bulletin*, **72**, 81, DOI: 10.1134/S1990341317030105
- Biryukov, A., Beskin, G., Karpov, S., et al., The first light of Mini-MegaTORTORA wide-field monitoring system. 2015, *Baltic Astronomy*, **24**, 100, DOI: 10.1515/astro-2017-0208
- Bloom, J. S., Perley, D. A., Li, W., et al., Observations of the Naked-Eye GRB 080319B: Implications of Nature's Brightest Explosion. 2009, *Astrophysical Journal*, **691**, 723, DOI: 10.1088/0004-637X/691/1/723
- Cazeneuve, D., Marchis, F., Blaclard, G., et al., ODNNet: A Convolutional Neural Network for Asteroid Occultation Detection. 2023, *Astronomical Journal*, **165**, 11, DOI: 10.3847/1538-3881/ac9c69
- FRIPON. 2023, <https://www.fripon.org/>
- Hankey, M., Perlerin, V., & Meisel, D., The all-sky-6 and the Video Meteor Archive system of the AMS Ltd. 2020, *Planetary Space Science*, **190**, 105005, DOI: 10.1016/j.pss.2020.105005

- Hudec, R., Astronomical photographic data archives: Recent status. 2019, *Astronomische Nachrichten*, **340**, 690, DOI: 10.1002/asna.201913676
- LCO. 2023, <https://lco.global/>
- NGTS. 2023, <https://www.eso.org/public/teles-instr/paranal-observatory/ngts/>
- OGLE. 2023, <http://ogle.astrouw.edu.pl/>
- Sako, S., Ohsawa, R., Takahashi, H., et al., The Tomo-e Gozen wide field CMOS camera for the Kiso Schmidt telescope. 2018, in Society of Photo-Optical Instrumentation Engineers (SPIE) Conference Series, Vol. **10702**, *Ground-based and Airborne Instrumentation for Astronomy VII*, ed. C. J. Evans, L. Simard, & H. Takami, 107020J
- Schaefer, B. E., Pedersen, H., Gouiffes, C., Poulsen, J. M., & Pizzichini, G., Optical flash background rates. 1987, *Astronomy and Astrophysics*, **174**, 338
- Tingay, S., High-cadence optical transient searches using drift scan imaging I: Proof of concept with a pre-prototype system. 2020, *Publications of the Astron. Soc. of Australia*, **37**, e015, DOI: 10.1017/pasa.2020.7
- Tingay, S. & Joubert, W., High cadence optical transient searches using drift scan imaging II: Event rate upper limits on optical transients of duration ≥ 21 ms and magnitude ≤ 6.6 . 2021, *Publications of the Astron. Soc. of Australia*, **38**, e001, DOI: 10.1017/pasa.2020.53

The rate of satellite glints in ZTF and LSST sky surveys

S. Karpov¹  and J. Peloton² 

¹ *CEICO, Institute of Physics of Czech Academy of Sciences, Na Slovance 1999/2, 182 00 Prague 8, Czech Republic (E-mail: karpov@fzu.cz)*

² *Université Paris-Saclay, CNRS/IN2P3, IJCLab, Orsay, France*

Received: June 30, 2023; Accepted: October 26, 2023

Abstract. We assess the impact of satellite glints – rapid flashes produced by reflections of a sunlight from flat surfaces of rotating satellites – on current and future deep sky surveys such as the ones conducted by the Zwicky Transient Facility (ZTF) and the Vera C. Rubin Observatory upcoming Legacy Survey of Space and Time (LSST). In addition to producing a large number of streaks polluting the images, artificial satellites and space debris also generate great amount of false point-source alerts hindering the search for new rapid astrophysical transients. To investigate the extent of this problem, we perform an analysis of isolated single frame events detected by ZTF in more than three years of its operation, and, using three different methods, assess the fraction of them related to artificial satellites to be at least 20%. The satellites causing them occupy all kinds of orbits around the Earth, and the duration of flashes produced by their rotation is from a fraction of a second down to milliseconds, with mean all-sky rate of up to 80,000 per hour.

Key words: surveys – transients – space vehicles – light pollution

1. Introduction

Modern large-scale time-domain sky surveys, like upcoming Vera C. Rubin Observatory Legacy Survey of Space and Time (Ivezić et al., 2019) and ongoing Zwicky Transient Facility (Bellm et al., 2018) offer an unprecedented possibility of not only detailed study of already known classes of transient objects, like variable stars, novae, supernovae, tidal disruption and microlensing events, AGNs and distant Solar System objects, but also of discovery of potentially new and exciting classes of astrophysical transients, especially in the still poorly studied region of shortest time scales. Indeed, despite long history of various experiments aimed towards investigations of transients on time scale of fractions of a second to a few seconds (Schaefer, 1987; Kehoe et al., 2002; Karpov et al., 2010, 2019; Richmond et al., 2020; Tingay & Joubert, 2021; Arimatsu et al., 2021), they had only a limited success in detecting initial phases of gamma-ray bursts (Racusin et al., 2008; Karpov et al., 2017a; Zhang et al., 2018), in part due to quite limited depth of these surveys.

On the other hand, the zoo of rapid optical transients is potentially extremely diverse, spanning from short intense flares on red dwarf stars to gamma-ray bursts and fast radio bursts (Burke-Spolaor, 2018). And while modern and upcoming surveys like ZTF and LSST have insufficient temporal resolution and cadence to properly sample the light curves of such events, due to extreme sensitivity they still may detect both their peaks and afterglows, as it was demonstrated by the recent ZTF discovery of orphan GRBs (Ho et al., 2020; Andreoni et al., 2021).

The search for rapid optical transients on sub-second time scales is significantly complicated by the large background of artificial events – satellite glints, or flares, caused by the sunlight reflection from solar panels or rotating antennae onboard artificial satellites orbiting the Earth. Such events may both have sub-second durations and be bright enough to be apparent even in smaller-scale wide-field surveys (Karpov et al., 2017b; Nir et al., 2021a; Corbett et al., 2020). Even in deep surveys with lower temporal resolution, where satellites typically produce extended streaks and trails easily detectable by their morphology, such rapid flashes may still generate point sources indistinguishable from stellar or extragalactic objects that may mimic e.g. gamma-ray bursts (Nir et al., 2021b).

In this article we investigate the impact of such satellite glints on the transients detectable in the ZTF alert data stream using the data archived by the FINK broker (Möller et al., 2020) between November 2019 and April 2023 (Section 2). We use several criteria for associating the alerts with satellites, based either on purely geometric analysis of the transients detected on individual exposure, morphological properties of the alert cutouts, or results of direct association of transient positions with propagated ephemerides of known catalogued satellites (Section 3). We then use these associations in order to derive the properties (duration and intrinsic brightness) of the flares, and estimate the all-sky rate of such events. Finally, we briefly discuss how these results may scale to LSST (Section 4).

2. Selection of candidate events

For this study we used a subset of alerts from ZTF public alert stream (Bellm et al., 2018) which are being processed and archived by FINK community alert broker¹ (Möller et al., 2020) since late 2019. This is an unfiltered, 5-sigma alert stream extracted from difference² images that primarily includes events from flux transients, variables, and Solar System objects. Detectable streaks, such as aircraft and satellite trails, as well as cosmic rays, are removed by the ZTF

¹<https://fink-broker.org>

²Difference images are produced by ZTF pipeline (Bellm et al., 2018) by subtracting the reference image from every science image acquired during the survey. The reference, or template, images are produced by co-adding large number of highest quality science images, and are updated periodically as a part of ZTF data release process.

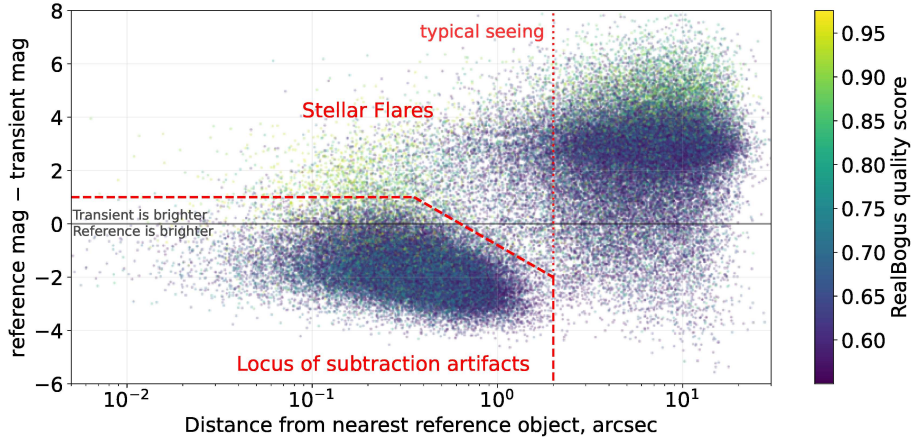


Figure 1. The difference between transient magnitude measured on difference image and the magnitude of nearest object from reference catalogue versus the distance to this nearest reference object for all events corresponding to non-repeating positive detections not coincident with Solar System objects. The value of RealBogus quality score is represented by the color of dots. Clearly visible cloud of lower-quality events in the lower part of the plot corresponds primarily to subtraction artefacts on stationary non-variable objects, as well as to occasional stellar variability like lower-amplitude stellar flares. Red dashed lines mark the extent of this “stellar locus” as used for rejection of these events.

processing pipeline (Masci et al., 2019) and `CreateTrackImage` software (Laher et al., 2014) prior to generating the alerts. Upon ingestion of alerts into FINK, two additional quality criteria (the real-bogus score³ being above 0.55, and there should be no prior-tagged bad pixels in a 5 x 5 pixel stamp around the alert position) are being applied.

In order to identify the events linked with artificial satellites, we started with a set of all non-repeating (i.e. appearing on just a single exposure, and not detected in consecutive observations on the same sky position) isolated alerts not connected to known stationary objects, as well as to known moving Solar System objects. To reject the latter, we excluded every alert that is within 30 arcseconds of current positions of objects from Minor Planet Center (MPC) database.

To exclude the events related to stationary objects we located and excluded the “stellar locus” on the plane defined by the distance of the transient to the

³Real-bogus score is a machine learning based quality score for the reliability of a transient candidate based on a number of pixel-based features computed around transient position (Mahabal et al., 2019). It has a range of values between 0 and 1, where values closer to 1 imply a more reliable candidate.

closest object in the reference catalogue and the difference of their magnitudes as shown in Fig. 1. This locus contains the alerts related to both occasional stellar variability (i.e. small amplitude stellar flares) and – most important for our analysis – the image subtraction artefacts. The characteristic features of the latter are their innate proximity, within couple of typical PSF sizes, to the objects visible on reference frame (and thus populating the reference catalogue), and the brightness not exceeding the one of reference object. This locus contains on average 50% percents of non-repeating alerts not connected to known Solar System objects.

This way we extracted a subset of 828063 candidate alerts, appearing on 164,432 of 252,532 (65.1%) individual exposures acquired by ZTF over 815 observational nights between Nov 2019 and Apr 2023, with 53,581 of these exposures (21% of all) containing 5 or more candidates.

These candidates constitute the natural sample for searching for both satellite glints and genuine rapid astrophysical transients as they contain all high-quality non-stellar and off-nuclear (i.e. located outside of centers of galaxies) alerts that manifest on just a single exposure, with most of the artefacts removed.

3. Identification of satellite glints

We employed several methods in order to isolate the candidates that are connected to flashes (glints) from artificial satellites among the candidates selected in Section 2. They are outlined in the following sub-sections.

3.1. Detection of tracklets

As significant fraction of all candidates appear on the frames in large groups, we attempted to detect quasi-linear structures among them – to identify the sequences of events located approximately along the same great circle inside individual exposure. While a few points may occur along the line just randomly, for 5 or more events it is highly unlikely for typical numbers of events per exposure we have. Such sequences of events – tracklets – correspond to rapidly spinning satellites that produce numerous short flashes during the ZTF exposure, shifting between them due to orbital motion.

The algorithm for detecting the tracklets starts with constructing great circles for every pair of candidates on the exposure, and keeping the ones with enough points close to them. The algorithm then gradually lifts the constraints on the distance and fits the second-order polynomial for the deviation from the great circle in order to properly capture longer tracks where linear approximation for orbital trajectory projection is no more sufficient. Finally, the algorithm merges together nearly co-linear tracks, and requires them to contain at least 5 points in order to be accepted.

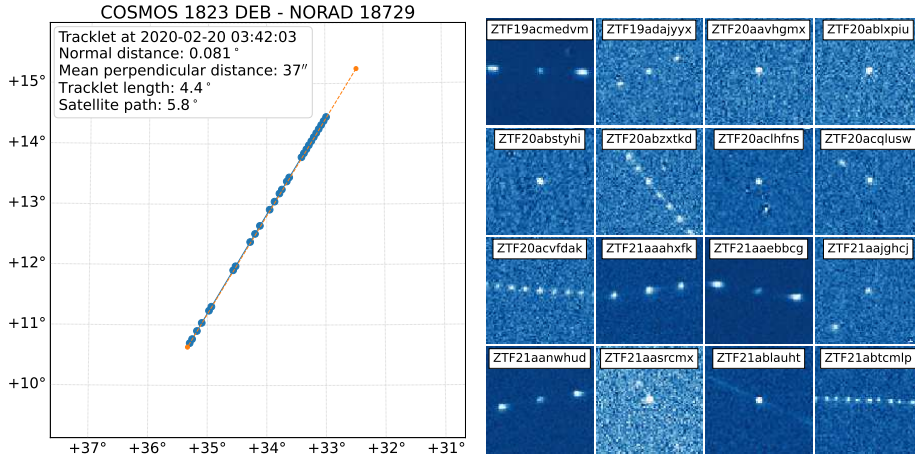


Figure 2. Left panel – example of a tracklet detected on a single ZTF exposure, plotted in celestial coordinates. The arc of a best matching satellite from NORAD catalogue during the exposure is also shown with orange dashed line. Right panel – example cutouts of difference images from ZTF alert packets corresponding to a random subset of events associated with tracklets. Large part of them show characteristic multi-peak structure, often symmetric in respect to the “main” event, while some fraction is still essentially isolated point sources.

Using this algorithm, we detected 10,170 individual tracklets that contain 116,389 (14.1%) of all candidates.

3.2. Cross-identification with NORAD satellite catalogue

We cross-matched detected tracklets with the positions of known satellites from public NORAD catalogue published by the Joint Space Operation Center (JSpOC). As the orbital elements rapidly evolve in time, we used sets of two-line elements (TLE) downloaded daily from <https://www.space-track.org> for the analysis of tracklets detected on the same day. Then, we propagated these orbital elements to the times of individual exposures using SKYFIELD package (Rhodes, 2019). We then selected the satellites with arcs during the exposure approximately co-linear with the tracklet and not shorter than its length, and with normal distance of tracklet points from satellite arc not exceeding 300 arc-seconds. For every tracklet we selected the satellite with smallest mean normal distance as a match.

This way, we associated 6,238 (61.3%) of all tracklets with catalogued satellites. Example of such association is shown in left panel of Fig. 2.

We also performed a “blind” association of individual candidates, regardless of them belonging to tracklets or not, with propagated positions of catalogued

satellites in a similar manner, but now requiring the candidate to lay closer than $60''$ from satellite arc, and to have the distance along the arc not exceeding its length, thus permitting for some acceptable error in the satellite fly-by time. This way, we acquired satellite associations for 95,279 (11.5%) candidates. Among them, 71,032 (74.6%) belong to the tracklets. In total, both variants (less restrictive one based on association of tracklets, and more strict one for matching positions of individual events) allowed us to associate 99,157 (12.0%) candidates with known satellites from NORAD catalogue.

3.3. Morphology of alert images

Right panel of Fig. 2 shows how a random subset of events belonging to tracklets look like on cutouts from ZTF difference images, i.e. with all stationary objects (stars, galaxies, etc) removed. Significant fraction of them shows multiple appearances of the transient inside the same cutout (with $60 \times 60''$ sizes) due to sufficiently rapid (quasi-) periodic variability due to fast rotation of the satellites.

In order to locate the events with such peculiar appearances in differential images we performed a simple morphological analysis of the cutouts⁴ of all candidates. To do so, we determined the regions of cutouts where brighter objects are apparent in the template images, and then performed peak detection above 2σ level everywhere except these regions in difference images using SEP code (Barbary, 2018). This way, we successfully detected peaks for 114,051 (98.0%) of all events belonging to tracklets, and for 86,790 (74.6%) of them detected two or more peaks per cutout. Among all candidates, 151,046 (18.2%) also displayed multiple peaks, which we may consider as a manifestation of satellite rotation.

4. Discussion

As described in Section 3, we used three different methods for identifying the events corresponding to satellite glints. Each of them has its own shortcomings, and thus they select slightly different subsets of events. Left panel of Fig. 3 shows a Venn diagram of the relation between the sets selected by each of the methods. In total, 194,298 (23.5%) candidates belong to either of three sets. Their distribution over the sky (right panel of Fig. 3) is significantly different from the rest of the candidates, and displays a prominent “belt” along the ecliptic equator, related to the flashes from geostationary satellites. The regular grid visible in the sky map of non-associated candidates is due to interplay of a fixed tiling strategy of ZTF survey observations, and significant excess of the events in several of 64 read-out channels of CCD mosaic covering ZTF focal plane. The latter suggest that it may be to some degree contaminated with noise

⁴Cutout images distributed within ZTF alert packets contain small portions of both science, reference and difference images around transient positions.

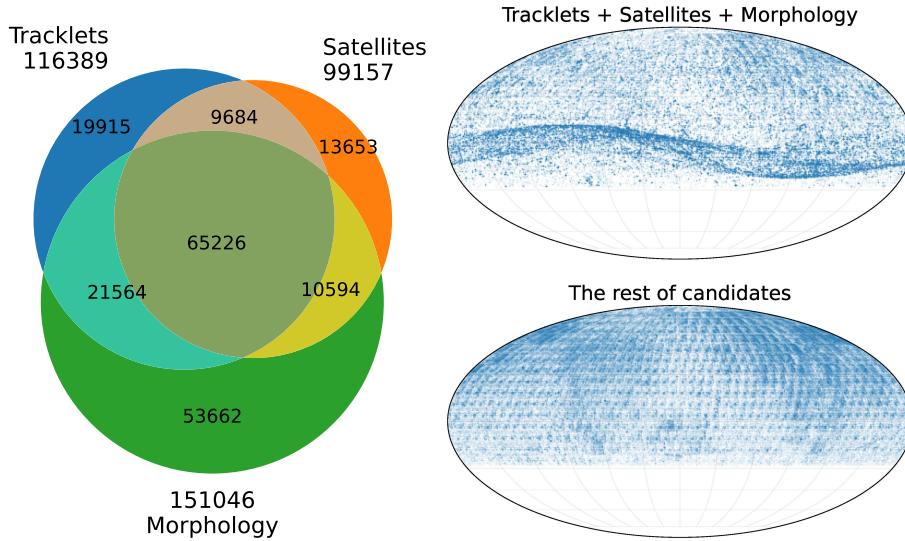


Figure 3. Left panel – Venn diagram of satellite associated events selected by three different methods as described in Section 3. In total, these events constitute 23.5% of all candidates. Right panel – sky maps in equatorial coordinates showing the distributions of events both associated with satellites using one of three methods outlined in Section 3, and not associated ones.

events. The rest of these non-satellite associated events is probably genuinely astrophysical, and contains e.g. large amplitude flares from late-type stars too faint to be seen in reference images, but their analysis is outside the scope of current work.

Upper panel of Fig. 4 shows the distribution of orbital parameters for the catalogued satellites successfully associated with flashes in Section 3.2. They occupy all major loci in the parameter space – near-Earth ones, geostationary satellites and highly inclined semi-synchronous *Molniya*-type orbits, with some of the satellites observed multiple times and producing large numbers of flares. Most of these satellites are inactive and debris ones, where random rotation is expected. Small number of still active satellites in the sample is most probably being stabilized by rotation.

For these events associated with individual catalogued satellites we may also constrain the duration of the flashes by comparing the length of the satellite arcs during the ZTF 30-seconds exposure with typical size of a point source in the images. As the ZTF pixel size is $1''$ (and typical seeing is $2''$), we may derive the duration (actually, an upper limit for it) of the flash as

$$\tau = 30 \cdot \frac{1''}{\text{arc length}} \text{ seconds.} \quad (1)$$

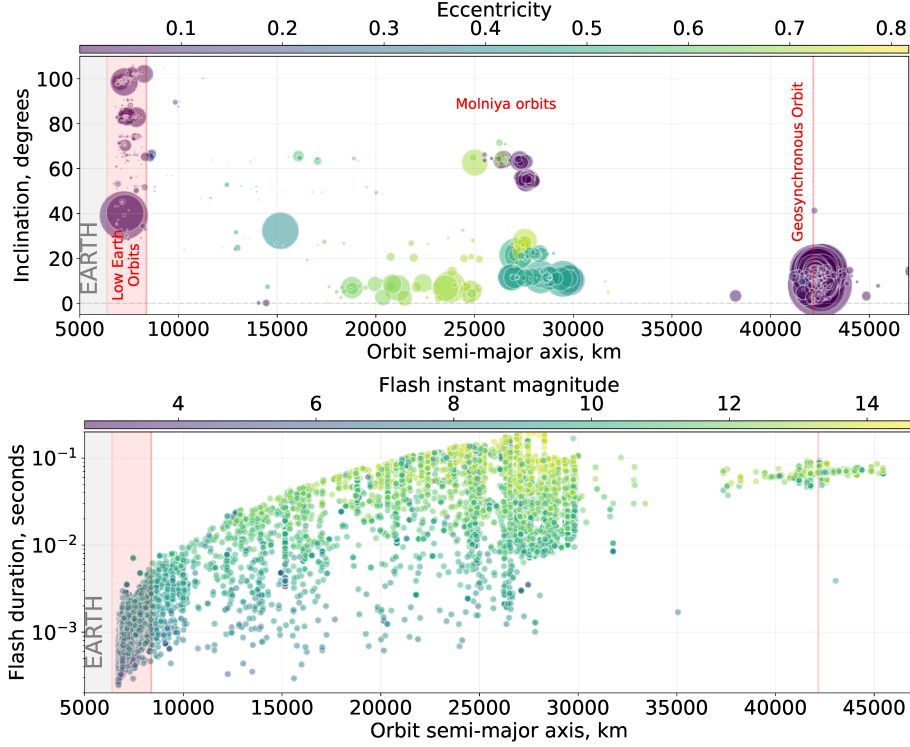


Figure 4. Upper panel – orbital parameters for the satellites from NORAD catalogue associated with tracklets as described in Section 3.2. Three zones of interest are displayed: Low-Earth orbits (with semi-major axis below an altitude of 2000 kilometers), *Molniya* orbits (centered on a semi-major axis corresponding to half a sidereal day, 26,000 kilometers, and an inclination of 63.4 degrees), and geosynchronous orbits. Each circle corresponds to a satellite, with size proportional to the number of its appearances in the dataset. Lower panel – distribution of flash durations of the events associated with known satellites as a function of their orbit semi-major axis. Color-coded is the instant brightness of the flashes, as they would be measurable in observations with sufficiently high temporal resolution.

On the other hand, instant brightness of the flash peak (the magnitude that would be measured if the temporal resolution of the observations would be high enough to fully resolve it) may be estimated as

$$\text{instant magnitude} = \text{mag} + 2.5 \log \frac{\tau}{30 \text{ seconds}}, \quad (2)$$

corresponding to the flashes being intrinsically brighter than they appear in ZTF images. The distribution of the duration of the flashes, as well as their

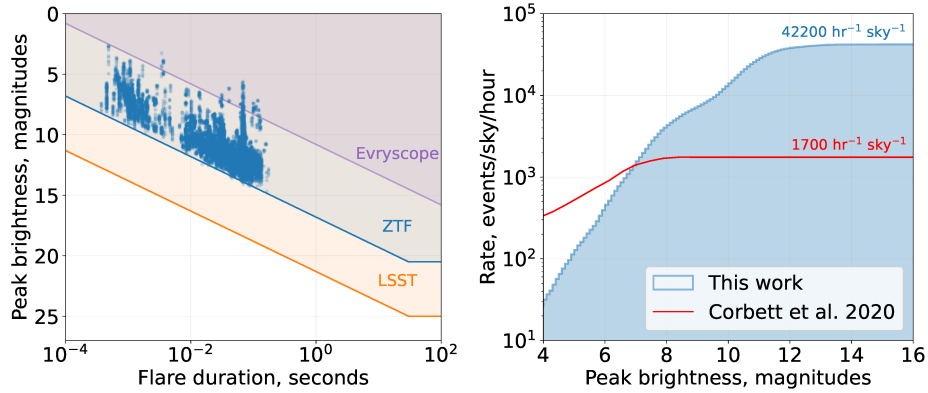


Figure 5. Left panel – distribution of flare duration and peak brightness for the events associated with catalogued satellites, together with detection limits for short flashes in three different sky surveys – Evryscope having 120 s typical exposures (Corbett et al., 2020), ZTF (Bellm et al., 2018), and upcoming Vera C. Rubin LSST (Ivezić et al., 2019), both having 30 s effective exposures. Right panel – cumulative distribution of the flash rate averaged over the whole sky as derived in this work, in comparison with results of Corbett et al. (2020) based on Evryscope observations.

intrinsic brightness, estimated this way is shown in lower panel of Fig. 4.

Effective detection limit of ZTF survey performed with a fixed exposure for the flashes of shorter duration is shown in left panel of Fig. 5, along with the same for upcoming Vera C. Rubin LSST (which will have the same effective 30-s exposure as ZTF), and Evryscope (Corbett et al., 2020). Based on the data from the latter survey, Corbett et al. (2020) reported the average all-sky rate of the satellite flashes to be around 1,800 per hour for the peak brightness above magnitude 8. The values of peak brightness that we derived above for the events matched with catalogued satellites in Section 3.2 may be used to update this rate estimate towards fainter flashes. The result is shown in right panel of Fig. 5. The rate is up to 42,000 events per hour from the whole sky, with the majority of flashes having instant brightness between 10 and 12 mag. For the whole set of events caused by glinting satellites (see left panel of Fig. 3) the all-sky rate is even higher, up to 80,000 events per hour. The difference of the rates for brightest events between ZTF and Evryscope data is significantly affected by both different saturation limits of these surveys, and by the fact that intrinsically brightest flashes are predominantly produced by the low-orbit satellites, which are less likely to stay point-like in ZTF than in Evryscope (whose pixel size is $13''$, so 13 times worse, while its typical 120 seconds exposure is only 4 times longer than ZTF one).

Extrapolating these results to upcoming LSST survey which is about to start

in less than a year is not trivial, as its pixel scale and seeing will be significantly better (0.2'' and 0.8'') than the ones of ZTF (1'' and 2''), while the detection limit will be at least 4 magnitudes deeper. The effect is twofold – some flashes that are seen as point-like in ZTF may become elongated, while the effective pixel crossing time will be smaller, and thus the quiescent trail of the satellite between the flashes will become fainter. The distribution of upper limits for the flare duration in lower panel of Fig. 4, and recent study of fainter debris on geostationary orbits by [Blake et al. \(2021\)](#) that revealed a large number of uncatalogued objects with significant amount of “tumbling” ones, suggest that LSST will also be significantly affected by satellite glints that will impact the detection of rapid flares of astrophysical origin.

5. Conclusion

In order to constrain the rate of satellite glints as seen by modern and upcoming large-scale sky surveys we analyzed a subset of events ZTF alert stream that are detectable just on single exposure and are not caused by sporadic stellar variability or subtraction artefacts, thus potentially containing rapid optical transients of astrophysical origin. Using three different methodologies – simple geometrical routine for associating the events on individual exposures into “tracklets” roughly along the the great circles, direct association of event positions with the arcs of catalogued NORAD satellites, and simple morphological analysis of the alert cutouts – we associated 23.5% of all these candidate events with satellite glints.

The glinting satellites occupy all possible orbits around the Earth, from low to medium to geosynchronous ones, and the durations of the observed flashes are as short as 10^{-1} – 10^{-3} seconds with instant brightness of $g=4$ – 14 magnitudes. The total rate of these flashes is on average up to 80,000 per hour from the whole sky, and is larger in the region along the celestial equator occupied by the flashes from geostationary satellites. Assuming that the proportion of objects orbiting the Earth increases with the decrease of their size, we expect deeper surveys such as the Vera C. Rubin LSST to detect much more events of this kind.

Acknowledgements. This work was developed within the Fink community and made use of the Fink community broker resources. Fink is supported by LSST-France and CNRS/IN2P3. This project has received financial support from the CNRS through the MITI interdisciplinary programs and from CNES. SK acknowledges support from the European Structural and Investment Fund and the Czech Ministry of Education, Youth and Sports (Project CoGraDS-CZ.02.1.01/0.0/0.0/15003/0000437).

References

Andreoni, I., Coughlin, M. W., Kool, E. C., et al., Fast-transient Searches in Real

- Time with ZTFReST: Identification of Three Optically-discovered Gamma-ray Burst Afterglows and New Constraints on the Kilonova Rate. 2021, *arXiv e-prints*, arXiv:2104.06352
- Arimatsu, K., Tsumura, K., Usui, F., Ootsubo, T., & Watanabe, J.-i., Detectability of Optical Transients with Timescales of Subseconds. 2021, *Astronomical Journal*, **161**, 135, DOI: 10.3847/1538-3881/abd94d
- Barbary, K. 2018, SEP: Source Extraction and Photometry
- Bellm, E. C., Kulkarni, S. R., Graham, M. J., et al., The Zwicky Transient Facility: System Overview, Performance, and First Results. 2018, *Publications of the Astronomical Society of the Pacific*, **131**, 018002, DOI: 10.1088/1538-3873/aecbe
- Blake, J. A., Chote, P., Pollacco, D., et al., DebrisWatch I: A survey of faint geosynchronous debris. 2021, *Advances in Space Research*, **67**, 360, DOI: 10.1016/j.asr.2020.08.008
- Burke-Spolaor, S., Multiple messengers of fast radio bursts. 2018, *Nature Astronomy*, **2**, 845, DOI: 10.1038/s41550-018-0630-x
- Corbett, H., Law, N. M., Soto, A. V., et al., Orbital Foregrounds for Ultra-short Duration Transients. 2020, *Astrophysical Journal, Letters*, **903**, L27, DOI: 10.3847/2041-8213/abee5
- Ho, A. Y. Q., Perley, D. A., Beniamini, P., et al., ZTF20aaajnksq (AT 2020blt): A Fast Optical Transient at $z \approx 2.9$ with No Detected Gamma-Ray Burst Counterpart. 2020, *Astrophysical Journal*, **905**, 98, DOI: 10.3847/1538-4357/abc34d
- Ivezic, Ž., Kahn, S. M., Tyson, J. A., et al., LSST: From Science Drivers to Reference Design and Anticipated Data Products. 2019, *Astrophysical Journal*, **873**, 111, DOI: 10.3847/1538-4357/ab042c
- Karpov, S., Beskin, G., Biryukov, A., et al., Observations of Transient Events with Mini-MegaTORTORA Wide-Field Monitoring System with Sub-Second Temporal Resolution. 2019, in *Revista Mexicana de Astronomia y Astrofisica Conference Series*, Vol. **51**, *Revista Mexicana de Astronomia y Astrofisica Conference Series*, 30–38
- Karpov, S., Beskin, G., Biryukov, A., et al., Observations of the Prompt Optical Emission of GRB 160625B with Mini-MegaTORTORA. 2017a, in *Astronomical Society of the Pacific Conference Series*, Vol. **510**, *Stars: From Collapse to Collapse*, ed. Y. Y. Balega, D. O. Kudryavtsev, I. I. Romanyuk, & I. A. Yakunin, 309
- Karpov, S., Beskin, G., Biryukov, A., et al., Untriggered search for rapid optical transients with Mini-MegaTORTORA wide-field monitoring system. 2017b, in *Proceedings of the International Astronomical Union*, Vol. **324**, *New Frontiers in Black Hole Astrophysics*, ed. A. Gomboc, 85–86
- Karpov, S., Beskin, G., Bondar, S., et al., Wide and Fast: Monitoring the Sky in Subsecond Domain with the FAVOR and TORTORA Cameras. 2010, *Advances in Astronomy*, **2010**, 784141, DOI: 10.1155/2010/784141
- Kehoe, R., Akerlof, C., Balsano, R., et al., An Untriggered Search for Optical Bursts. 2002, *Astrophysical Journal*, **577**, 845, DOI: 10.1086/342231

- Laher, R. R., Surace, J., Grillmair, C. J., et al., IPAC Image Processing and Data Archiving for the Palomar Transient Factory. 2014, *Publications of the ASP*, **126**, 674, DOI: 10.1086/677351
- Mahabal, A., Rebbapragada, U., Walters, R., et al., Machine Learning for the Zwicky Transient Facility. 2019, *Publications of the ASP*, **131**, 038002, DOI: 10.1088/1538-3873/aaf3fa
- Masci, F. J., Laher, R. R., Rusholme, B., et al., The Zwicky Transient Facility: Data Processing, Products, and Archive. 2019, *Publications of the ASP*, **131**, 018003, DOI: 10.1088/1538-3873/aae8ac
- Möller, A., Peloton, J., Ishida, E. E. O., et al., fink, a new generation of broker for the LSST community. 2020, *Monthly Notices of the Royal Astronomical Society*, **501**, 3272, DOI: 10.1093/mnras/staa3602
- Nir, G., Ofek, E. O., Ben-Ami, S., et al., A high-rate foreground of sub-second flares from geosynchronous satellites. 2021a, *Monthly Notices of the RAS*, **505**, 2477, DOI: 10.1093/mnras/stab1437
- Nir, G., Ofek, E. O., & Gal-Yam, A., The GN-z11-Flash Event can be a Satellite Glint. 2021b, *Research Notes of the American Astronomical Society*, **5**, 27, DOI: 10.3847/2515-5172/abe540
- Racusin, J. L., Karpov, S. V., Sokolowski, M., et al., Broadband observations of the naked-eye γ -ray burst GRB080319B. 2008, *Nature*, **455**, 183, DOI: 10.1038/nature07270
- Rhodes, B. 2019, Skyfield: High precision research-grade positions for planets and Earth satellites generator
- Richmond, M. W., Tanaka, M., Morokuma, T., et al., An optical search for transients lasting a few seconds. 2020, *Publications of the ASJ*, **72**, 3, DOI: 10.1093/pasj/psz120
- Schaefer, B., Optical Flash Background Rates. 1987, *A&A*, **174**, 338
- Tingay, S. & Joubert, W., High cadence optical transient searches using drift scan imaging II: Event rate upper limits on optical transients of duration ≥ 21 ms and magnitude ≤ 6.6 . 2021, *Publications of the Astron. Soc. of Australia*, **38**, e001, DOI: 10.1017/pasa.2020.53
- Zhang, B. B., Zhang, B., Castro-Tirado, A. J., et al., Transition from fireball to Poynting-flux-dominated outflow in the three-episode GRB 160625B. 2018, *Nature Astronomy*, **2**, 69, DOI: 10.1038/s41550-017-0309-8

Long term follow-up coverage of Gaia photometric alert sources by Ondrejov robotic telescopes

R. Hudec^{1,2} , M. Jelínek¹  and J. Štrobl¹ 

¹ *Astronomical Institute of the Czech Academy of Sciences
251 65 Ondřejov, The Czech Republic*

² *Czech Technical University in Prague, Faculty of Electrical Engineering,
(E-mail: hudecren@fel.cvut.cz)*

Received: August 22, 2023; Accepted: November 8, 2023

Abstract. The robotic telescopes at the Ondrejov Observatory are providing long-term optical multi-color coverage for selected 25 Gaia alert triggers located in the northern sky hemisphere. I will present and briefly discuss examples of selected results, mostly unpublished, obtained with these devices. In addition to that, I will present and discuss the potential of large historical photographic plate archives located around the globe as sources of both photometric as well as spectroscopic data. They allow us to perform the long-term study of photometric and spectroscopic evolution for astrophysical sources in general and for Gaia alert sources in particular. Some of these databases were digitized and on-line access is provided.

Key words: Gaia – robotic telescopes – multicolor photometry

1. Introduction

The robotic telescopes (RT) at the Ondrejov Observatory (recently 3 RTs: CTAN/FRAM (recently at La Palma), D50, BART/SBT), apart from gamma-ray bursts (GRB) follow-up, provide valuable data for analyses of various types of high-energy (HE) sources (Nekola et al., 2009, 2010; Hudec, 2019; Štrobl et al., 2019). Up to 100 targets are in the list for continuous monitoring, mostly INTEGRAL HE sources, blazars, cataclysmic variables (CVs), and newly detected Gaia alert sources. An automated data pipeline was developed by M. Jelinek allowing these data to be evaluated in an efficient way. There are more than 2 million CCD frames in the database, with more than 2 billion star images. The telescopes support also various satellite observing campaigns and GRBs alert follow-up (Jelínek et al., 2022; Oganessian et al., 2023).

2. Gaia photometric alert sources monitored

The following Gaia photometric alert targets (Wyrzykowski et al., 2012) are observed by the D50 robotic telescope on a daily basis, weather permitting as follows. Note that this list is regularly updated according to scientific demands.

```
id="1111" name="Gaia16aye - Ayers Rock"
id="1129" name="Gaia18arn (Arnica) - microlensing event"
id="1137" name="Gaia18cik - microlensing event"
id="1133" name="Gaia18cjk - microlensing event"
id="1138" name="Gaia18clv - microlensing event"
id="1136" name="Gaia18chq - microlensing event"
id="1145" name="Gaia18cmy - microlensing event"
id="1153" name="Gaia21bnh"
id="1156" name="ZTF18aarippg (binary SMBH merger)"
id="1157" name="Gaia22awa - microlensing event"
```

and the following Gaia alert targets are observed less frequently on a weekly basis, as follows.

```
id="1122" name="Gaia17cem - fading galaxy centre"
id="1123" name="Gaia16bnz - very bright CV"
id="1144" name="Gaia18cnz - probably Mira"
id="1147" name="Gaia17bpi"
```

3. Examples of monitoring data obtained

In this section, we give examples of monitoring (multicolor photometric data) for selected Gaia photometric alerts¹ gained, mostly by the Ondrejov D50 RT.

- Gaia16aye. 1.2 magnitude rise in red star near Galactic Plane. From BP/RP red spectrum. Microlensing trigger, confirmed and published. The lens system consists of two main sequence stars with Solar masses 0.57 ± 0.05 and 0.36 ± 0.03, at a distance of 780 pc (2,500 ly), and an orbital period of 2.88 years (Wyrzykowski et al., 2020).
- Gaia17cem. Gaia source on Seyfert 1 Galaxy 2MASX J17085915+2153082 dims by 1.2 mags over ~4 months. Daily means are plotted (Fig. 2).
- Gaia16bnz. Classification: Gaia16bnz is a new CV with 2 epochs variable LAMOST spectra taken in 2015 October and December (Huo et al., 2020).

¹<https://gsaweb.ast.cam.ac.uk/alerts>

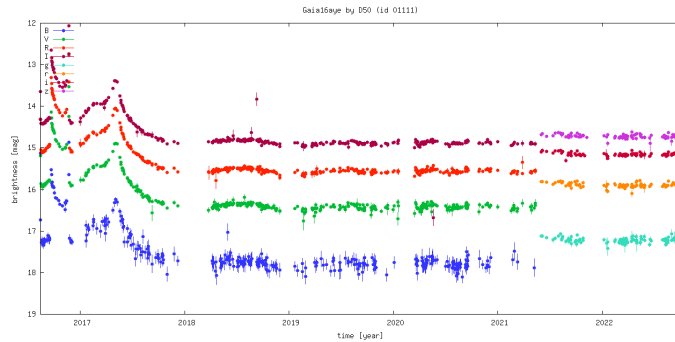


Figure 1. Gaia16aye, 1.2 mag rise in red star near Galactic Plane. BP and RP (Gaia blue and red photometers) indicate red spectrum of this source. Microlensing trigger, confirmed and published (Wyrzykowski et al., 2020). The lens system consists of two main sequence stars with Solar masses 0.57 ± 0.05 and 0.36 ± 0.03 , at a distance of 780 pc (2,500 ly), and an orbital period of 2.88 years (Wyrzykowski et al., 2020)

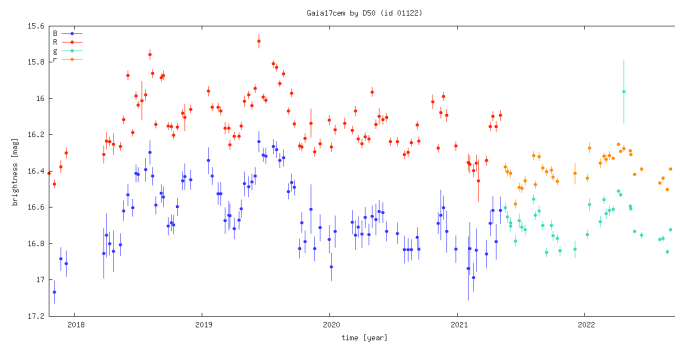


Figure 2. Gaia17cem, Gaia source on Seyfert 1 Galaxy 2MASX J17085915+2153082 dims by 1.2 mags over ~ 4 months. Daily means are plotted.

- Gaia18cm. 2 mag brightening of red Gaia source. BP/RP spectra are red. Late-type star showing emission in H α line, very likely T Tauri star. Originally misclassified as SN ²
- Gaia17bpi. Classification: A new FU Ori Type variable according to spectrum Hanks et al. (2020).

²<http://gsaweb.ast.cam.ac.uk/alerts/alert/Gaia18cm/>

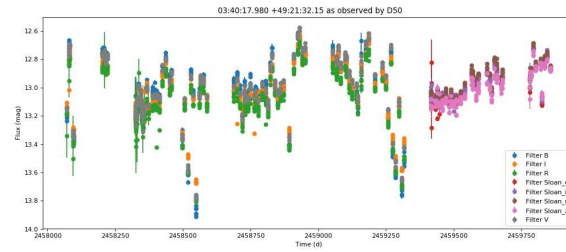


Figure 3. Gaia16bnz. All points, last 5 years Classification: Gaia16bnz is a new CV with 2 epochs variable LAMOST spectra taken in 2015 October and December (Huo et al., 2020)

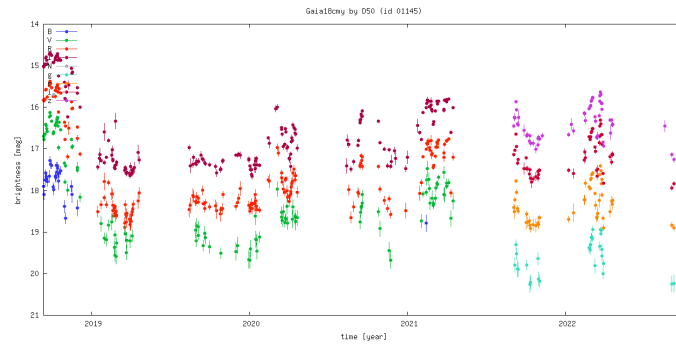


Figure 4. Gaia18cmj. 2 mag brightening of red Gaia source. BP/RP spectra red. Late-type star showing emission in H α line, very likely T Tauri star. Originally misclassified as a supernova (SN).

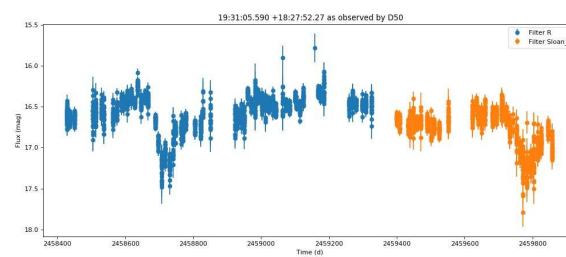


Figure 5. Gaia17bpi. All points during the last 5 years are plotted. Classification: A new FU Ori Type variable star according to spectrum (Hankins et al., 2020).

- Gaia21blj. ~ 5.5 mag outburst in a known cataclysmic variable (CV) TT Boo. Blue spectra from Gaia BP/RP ³.

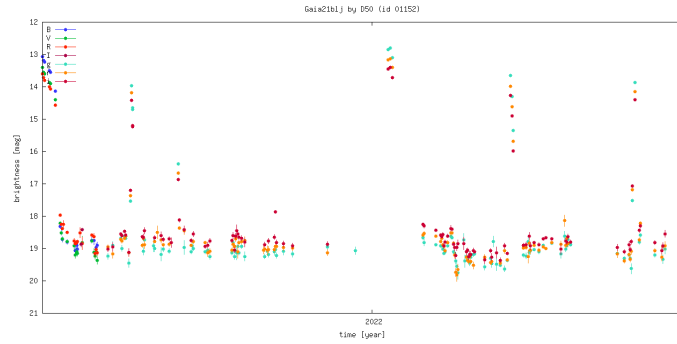


Figure 6. Gaia21blj, ~ 5.5 mag outburst in known CV TT Boo. Blue spectra from Gaia BP/RP³

- Gaia21bnh. Known CV RX J1715.6+6856 in outburst⁴.

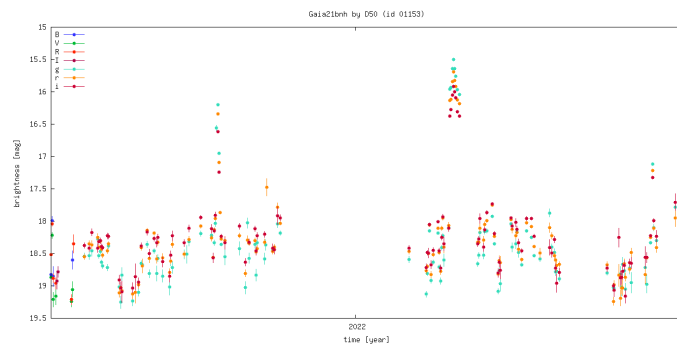


Figure 7. Gaia21bnh, known CV RX J1715.6+6856 in outburst. ⁴

- Gaia21azb. ~ 2.3 mag rise in Galactic plane source – candidate microlensing event. BP/RP spectrum is red. Unclassified. No spectra available. ⁵

³<http://gsaweb.ast.cam.ac.uk/alerts/alert/Gaia21blj/>

⁴<http://gsaweb.ast.cam.ac.uk/alerts/alert/Gaia21bnh/>

⁵<http://gsaweb.ast.cam.ac.uk/alerts/Gaia21azb/>

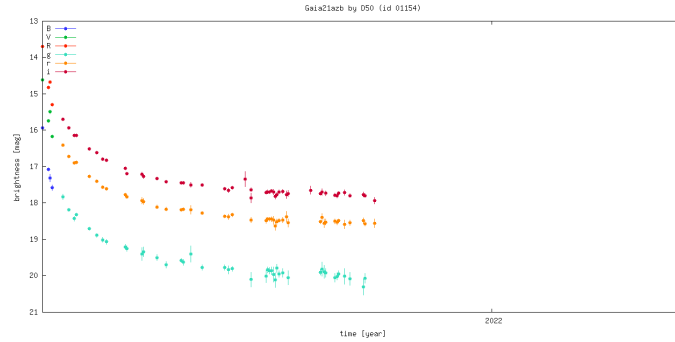


Figure 8. Gaia21azb, ~ 2.3 magnitude rise in Galactic plane source – candidate microlensing event. BP/RP spectrum is red. Unclassified. No spectra available.⁵

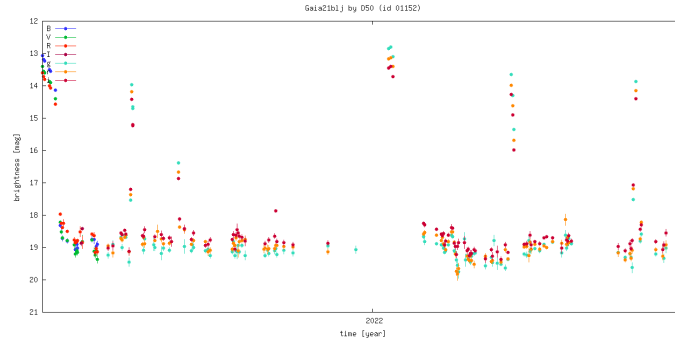


Figure 9. Gaia21blj, ~ 5.5 mag outburst in known CV TT Boo. Blue spectra from Gaia BP/RP³

- Gaia18arn. Gaia source in the Galactic plane brightens by ~ 0.25 mags. Classification strong H α emission reddened Be star. BP/RP spectrum is red.⁶
- Gaia18cjk. Long-term brightening of ~ 1 mag in Gaia source in Galactic plane, candidate microlensing event.⁷
- Gaia18cmk. Gaia source near Galactic plane brightens by almost 1 mag, no spectra available, confirmed microlensing trigger (Mróz et al., 2020).
- Gaia18cmk. Our light curve is not complete, we observed the target soon after the maximum, the pulse had an amplitude of (0.660.02) mag and a

⁶<http://gsaweb.ast.cam.ac.uk/alerts/alert/Gaia18arn/>

⁷<http://gsaweb.ast.cam.ac.uk/alerts/alert/Gaia18cjk/>

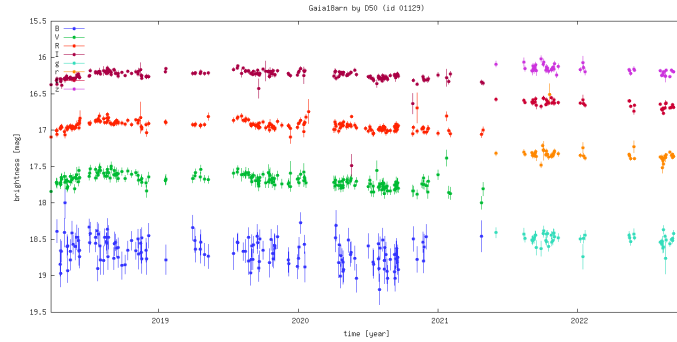


Figure 10. Gaia18arn. Gaia source in the Galactic plane brightens by 0.25 mags. Classification strong H α emission reddened Be star. BP/RP spectrum is red.⁶

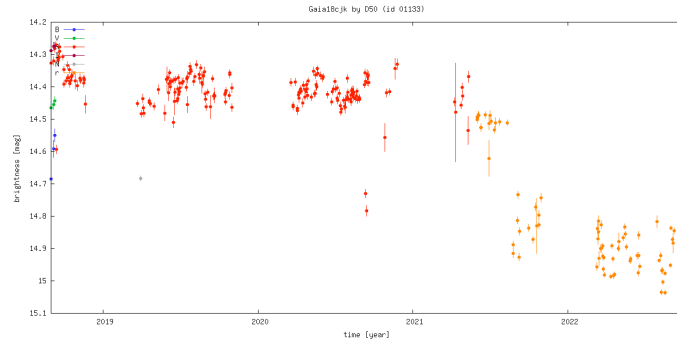


Figure 11. Gaia18cjk. Long-term brightening of ~ 1 mag in Gaia source in Galactic plane, candidate microlensing event.⁷

duration FWHM = (45.11.3) days. The object was observed from February 10, 2019 until June 10, 2021, when we decided to stop the monitoring as there was no activity for two years.

- Gaia18clv. A faint Gaia source in the Galactic Plane slowly rises by almost 3 mags. Classification as a binary microlensing event is probably wrong due to the long-term light curve.⁸
- Gaia18cnz. Very red spectrum, also from Gaia RP/BP. M-type supergiant, very likely Mira variable.⁹

⁸<http://gsaweb.ast.cam.ac.uk/alerts/alert/Gaia18clv/>

⁹<http://gsaweb.ast.cam.ac.uk/alerts/alert/Gaia18cnz/>

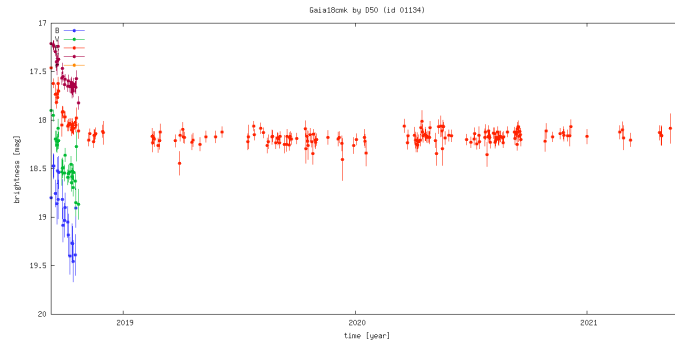


Figure 12. Gaia18cmk Gaia source near Galactic plane brightens by almost 1 mag, no spectra, confirmed microlensing trigger (Mróz et al., 2020).

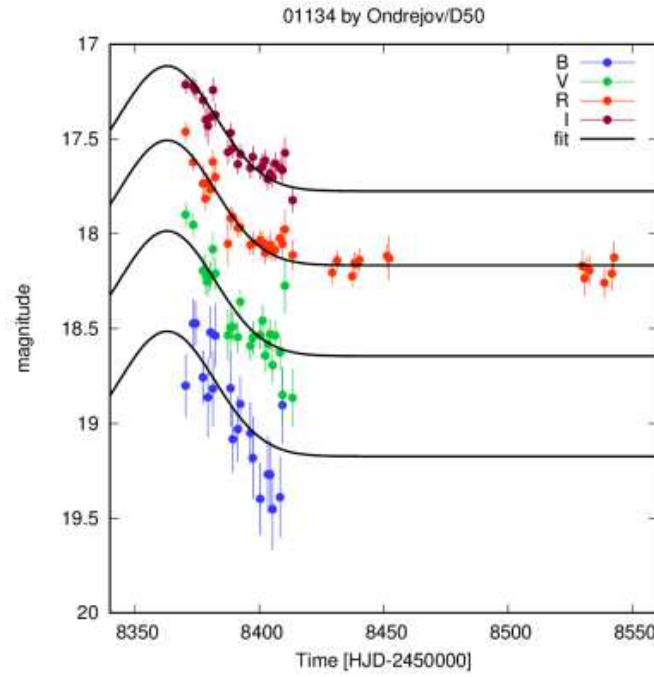


Figure 13. Gaia18cmk. Our light curve is not complete, we observed soon after the maximum, that pulse had an amplitude of (0.660.02) mag and duration FWHM = (45.11.3) days. Observed from February 10, 2019 until June 10, 2021, when we decided to stop the target after 2 years without activity.

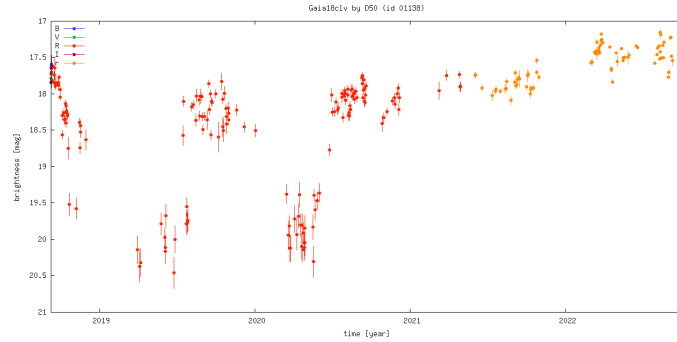


Figure 14. Gaia18clv, faint Gaia source in the Galactic Plane slowly rises by almost 3 mags. The binary microlensing event classification is probably wrong due to the long-term light curve.⁸

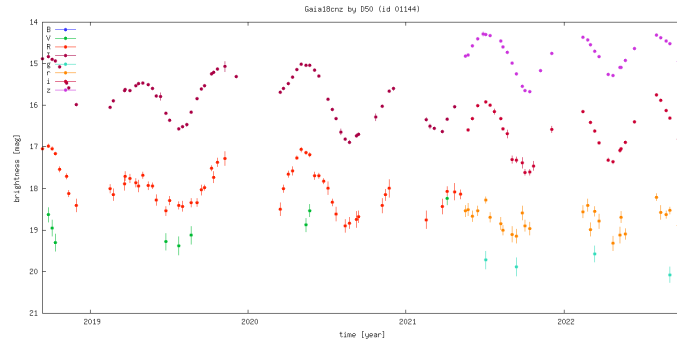


Figure 15. Gaia18cnz. Very red spectrum, also from Gaia RP/BP. M-type supergiant, very likely Mira variable.⁹

4. TT Bootis: an example of gaining new results on classified Gaia alert trigger

TT Bootis is a poorly investigated dwarf nova despite of its large-amplitude outbursts. The star is located at RA 224.43643 and DEC 40.72790 (914:57:44.74, 40:43:40.44) and in galactic coords. at 968.7414, 60.703850.

Multi-station photometry of TT Boo was reported during its June 2004 superoutburst however other outbursts are poorly investigated. The amplitude of the superoutburst in June 2004 was about 5.5 mag and its length was about 22 days. The star showed a small re-brightening starting around the 9th day of the superoutburst. During the entire bright state we observed clear superhumps with amplitudes from 0.07 mag to 0.26 mag and a mean period of $P_{sh}=0.0779589(47)$

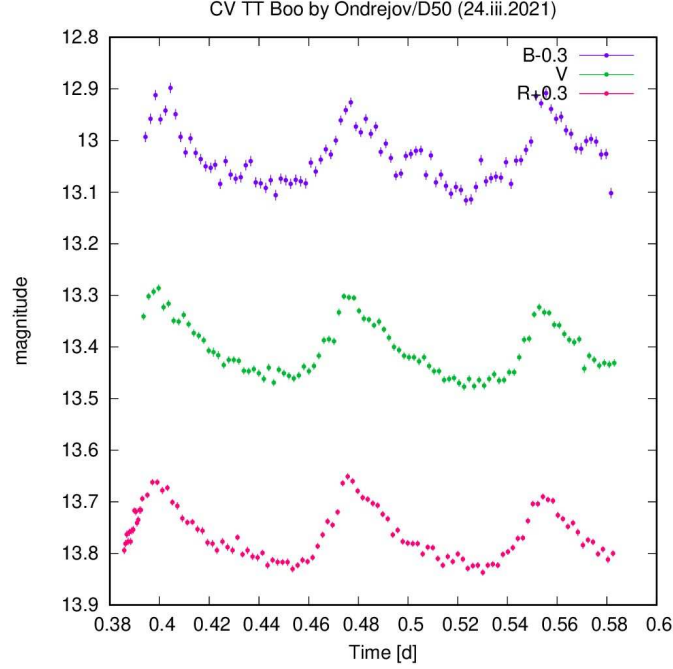


Figure 16. TT Boo, an example of searches for fast intra-night variations.

days (112.261 ± 0.007 min). The period was found not constant but decreased at the beginning and the end of superoutburst and increased in the middle phase (Olech et al., 2004).

The brightening of TT Bootis was alerted as Gaia Scientific Alert Gaia21blj with the Alerting date 2021-03-21 14:23:02 (Julian date 2459295.10) and Alerting magnitude of 13.53 (Historic Gaia magnitude 17.19). The provided LDS (low dispersion spectra) data from Gaia BP and RP Photometers indicate the blue color of the source.

We have performed photometric sets lasting most of the night in order to study TT Boo variability during its 2021 outburst. Eventually, we acquired 6 nights of the outburst, obtaining almost 2000 photometric points in filters B, V and R.

Our observations have revealed five outbursts not described in the scientific literature in multi-color photometry. We plan to publish these data later in a more detailed scientific publication (Hudec et al., 2023, in preparation).

5. Adding historical epochs

We note that in addition to follow-up and monitoring by recent robotic telescopes, additional photometric data can be obtained from astronomical data archives namely large collections of astronomical photographic plates. These databases can add photometry for these sources typically for epochs between 1890 and 1980 including faint sources down to magnitude 20 (Hudec, 2019) (Hudec, 2018). This approach can extend the photometric coverage for selected Gaia alert sources for several decades or even more.

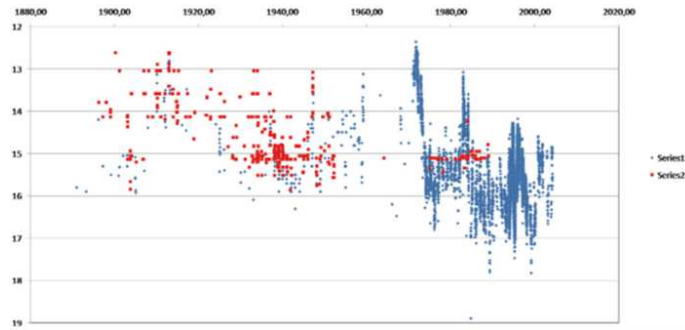


Figure 17. Example of very long-term (more than 100 years) light curve based on astronomical photographic plate archives: blazar OJ287 (supermassive binary black hole candidate).

6. Conclusions

The Ondrejov Observatory robotic telescopes provide valuable data for various aspects of high-energy astrophysics including GRBs alerts. Furthermore they can be efficiently used also for other tasks of modern astrophysics such as follow-up and dense and long-term multicolor monitoring of Gaia satellite photometric alert sources.

Acknowledgements. The research leading to these results has received partial funding from the European Unions Horizon 2020 Programme under the AHEAD2020 project (grant agreement n. 871158). Also, support by the project RVO:67985815 is acknowledged.

References

Hankins, M., Hillenbrand, L. A., De, K., et al., Palomar Gattini-IR discovery and

- spectroscopic classification of a highly reddened YSO in outburst. 2020, *The Astronomer's Telegram*, **13902**, 1
- Hudec, R., Astrophysics with digitized astronomical plate archives. 2018, *Astronomische Nachrichten*, **339**, 408, DOI: 10.1002/asna.201813515
- Hudec, R., Astronomical photographic data archives: Recent status. 2019, *Astronomische Nachrichten*, **340**, 690, DOI: 10.1002/asna.201913676
- Huo, Z., Dennefeld, M., Liu, X., Pursimo, T., & Zhang, T., Characterizing some Gaia Alerts with LAMOST and SDSS. 2020, *Astrophysics and Space Science*, **365**, 89, DOI: 10.1007/s10509-020-03804-7
- Jelínek, M., Topinka, M., Karpov, S., et al., GRB 190919B: Rapid optical rise explained as a flaring activity. 2022, *Astronomy and Astrophysics*, **662**, A126, DOI: 10.1051/0004-6361/202143010
- Mróz, P., Street, R. A., Bachelet, E., et al., Gravitational Microlensing Events from the First Year of the Northern Galactic Plane Survey by the Zwicky Transient Facility. 2020, *Research Notes of the American Astronomical Society*, **4**, 13, DOI: 10.3847/2515-5172/ab7021
- Nekola, M., Hudec, R., Jelínek, M., et al., Burst Alert Robotic Telescope and Optical Afterglows. 2009, *Baltic Astronomy*, **18**, 374
- Nekola, M., Hudec, R., Jelínek, M., et al., BART: The Czech Autonomous Observatory. 2010, *Advances in Astronomy*, **2010**, 103986, DOI: 10.1155/2010/103986
- Oganesyan, G., Karpov, S., Salafia, O. S., et al., Exceptionally bright optical emission from a rare and distant gamma-ray burst. 2023, *Nature Astronomy*, DOI: 10.1038/s41550-023-01972-4
- Olech, A., Cook, L. M., Złoczewski, K., et al., Curious Variables Experiment (CURVE). TT Bootis – Superhump Period Change Pattern Confirmed. 2004, *Acta Astronomica*, **54**, 233
- Štrobl, J., Jelínek, M., & Hudec, R., Small Binocular Telescope: The new epoch of Burst Alert Robotic Telescope. 2019, *Astronomische Nachrichten*, **340**, 633, DOI: 10.1002/asna.201913668
- Wyrzykowski, L., Hodgkin, S., Blogorodnova, N., Kozlov, S., & Burgon, R., Photometric Science Alerts from Gaia. 2012, in *2nd Gaia Follow-up Network for Solar System Objects*, 21
- Wyrzykowski, L., Mróz, P., Rybicki, K. A., et al., Full orbital solution for the binary system in the northern Galactic disc microlensing event Gaia16aye. 2020, *Astronomy and Astrophysics*, **633**, A98, DOI: 10.1051/0004-6361/201935097

Gamma-Ray Bursts' redshift distribution's dependence on their duration

S. Pinter¹, L.G. Balazs^{2,3}, Z. Bagoly^{1,2} and I. Horvath¹

¹ *University of Public Service, Budapest, Hungary (E-mail: sandor.pinter@uni-nke.hu)*

² *Eötvös University, Budapest, Hungary*

³ *Konkoly Observatory, Research Centre for Astronomy and Earth Sciences, Budapest, Hungary*

Received: July 6, 2023; Accepted: October 30, 2023

Abstract. Gamma-ray bursts (GRBs) are distant, extremely energetic, short (about 0.1-1000 sec) cosmic transients, which could sample the whole observable Universe. Two of the Gamma-Ray Bursts' important properties are the duration and the distance of the burst. We analyzed these two important quantities of the phenomena. We mapped their two-dimensional distribution and explored some suspicious areas. As it is well known the short GRBs are closer than the others, hence we search for parts in the Universe where the GRBs duration differs from the others. We also analyze whether there are any areas where the redshifts are differing.

Key words: data analysis – gamma-ray bursts

1. Introduction

According to Mészáros (2006), gamma-ray bursts (GRBs) are the most energetic explosions in the distant Universe. The most massive stars collapsing (collapsar model) (MacFadyen & Woosley, 1999; Zhang & Mészáros, 2002) and compact stars combining to become black holes or neutron stars are the two main models that potentially account for GRB events (Eichler et al., 1989). The second model had been validated by the finding of GW170814/GRB170814A (Abbott et al., 2017; Goldstein et al., 2017; Horváth et al., 2018; Bagoly et al., 2016, 2017).

Compared to star merging events, collapsing events are often longer and softer. Horváth (1998) based its identification of a third group on the duration–hardness plane (Horváth et al., 2004, 2006; Rípa & Mészáros, 2016; Horváth et al., 2018). Although the physical makeup of this intermediate group was not completely understood, it appears that the X-ray flash events may be related to the intermediate GRBs (Horváth et al., 2010; Pinter et al., 2017; Bi et al., 2018) and Balazs et al. (1998) showed that the sky distribution of GRBs not isotropic, since then, the topic has raised many questions and has therefore been actively researched in various databases (e.g. observations with BATSE: Vavrek

et al. (2008); Balázs et al. (1999); Hakkila et al. (2018), with Fermi: Tóth et al. (2019); Horváth et al. (2019), and with Swift & Fermi data: Pérez-Ramírez et al. (2010); Hakkila et al. (2018); Bagoly et al. (2022)

As a result, the Giant GRB Ring (Balázs et al., 2015, 2018) and the Hercules-Corona Borealis Great Wall (Horváth et al., 2014, 2015; Horvath et al., 2020), the two greatest structures in the Universe, were found. The relationship between the location of the GRBs and their duration became immediately apparent following the first redshift measurement: the short GRBs are positioned closer than the lengthy GRBs. But because GRBs happen over such a long period of time, it is possible that some of their characteristics vary with distance (Bagoly et al., 2003; Suleiman et al., 2022; Kovács et al., 2019; Hatsukade et al., 2019; Toth et al., 2019).

One of the largest structures yet discovered, the ring of GRBs has a diameter of around 1.72 Gpc (5.6 billion light years) and is located at a distance of about 2.8 Gpc (9.1 billion light years) from Earth with a redshift of between 0.78 and 0.86. The ring, which is made up of nine GRBs, may be connected to a cosmic structure. Given recognized theoretical models, such a concentration thus seems incredibly implausible. There are theories that mention the presence of a massive supergalactic structure (Eingorn et al., 2023a,b). With a mean size of almost 5.6 billion light years, this would be an incredibly large structure of the universe. Because of its connection to star formation, such a supercluster can explain the GRBs' significant overdensity. It would be one of the biggest structures in the observable world if such a structure actually exist (Balázs et al., 2015, 2018).

2. Data selection & methods

Currently, nearly five hundred redshifts have been observed for GRBs. The Caltech GRBOX web-page contains most of them, therefore, in this analysis we use their data set (<https://sites.astro.caltech.edu/grbox/grbox.php>) On Fig. 1 we show the redshift vs. duration distribution of these 474 GRBOX GRBs.

To study whether the redshift distribution depends on the duration (T_{90}) parameter, one can use several statistical tests. Here, we ordered the GRBs by duration and chose n consecutive ones. Since there are few short bursts with redshift bigger than one, we omitted the 53 GRBs which had $T_{90} \leq 5s$, and we analyzed only the remaining 421 GRBs. This group's redshift distribution was compared with the complementary $421 - n$ GRBs' redshift distribution using a Kolmogorov-Smirnov test (KS). We compared the redshift distributions starting the group at the k -th position. We carried out this process for different group sizes from $n = 8$ to $n = 99$. As an example, Fig. 2 shows the KS p value's (in logarithmic scale) dependence of k for $n = 18, 40$ and 63 , respectively. Note that the short part was cut from the figures, since p is extremely low in the short

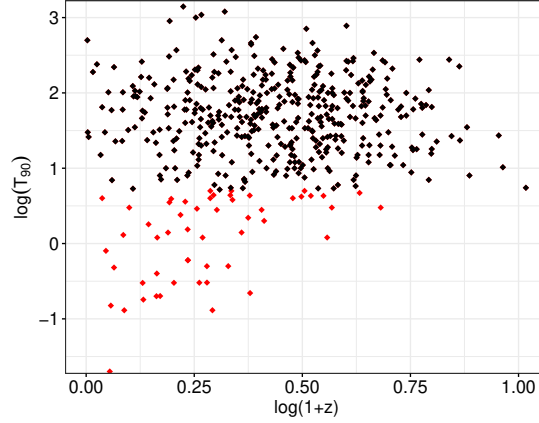


Figure 1. Redshift vs. duration (T_{90}) distribution of the 421 non-short GRBs marked with black, and the omitted 53 GRBs with red.

duration area, which also means high significance. The green (0.0455) and blue (0.0027) lines show 2 and 3 sigma significance, respectively.

One can make a similar analysis by swapping the variables: order the GRBs by redshift, select a redshift interval, then compare the duration distribution of this subsample with the duration distribution of the complementary sample. We omitted the 53 GRBs which had $T_{90} \leq 5s$, too. Here we ordered the GRBs by redshift and chose the closest, consecutive n GRBs and compared the n closest GRBs' duration distribution with the $421 - n$ GRBs' duration distribution, performing the Kolmogorov-Smirnov test (KS). We repeated this process starting from the k -th GRB and repeated the process with a block size of n running from 8 to 99.

3. Results

Fig. 3 shows the two-parameter (n , duration) KS p value. The p value reaches 0.0027 in two areas, the $16s < T_{90} < 20s$, $12 < n < 21$ and $49 < T_{90} < 61$, $23 < n < 36$. In these two areas the GRBs' T_{90} distribution differs significantly (more than 3σ) from the rest.

Fig. 4 shows the two-parameter (n , redshift) p value. The p value reaches 0.0027 in two areas, the $1.49 < z < 1.61$, $19 < n < 38$ and $2.91 < z < 3.075$, $11 < n < 19$ (Horvath et al., 2022). In these two areas the GRBs' redshift distribution differs significantly (more than 3σ) from the rest of the GRBs'.

We must emphasize that the KS test requires independent and identically distributed (IID) random variables, but the above method does not fulfil this

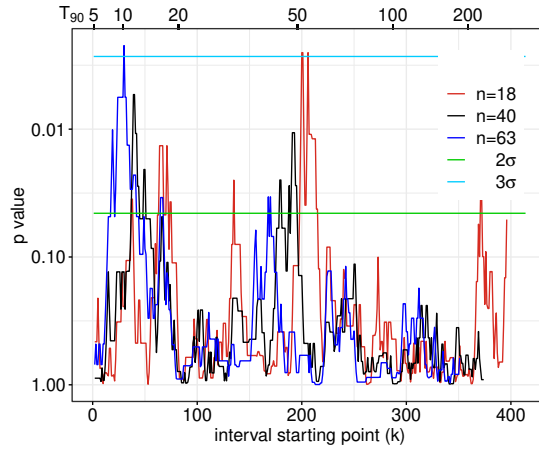


Figure 2. The logarithm of KS test p value as a function of the starting number of the n GRBs. Green (light blue) line marks the 2 (3) sigma significance level.

criteria since the n consecutive values are overlapping with each other until the difference between starting points is greater than n .

Please note, that we do not claim that there is any physical difference between the regions found in this study and the rest of the GRBs. We would like to point out that these areas are remarkable, and worth studying in more details in the future.

Acknowledgements. The authors thank the Hungarian TKP2021-NVA-16 and OTKA K-146092 program for their support.

References

- Abbott, B. P., Abbott, R., Abbott, T. D., et al., GW170814: A Three-Detector Observation of Gravitational Waves from a Binary Black Hole Coalescence. 2017, *Physical Review Letters*, **119**, 141101, DOI: 10.1103/PhysRevLett.119.141101
- Bagoly, Z., Csabai, I., Mészáros, A., et al., Gamma photometric redshifts for long gamma-ray bursts. 2003, *Astronomy and Astrophysics*, **398**, 919, DOI: 10.1051/0004-6361:20021724
- Bagoly, Z., Horvath, I., Racz, I. I., Balázs, L. G., & Tóth, L. V., The Spatial Distribution of Gamma-Ray Bursts with Measured Redshifts from 24 Years of Observation. 2022, *Universe*, **8**, 342, DOI: 10.3390/universe8070342
- Bagoly, Z., Szécsi, D., Balázs, L. G., et al., Fermi GBM transient searches with ADWO. 2017, *Contributions of the Astronomical Observatory Skalnaté Pleso*, **47**, 76

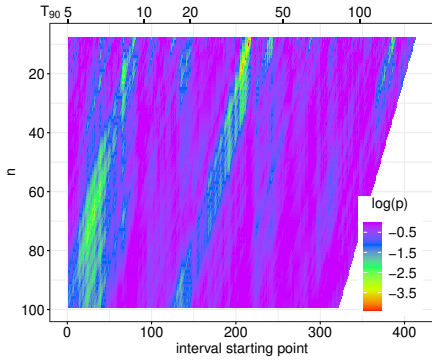


Figure 3. The two-parameter (n , duration) KS test p value surface plot using the 421 non-short GRBs. The 3σ significance level is the color associated with $\log_{10}(p) \approx -2.57$.

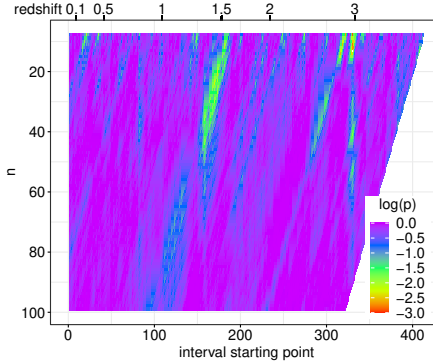


Figure 4. The two-parameter (n , redshift) KS test p value surface plot using the 421 non-short GRBs. The 3σ significance level is the color associated with $\log_{10}(p) \approx -2.57$.

- Bagoly, Z., Szécsi, D., Balázs, L. G., et al., Searching for electromagnetic counterpart of LIGO gravitational waves in the Fermi GBM data with ADWO. 2016, *Astronomy and Astrophysics*, **593**, L10, DOI: 10.1051/0004-6361/201628569
- Balázs, L. G., Bagoly, Z., Hakkila, J. E., et al., A giant ring-like structure at $0.78 < z < 0.86$ displayed by GRBs. 2015, *Monthly Notices of the RAS*, **452**, 2236, DOI: 10.1093/mnras/stv1421
- Balazs, L. G., Meszaros, A., & Horvath, I., Anisotropy of the sky distribution of gamma-ray bursts. 1998, *Astronomy and Astrophysics*, **339**, 1, DOI: 10.48550/arXiv.astro-ph/9807006
- Balázs, L. G., Mészáros, A., Horváth, I., & Vavrek, R., An intrinsic anisotropy in the angular distribution of gamma-ray bursts. 1999, *Astronomy and Astrophysics, Supplement*, **138**, 417, DOI: 10.1051/aas:1999290
- Balázs, L. G., Rejtő, L., & Tusnády, G., Some statistical remarks on the giant GRB ring. 2018, *Monthly Notices of the RAS*, **473**, 3169, DOI: 10.1093/mnras/stx2550
- Bi, X., Mao, J., Liu, C., & Bai, J.-M., Statistical Study of the Swift X-Ray Flash and X-Ray Rich Gamma-Ray Bursts. 2018, *Astrophysical Journal*, **866**, 97, DOI: 10.3847/1538-4357/aadcf8
- Eichler, D., Livio, M., Piran, T., & Schramm, D. N., Nucleosynthesis, neutrino bursts and gamma-rays from coalescing neutron stars. 1989, *Nature*, **340**, 126, DOI: 10.1038/340126a0
- Eingorn, M., O'Briant, B., Diouf, A., & Zhuk, A., Backreaction in cosmic screening approach. 2023a, *Physics Letters B*, **839**, 137797, DOI: 10.1016/j.physletb.2023.137797

- Eingorn, M., Yilmaz, E., Emrah Yükselci, A., & Zhuk, A., Suppression of matter density growth at scales exceeding the cosmic screening length. 2023b, *arXiv e-prints*, arXiv:2307.06920, DOI: 10.48550/arXiv.2307.06920
- Goldstein, A., Veres, P., Burns, E., et al., An Ordinary Short Gamma-Ray Burst with Extraordinary Implications: Fermi-GBM Detection of GRB 170817A. 2017, *Astrophysical Journal, Letters*, **848**, L14, DOI: 10.3847/2041-8213/aa8f41
- Hakkila, J., Horváth, I., Hofesmann, E., & Lesage, S., Properties of Short Gamma-ray Burst Pulses from a BATSE TTE GRB Pulse Catalog. 2018, *Astrophysical Journal*, **855**, 101, DOI: 10.3847/1538-4357/aaac2b
- Hatsukade, B., Hashimoto, T., Kohno, K., et al., Molecular Gas Properties in the Host Galaxy of GRB 080207. 2019, *Astrophysical Journal*, **876**, 91, DOI: 10.3847/1538-4357/ab1649
- Horváth, I., A Third Class of Gamma-Ray Bursts? 1998, *Astrophysical Journal*, **508**, 757, DOI: 10.1086/306416
- Horváth, I., Bagoly, Z., Balázs, L. G., et al., Detailed Classification of Swift 's Gamma-ray Bursts. 2010, *Astrophysical Journal*, **713**, 552, DOI: 10.1088/0004-637X/713/1/552
- Horváth, I., Bagoly, Z., Hakkila, J., & Tóth, L. V., New data support the existence of the Hercules-Corona Borealis Great Wall. 2015, *Astronomy and Astrophysics*, **584**, A48, DOI: 10.1051/0004-6361/201424829
- Horváth, I., Balázs, L. G., Bagoly, Z., Ryde, F., & Mészáros, A., A new definition of the intermediate group of gamma-ray bursts. 2006, *Astronomy and Astrophysics*, **447**, 23, DOI: 10.1051/0004-6361:20041129
- Horváth, I., Hakkila, J., & Bagoly, Z., Possible structure in the GRB sky distribution at redshift two. 2014, *Astronomy and Astrophysics*, **561**, L12, DOI: 10.1051/0004-6361/201323020
- Horváth, I., Hakkila, J., Bagoly, Z., et al., Multidimensional analysis of Fermi GBM gamma-ray bursts. 2019, *Astrophysics and Space Science*, **364**, 105, DOI: 10.1007/s10509-019-3585-1
- Horváth, I., Mészáros, A., Balázs, L. G., & Bagoly, Z., Where is the Third Subgroup of Gamma-Ray Bursts? 2004, *Baltic Astronomy*, **13**, 217, DOI: 10.48550/arXiv.astro-ph/0507688
- Horvath, I., Racz, I. I., Bagoly, Z., Balázs, L. G., & Pinter, S., Does the GRB Duration Depend on Redshift? 2022, *Universe*, **8**, 221, DOI: 10.3390/universe8040221
- Horvath, I., Szécsi, D., Hakkila, J., et al., The clustering of gamma-ray bursts in the Hercules-Corona Borealis Great Wall: the largest structure in the Universe? 2020, *Monthly Notices of the RAS*, **498**, 2544, DOI: 10.1093/mnras/staa2460
- Horváth, I., Tóth, B. G., Hakkila, J., et al., Classifying GRB 170817A/GW170817 in a Fermi duration-hardness plane. 2018, *Astrophysics and Space Science*, **363**, 53, DOI: 10.1007/s10509-018-3274-5

- Kovács, T. O., Burgarella, D., Kaneda, H., et al., Star formation and polycyclic aromatic hydrocarbons in ELAIS N1 galaxies as seen by AKARI. 2019, *Publications of the ASJ*, **71**, 27, DOI: 10.1093/pasj/psy145
- MacFadyen, A. I. & Woosley, S. E., Collapsars: Gamma-Ray Bursts and Explosions in “Failed Supernovae”. 1999, *Astrophysical Journal*, **524**, 262, DOI: 10.1086/307790
- Mészáros, P., Gamma-ray bursts. 2006, *Reports on Progress in Physics*, **69**, 2259, DOI: 10.1088/0034-4885/69/8/R01
- Pérez-Ramírez, D., de Ugarte Postigo, A., Gorosabel, J., et al., Detection of the high z GRB 080913 and its implications on progenitors and energy extraction mechanisms. 2010, *Astronomy and Astrophysics*, **510**, A105, DOI: 10.1051/0004-6361/200811151
- Pinter, S., Bagoly, Z., Balázs, L. G., et al., Resolving the structure of the Galactic foreground using Herschel measurements and the Kriging technique. 2017, *Proceedings of the International Astronomical Union*, **12**, 168–169, DOI: 10.1017/S1743921317011097
- Suleiman, N., Noboriguchi, A., Toba, Y., et al., The statistical properties of 28 IR-bright dust-obscured galaxies and SED modelling using CIGALE. 2022, *Publications of the ASJ*, **74**, 1157, DOI: 10.1093/pasj/psac061
- Tóth, B. G., Rácz, I. I., & Horváth, I., Gaussian-mixture-model-based cluster analysis of gamma-ray bursts in the BATSE catalog. 2019, *Monthly Notices of the RAS*, **486**, 4823, DOI: 10.1093/mnras/stz1188
- Toth, L. V., Doi, Y., Zahorecz, S., et al., Galactic foreground of gamma-ray bursts from AKARI Far-Infrared Surveyor. 2019, *Publications of the ASJ*, **71**, 10, DOI: 10.1093/pasj/psy123
- Řípa, J. & Mészáros, A., On the connection of gamma-ray bursts and X-ray flashes in the BATSE and RHESSI databases. 2016, *Astrophysics and Space Science*, **361**, 370, DOI: 10.1007/s10509-016-2960-4
- Vavrek, R., Balázs, L. G., Mészáros, A., Horváth, I., & Bagoly, Z., Testing the randomness in the sky-distribution of gamma-ray bursts. 2008, *Monthly Notices of the RAS*, **391**, 1741, DOI: 10.1111/j.1365-2966.2008.13635.x
- Zhang, B. & Mészáros, P., An Analysis of Gamma-Ray Burst Spectral Break Models. 2002, *Astrophysical Journal*, **581**, 1236, DOI: 10.1086/344338

Estimating GRBs' cosmological distances

I.I. Racz 

*University of Public Service, Budapest, Hungary (E-mail:
racz.istvan@uni-nke.hu)*

Received: June 28, 2023; Accepted: October 25, 2023

Abstract. Several thousand gamma-ray bursts have been observed but more than 500 events have known distances. Numerous papers have shown huge structures in the Universe based on GRBs. We want to examine the distribution of the GRBs' distances, to give an estimation on the distances of those GRBs which have no measured redshifts. The GRB catalogs contain more than 100 physical parameters among which there can be parameters dependent on distance. In this work we examined the distances of Swift GRBs with machine learning methods. For the regression of the distances we used both Random Forest and XGBoost regression algorithms. We found an 0.76 strength correlation between the regressed and measured redshift.

Key words: methods: numerical – gamma-ray burst: general – cosmology: observations

1. Introduction

The Gamma-ray bursts (GRBs) are the most energetic explosions in the far Universe (Mészáros, 2006; Kumar & Zhang, 2015). Two main models can explain GRB events: the collapse of the most massive stars (collapsar model) (MacFadyen & Woosley, 1999; Zhang & Mészáros, 2002) and the merging of compact stars as black holes or neutron stars (Eichler et al., 1989). The discovery of GW170814/GRB170814A had validated the second model (Abbott et al., 2017; Goldstein et al., 2017; Bagoly et al., 2016, 2017; Horváth et al., 2018).

It seems that we can distinguish between the two models based on the duration or hardness of the burst. The collapsing events are typically longer and softer than the star merging ones. A third group was identified by Horváth (1998) based on the duration–hardness plane (Horváth et al., 2004, 2006; Kóbori et al., 2020). The physical model of this intermediate group could not be perfectly determined but it seems that the X-ray flash events could have a connection to the intermediate GRBs (Horváth et al., 2010; Veres et al., 2010; Pinter et al., 2017; Bi et al., 2018). Balazs et al. (1998) showed that the sky distribution of GRBs not isotropic, since then, more and more signs indicate that the sky distribution of GRBs shows significant anisotropies (Balázs et al., 1999; Mészáros et al., 2000a,b; Vavrek et al., 2008; Pérez-Ramírez et al., 2010; Hakkila et al., 2018; Horváth et al., 2019; Tóth et al., 2019; Horvath et al., 2020).

Several thousand GRBs were discovered but only a few hundred redshifts are known. The first redshift measurement was taken in 1997 (GRB970508) (Metzger et al., 1997b,a; Reichart, 1998) in spite of the first GRB event being discovered in the 2nd of July, 1967 (Klebesadel et al., 1973). For the spectroscopy redshift measurement the precise position of the transient is necessary which we can get from the afterglow because the position errors of gamma detectors are usually several arcminutes. To examine the spatial distribution of the GRBs it is an essential question to determine their distances (Mészáros et al., 2000b,a; Horvath et al., 2022). Balázs et al. (2015) and Horváth et al. (2014) discovered two massive structures, the Giant GRB Ring and the Hercules-Corona Borealis Great Wall, which were formed by gamma-ray bursts. As of our current understanding, these objects are the largest cosmic structures in the Universe (Horváth et al., 2015; Balázs et al., 2018).

The highest spectroscopic redshift GRB was published by Tanvir et al. (2009), that time it was the most distant object in the Universe (Bagoly et al., 2019). We think that the GRB redshift distribution extending at least to $z \approx 10$ and their association with explosive death of massive stars (therefore the GRBs) can be a unique and powerful tool for cosmology (Tanvir et al., 2021). Two fresh projects (e.g. Space Variable Objects Monitor (SVOM) and Transient High-Energy Sky and Early Universe Surveyor (THESEUS) satellites) will try to answer these key questions locating hundreds of GRBs, including those which have high redshift ($z > 6$) (Zhao et al., 2012; Amati et al., 2018b).

It became clear shortly after the first redshift measurement that the distance of the GRBs show a relation to their duration (Katz & Canel, 1996; Piran, 2004). The observed sample shows that the harder, short GRBs are located closer than the softer, long GRBs (D'Avanzo, 2015; Horvath et al., 2022). This is not necessarily a statement about where short bursts occur versus where long bursts occur. Instead, it merely illustrates how challenging it is to spot a brief burst. The detection process is less sensitive to short bursts, so triggering on a shorter (and thus noisier) window for a short burst is much complicated. Additionally, since the detection of afterglow is so crucial to the identification of hosts and redshifts – which is also more difficult for short events – thus less is known about the distribution of short bursts. Also Rácz et al. (2018) examined redshift distributions within GRB spectral groups and discovered no distinction between spectral types within the bounds of statistical inference. Since there aren't any concrete proof that the closer peak of the short GRB is just a selection effect, this question is left unanswered. Moreover, this effect is well understandable because the star forming rate is decreasing in time; the timescale to have extremely high mass stars is shorter than the timescale needed to have already compact objects. However, high SFR is needed to form supermassive stars.

Understanding the high- z Universe is one of the main open issues in cosmology. The already mentioned THESEUS project will examine e.g., the star formation rate and metallicity evolution of the inter-stellar and inter-galactic medium, signatures of Pop III stars, sources and physics of re-ionization, and

the faint end of the galaxy luminosity function by observing distant GRBs and other γ - and X-ray sources up to the redshift of ≈ 10 (Stratta et al., 2018; Amati et al., 2018a).

In this article, I focus on estimating the redshift of GRBs using machine learning methods, which can bring us closer to a more efficient investigation of the spatial distribution of these bursts and the identification of high-redshift GRBs.

We explain the GRB catalogs and parameters used in Sec. 2. In Sec. 3 we show two machine-learning algorithms which can be used for both regression and classification. Our results can be seen in Sec. 4. We discuss the results in Sec 5. Finally, in Sec. 6 a short summary can be read.

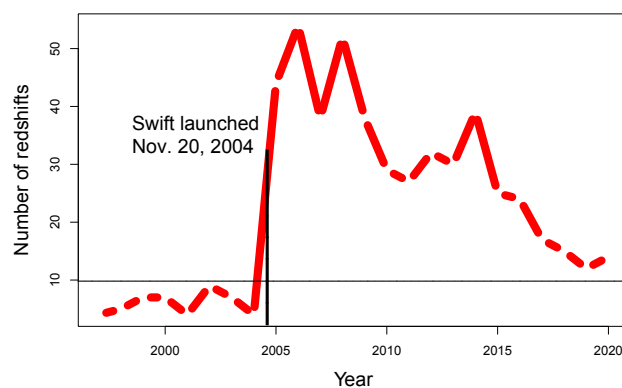


Figure 1. The regressive tendency is clearly seen from the peak after the launching of Swift. In a few years redshift measurements will be made for only a few GRBs every year.

1.1. Annual distribution of redshift measurement

Everyone knows that most of GRBs with redshifts can be found among the GRBs detected by the Swift telescope. By 2023, the Swift telescope detected about 1500 GRBs, performed XRT X-ray measurements in 80 percent cases, and a third of cases identified with also the UVOT instrument. We conducted a survey to examine the relationship between the number of observations and the number of redshift measurements. We examined about 1350 Swift bursts, including 408 cases of spectroscopic redshift measurements with ground-based telescopes. Interesting fact that among that GRBs with redshift measurements there were only 22 cases when UVOT observations hasn't been involved. 386

GRBs, or almost 95 percent of GRBs, were observed by UVOT. The typical error of the celestial coordinates given by UVOT is a few arcseconds, which is already accurate enough for ground-based observers to perform spectroscopic measurements. So it is clear that the accurate localization of GRBs is an essential issue for ground-based observers, who can be do the spectroscopic redshift measurements.

In contrast, there is also an interesting trend that can be observed in the annual decrease of redshift measurements. It is clear that when Swift started in 2004, the number of sightings had a drastic increase, but it has been slowing down exponentially ever since. In our personal opinion, the decreasing interest in GRBs is the reason behind that. The trend shows that by the middle of the decade we will reach a few observations a year, evoking times before Swift. Unfortunately, the decrease in ground-based observations cannot be ignored, but it would still be necessary for efficiently examine the GRBs to know their exact celestial location. It is an obvious fact that the measured physical parameters depend on distance, but the impact is relatively smaller than the GRB's own variability, and the mechanism is very complex so it is hard to specify with simple statistical methods. The machine learning techniques may help amplifying the underlying subtle relations between the observed physical parameters and the distance.

2. Data

The *Neil Gehrels Swift Observatory* (formerly known as 'Swift' Space Telescope) is a robotic spacecraft which was launched into orbit on 20 November, 2004, four years after the mission of the Compton Gamma Ray Observatory has ended.

Swift, being a multi-wavelength space observatory, is dedicated to the study of GRBs. It has three instruments with different energy ranges to observe GRBs together with their afterglows in the gamma-ray (Barthelmy et al., 2005), X-ray (Burrows et al., 2005), ultraviolet and optical wavebands (Roming et al., 2005). The Swift discovered more than 1500 GRBs from which more than one thousand X-ray afterglows were detected. In this work we studied these events.

2.1. Main Swift GRB catalogs

The Swift Gamma-Ray Burst Table is a public catalog of the Swift GRB observations. This table is available on the webpage of NASA¹. The catalog contains the most γ parameters as well as some X-ray and UV-optical parameters and comments from all three Swift instruments. Every GRB has a name from the observation date, a trigger number, gamma position and position error. The following parameters have been recorded in the table: duration of gamma radiation (T90), γ fluence, γ 1-sec peak photon flux and the photon index and spectrum

¹https://swift.gsfc.nasa.gov/archive/grb_table/

type (calculated from the γ spectrum) which can be simple power-law or cutoff power-law. On both the X-ray and the UV-optical observations the time to first observation in seconds is available, which are essential values. If this duration is too long the afterglow observation is probably incomplete because the telescope turned on the target more slowly, so the beginning of the observation was lost. The table contains 6 further X-ray parameters and 7 UV-optical magnitudes (X-ray early/11hours/24hours flux, initial temporal index, spectral index, intrinsic hydrogen column density, V, B, U, UVW1, UVW2, UVM2, White magnitude).

The mission was developed in a joint partnership as an international consortium from the United States, the United Kingdom, and Italy. The XRT observations are being analyzed by the U.K. partners. There is a similar public catalog 'The Swift-XRT GRB Catalogue'² from the UK Swift Science Data Centre (UKSSDC), where all XRT light curves and spectra data are published. Both official Swift catalogs contain the redshift values but we used other sources to validate these data.

2.2. GRB distances

We used two additional catalogs of redshift measurements. The Jochen Greiner's GRB table ³ is a subjective collection of information on the results of GRBs. The Gamma-Ray Burst Online Index (GRBox) ⁴ gives what appears to be the most likely redshift, but there are some possibilities for these catalogs to have mistyping or other errors. To eliminate the errors we compared the redshifts from the different sources and in several cases we needed to check the GCN (Gamma-ray Coordinates Network) notes to make sure we used the right redshift data. Earlier Balázs et al. (2015, 2018) and Horváth et al. (2015) have published a similar dataset which can be considered complete until September 2015. We completed this list with the newer redshift measurements.

2.3. Catalog merging

We joined the above data sources and for the best results we checked exhaustively the numerical values in the catalog and in the merged dataframe. We added more indicator variables instead of the not numerical information e.g. the upper limits vs. precise measurement or the forms of the X-ray light curves.

3. Methods

Machine learning uses statistical techniques to give computer systems the ability to progressively improve performance on a specific task with data. In this article we tried to estimate the redshift of GRBs with the physical parameters.

²http://www.swift.ac.uk/xrt_live_cat/

³<http://www.mpe.mpg.de/~jcg/grbgen.html>

⁴<https://sites.astro.caltech.edu/grbox/grbox.php>

This work can overlap with computational statistics, too. The machine learning algorithms can be unsupervised and be used to learn and establish baseline behavioral profiles for various entities and then be used to find meaningful anomalies and weak connections.

We need to distinguish between classification problems and regression tasks. If we already have established classes, then placing our data into these classes is called a classification procedure. If we want to estimate a continuous quantity from our existing data, then we use regression analysis.

The machine learning algorithms used by us have different versions for both types of analysis. To measure the goodness of estimation for the regression we calculated the correlation between the estimated and catalog redshift. The more accurate our estimations are, the higher correlation should be shown by the results.

3.1. Random Forest

A Random Forest is an ensemble of decision trees which may be used both for classification and regression (Breiman, 2001). It is a meta estimator that fits a number of decision trees on various bootstrap samples of the dataset and uses averaging to improve the predictive accuracy and control over-fitting. The individual trees are further decorrelated by randomly subsampling the variables considered for each split during the growth of the decision trees. Random Forests correct for the habit of decision trees to overfit their training set.

3.2. Gradient boosted trees, XGBoost

Gradient boosted trees, especially an implementation named, eXtreme Gradient Boosting (XGBoost) has recently been dominating machine learning competitions (Chen & Guestrin, 2016). Boosted decision trees are the ensemble of simple decision trees, where trees are added sequentially to the ensemble. Each additional tree is trained to correct the errors made by the ensemble of previous trees. New trees are added until no further improvements can be made on a validation dataset. During the addition of new trees, gradient boosting grows the best trees by optimizing a loss function which is made up of the error of predictions and a regularization term which describes the complexity of the trees.

3.3. Cross-validation

I used the Python 'sklearn.model_selection.KFold' function for cross-validation (Pedregosa et al., 2011). In this function, the 'n_splits' variable specifies the number of parts (folds) into which the original dataset is divided during cross-validation. To train the model, one of these parts (train) is used, while the others (test) are used for model evaluation. This process is repeated several

times, ensuring that each part is used for training and evaluation, thus helping estimate the model's performance. Since the choice of the cross-validation value depends on the dataset, the problem, and computational constraints, it's worth experimenting to find the most suitable value. The value I chose was 10, but I also examined cases with 3, 5, and 20. I obtained the best results with a value of 10; beyond this, the efficiency significantly decreased due to the low number of elements.

4. Results

4.1. Input dataframe

The final dataframe contains more than 200 variables for the GRBs including γ -, X-ray and optical physical parameters and observation indicators (like upper limit markers). Based on physical considerations we did not use several parameters (e.g. sky coordinate or galactic column density) which should not affect redshift.

We used multiple steps to improve the correlation starting from the procedure introduced by [Ukwatta et al. \(2016\)](#), these steps are explained in the following subsections.

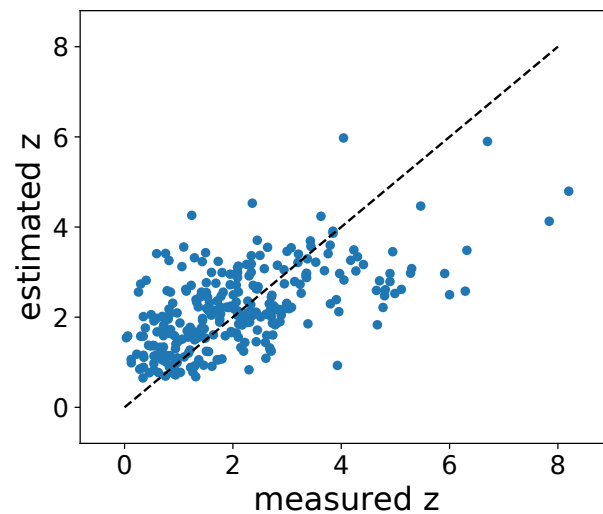


Figure 2. We repeated the method that was published in 2016 (identical data set and method). We obtained the same result; the Pearson's correlation coefficient was 0.57 ± 0.01 . The dashed line is the identity function ($y = x$).

We created a subsample from our catalog which was identical to the published catalog by [Ukwatta et al. \(2016\)](#). In this subsample we used data of the pre 2015 GRBs only, and only from the 'grbtable' catalog. Using the same algorithms and parameters as the aforementioned article we were able to reproduce the same results with a minor change in the cross-validation value from 20% to 10% for the bigger training sample. We varied the earlier statement and found a 0.57 ± 0.02 correlation between the estimated and measured redshift (Fig. 2).

4.2. Results of Machine-z

We also examined several datasets, methods, and settings to improve the results.

We thought that the correlation improves significantly with adding newer observations to our data but using the same parameters as mentioned before. We have about 400 GRBs with measured spectroscopical redshift contrary to the previous steps where about 280 objects were used. We found that increasing the number of observations didn't change the correlation significantly between the estimated and measured redshift.

Then we used XGBoost method besides the simple Random Forest Estimator. We found that the correlation is equal to the result of random forest, 0.57 ± 0.1 , but the variance was significantly smaller. It means that the XGBoost method is robust and – in addition – it is also faster.

4.2.1. Using other parameters and data cleaning

We checked the correlation between redshift and other physical parameters and indicators. The correlations were very weak, the highest coefficient was about 0.3 (using the UVOT parameters). We selected 20 parameters which showed the best correlation (Table 1). Because the catalog also contains several similar variables (e.g. X-ray flux from the 'grbtable' and from the UKSSDC catalog) in this step we used only one of them. In the final dataset we used the following parameters: γ flux, X-ray fluxes (early, 11hours, 24hours), all UVOT parameters and the intrinsic hydrogen column densities (both of WT and PC observation mode).

We examined the distribution of the first observation times of both XRT and UVOT. We found that it follows the standard distribution until about 150 sec for XRT and 200 sec for UVOT. It means that the sample can be considered complete, and after that 150 and 200 sec we marked the GRBs outlier and we skipped these records. This step seems valid because the correlation improved significantly to 0.66.

4.2.2. Final setting (Weighted XGBoost)

In the final step we changed the training sample from the redshift to $\lg(1+z)$ because this quantity can be interpreted as the physical distance (approximates

Table 1. There are thousands parameters for the GRBs as flux, fluence, spectral components. This table shows that 20 parameters which we used for the regression. UVOT data can be categorized into two groups. We can observe the values measured with the filters ('val') and determine whether this data represents an exact value or just an upper limit ('type').

The selected 20 parameters
BAT 1-sec PeakPhoton Flux
BAT 1-sec PeakPhoton Flux Error
BAT Fluence
XRT Early Flux
XRT Flux 11h
XRT Flux 24h
XRT WT Spec Ave N(H)
XRT PC Spec Ave N(H)
UVOT Magnitude type
UVOT B type
UVOT U val
UVOT U type
UVOT UVW1 val
UVOT UVW1 type
UVOT UVW2 val
UVOT UVW2 type
UVOT UVM2 val
UVOT UVM2 type
UVOT White val
UVOT White type

the co-moving distance well). The best results were obtained when we also used the errors of redshifts as fitting weights. This could be only done with the XGBoost method. I calculated the both Pearson's and Spearman's correlation using the obtained data, which in both cases yielded a value of 0.759 ± 0.0078 . In addition, I examined the coefficient of determination, as we are dealing with a rather linear relationship. I obtained a value of 0.47 for R^2 . Moreover, assuming this linear relationship between the measured and estimated values, I calculated the covariance matrix, which shows the Eq. 1.

$$Cov(z_{measured}, z_{predicted}) = \begin{pmatrix} 1.578 & 0.758 \\ 0.758 & 0.639 \end{pmatrix} \quad (1)$$

Fig. 3 shows a significant improvement in correlation. Therefore, we fitted the linear conversion line and we executed this re-normalization. This process did not affect the correlation but the results became more plausible and seemingly less affected by systematic errors from the fitting compared to Fig. 2. Finally, we transformed back the $\lg(1+z)$ data to the classical redshifts which can be seen in Fig. 4.

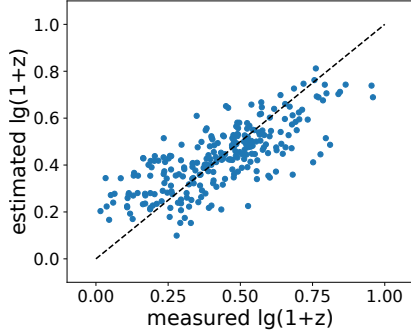


Figure 3. This plot shows the correlation between the regressed and measured redshift. We found the best correlation when we trained the algorithm with the $\lg(1+z)$ - which is equivalent the real distance -, weighted redshifts and skipped the outliers. The correlation coefficient in this case was 0.759 ± 0.0078 .

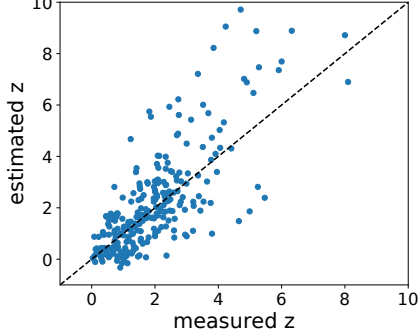


Figure 4. We transformed back the logarithmic values to original data and the correlation between the measured and estimated redshift can be seen. The dashed line shows the identical straight line.

5. Discussion

5.1. Reliability of results

So far we used the Swift XRT spectrum parameters from the UKSSDC catalog. This catalog contained the intrinsic column density values, which we used for both the regression. This physical parameter was calculated from the X-ray spectrum with the fitting method which was published by [Evans et al. \(2009\)](#). In the spectral fitting we can use the redshift information, because the intrinsic hydrogen column density depends on the redshift (see in Section 2, [RÁCZ & Hortobágyi \(2018\)](#)). As where the redshifts were measured and the redshifts were used in calculating intrinsic hydrogen column density, it could have affected the result of the regression.

We calculated the statistically unified intrinsic hydrogen column densities with the better resolution foreground ([Toth et al., 2019](#); [Hatsukade et al., 2019](#); [Kovács et al., 2019](#); [Suleiman et al., 2022](#)). We used the 5 arcminutes foreground which were obtained from Planck measurements ([RÁCZ et al., 2017](#); [Pinter, 2018](#)). We made the fit without the redshift information – with the same other settings as the catalog parameters –, so the hydrogen column densities were statistically comparable. This $N(H)$ showed weak correlation with the redshift as the catalog values.

Then we repeated the regression with the new Planck based $N(H)$ param-

eter. We found that the prediction was very sensitive to this feature without the UKSSDC column density. The correlation of the prediction decreased from 0.76 to 0.56, but this value will be improved by the new redshift measurements. Comparing the previously used and the newly employed column density data, in some cases, significant discrepancies are observed, which have led to the decrease in the correlation mentioned above. However, a thorough examination of these cases goes beyond the scope of this article, but it is imperative to investigate this direction in the near future.

6. Summary and conclusions

The Swift telescope found roughly 1500 GRBs, measured X-rays in 80% of the cases, and also the UVOT instrument observed the bursts in 30% of the cases. Less than 500 of the thousands of gamma-ray bursts that have been seen have distances that are known. After the peak of the GRBs redshift measurement number (2006-2008), the frequency of observations shows a constant decrease. In order to provide an estimate for the distances of those GRBs without known redshifts, we wished to look at the distribution of GRB distances. More than 100 physical parameters, including quite a few that depend on distance, may be found in the GRB catalogs. In this study, we used machine learning techniques to investigate the Swift GRBs' distances. We first assembled a common database from various online GRB catalogs, which we then purified of inaccurate information. Both the Random Forest and XGBoost regression techniques were utilized for the regression of the distances. The regressed and measured redshifts showed a 0.76 correlation, according to our research. Finally, we looked at the results' dependability and offered suggestions for how to make them better.

Acknowledgements. The authors thank the Hungarian TKP2021-NVA-16 and OTKA K-146092 program for their support. The authors appreciate the anonymous referee's insightful criticism and advice.

References

- Abbott, B. P., Abbott, R., Abbott, T. D., et al., GW170814: A Three-Detector Observation of Gravitational Waves from a Binary Black Hole Coalescence. 2017, *Physical Review Letters*, **119**, 141101, DOI: 10.1103/PhysRevLett.119.141101
- Amati, L., Bozzo, E., Götz, D., O'Brien, P., & Della Valle, M., The THESEUS Workshop 2017. 2018a, *Mem. Societa Astronomica Italiana*, **89**, 118
- Amati, L., O'Brien, P., Götz, D., et al., The THESEUS space mission concept: science case, design and expected performances. 2018b, *Advances in Space Research*, **62**, 191, DOI: 10.1016/j.asr.2018.03.010
- Bagoly, Z., Balázs, L. G., Galgóczi, G., et al., Transient detection capabilities of small satellite gamma-ray detectors. 2019, *Astronomische Nachrichten*, **340**, 681, DOI: 10.1002/asna.201913675

- Bagoly, Z., Szécsi, D., Balázs, L. G., et al., Fermi GBM transient searches with ADWO. 2017, *Contributions of the Astronomical Observatory Skalnaté Pleso*, **47**, 76
- Bagoly, Z., Szécsi, D., Balázs, L. G., et al., Searching for electromagnetic counterpart of LIGO gravitational waves in the Fermi GBM data with ADWO. 2016, *Astronomy and Astrophysics*, **593**, L10, DOI: 10.1051/0004-6361/201628569
- Balázs, L. G., Bagoly, Z., Hakkila, J. E., et al., A giant ring-like structure at $0.78 < z < 0.86$ displayed by GRBs. 2015, *Monthly Notices of the RAS*, **452**, 2236, DOI: 10.1093/mnras/stv1421
- Balazs, L. G., Meszaros, A., & Horvath, I., Anisotropy of the sky distribution of gamma-ray bursts. 1998, *Astronomy and Astrophysics*, **339**, 1, DOI: 10.48550/arXiv.astro-ph/9807006
- Balázs, L. G., Mészáros, A., Horváth, I., & Vavrek, R., An intrinsic anisotropy in the angular distribution of gamma-ray bursts. 1999, *Astronomy and Astrophysics, Supplement*, **138**, 417, DOI: 10.1051/aas:1999290
- Balázs, L. G., Rejtő, L., & Tusnády, G., Some statistical remarks on the giant GRB ring. 2018, *Monthly Notices of the RAS*, **473**, 3169, DOI: 10.1093/mnras/stx2550
- Barthelmy, S. D., Barbier, L. M., Cummings, J. R., et al., The Burst Alert Telescope (BAT) on the SWIFT Midex Mission. 2005, *Space Science Reviews*, **120**, 143, DOI: 10.1007/s11214-005-5096-3
- Bi, X., Mao, J., Liu, C., & Bai, J.-M., Statistical Study of the Swift X-Ray Flash and X-Ray Rich Gamma-Ray Bursts. 2018, *Astrophysical Journal*, **866**, 97, DOI: 10.3847/1538-4357/aadcf8
- Breiman, L., Random Forests. 2001, *Machine Learning*, **45**, 5, DOI: 10.1023/A:1010933404324
- Burrows, D. N., Hill, J. E., Nousek, J. A., et al., The Swift X-Ray Telescope. 2005, *Space Science Reviews*, **120**, 165, DOI: 10.1007/s11214-005-5097-2
- Chen, T. & Guestrin, C., XGBoost: A Scalable Tree Boosting System. 2016, *arXiv e-prints*, arXiv:1603.02754, DOI: 10.48550/arXiv.1603.02754
- D'Avanzo, P., Short gamma-ray bursts: A review. 2015, *Journal of High Energy Astrophysics*, **7**, 73, DOI: 10.1016/j.jheap.2015.07.002
- Eichler, D., Livio, M., Piran, T., & Schramm, D. N., Nucleosynthesis, neutrino bursts and gamma-rays from coalescing neutron stars. 1989, *Nature*, **340**, 126, DOI: 10.1038/340126a0
- Evans, P. A., Beardmore, A. P., Page, K. L., et al., Methods and results of an automatic analysis of a complete sample of Swift-XRT observations of GRBs. 2009, *Monthly Notices of the RAS*, **397**, 1177, DOI: 10.1111/j.1365-2966.2009.14913.x
- Goldstein, A., Veres, P., Burns, E., et al., An Ordinary Short Gamma-Ray Burst with Extraordinary Implications: Fermi-GBM Detection of GRB 170817A. 2017, *Astrophysical Journal, Letters*, **848**, L14, DOI: 10.3847/2041-8213/aa8f41
- Hakkila, J., Horváth, I., Hofesmann, E., & Lesage, S., Properties of Short Gamma-ray Burst Pulses from a BATSE TTE GRB Pulse Catalog. 2018, *Astrophysical Journal*, **855**, 101, DOI: 10.3847/1538-4357/aaac2b

- Hatsukade, B., Hashimoto, T., Kohno, K., et al., Molecular Gas Properties in the Host Galaxy of GRB 080207. 2019, *Astrophysical Journal*, **876**, 91, DOI: 10.3847/1538-4357/ab1649
- Horváth, I., A Third Class of Gamma-Ray Bursts? 1998, *Astrophysical Journal*, **508**, 757, DOI: 10.1086/306416
- Horváth, I., Bagoly, Z., Balázs, L. G., et al., Detailed Classification of Swift 's Gamma-ray Bursts. 2010, *Astrophysical Journal*, **713**, 552, DOI: 10.1088/0004-637X/713/1/552
- Horváth, I., Bagoly, Z., Hakkila, J., & Tóth, L. V., New data support the existence of the Hercules-Corona Borealis Great Wall. 2015, *Astronomy and Astrophysics*, **584**, A48, DOI: 10.1051/0004-6361/201424829
- Horváth, I., Balázs, L. G., Bagoly, Z., Ryde, F., & Mészáros, A., A new definition of the intermediate group of gamma-ray bursts. 2006, *Astronomy and Astrophysics*, **447**, 23, DOI: 10.1051/0004-6361:20041129
- Horváth, I., Hakkila, J., & Bagoly, Z., Possible structure in the GRB sky distribution at redshift two. 2014, *Astronomy and Astrophysics*, **561**, L12, DOI: 10.1051/0004-6361/201323020
- Horváth, I., Hakkila, J., Bagoly, Z., et al., Multidimensional analysis of Fermi GBM gamma-ray bursts. 2019, *Astrophysics and Space Science*, **364**, 105, DOI: 10.1007/s10509-019-3585-1
- Horváth, I., Mészáros, A., Balázs, L. G., & Bagoly, Z., Where is the Third Subgroup of Gamma-Ray Bursts? 2004, *Baltic Astronomy*, **13**, 217, DOI: 10.48550/arXiv.astroph/0507688
- Horvath, I., Racz, I. I., Bagoly, Z., Balázs, L. G., & Pinter, S., Does the GRB Duration Depend on Redshift? 2022, *Universe*, **8**, 221, DOI: 10.3390/universe8040221
- Horvath, I., Szécsi, D., Hakkila, J., et al., The clustering of gamma-ray bursts in the Hercules-Corona Borealis Great Wall: the largest structure in the Universe? 2020, *Monthly Notices of the RAS*, **498**, 2544, DOI: 10.1093/mnras/staa2460
- Horváth, I., Tóth, B. G., Hakkila, J., et al., Classifying GRB 170817A/GW170817 in a Fermi duration-hardness plane. 2018, *Astrophysics and Space Science*, **363**, 53, DOI: 10.1007/s10509-018-3274-5
- Katz, J. I. & Canel, L. M., The Long and the Short of Gamma-Ray Bursts. 1996, *Astrophysical Journal*, **471**, 915, DOI: 10.1086/178018
- Klebesadel, R. W., Strong, I. B., & Olson, R. A., Observations of Gamma-Ray Bursts of Cosmic Origin. 1973, *Astrophysical Journal, Letters*, **182**, L85, DOI: 10.1086/181225
- Kóbori, J., Bagoly, Z., & Balázs, L. G., Kilonova rates from spherical and axisymmetrical models. 2020, *Monthly Notices of the RAS*, **494**, 4343, DOI: 10.1093/mnras/staa1034
- Kovács, T. O., Burgarella, D., Kaneda, H., et al., Star formation and polycyclic aromatic hydrocarbons in ELAIS N1 galaxies as seen by AKARI. 2019, *Publications of the ASJ*, **71**, 27, DOI: 10.1093/pasj/psy145

- Kumar, P. & Zhang, B., The physics of gamma-ray bursts & relativistic jets. 2015, *Physics Reports*, **561**, 1, DOI: 10.1016/j.physrep.2014.09.008
- MacFadyen, A. I. & Woosley, S. E., Collapsars: Gamma-Ray Bursts and Explosions in “Failed Supernovae”. 1999, *Astrophysical Journal*, **524**, 262, DOI: 10.1086/307790
- Mészáros, A., Bagoly, Z., Horváth, I., Balázs, L. G., & Vavrek, R., A Remarkable Angular Distribution of the Intermediate Subclass of Gamma-Ray Bursts. 2000a, *Astrophysical Journal*, **539**, 98, DOI: 10.1086/309193
- Mészáros, A., Bagoly, Z., & Vavrek, R., On the existence of the intrinsic anisotropies in the angular distributions of gamma-ray bursts. 2000b, *Astronomy and Astrophysics*, **354**, 1, DOI: 10.48550/arXiv.astro-ph/9912037
- Mészáros, P., Gamma-ray bursts. 2006, *Reports on Progress in Physics*, **69**, 2259, DOI: 10.1088/0034-4885/69/8/R01
- Metzger, M. R., Cohen, J. G., Chaffee, F. H., & Blandford, R. D., GRB 970508. 1997a, *IAU Circulars*, **6676**
- Metzger, M. R., Djorgovski, S. G., Kulkarni, S. R., et al., Spectral constraints on the redshift of the optical counterpart to the γ -ray burst of 8 May 1997. 1997b, *Nature*, **387**, 878, DOI: 10.1038/43132
- Pedregosa, F., Varoquaux, G., Gramfort, A., et al., Scikit-learn: Machine Learning in Python. 2011, *Journal of Machine Learning Research*, **12**, 2825
- Pérez-Ramírez, D., de Ugarte Postigo, A., Gorosabel, J., et al., Detection of the high z GRB 080913 and its implications on progenitors and energy extraction mechanisms. 2010, *Astronomy and Astrophysics*, **510**, A105, DOI: 10.1051/0004-6361/200811151
- Pinter, S., Multi-messenger studies of γ -ray bursts and their cosmic environment. 2018, *Astronomische Nachrichten*, **339**, 336, DOI: 10.1002/asna.201813501
- Pinter, S., Bagoly, Z., Balázs, L. G., et al., Resolving the structure of the Galactic foreground using Herschel measurements and the Kriging technique. 2017, *Proceedings of the International Astronomical Union*, **12**, 168–169, DOI: 10.1017/S1743921317011097
- Piran, T., The physics of gamma-ray bursts. 2004, *Reviews of Modern Physics*, **76**, 1143, DOI: 10.1103/RevModPhys.76.1143
- Rácz, I. I., Bagoly, Z., Tóth, L. V., et al., Galactic and extragalactic hydrogen in the X-ray spectra of Gamma Ray Bursts. 2017, *Contributions of the Astronomical Observatory Skalnaté Pleso*, **47**, 100
- Rácz, I. I., Balázs, L. G., Horvath, I., Tóth, L. V., & Bagoly, Z., Statistical properties of Fermi GBM GRBs' spectra. 2018, *Monthly Notices of the RAS*, **475**, 306, DOI: 10.1093/mnras/stx3152
- Rácz, I. I. & Hortobagyi, A. J., Studying the variability of the X-ray spectral parameters of high-redshift GRBs' afterglows. 2018, *Astronomische Nachrichten*, **339**, 347, DOI: 10.1002/asna.201813503
- Reichart, D. E., The Redshift of GRB 970508. 1998, *Astrophysical Journal, Letters*, **495**, L99, DOI: 10.1086/311222

- Roming, P. W. A., Kennedy, T. E., Mason, K. O., et al., The Swift Ultra-Violet/Optical Telescope. 2005, *Space Science Reviews*, **120**, 95, DOI: 10.1007/s11214-005-5095-4
- Stratta, G., Ciolfi, R., Amati, L., et al., THESEUS: A key space mission concept for Multi-Messenger Astrophysics. 2018, *Advances in Space Research*, **62**, 662, DOI: 10.1016/j.asr.2018.04.013
- Suleiman, N., Noboriguchi, A., Toba, Y., et al., The statistical properties of 28 IR-bright dust-obscured galaxies and SED modelling using CIGALE. 2022, *Publications of the ASJ*, **74**, 1157, DOI: 10.1093/pasj/psac061
- Tanvir, N. R., Fox, D. B., Levan, A. J., et al., A γ -ray burst at a redshift of $z \sim 8.2$. 2009, *Nature*, **461**, 1254, DOI: 10.1038/nature08459
- Tanvir, N. R., Le Floch, E., Christensen, L., et al., Exploration of the high-redshift universe enabled by THESEUS. 2021, *Experimental Astronomy*, **52**, 219, DOI: 10.1007/s10686-021-09778-w
- Tóth, B. G., RÁCZ, I. I., & Horváth, I., Gaussian-mixture-model-based cluster analysis of gamma-ray bursts in the BATSE catalog. 2019, *Monthly Notices of the RAS*, **486**, 4823, DOI: 10.1093/mnras/stz1188
- Toth, L. V., Doi, Y., Zahorecz, S., et al., Galactic foreground of gamma-ray bursts from AKARI Far-Infrared Surveyor. 2019, *Publications of the ASJ*, **71**, 10, DOI: 10.1093/pasj/psy123
- Ukwatta, T. N., Woźniak, P. R., & Gehrels, N., Machine-z: rapid machine-learned redshift indicator for Swift gamma-ray bursts. 2016, *Monthly Notices of the RAS*, **458**, 3821, DOI: 10.1093/mnras/stw559
- Vavrek, R., Balázs, L. G., Mészáros, A., Horváth, I., & Bagoly, Z., Testing the randomness in the sky-distribution of gamma-ray bursts. 2008, *Monthly Notices of the RAS*, **391**, 1741, DOI: 10.1111/j.1365-2966.2008.13635.x
- Veres, P., Bagoly, Z., Horváth, I., Mészáros, A., & Balázs, L. G., A Distinct Peak-flux Distribution of the Third Class of Gamma-ray Bursts: A Possible Signature of X-ray Flashes? 2010, *Astrophysical Journal*, **725**, 1955, DOI: 10.1088/0004-637X/725/2/1955
- Zhang, B. & Mészáros, P., An Analysis of Gamma-Ray Burst Spectral Break Models. 2002, *Astrophysical Journal*, **581**, 1236, DOI: 10.1086/344338
- Zhao, D., Cordier, B., Sizun, P., et al., Influence of the Earth on the background and the sensitivity of the GRM and ECLAIRs instruments aboard the Chinese-French mission SVOM. 2012, *Experimental Astronomy*, **34**, 705, DOI: 10.1007/s10686-012-9313-2

Redshift dependence of GRBs' observed parameters

I.I. Racz^{1,2}, L.G. Balazs^{3,4} and I. Horvath¹

¹ *University of Public Service, Budapest, Hungary (E-mail: racz.istvan@uni-nke.hu)*

² *Department of Astronomy, Eötvös University, Budapest, Hungary*

³ *Konkoly Observatory, Research Centre for Astronomy and Earth Sciences, Budapest, Hungary*

Received: June 28, 2023; Accepted: October 9, 2023

Abstract. GRBs are extremely energetic short cosmic transients. Due to their huge energy output in a short time they can be observed at very large cosmological distances. Actually, they sample the whole observable Universe. As a consequence of their large distances, their observed duration, fluence and peak flux depend on the redshift. In the reality, however, this dependence can be observed only in the case if the intrinsic variance of these quantities in comoving frame do not exceed significantly that coming from different redshifts of the GRBs. Nevertheless, it is an important question whether the redshift dependence of the observed quantities could be extracted from the observational data. Using a training set consisting of GRBs having measured physical parameters and redshifts we are looking for the effect of the redshift on the observed data, using techniques available in multivariate data analysis. Creating a 3D parameter space from duration, fluence and peak flux, we define partitions in the distribution of data points and compare the redshift distributions within these partitions. Partitioning will be made by some hierarchical clustering algorithm and cutting the obtained agglomeration tree at different places to get partitions of different numbers. The distributions of redshifts within the partitions, obtained in this way, will be compared to see if there is any difference in redshift distribution between partitions at all.

Key words: gamma-ray burts – cosmology – statistical

1. Introduction

The Gamma-ray bursts (GRBs) are the most energetic events in the far Universe (Mészáros, 2006; Kumar & Zhang, 2015; Zhang, 2018). There are two main different physical model for the origin these events (Kouveliotou et al., 1993) but some studies raise the possibility of more models. First the collapse of the most massive stars (collapsar model) (MacFadyen & Woosley, 1999; Zhang & Mészáros, 2002) and second the merging of compact objects (like black holes or neutron stars) (Eichler et al., 1989; Hakkila et al., 2018). The discovery of

GW170814/GRB170814A had validated the second model (Abbott et al., 2017; Goldstein et al., 2017; Bagoly et al., 2016; Tóth et al., 2019). Since then, it has been a recurring theme that there may be other sub-types of bursts (Horváth et al., 2018, 2019). The two types of GRBs have different duration and hardness. The long GRBs have softer and the short GRBs have harder spectra. In 1998, Horváth (1998); Mukherjee et al. (1998) identified a third group on the duration–hardness plane (Horváth et al., 2006). These events can be associated with the X-ray flash events (Veres et al., 2010; Horváth et al., 2010; Pinter et al., 2017; Bi et al., 2018).

Balazs et al. (1998) suggested that the distribution of GRBs may show some angular anisotropy, and after the millennium many studies dealt with the GRBs angular and spatial distribution ((Mészáros et al., 2000a,b; Vavrek et al., 2008; Tarnopolski, 2017)). Of this, there were discovering the two largest structures in the Universe, the Giant GRB Ring (Balázs et al., 2015, 2018) and the Hercules-Corona Borealis Great Wall (Horváth et al., 2014, 2015; Horvath et al., 2020). In addition to all this, several other anomalies (differences from isotropy and homogeneity) were identified based on the angular and spatial distribution of GRBs (Balázs et al., 1999; Pinter, 2018; Tóth et al., 2019; Horvath et al., 2022) It became clear shortly after the first redshift measurement that the distance of the GRBs shows a relation to their duration: the short GRBs are located closer than the long GRBs. But since GRBs occur over a tremendous time scale, it can be suggested that certain properties of them change based on the distance (Bagoly et al., 2003; Pérez-Ramírez et al., 2010; Kovács et al., 2019; Hatsukade et al., 2019; Toth et al., 2019; Suleiman et al., 2022). Among other things, De Cia et al. (2012) discovered that the host galaxy must possess very particular chemical characteristics in order for long GRBs to form. We must acknowledge, however, that the chemical composition of galaxies and the entire universe is subject to change over time. This change can be seen in the characteristics of GRBs, such as the lack of absorption lines (De Cia et al., 2011b) or the rapidity of GRB light curves (Vetere et al., 2006; De Cia et al., 2011a).

It is still questionable how the distance of GRBs can cause differences in other physical parameters within different groups, i.e. how GRBs produced at different distances, in different eras differ in their main physical parameters.

2. Data and Methods

We used the data available at the GRB table of the Swift satellite¹, which we preliminarily cleaned of faulty records. Instead of the observed values one may use these values' logarithms to reduce the effect of outliers. In some cases, however, it is necessary to exclude the outliers altogether from further computations, since they significantly distort the linear correlation between the variables.

¹https://swift.gsfc.nasa.gov/archive/grb_table/

For this we made a comprehensive outlier diagnostics using *boxplot* procedure (McGill et al., 1978) of **R** package (R Core Team, 2021).

2.1. Outlier diagnostics

Outlier is a data point that differs significantly from other observations. An outlier may be due to variability in the measurement or it may indicate experimental errors. In the following we use **R** packages **outliers** (Tukey, 1977). The definition of an outlier is somewhat arbitrary. The scores routine of the **outliers** package assigns some probability to all of the cases of an univariate sample. The critical probability for identifying a case as an outlier can be a fixed error probability of rejecting a sample element although it comes from the parent distribution.

(Fisher, 1992) suggested $p = 0.05$ value for critical probability. We used this threshold, for rejecting the null hypothesis and we will conclude that the lowest/highest value is an outlier. Due to the nature of the problem, this level of significance is acceptable to us, without significantly increasing second kind of errors. Accordingly, if the scores procedure assigns $p_s < p/N$ (N is the sample size), we may reject this case as an outlier.

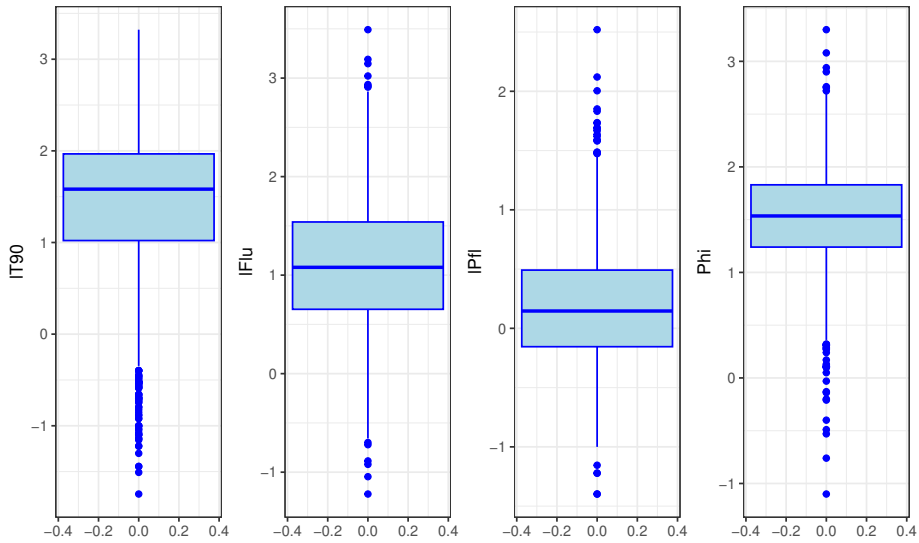


Figure 1. Outliers' diagnostics in BAT data with R boxplot procedures. The critical probability was $p = 0.05$, and the blue points show the excluded data.

After excluding the outliers, we studied the correlations between the main observed parameters of Swift GRBs. This can be seen in the Fig. 2. We used four

parameters from the database, the T_{90} duration, Gamma Fluence, Gamma Peak Flux, and the Gamma Photon index. We can see a weak correlation between the fluence and duration or peak flux. This is easy to understand, since the fluence is the summed energy emitted during the entire duration, i.e. the integral of the instantaneous brightness over time, and the peak flux is the brightness measured at the interval around the maxima of the burst.

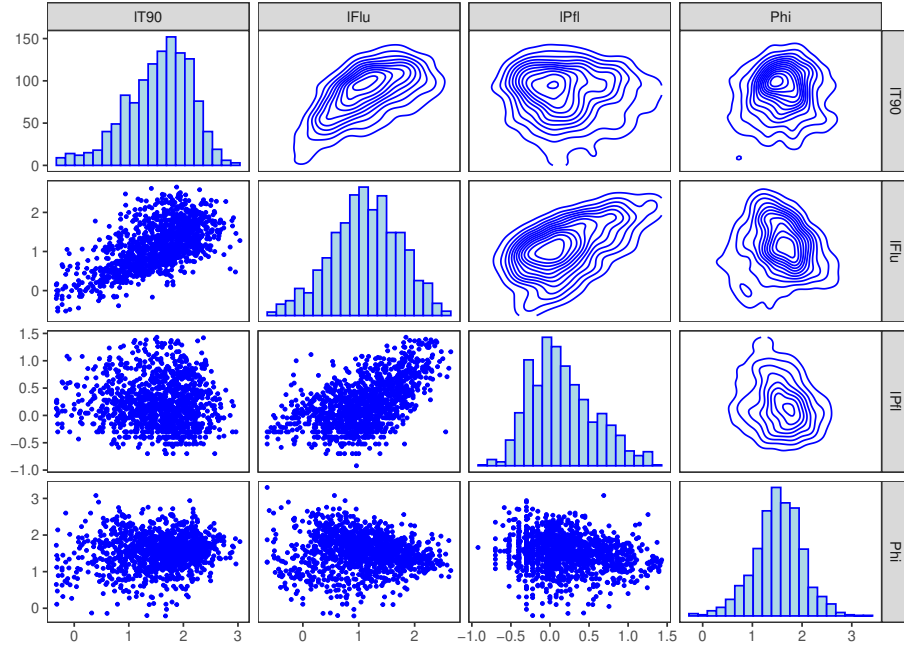


Figure 2. Distributions of Swift BAT data without the outliers. In the diagonal we show the histogram of T_{90} , Fluence, Peak flux, and Photon index, respectively. On the top and bottom triangle the 2D density and scatter plots are shown for each pairs of observed parameters, respectively. For example, the connection between Fluence and T_{90} parameters is clearly visible.

3. Results

3.1. Measuring the similarity between GRBs

To study the relationship between the characteristic physical parameters of GRBs and the redshift, we divide the parameter space into regions of similar objects in their parameters. The distance (similarity) between GRBs will be

measured in Euclidean metrics. The orthogonal coordinates required for the Euclidean metric can be obtained from the original variables using PCA (Principal Component Analysis) (Jolliffe, 1986). For performing PCA we used the *PCA()* procedure in **FactoMineR** library (Lê et al., 2008) of the **R** statistical package. Our final goal was to look for dependence of the observed physical parameters (duration, fluence, peak flux, photon index) on the redshift. The strength of this dependence is a function of the ratio between the variance of redshift within and between partitions.

3.2. Partitioning parameter space of PCs

After getting orthogonal coordinates (principal components (PCs) from PCA) we perform hierarchical cluster analysis. We cut the cluster tree (dendrogram) resulted to a given number of partitions. We divide the redshifts of GRBs according to the partitions obtained in order to see significant differences, if any, in redshift distributions between partitions. The significance of difference in redshift distributions between partitions was tested using the Kruskal-Wallis non-parametric test (Kruskal & Wallis, 1952).

3.3. Estimating optimal number of partitions

For getting the optimum number of partitions we use *NbClust()* procedure in **NbClust**(Charrad et al., 2014) library of **R**. After getting the optimum number of clusters we performed hierarchic clustering using *hcut()* procedure in R's **Factoextra** library cutting the dendrogram obtained at the optimum number of clusters getting above (see Fig.3,4) and we calculated the relevant values within each group (Table 1).

The clustering yielded three as an optimal number of groups in the PC1–PC2 plane according to the Kruskal-Wallis rank summary test, with a chi-square of 10.839 and a significance p-value of 0.004429.

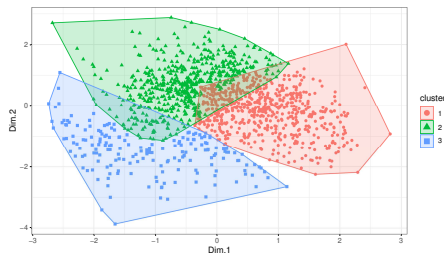


Figure 3. Clustering results of the three groups in the first and second PC plane.

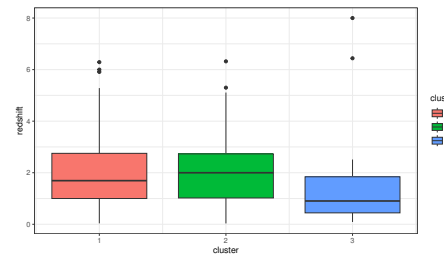


Figure 4. Comparing the redshift within the three groups.

Table 1. We clustered the GRBs with `NbClust()` procedure, and the optimal number of cluster was three. The table contains the median observed parameters of each group.

Groups no.	Redshift	T ₉₀	Fluence	Peak Flux	Photon index
1	1.6920	64.00	37.00	3.10	1.47
2	1.9990	36.25	6.00	0.80	1.90
3	0.9035	1.60	3.65	1.73	0.88

3.4. Redshift dependence of parameters with 6 partitions

Although the *NbClust* procedure yielded 3 as the optimal number of GRB groups, there is a second maxima in the number of optimal clusters histogram, at the number of 6. We repeat the previous procedure with a cluster number of 6 (see Fig. 5,6 and Table 2). The Kruskal-Wallis rank summary test has yielded a chi-square of 22.095 and a significance p-value of 0.0005022.

As one can see, the clusters' dependence on redshift is much stronger than in the previous case, where there were only three groups.

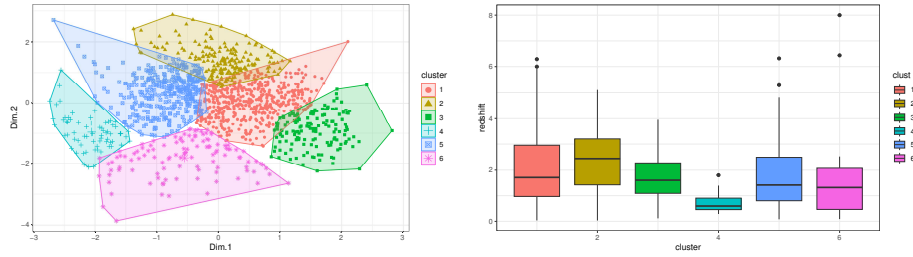


Figure 5. Clustering results of the six groups.

Figure 6. Comparing the redshift within the six groups.

Table 2. The table shows the 6 groups' median values similar to Table 1.

Groups no.	Redshift	T ₉₀	Fluence	Peak Flux	Photon index
1	1.7100	64.00	25.70	2.50	1.530
2	2.4281	154.50	13.55	0.65	1.965
3	1.6034	65.15	138.00	12.35	1.280
4	0.5960	0.30	0.44	1.00	1.280
5	1.4160	11.15	3.39	0.98	1.810
6	1.3195	4.20	6.70	3.86	0.820

3.5. Redshift dependence of T90, Fluence, Peak flux and Photon index

The redshift-dependent relationship between the duration, fluence, peak flux, and photon index values obtained from GRB observations can be seen in Fig. 7 and 8. In these figures significant internal variances can be seen in each parameter. Their corresponding values in a co-moving system can be obtained from the currently best-fitting world model, however, this can only be done if the intrinsic value of the relevant parameters is known. With the present data, the scattering within the parameters covers their weak redshift dependence. Therefore, the position of the groups according to distance cannot be investigated with adequate statistical significance in this work.

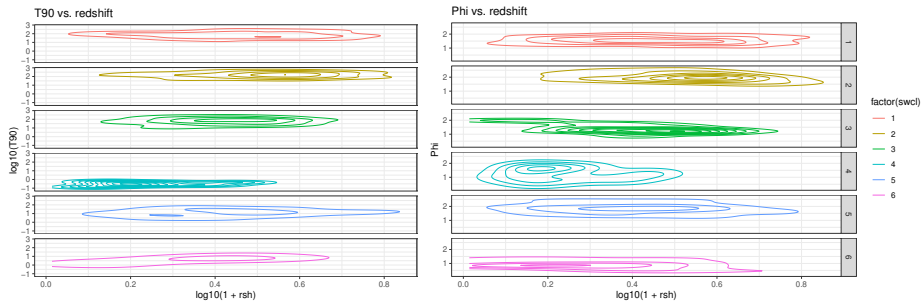


Figure 7. T90 and Photon index vs. redshift

4. Conclusions

The T90 duration appears to have the tightest correlation with redshift. In contrast, peak flux has no correlation with redshift. Fluence correlates with redshift due to its positive correlation with T90 (since fluence can be approximated with the product of peak flux and duration).

It is worth mentioning that the range of $\log_{10}(T90)$ is much higher than of $\log_{10}(1 + z)$ so the obtained relationship can not interpreted as a simple cosmological time dilatation. The distribution of absolute brightness is different in within different groups, so the detection threshold defines different sampling volumes and differences in the median of redshift data.

The angular distributions reflect the selection effect due to the galactic foreground extinction (see Fig. 9). The top left panel shows some density enhancement by visual impression, not seen in other ones. The bottom right panel seems to have an asymmetry in galactic latitudes but it based on a low number of sample points.

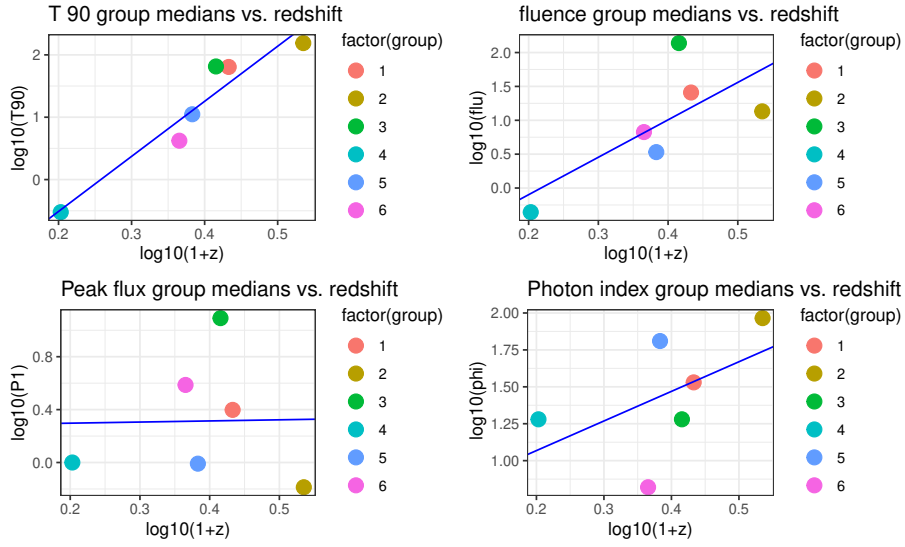


Figure 8. Redshift dependence of T90, Fluence, Peak flux, Photon index of the different partitions. Blue lines in the Figures represent the best fitting linear relationship between redshift and GRB variables.

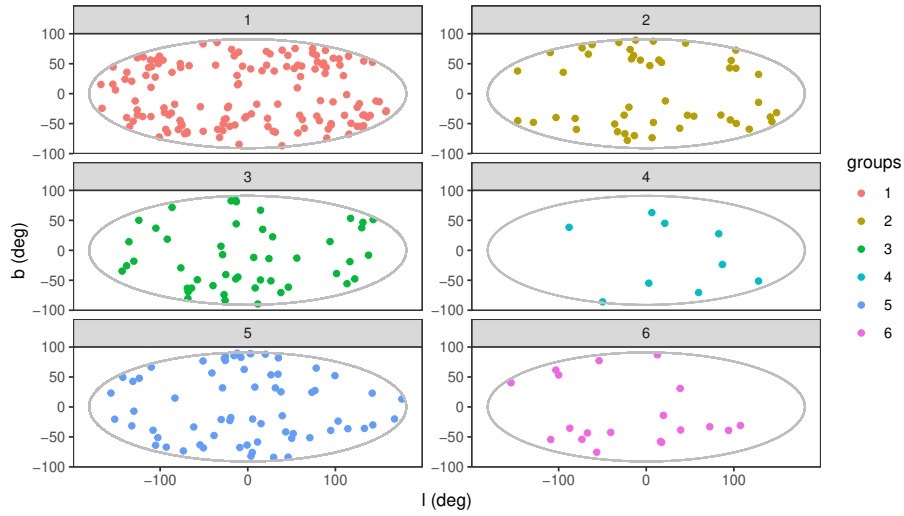


Figure 9. Aitoff projection of angular distributions of the 6 groups. The bottom right panel appears to have an asymmetry in galactic latitudes, but it is based on a small sample size.

Acknowledgements. The authors thank the Hungarian TKP2021-NVA-16 and OTKA K-146092 program for their support. The authors appreciate the anonymous referee's insightful criticism and advice.

References

- Abbott, B. P., Abbott, R., Abbott, T. D., et al., GW170814: A Three-Detector Observation of Gravitational Waves from a Binary Black Hole Coalescence. 2017, *Physical Review Letters*, **119**, 141101, DOI: 10.1103/PhysRevLett.119.141101
- Bagoly, Z., Csabai, I., Mészáros, A., et al., Gamma photometric redshifts for long gamma-ray bursts. 2003, *Astronomy and Astrophysics*, **398**, 919, DOI: 10.1051/0004-6361:20021724
- Bagoly, Z., Szécsi, D., Balázs, L. G., et al., Searching for electromagnetic counterpart of LIGO gravitational waves in the Fermi GBM data with ADWO. 2016, *Astronomy and Astrophysics*, **593**, L10, DOI: 10.1051/0004-6361/201628569
- Balázs, L. G., Bagoly, Z., Hakkila, J. E., et al., A giant ring-like structure at $0.78 < z < 0.86$ displayed by GRBs. 2015, *Monthly Notices of the RAS*, **452**, 2236, DOI: 10.1093/mnras/stv1421
- Balazs, L. G., Meszaros, A., & Horvath, I., Anisotropy of the sky distribution of gamma-ray bursts. 1998, *Astronomy and Astrophysics*, **339**, 1, DOI: 10.48550/arXiv.astro-ph/9807006
- Balázs, L. G., Mészáros, A., Horváth, I., & Vavrek, R., An intrinsic anisotropy in the angular distribution of gamma-ray bursts. 1999, *Astronomy and Astrophysics, Supplement*, **138**, 417, DOI: 10.1051/aas:1999290
- Balázs, L. G., Rejtő, L., & Tusnády, G., Some statistical remarks on the giant GRB ring. 2018, *Monthly Notices of the RAS*, **473**, 3169, DOI: 10.1093/mnras/stx2550
- Bi, X., Mao, J., Liu, C., & Bai, J.-M., Statistical Study of the Swift X-Ray Flash and X-Ray Rich Gamma-Ray Bursts. 2018, *Astrophysical Journal*, **866**, 97, DOI: 10.3847/1538-4357/aadcf8
- Charrad, M., Ghazzali, N., Boiteau, V., & Niknafs, A., NbClust: An R Package for Determining the Relevant Number of Clusters in a Data Set. 2014, *Journal of Statistical Software*, **61**, 1
- De Cia, A., Jakobsson, P., Björnsson, G., et al., Probing gamma-ray burst environments with time variability: ULTRASPEC fast imaging of GRB 080210. 2011a, *Monthly Notices of the RAS*, **412**, 2229, DOI: 10.1111/j.1365-2966.2010.18046.x
- De Cia, A., Ledoux, C., Fox, A. J., et al., Rapid-response mode VLT/UVES spectroscopy of super iron-rich gas exposed to GRB 080310. Evidence of ionization in action and episodic star formation in the host. 2012, *Astronomy and Astrophysics*, **545**, A64, DOI: 10.1051/0004-6361/201218884
- De Cia, A., Starling, R. L. C., Wiersema, K., et al., GRB 070125 and the environments of spectral-line poor afterglow absorbers. 2011b, *Monthly Notices of the RAS*, **418**, 129, DOI: 10.1111/j.1365-2966.2011.19471.x

- Eichler, D., Livio, M., Piran, T., & Schramm, D. N., Nucleosynthesis, neutrino bursts and gamma-rays from coalescing neutron stars. 1989, *Nature*, **340**, 126, DOI: 10.1038/340126a0
- Fisher, R. A. 1992, *Statistical Methods for Research Workers*, ed. S. Kotz & N. L. Johnson (New York, NY: Springer New York), 66–70
- Goldstein, A., Veres, P., Burns, E., et al., An Ordinary Short Gamma-Ray Burst with Extraordinary Implications: Fermi-GBM Detection of GRB 170817A. 2017, *Astrophysical Journal, Letters*, **848**, L14, DOI: 10.3847/2041-8213/aa8f41
- Hakkila, J., Horváth, I., Hofesmann, E., & Lesage, S., Properties of Short Gamma-ray Burst Pulses from a BATSE TTE GRB Pulse Catalog. 2018, *Astrophysical Journal*, **855**, 101, DOI: 10.3847/1538-4357/aaac2b
- Hatsukade, B., Hashimoto, T., Kohno, K., et al., Molecular Gas Properties in the Host Galaxy of GRB 080207. 2019, *Astrophysical Journal*, **876**, 91, DOI: 10.3847/1538-4357/ab1649
- Horváth, I., A Third Class of Gamma-Ray Bursts? 1998, *Astrophysical Journal*, **508**, 757, DOI: 10.1086/306416
- Horváth, I., Bagoly, Z., Balázs, L. G., et al., Detailed Classification of Swift 's Gamma-ray Bursts. 2010, *Astrophysical Journal*, **713**, 552, DOI: 10.1088/0004-637X/713/1/552
- Horváth, I., Bagoly, Z., Hakkila, J., & Tóth, L. V., New data support the existence of the Hercules-Corona Borealis Great Wall. 2015, *Astronomy and Astrophysics*, **584**, A48, DOI: 10.1051/0004-6361/201424829
- Horváth, I., Balázs, L. G., Bagoly, Z., Ryde, F., & Mészáros, A., A new definition of the intermediate group of gamma-ray bursts. 2006, *Astronomy and Astrophysics*, **447**, 23, DOI: 10.1051/0004-6361:20041129
- Horváth, I., Hakkila, J., & Bagoly, Z., Possible structure in the GRB sky distribution at redshift two. 2014, *Astronomy and Astrophysics*, **561**, L12, DOI: 10.1051/0004-6361/201323020
- Horváth, I., Hakkila, J., Bagoly, Z., et al., Multidimensional analysis of Fermi GBM gamma-ray bursts. 2019, *Astrophysics and Space Science*, **364**, 105, DOI: 10.1007/s10509-019-3585-1
- Horvath, I., Racz, I. I., Bagoly, Z., Balázs, L. G., & Pinter, S., Does the GRB Duration Depend on Redshift? 2022, *Universe*, **8**, 221, DOI: 10.3390/universe8040221
- Horvath, I., Szécsi, D., Hakkila, J., et al., The clustering of gamma-ray bursts in the Hercules-Corona Borealis Great Wall: the largest structure in the Universe? 2020, *Monthly Notices of the RAS*, **498**, 2544, DOI: 10.1093/mnras/staa2460
- Horváth, I., Tóth, B. G., Hakkila, J., et al., Classifying GRB 170817A/GW170817 in a Fermi duration-hardness plane. 2018, *Astrophysics and Space Science*, **363**, 53, DOI: 10.1007/s10509-018-3274-5
- Jolliffe, I. 1986, *Principal Component Analysis* (Springer Verlag)

- Kouveliotou, C., Meegan, C. A., Fishman, G. J., et al., Identification of two classes of gamma-ray bursts. 1993, *Astrophysical Journal, Letters*, **413**, L101, DOI: 10.1086/186969
- Kovács, T. O., Burgarella, D., Kaneda, H., et al., Star formation and polycyclic aromatic hydrocarbons in ELAIS N1 galaxies as seen by AKARI. 2019, *Publications of the ASJ*, **71**, 27, DOI: 10.1093/pasj/psy145
- Kruskal, W. H. & Wallis, W. A., Use of Ranks in One-Criterion Variance Analysis. 1952, *Journal of the American Statistical Association*, **47**, 583, DOI: 10.1080/01621459.1952.10483441
- Kumar, P. & Zhang, B., The physics of gamma-ray bursts & relativistic jets. 2015, *Physics Reports*, **561**, 1, DOI: 10.1016/j.physrep.2014.09.008
- Lê, S., Josse, J., & Husson, F., FactoMineR: A Package for Multivariate Analysis. 2008, *Journal of Statistical Software*, **25**, 1, DOI: 10.18637/jss.v025.i01
- MacFadyen, A. I. & Woosley, S. E., Collapsars: Gamma-Ray Bursts and Explosions in “Failed Supernovae”. 1999, *Astrophysical Journal*, **524**, 262, DOI: 10.1086/307790
- McGill, R., Tukey, J. W., & Larsen, W. A., Variations of box plots. 1978, *The American Statistician*, **32**, 12
- Mészáros, A., Bagoly, Z., Horváth, I., Balázs, L. G., & Vavrek, R., A Remarkable Angular Distribution of the Intermediate Subclass of Gamma-Ray Bursts. 2000a, *Astrophysical Journal*, **539**, 98, DOI: 10.1086/309193
- Mészáros, A., Bagoly, Z., & Vavrek, R., On the existence of the intrinsic anisotropies in the angular distributions of gamma-ray bursts. 2000b, *Astronomy and Astrophysics*, **354**, 1
- Mészáros, P., Gamma-ray bursts. 2006, *Reports on Progress in Physics*, **69**, 2259, DOI: 10.1088/0034-4885/69/8/R01
- Mukherjee, S., Feigelson, E. D., Jogesh Babu, G., et al., Three Types of Gamma-Ray Bursts. 1998, *Astrophysical Journal*, **508**, 314, DOI: 10.1086/306386
- Pérez-Ramírez, D., de Ugarte Postigo, A., Gorosabel, J., et al., Detection of the high z GRB 080913 and its implications on progenitors and energy extraction mechanisms. 2010, *Astronomy and Astrophysics*, **510**, A105, DOI: 10.1051/0004-6361/200811151
- Pinter, S., Multi-messenger studies of γ -ray bursts and their cosmic environment. 2018, *Astronomische Nachrichten*, **339**, 336, DOI: 10.1002/asna.201813501
- Pinter, S., Bagoly, Z., Balázs, L. G., et al., Resolving the structure of the Galactic foreground using Herschel measurements and the Kriging technique. 2017, *Proceedings of the International Astronomical Union*, **12**, 168–169, DOI: 10.1017/S1743921317011097
- R Core Team. 2021, R: A Language and Environment for Statistical Computing, R Foundation for Statistical Computing, Vienna, Austria
- Suleiman, N., Noboriguchi, A., Toba, Y., et al., The statistical properties of 28 IR-bright dust-obscured galaxies and SED modelling using CIGALE. 2022, *Publications of the ASJ*, **74**, 1157, DOI: 10.1093/pasj/psac061

- Tarnopolski, M., Testing the anisotropy in the angular distribution of Fermi/GBM gamma-ray bursts. 2017, *Monthly Notices of the RAS*, **472**, 4819, DOI: 10.1093/mnras/stx2356
- Tóth, B. G., RÁCZ, I. I., & Horváth, I., Gaussian-mixture-model-based cluster analysis of gamma-ray bursts in the BATSE catalog. 2019, *Monthly Notices of the RAS*, **486**, 4823, DOI: 10.1093/mnras/stz1188
- Toth, L. V., Doi, Y., Zahorecz, S., et al., Galactic foreground of gamma-ray bursts from AKARI Far-Infrared Surveyor. 2019, *Publications of the ASJ*, **71**, 10, DOI: 10.1093/pasj/psy123
- Tukey, J. W. 1977, *Exploration Data Analysis*, Box-and-Whisker Plots (Addison-Wesley), 39–43
- Vavrek, R., Balázs, L. G., Mészáros, A., Horváth, I., & Bagoly, Z., Testing the randomness in the sky-distribution of gamma-ray bursts. 2008, *Monthly Notices of the RAS*, **391**, 1741, DOI: 10.1111/j.1365-2966.2008.13635.x
- Veres, P., Bagoly, Z., Horváth, I., Mészáros, A., & Balázs, L. G., A Distinct Peak-flux Distribution of the Third Class of Gamma-ray Bursts: A Possible Signature of X-ray Flashes? 2010, *Astrophysical Journal*, **725**, 1955, DOI: 10.1088/0004-637X/725/2/1955
- Vetere, L., Massaro, E., Costa, E., Soffitta, P., & Ventura, G., Slow and fast components in the X-ray light curves of gamma-ray bursts. 2006, *Astronomy and Astrophysics*, **447**, 499, DOI: 10.1051/0004-6361:20053800
- Zhang, B. 2018, *The Physics of Gamma-Ray Bursts* (Cambridge University Press)
- Zhang, B. & Mészáros, P., An Analysis of Gamma-Ray Burst Spectral Break Models. 2002, *Astrophysical Journal*, **581**, 1236, DOI: 10.1086/344338

Photometric pipeline for robotic telescopes

M. Jelínek 

ASÚ AV ČR Ondřejov, Czech Republic (E-mail: mates@asu.cas.cz)

Received: June 30, 2023; Accepted: November 4, 2023

Abstract. PYRT is a software package to automatically process and calibrate photometric images obtained by robotic telescopes. The response model to be fitted is described with terms provided from the command line or a configuration file. It also has a limited capability to improve the astrometric solution of wide-field images.

The pipeline was used to process several million images obtained by the D50 telescope at Ondřejov. At present, it is in the process of being implemented for the wide-field Small Binocular Telescope, also at Ondřejov. It has also been tested to successfully solve a wide range of images from other telescopes ranging from large-aperture professional instruments to wide-field systems and all-sky cameras.

Key words: image processing – photometry – automation

1. Introduction

Ground-based robotic telescopes are an important tool of modern astronomy. Photometric imaging is just one example of the wide range of tasks these devices can perform in all fields of observational astronomy.

Everyone who has ever processed a photometric image has faced the problem of estimating the zeropoint, which may change not just between frames, but also across the field of view of a single frame. The principal tool of the PYRT package `dophot` is a tool to do just that, in a manner that is consistent and reliable when dealing with large quantities of frames. The package provides further tools to prepare and visualize the data in order to fit a wide range of input images.

In practice, a photometric solution of an image is closely bound to a correct mapping of its image plane coordinates to the world coordinate system (WCS, as described by [Calabretta & Greisen 2000](#)). For images with a narrow field of view, `astrometry.net` ([Lang et al., 2012](#)) provides a practically perfect solution. However, for wider-field images the projection introduces distortion which its Simple Image Polynomial (SIP) corrections have difficulty handling well. In support of wide-field imaging, `dophot` provides an optional WCS refit capability using a photometrically selected set of objects.

2. Methods

The input of the photometric calibration process is an image or set of images with a WCS header which does not have to be absolutely precise. We use `ssextractor` (Bertin & Arnouts, 1996) or `IRAF/daophot` (Stetson et al., 1990) to detect and extract raw fluxes and positions from the bitmap and using this information, we perform photometric calibration with standard stars within the field of view. The secondary standards are taken from the Atlas (Tonry et al., 2018) catalogue, which uses PanSTARRS (Kaiser et al., 2010) photometry for faint stars complemented with measurements from other sources for stars brighter than mag. 9. Under ideal conditions, we search for the zeropoint Z that minimizes δM_n for n stars

$$\delta M_n = Z - 2.5 \log_{10} I_n - m_n,$$

Which leads to an (error-weighted) arithmetic average. However, the reality is almost never this simple.

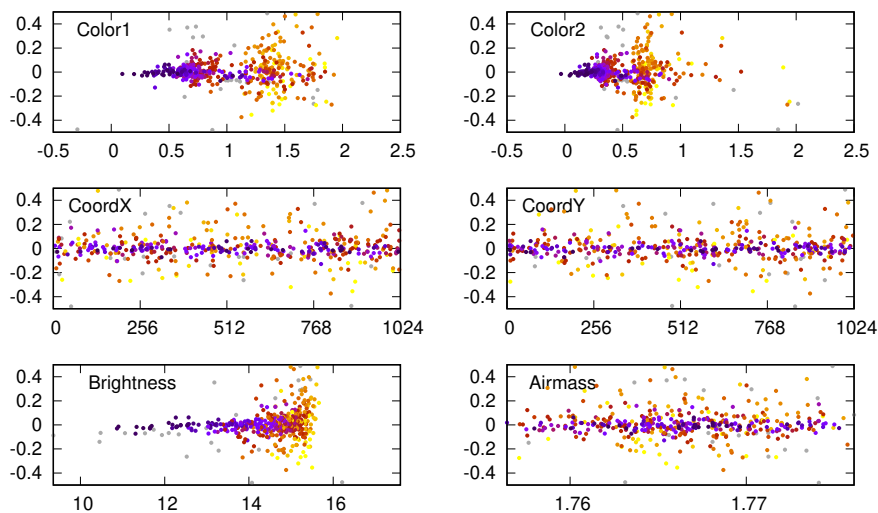


Figure 1. An example of residual plot of a photometric fit. Top two are scatter plots of color indexes ($g-r$) and ($r-i$), the second row are X/Y coordinates and the bottom row are scatter plots along detected brightness and airmass.

2.1. Terms

Variation of the photometric response may be fitted along eight main variables: four color indexes, both positional axes of the image, brightness of the object

and airmass. The fitted model parameters, known as *terms* in `dophot`, follow a simple alphanumeric syntax, for easy reference.

Most of the fitting is realised by polynomial terms, which start with "P" followed by the numeric order and the letter referring to the fitted axis. For example P3X refers to a third degree polynomial along X-axis, i.e. a $P3X.x^3$ would be summed to every reference star brightness. More than one axis may be referred to in one term, so that P2X2Y would stand for $P2X2Y.x^2.y^2$ and so on. Color axes are coded as C,D,E and F. At present with the Atlas catalogue, they stand for $(g' - r')$, $(r' - i')$, $(i' - z')$ and $(z' - J)$ color indices respectively, so that PC is a color term $PC(g' - r')$. A means airmass, R stands for radius from the center in this context.

Dophot is meant to be usable in routine automated operation, as a tool to study the optimal parameter configuration as well as to calibrate random contributed images. To automate, the routine would work with a single image, the typical parameter values would be imported from a configuration file and be refitted only to find small adjustments. Some of the parameters may be also loaded and kept fixed.

Some values are difficult to obtain and make sense only while fitting simultaneously many images. An excellent example of this can be the linear atmospheric reddening (PXC), a term that depends both on an object color index and airmass. Unless there is a good sampling of airmass range, the value of atmospheric reddening cannot be reliably estimated. To obtain this kind of parameters, the fitting can be run with a larger set of images being fitted simultaneously, with most parameters being common among the entire data set and the zeropoints and optionally an X/Y tilt of the response be specific for each frame. Once measured, the example value of PXC would stay fixed when calibrating images one by one.

In theory, all images from a single instrument run could be fitted simultaneously with all the effects included in the model. This approach is, however, not practical for memory and speed limitations. Also, for real-time processing, single-image fitting is desirable.

2.2. Object identification

Object positions in the image are not precise, rather they are noisy 2D positions and an identification with a naive approach is rather slow. Misidentifications can introduce undesired bias to the result, and need to be dealt with if we do not require a perfect WCS solution.

PYRT uses a KDTree algorithm in order to speed up the identifications. All nearby objects are treated equally at first, but during the fit the sigma clipping would mask any conflicting pairs. To minimize the effect of outliers to the initial solution, the initial set of zeropoints is estimated with the median and we use Cauchy's delinearization of residuals during the fine fit.

2.3. Astrometry

Images from the Small Binocular Telescope (SBT, Štrobl et al. 2019) have 4096 x 4096 pixels, FWHM 1.5 and typically around 100.000 objects. Such frames put packages such as `astrometry.net` (Lang et al., 2012) and `SCAMP` (Bertin, 2006) to serious test. While both are able to provide a correct astrometric solution based on polynomial distortion mapping, there are glitches caused by misidentification of an object and in practice neither package is sufficiently reliable.

PYRT now has an experimental feature that allows fitting a few uncommon WCS projection types in order to accommodate large-format and wide field images. Namely, we use the photometrically-selected dataset to fit zenithal polynomial projection (ZPN), zenithal equal area (ZEA) and zenithal perspective (AZP). For the SBT images we achieve very good results with ZPN projection.

PROJ	=	ZPN	fixed	
PV2-1	=	1.000000	fixed	
CD1-1	=	-0.000872551581	± 0.000000000104	(-3.141")
CD1-2	=	0.000010042013	± 0.000000000087	(0.036")
CD2-1	=	0.000010320805	± 0.000000000089	(0.037")
CD2-2	=	0.000872719794	± 0.000000000102	(3.142")
CRVAL1	=	350.2110758	± 0.0000052	
CRVAL2	=	77.5829211	± 0.0000027	
PV2-3	=	8.27432	± 0.00032	
PV2-5	=	377.34	± 0.23	
CRPIX1	=	2118.9358	± 0.0013	
CRPIX2	=	2072.5532	± 0.0032	
SIGMA	=	0.112		

Table 1. An example WCS/ZPN astrometric solution of an image taken by camera C1 of the Small Binocular Telescope. The ZPN polynomial terms are the PV2-n values. See Calabretta & Greisen (2000) for the keyword meaning and further details.

2.4. Requirements

The entire package is implemented in `python3` and uses `numpy`, `scipy`, `sklearn` and `astropy` packages, and to function properly, the Atlas catalogue needs to be available locally and `sExtractor` should be installed to provide object detection.

3. Solving common problems

3.1. Flat field correction

Flatfields do often not correct properly. The typical twilight-sky flatfield is, in fact, a combination of transmitted and scattered light. Most telescopes have at least a natural form of response drop towards the image edges, caused by the cosine projection of the pupil to the sky, and some level of vignetting may also play a role. Sky-based (and also homogeneously illuminated plane) flat-field correction often simply adds the scattered light, causing overcorrection in the image edges. Also, a gradient illumination may introduce a tilt in response along the image plane. With image-plane response fitting, these problems are easy to fix.

3.2. Clouds

Varying thickness of haze and cirrus seriously affects photometry, not just by reducing sensitivity in the field and introducing parasite light, clouds introduce patterns of varying response. For narrow-field imaging, atmospheric conditions may be corrected for by simply introducing a low-order polynomial in image coordinates. For SBT's $3.5^\circ \times 3.5^\circ$ frames, this approach has limited use and a mesh of sample values is expected to solve the issue in future versions of the package. At present, SBT frames where a simple polynomial response model does not fit well, i.e. the variance of residuals is larger than a fixed value, are understood as being tainted by weather and are not used.

If more complex polynomials need to be used to deal with problematic response (typically clouds), the Runge phenomenon (i.e. oscillation at the edges) may step in and distort corners, edges or sparsely populated areas. To deal with such situations, we are considering implementing an interpolated mesh grid approach in some future version.

3.3. Color response

Transmission bandpasses differ between instruments. One of `dophot`'s essential features is providing color term fitting on the complete sample of objects. With standard filters, the necessary correction may be as simple as a small linear term to correct for a small shift in response, but for frames taken without filter or a non-standard filter, it is necessary to use more colors and even a second degree polynomial term in order to obtain a satisfactory fit.

By its nature, `dophot` produces magnitudes in an instrumental system. If the obtained values need to be directly compared with standard measurements, further steps need to be taken to transform the dataset to a standard photometric system (harmonisation). For this reason, it is a good practice not to let the color response vary for every image in the set. The principal aim of the fitting is to create a lightcurve — a single filter time series of the object brightness.

Subtle changes in a freely-fitted color term make our life harder. They would cause every point of the lightcurve to be in a slightly different filter, which introduces noise in the lightcurves of measured objects. The color-related noise would cancel out after harmonisation, but this step is often omitted for the sake of simplicity. We therefore measure the color response in a larger sample of objects from different fields and varying airmasses, store the results in a model file and use them as fixed parameters during routine operation.

3.4. Weighted image coadding

The in-process knowledge of the response function and background noise allows for construction of an artificial flat field and weight frame. These frames can be used to weight-combine many frames with varying image quality to obtain an optimal coadd for the best photometric sensitivity. In the High Energy Astrophysics (HEA) group, this is often used when searching for faint GRB optical afterglows.

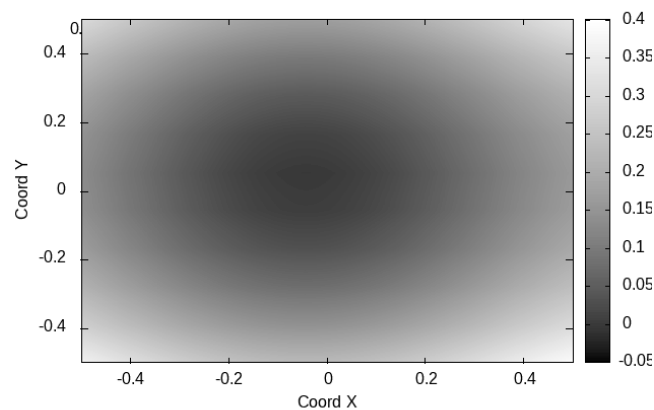


Figure 2. An example of flat-field correction computed by PYRT for a frame from the D50 telescope. Note the edges overcorrected by ~ 0.3 mag

3.5. Non-linearity

Response nonlinearity is best treated directly during image processing. Sometimes, the image was not treated or there is a residual nonlinearity in the data, which may affect all objects, just the brightest ones or even the faint end of the dataset. A linear or polynomial term may be introduced, but a great care should be taken, as this destabilizes the minimizing process and can lead to an

incorrect output. In any case, images can be treated, but need to be treated one by one, ideally reviewing the results. If saturation is a problem, `dophot` allows for an easier and safer way of omitting the brightest objects from the fit.

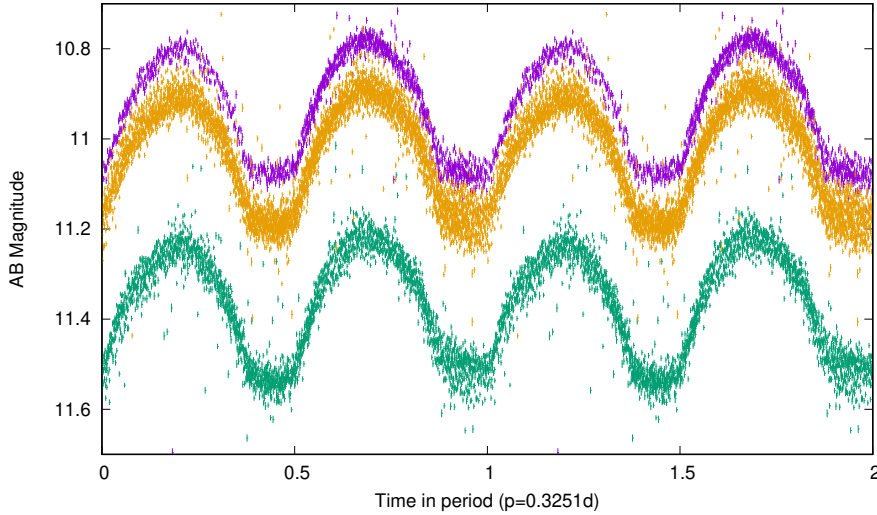


Figure 3. A lightcurve of a W UMa star NSVS 9023048 from images taken by SBT. NSVS was not a target of the frames, it was searched for only when the complete set of output was available and received no special treatment. The period and coordinates were taken from AAVSO’s VSX webpage (Watson, 2012; Gettel et al., 2006). Filters from bottom to top are SDSS g' , r' and i'

4. Results

Images taken by the D50 (Nekola et al., 2010) telescope are processed automatically and the resulting photometry of every detected object is stored in a Q3C-based (Koposov & Bartunov, 2006) photometric database. This way, a lightcurve of any object seen by the telescope can be searched in seconds.

Frames taken by the SBT are planned to be treated in the same way. For now, an important issue with the frames having incorrect astrometric solution has been solved by implementing a built-in astrometric fit. Once the code to do this is mature enough, SBT will also contribute to the photometric database.

PYRT was used also to prepare the frames for image subtraction with *hot pants* (Becker, 2015). In particular, image subtraction of SBT frames was impossible without their precise WCS mapping. The images may also be corrected

for response and some awkward-looking outputs of the image subtraction were resolved this way.

The output of PYRT at the D50 telescope is being imported to a Q3C-based database, to allow for quick cone searches of objects. This way, lightcurves for any stationary object observed with D50 can be produced in a matter of seconds.

5. Conclusions

I present a Python photometric package centered around automated and semi-automated processing of astronomical photometric images. The package's input are raw fluxes, x/y positions and a WCS mapping of the frame. The model is described by alphanumerically designated easy to remember terms. The output is a listing of AB magnitudes of each object detected in the frame. An experimental feature performs also a precise astrometric solution with the photometrically-selected set of objects. The package is in active use at D50 and SBT telescopes in Ondřejov and is available on request from the author in hope that it would be useful to others.

Acknowledgements. I would like to thank the anonymous referee for useful comments that improved the paper and to Ronan Cunniffe for a fruitful discussion. This work was funded by the Mid-term plan for research activities ASU:67985815.

References

- Becker, A. 2015, HOTPANTS: High Order Transform of PSF ANd Template Subtraction, *Astrophysics Source Code Library*, record ascl:1504.004
- Bertin, E., Automatic Astrometric and Photometric Calibration with SCAMP. 2006, in *Astronomical Society of the Pacific Conference Series*, Vol. **351**, *Astronomical Data Analysis Software and Systems XV*, ed. C. Gabriel, C. Arviset, D. Ponz, & S. Enrique, 112
- Bertin, E. & Arnouts, S., SExtractor: Software for source extraction. 1996, *Astronomy and Astrophysics, Supplement*, **117**, 393, DOI: 10.1051/aas:1996164
- Calabretta, M. & Greisen, E. W., Representations of World Coordinates in FITS. 2000, in *Astronomical Society of the Pacific Conference Series*, Vol. **216**, *Astronomical Data Analysis Software and Systems IX*, ed. N. Manset, C. Veillet, & D. Crabtree, 571
- Gettel, S. J., Geske, M. T., & McKay, T. A., A Catalog of 1022 Bright Contact Binary Stars. 2006, *Astronomical Journal*, **131**, 621, DOI: 10.1086/498016
- Kaiser, N., Burgett, W., Chambers, K., et al., The Pan-STARRS wide-field optical/NIR imaging survey. 2010, in *Society of Photo-Optical Instrumentation Engineers (SPIE) Conference Series*, Vol. **7733**, *Ground-based and Airborne Telescopes III*, ed. L. M. Stepp, R. Gilmozzi, & H. J. Hall, 77330E

- Koposov, S. & Bartunov, O., Q3C, Quad Tree Cube – The new Sky-indexing Concept for Huge Astronomical Catalogues and its Realization for Main Astronomical Queries (Cone Search and Xmatch) in Open Source Database PostgreSQL. 2006, in Astronomical Society of the Pacific Conference Series, Vol. **351**, *Astronomical Data Analysis Software and Systems XV*, ed. C. Gabriel, C. Arviset, D. Ponz, & S. Enrique, 735
- Lang, D., Hogg, D. W., Mierle, K., Blanton, M., & Roweis, S. 2012, Astrometry.net: Astrometric calibration of images, Astrophysics Source Code Library, record ascl:1208.001
- Nekola, M., Hudec, R., Jelínek, M., et al., Robotic telescopes for high energy astrophysics in Ondřejov. 2010, *Experimental Astronomy*, **28**, 79, DOI: 10.1007/s10686-010-9190-5
- Stetson, P. B., Davis, L. E., & Crabtree, D. R., Future development of the DAOPHOT crowded-field photometry package. 1990, in Astronomical Society of the Pacific Conference Series, Vol. **8**, *CCDs in astronomy*, ed. G. H. Jacoby, 289–304
- Tonry, J. L., Denneau, L., Flewelling, H., et al., The ATLAS All-Sky Stellar Reference Catalog. 2018, *Astrophysical Journal*, **867**, 105, DOI: 10.3847/1538-4357/aae386
- Štrobl, J., Jelínek, M., & Hudec, R., Small Binocular Telescope: The new epoch of Burst Alert Robotic Telescope. 2019, *Astronomische Nachrichten*, **340**, 633, DOI: 10.1002/asna.201913668
- Watson, C. L., VSX: The Next Generation. 2012, *Journal of the American Association of Variable Star Observers*, **40**, 431

X-ray astrophysics as secondary science with ESA/China SMILE satellite

R. Hudec^{1,2,3} , V. Šimon^{1,2}  and A. Read⁴

¹ *Czech Technical University in Prague, Faculty of Electrical Engineering,
16627 Prague, Czech Republic (E-mail: hudec@fel.cvut.cz)*

² *Astronomical Institute of the Czech Academy of Sciences
251 65 Ondřejov, The Czech Republic*

³ *Engelhardt Observatory, Kazan Federal University, Kazan, Republic of
Tatarstan*

⁴ *University of Leicester, Leicester, Great Britain*

Received: July 15, 2023; Accepted: September 23, 2023

Abstract. We present and discuss the feasibility of X-ray astrophysics with ESA–China *SMILE* satellite designed to investigate the Earth’s magnetosphere’s dynamic response to the solar wind’s impact. We plan to study celestial X-ray targets as a secondary science for the onboard wide-field X-ray telescope SXI and related Czech participation in this mission. The Solar Wind Magnetosphere Ionosphere Link Explorer, or *SMILE*, is a joint mission between the European Space Agency (ESA) and the Chinese Academy of Sciences (CAS). We show that SXI can also provide wide-field imaging of the sky in the soft X-ray region ($E = 0.15 - 3$ keV) and observe the long-term activity of cosmic X-ray sources. We show the stability of the orientation of the field of view of the SXI telescope; it will undergo only minor changes during several years of the planned operation. Therefore, observing the long-term soft X-ray activity of cosmic sources, e.g., those in the Magellanic Clouds, will be possible.

Key words: ESA SMILE – SXI – X-ray astrophysics

1. Introduction

ESA–CAS mission *SMILE* is not an astrophysical mission, as X-ray emission also occurs much more nearby, namely in Earth’s atmosphere and Earth’s magnetosphere (Branduardi-Raymont et al., 2016; Wang et al., 2018; Branduardi-Raymont et al., 2017) and this is the primary mission goal.

SMILE (Solar wind Magnetosphere Ionosphere Link Explorer) is a space mission that aims to measure Earth’s global system responses to solar wind and geomagnetic variations (Branduardi-Raymont et al., 2016). It will investigate the dynamic response of the Earth’s magnetosphere to the impact of the solar wind in a unique manner, never attempted before: it will combine soft X-ray

imaging of the Earth's magnetopause and magnetospheric cusps with simultaneous UV imaging of the Northern aurora.

For the first time, we will be able to trace and link the processes of solar wind injection in the magnetosphere with those acting on the charged particles precipitating into the cusps and, eventually the aurora. *SMILE* will also carry in-situ instrumentation to monitor the solar wind conditions so that the simultaneous X-ray and UV images can be compared and contrasted directly and self-sufficiently with the upstream driving conditions. With its unparalleled payload, *SMILE* will provide answers to many of the open questions in solar-terrestrial relationships in a thoroughly novel way.

2. The *SMILE* payload

The following instrumentation forms the scientific payload for the *SMILE* satellite (Branduardi-Raymont et al., 2016).

SXI: a telescope with a wide field of view (FOV) (26.5×15.5 degrees) Lobster-Eye X-ray optic based on microchannel plate technology and CCD detector at the focal plane (Sembay et al., 2016). The SXI will observe the dayside magnetospheric boundaries' location, shape, and motion. X-rays in the Earth's exosphere result from the charge exchange interaction between ions in the solar wind and neutrals, such as hydrogen in the Earth's exosphere and interplanetary space. PI: Steve Sembay, University of Leicester, UK.

UVI: a wide field of view optic sensitive to the Lyman-Birge-Hopffman band of ultraviolet radiation (120–190 nm). Filters and coatings will be used to suppress day glow. The UVI will observe the polar cap and measure the location and width of the auroral oval. It will also observe transient and localized brightenings that occur on the auroral oval edges. PI: Eric Donovan, University of Calgary, Canada.

LIA: a wide field of view proton and alpha particle analyzer. This will determine the basic moments of the solar wind and magnetosheath ion distributions, such as velocity, density, temperature, and the heat flux vector. These measurements, taken simultaneously with the UV and X-ray images, obviate the concerns of arrival times and spatial extents when external solar wind monitors at the distant Lagrangian Point L1 are used. The LIA will include a top-hat-type electrostatic analyzer. The center plane of the field of view will be parallel to the ecliptic to ensure that the solar wind and average plasma sheet flow directions remain within the field of view. A larger dynamic range will be obtained using a variable geometric factor system. PI: Lei Dai, National Space Science Center, Chinese Academy of Sciences, China.

MAG: a dual-redundant digital fluxgate magnetometer with two tri-axial fluxgate sensors connected by a boom to a spacecraft-mounted electronics box. The accompanying electronics unit consists of an FPGA digital processing unit

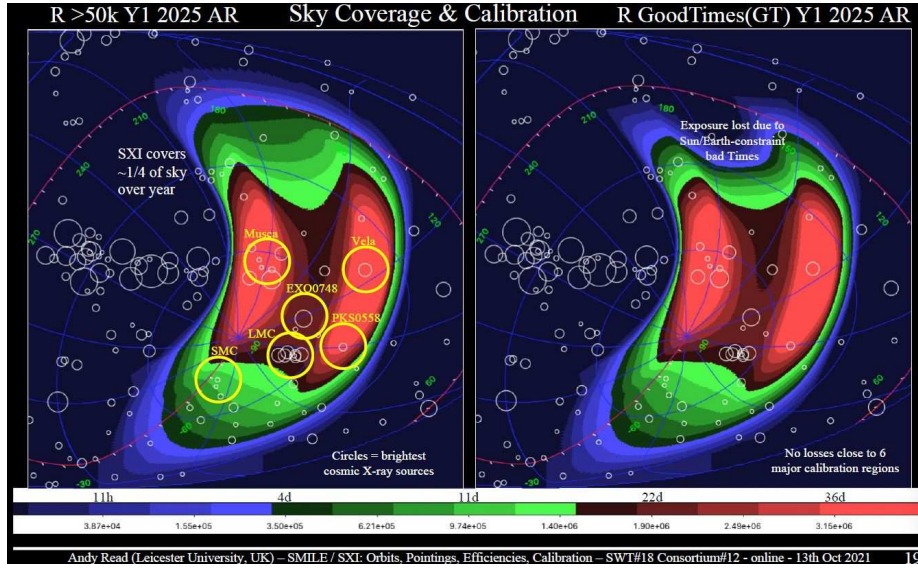


Figure 1. The SXI Sky Coverage and Calibration, the year 2025, simulation by Andrew Read.

with a DC-DC converter. PI: Lei Li, National Space Science Center, Chinese Academy of Sciences (CAS), China.

For X-ray astrophysics, the essential payload is the SXI telescope, as the FOV of this telescope will cover a relatively large fraction of the sky during the mission lifetime with many astrophysical X-ray sources included (Figs. 1 and 2).

Figures 1 and 2 also show the stability of FOV of SXI; it will undergo only minor changes during several years of the planned operation. Therefore, the Magellanic Clouds will be stably observable by this telescope, and observing the long-term soft X-ray activity of cosmic sources located in these galaxies or the directions to their surroundings will be possible (see below for more).

3. Czech Participation in *SMILE*

The Czech participation is based on very long experience with imaging X-ray telescopes and monitors in the Czech Republic with emphasis on wide field X-ray monitors Lobster Eye type. There is essential background in the Czech Republic in the design and the development of wide-field imaging X-ray telescopes based on innovative Lobster-Eye X-ray optics (Hudec et al., 2017b,a, 2015; Pina et al., 2014).

The expected Czech contribution is based on scientific and data evaluation software and data analyses, with emphasis on the SXI telescope. The data and

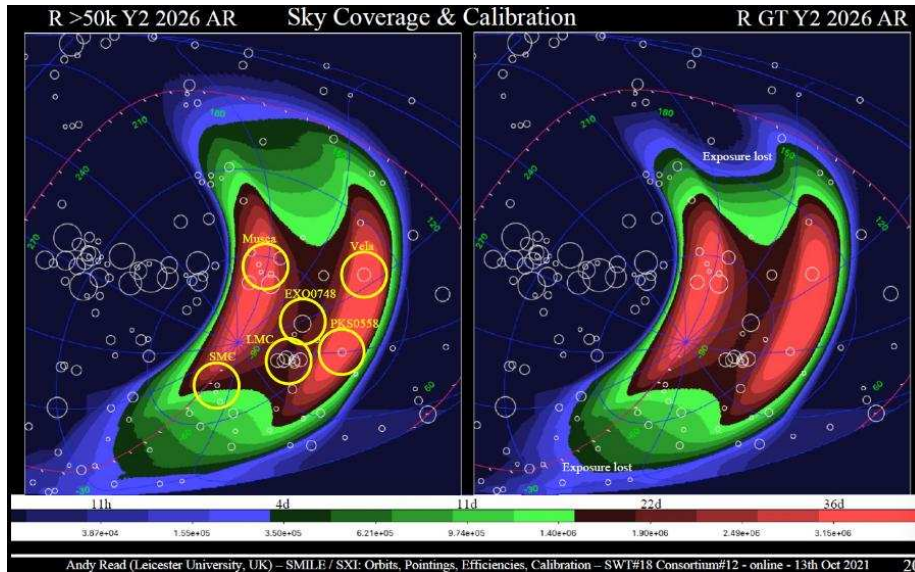


Figure 2. The SXI Sky Coverage and Calibration, the year 2026, simulation by Andrew Read. It is evident that the sky coverage is not very different from the year 2025.

scientific analyses for celestial X-ray sources passing through the SXI FOV, also the secondary science with SXI data, represent another potential interest of the Czech team.

The Czech Technical University represents the leading institution in the Czech Republic in the education of space science and engineering in addition to that participating in numerous space projects ¹ so there is a significant potential for the involvement of students, Ph.D. students, and postdocs in the *SMILE* project.

4. Examples of astrophysically important X-ray sources in the SXI FOV

4.1. X-ray binaries

High-mass and low-mass X-ray binaries (HMXBs and LMXBs) contain mass-accreting neutron stars or black holes. Reviews of these systems can be found, e.g., in Lewin et al. (1995) and Lewin & van der Klis (2006). They are promising bright X-ray binaries for SXI/*SMILE*. The examples located in the Magellanic Clouds are listed below.

¹<https://www.fel.cvut.cz/en/research/space-activities.html>

We note that the detectability of the object strongly depends on its activity. In X-ray binaries, the intensity of X-ray emission strongly increases during active states (outbursts, episodes of the high states); often there are no large spectral variations in the soft X-ray band ($E = 0.15 - 3$ keV).

Timescales of activity expected to be monitored with *SXI/SMILE* are as follows: (i) state transitions—days (but unpredictable), (ii) outbursts—days to months (usually unpredictable, but cycles are possible) here even bins of 1-day flux can provide valuable information.

Examples of luminous neutron-star or black-hole accretors clustering in the Magellanic Clouds and hence observable by *SXI/SMILE* (Figs. 1 and 2) are listed below:

- LMC X-2: low-mass X-ray binary, neutron star accretor, Z-source (Hasinger & van der Klis, 1989; Agrawal & Nandi, 2020).
- LMC X-3: high-mass X-ray binary, donor of $3.63 M_{\odot}$, black hole of $6.98 M_{\odot}$ (Orosz et al., 2014). The long-term variability – a high amplitude of the factor of about 4 on a 100-200 d time-scale (Cowley et al., 1991).
- SMC X-1: high-mass X-ray binary with the neutron star accreting matter from its early-type companion (Reynolds et al., 1993), strong super-orbital modulation (about 60 days) (Clarkson et al., 2003) (possibly occultation by a precessing and warped disk (Ogilvie & Dubus, 2001)).
- SMC X-2: neutron star+Be binary with orbital period 18.62 d (Schurch et al., 2011), transient X-ray pulsar, luminosity of a rare outburst 5.5×10^{38} erg s⁻¹ in 1-70 keV range, spin period of the pulsar 2.37 s (Jaisawal & Naik, 2016).

4.2. Cataclysmic variables

Cataclysmic variables (CVs) contain the white dwarf accretors. The processes in the transferring matter and the accretion regions on the white dwarf often dominate their emission. In these objects, X-ray emission intensity strongly depends on the X-ray band and the activity state in a given CV (Warner, 1995).

Classical novae in an explosion can represent suitable X-ray transients for observing with *SXI/SMILE*. Nova explosion in the FOV of *SXI* can result in a bright, very soft X-ray source for days to months. A hydrostatic nuclear burning on the white dwarf surface generates soft X-rays. They represent an active X-ray source from the start of the explosion (visible only later when the ejected nebula cleared as it expanded). In medium X-rays, an interaction of the expanding envelope and density inhomogeneities are represented (Krautter et al., 1996; Warner, 1995).

X-ray luminosity of most CVs enables their detection only if they are in our Galaxy. We expect the CVs detected by *SXI/SMILE* to be usually located in our Galaxy (foreground objects). Nevertheless, the wide FOV of *SXI* will give

an excellent chance to compare their X-ray flux with optical emission in various activity states from the ground-based stations (e.g., AAVSO).

4.3. Supersoft X-ray sources

This unique CV type contains white dwarf accretors that undergo hydrogen burning (even steady-state) of the accreted matter. It often makes them very luminous X-ray sources of very soft X-ray emission, even close to the Eddington luminosity.

These objects have typical orbital periods of several hours, very soft X-ray spectra, and bolometric luminosity (including a very soft X-ray band) at least sometimes at least 10^{37} or 10^{38} ergs $^{-1}$ (van den Heuvel et al., 1992). Intense soft X-ray emission ($E \leq 1$ keV) can be expected (its detectability depends on the interstellar extinction and metallicity of the source) (van den Heuvel et al., 1992).

Table 1. Promising binary supersoft X-ray sources in the fields covered by SXI/*SMILE* in Figs. 1 and 2. The system parameters are given in Greiner (1996).

Object
LMC:
RX J0439.8-6819
RX J0513.9-6951
RX J0527.8-6954
RX J0537.7-7034
CAL83
CAL87
SMC:
1E 0035.4-7230

Vigorous activity in various spectral bands is common in these sources. They are detectable mainly in the Magellanic Clouds in FOV of SXI/*SMILE*. Dense monitoring in a soft X-ray band will enable investigation of the profile of the light curve and its relation on the orbital timescale (several hours or a few days) to the variations on the scale of months or years.

5. Conclusions

The *SMILE* satellite with innovative instrumentation onboard, including a Lobster Eye X-ray telescope, will study X-rays from the magnetosphere. However, the wide-field X-ray images provided by the onboard SXI telescope can be used for X-ray astrophysics as secondary science, as well. Celestial X-ray sources represent important secondary science for SXI, as they will enable a study of the

long-term activity of X-ray binary sources by this instrument. A dense coverage will also allow a search for rare and/or unexpected phenomena (also renewing the activity of "sleeping" transients).

A search for the accompanying spectral variations (changes of hardness ratios) and transitions between the states of activity (caused, e.g., by structural changes of the emitting regions) will also be possible.

Acknowledgements. The research leading to these results has received funding from the European Unions Horizon 2020 Programme under the AHEAD2020 project (grant agreement n. 871158). Also, support by the project RVO:67985815 is acknowledged.

References

- Agrawal, V. K. & Nandi, A., AstroSat view of LMC X-2: evolution of broad-band X-ray spectral properties along a complete Z-track. 2020, *MNRAS*, **497**, 3726, DOI: 10.1093/mnras/staa2063
- Branduardi-Raymont, G., Wang, C., Sembay, S., et al., SMILE: A Novel and Global Way to Explore Solar-Terrestrial Relationships. 2016, in *AGU Fall Meeting Abstracts*, SH31C-07
- Branduardi-Raymont, G., Wang, C., & Smile Collaboration, SMILE: Novel and global X-ray imaging of the Sun-Earth connection. 2017, in *The X-ray Universe 2017*, 46
- Clarkson, W. I., Charles, P. A., Coe, M. J., et al., Long-term properties of accretion discs in X-ray binaries - I. The variable third period in SMC X-1. 2003, *MNRAS*, **339**, 447, DOI: 10.1046/j.1365-8711.2003.06176.x
- Cowley, A. P., Schmidtke, P. C., Ebisawa, K., et al., Discovery of a Long-Term Periodic Variation in LMC X-3. 1991, *ApJ*, **381**, 526, DOI: 10.1086/170676
- Greiner, J., Catalog of Luminous Supersoft X-Ray Sources. in , *Supersoft X-Ray Sources, Proceedings of the International Workshop Held in Garching, Germany, 28 February - 1 March 1996. Lecture Notes in Physics*, Vol. **472**, 299-337
- Hasinger, G. & van der Klis, M., Two patterns of correlated X-ray timing and spectral behaviour in low-mass X-ray binaries. 1989, *A&A*, **225**, 79
- Hudec, R., Pina, L., & Inneman, A., Novel wide-field x-ray optics for space. 2017a, in Society of Photo-Optical Instrumentation Engineers (SPIE) Conference Series, Vol. **10569**, *Society of Photo-Optical Instrumentation Engineers (SPIE) Conference Series*, 105692F
- Hudec, R., Pina, L., Inneman, A., & Tichy, V., Applications of lobster eye optics. 2015, in Society of Photo-Optical Instrumentation Engineers (SPIE) Conference Series, Vol. **9510**, *EUV and X-ray Optics: Synergy between Laboratory and Space IV*, 95100A
- Hudec, R., Sveda, L., Pina, L., et al., LOBSTER: new space x-ray telescopes. 2017b, in Society of Photo-Optical Instrumentation Engineers (SPIE) Conference Series,

- Vol. **10567**, *Society of Photo-Optical Instrumentation Engineers (SPIE) Conference Series*, 1056719
- Jaisawal, G. K. & Naik, S., Detection of cyclotron resonance scattering feature in high-mass X-ray binary pulsar SMC X-2. 2016, *MNRAS*, **461**, L97, DOI: 10.1093/mnras/slw108
- Krautter, J., Oegelman, H., Starrfield, S., Wichmann, R., & Pfeffermann, E., ROSAT X-Ray Observations of Nova V1974 Cygni: The Rise and Fall of the Brightest Supersoft X-Ray Source. 1996, *Astrophysical Journal*, **456**, 788, DOI: 10.1086/176697
- Lewin, W. H. G. & van der Klis, M. 2006, *Compact Stellar X-ray Sources*
- Lewin, W. H. G., van Paradijs, J., & van den Heuvel, E. P. 1995, *X-ray binaries*
- Ogilvie, G. I. & Dubus, G., Precessing warped accretion discs in X-ray binaries. 2001, *MNRAS*, **320**, 485, DOI: 10.1046/j.1365-8711.2001.04011.x
- Orosz, J. A., Steiner, J. F., McClintock, J. E., et al., The Mass of the Black Hole in LMC X-3. 2014, *ApJ*, **794**, article id. 154, 18 pp., DOI: 10.1088/0004-637X/794/2/154
- Pina, L., Burrows, D., Cash, W., et al., X-ray monitoring for astrophysical applications. 2014, in Society of Photo-Optical Instrumentation Engineers (SPIE) Conference Series, Vol. **9207**, *Advances in X-Ray/EUV Optics and Components IX*, 92070T
- Reynolds, A. P., Hilditch, R. W., Bell, S. A., & Hill, G., Optical spectroscopy of the massive X-ray binary SMC X-1/Sk 160. 1993, *MNRAS*, **261**, 337, DOI: 10.1093/mnras/261.2.337
- Schurch, M. P. E., Coe, M. J., McBride, V. A., et al., Orbital period determinations for four SMC Be/X-ray binaries. 2011, *MNRAS*, **412**, 391, DOI: 10.1111/j.1365-2966.2010.17914.x
- Sembay, S., Branduardi-Raymont, G., Drumm, P., et al., The Soft X-ray Imager (SXI) on the SMILE Mission. 2016, in *AGU Fall Meeting Abstracts*, SM44A-04
- van den Heuvel, E. P. J., Bhattacharya, D., Nomoto, K., & Rappaport, S. A., Accreting white dwarf models for CAL 83, CAL 87 and other ultrasoft X-ray sources in the LMC. 1992, *A&A*, **262**, 97
- Wang, C., Escoubet, C. P., & Branduardi-Raymont, G., Update on SMILE - A new mission to image the magnetosphere. in , *42nd COSPAR Scientific Assembly*, Vol. **42**, D3.2-18-18
- Warner, B. *Cataclysmic variable stars*, , Vol. **28**

Comparison of Gaia BP/RP spectra with LDS (Low Dispersion Spectroscopy) photographic sky surveys

R. Hudec^{1,2,3} 

¹ *Czech Technical University in Prague, Faculty of Electrical Engineering
(E-mail: hudec@fel.cvut.cz)*

² *Astronomical Institute of the Czech Academy of Sciences
251 65 Ondřejov, The Czech Republic*

³ *Engelhardt Observatory, Kazan Federal University, Kazan, Republic of
Tatarstan*

Received: July 13, 2023; Accepted: October 2, 2023

Abstract. Blue (BP) and Red (RP) Photometer low-resolution spectral data is one of the exciting new products in the third data release of ESA satellite Gaia (Gaia DR3)¹. The Gaia "photometric mode" RP/BP generates ultra-low-dispersion prism spectra of celestial sources. The LDS (Low-Dispersion Spectroscopy) astrophysics was evolved and performed at numerous observatories (many in US) between ca 1909 and 1980. Mostly LDS with Schmidt telescopes was performed (plates with objective prism). These data were used in the past for various projects e.g. QSO, emission line and H α surveys, star classifications, etc. but little used after 1980. My estimate is that there are more than 100 million LDS star spectra in these databases. I will discuss their astrophysical scientific potential in recent astrophysics. I will show that these data can be used e.g. for the redshift estimation and study of High z Universe)

Key words: Gaia – spectroscopy – low dispersive spectroscopy

1. Introduction

Blue (BP) and Red (RP) Photometer low-resolution spectral data (Low dispersion spectra, LDS) is one of the exciting new products in Gaia Data Release 3 (Gaia DR3)² Montegriffo et al. (2023); De Angeli et al. (2023); Zhang et al. (2023); Witten et al. (2022); Carrasco et al. (2021) (Figs. 1, 2, 3)³. LDS data are also available in numerous historical photographic sky surveys (access after digitization). My estimate is that there are more than 100 million LDS star spectra are in these databases.

¹<https://gaia.aip.de/cms/services/spectra-access/>

²<https://gaia.aip.de/cms/services/spectra-access/>

³https://www.gaia.ac.uk/sites/default/files/media/images/bpi_spec.jpeg,
https://www.cosmos.esa.int/web/gaia/iow_20201222

These archival data have the potential to add historical epochs to recent LDS provided by Gaia RP/BP [Hudec & Hudec \(2011\)](#) [Hudec et al. \(2012\)](#). (Large) spectral variations with time (so far little exploited) can be studied this way effectively. Also, recent astrophysical tasks, e.g. searches for high z objects and optical counterparts of GRBs, represent an important application of these data [Hudec & Šimon \(2012\)](#) [Hudec & Hudec \(2013\)](#) [Hudec \(2018a\)](#) [Hudec \(2018b\)](#).

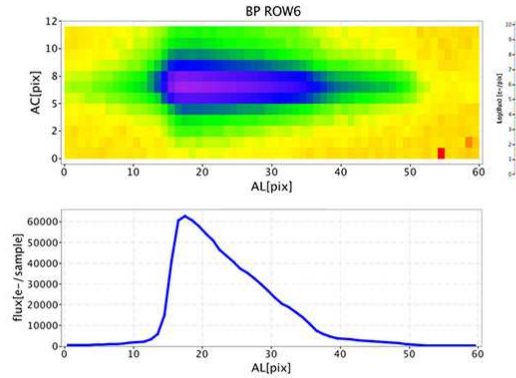


Figure 1. Examples of Gaia BP/RP LDS https://www.gaia.ac.uk/sites/default/files/media/images/bp_spec.jpeg.

2. Astrophysics with LDS in the past

The LDS (Low-Dispersion Spectroscopy) astrophysics was evolved and performed at numerous observatories (many in the US) between ~ 1909 and ~ 1980 (Figs. 4, 5). Mostly was LDS performed with Schmidt telescopes (photographic plates with an objective prism in front of the telescope). This approach was used for various projects e.g. QSO, emission line and H α surveys, star classifications, etc., but was little used after ~ 1980 . Today knowledge in the astronomical community is very limited.

The most important LDS Plate Surveys/Databases for providing historical epochs for Gaia BP, RP are as follows:

1. German La Paz Bolivia Expedition, 1926–1929: Southern Sky Coverage D
2. Hamburg Quasar Spectral Survey D

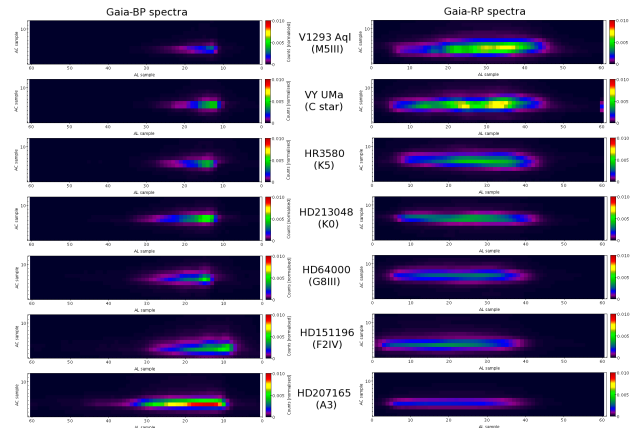


Figure 2. Examples of Gaia BP/RP LDS https://www.gaia.ac.uk/sites/default/files/media/images/bp_spec.jpeg.

3. Byurakan Spectral Survey D

4. Northern Halpha MtWilson-Michigan Sky Survey PD

5. Southern Halpha MtWilson-Michigan Sky Survey PD (Figs. 6, 7, 8). (here D = Digitised, PD=Partly Digitised)

The Digitized First Byurakan Survey (DFBS) is the digitized version of the First Byurakan Survey (FBS). It is the largest photographic LDS spectroscopic database in the world, providing low-dispersion spectra for 20,000,000 objects on 1139 FBS fields = 17,056 deg² with online access. Sky coverage: DEC \geq -15 deg, all RA (except the Milky Way). The survey is based on prisma spectral plates taken by by 1 m aperture Schmidt telescope. The limiting magnitude amounts to 17.5 in V, The spectral range is 340–690 nm, spectral resolution 5 nm, and dispersion: 180 nm/mm near H-gamma

The Hamburg survey is a wide-angle objective prism survey searching for quasars with B brighter than 17.5 on the northern sky. The survey plates have been taken with the former Hamburg Schmidt telescope, which is located at Calar Alto/Spain since 1980. For the survey, the 1.7-degree prism was used providing unwidened objective prism spectra with a dispersion of 139 nm/mm at Hgamma. Under conditions of good seeing the FWHM of the images is 30 m (plate resolution) giving a spectral resolution of 4.5 nm at Hgamma on the objective-prism plates. The survey has online access.

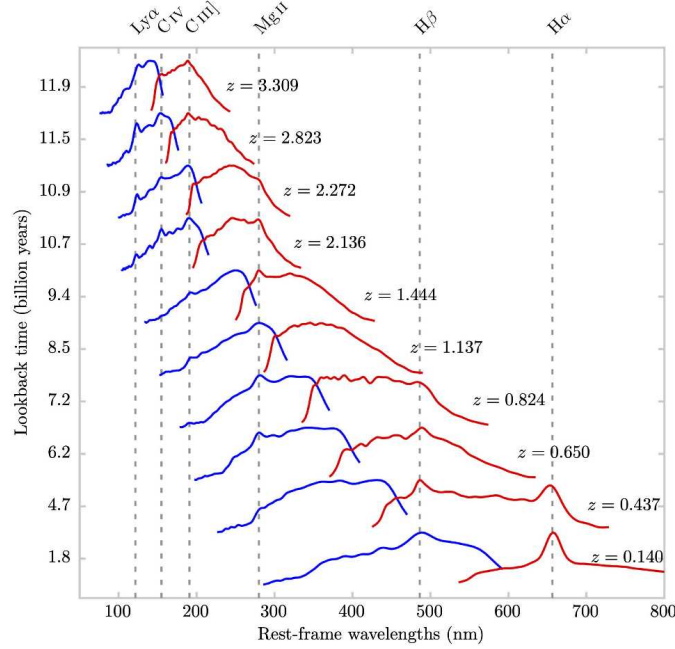


Figure 3. Gaia low-resolution BP and RP spectra (blue and red, respectively) of ten known quasars selected with apparent G magnitudes between 17 and 18. The QSO spectra are plotted in their rest-frame https://www.cosmos.esa.int/web/gaia/iow_20201222.

3. Astrophysics with Ultra LDS provided by Gaia RP/BP

The Gaia BP/RP LDS is able to provide (i) Continuum profiles, including high z objects (ii) Searches for objects with strong emission lines (iii) Searches for strong variable emission lines and (iv) Prominent spectral variability.

There is also the possibility of spectroscopic Gaia alerts and Follow-up by ground-based RTs with LDS. As already mentioned, the plate sky surveys can add long-term coverage and historical epochs to these analyses [Hudec & Hudec \(2013\)](#) [Hudec \(2019\)](#).

The Gaia BP/RP provides a unique chance to provide early or simultaneous LDS for GRBs (so far LDS mostly late), chance to recognize/classify OAs and OTs of GRBs using LDS and/or color information, chance to detect/study orphan OAs of GRBs, Study possible spectral time changes/evolution, and Chance of redshift estimation up to $z \sim 7$ and study of high z Universe (Figs. 9, 10).

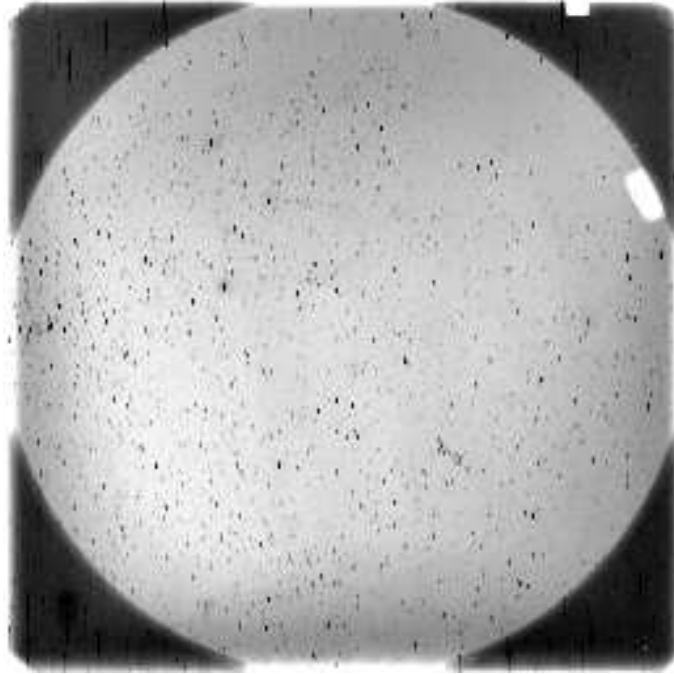


Figure 4. Example of digitized LDS photographic plate, PARI USA. Scan of a plate from the PARI Case Western Reserve Univ. collection. This plate (#10246) was taken on November 17, 1974 (dec= +23.5, RA= 4h50m) and is part of the Tau Cloud Survey. The exposure is 72min, Emulsion 103aE, Filter = OG2, 1.8 deg prisma.

4. Conclusion

With Gaia BP/RP, LDS spectral data are available for huge number of celestial sources, both galactic as well as extragalactic. Adding historical epochs to these data obtained from digitized LDS photographic surveys will allow large spectral variations over long time intervals (up to 100 years) to be studied. Both types of LDS can be also used for searches for highly redshifted objects up to $z \sim 7$.

Acknowledgements.

The research leading to these results has received funding from the European Unions Horizon 2020 Programme under the AHEAD2020 project (grant agreement n. 871158). Also, support by the project RVO:67985815 is acknowledged.

References

Carrasco, J. M., Weiler, M., Jordi, C., et al., Internal calibration of Gaia BP/RP



Figure 5. Early photographic LDS plate, Lick Observatory, USA, 1909.

low-resolution spectra. 2021, *Astronomy and Astrophysics*, **652**, A86, DOI: 10.1051/0004-6361/202141249

De Angeli, F., Weiler, M., Montegriffo, P., et al., Gaia Data Release 3. Processing and validation of BP/RP low-resolution spectral data. 2023, *Astronomy and Astrophysics*, **674**, A2, DOI: 10.1051/0004-6361/202243680

Hudec, R., Astrophysics with digitized astronomical plate archives. 2018a, *Astronomische Nachrichten*, **339**, 408, DOI: 10.1002/asna.201813515

Hudec, R., Low-dispersion spectroscopy with cubesats and photographic plates. 2018b, *Astronomische Nachrichten*, **339**, 416, DOI: 10.1002/asna.201813517

Hudec, R., Astronomical photographic data archives: Recent status. 2019, *Astronomische Nachrichten*, **340**, 690, DOI: 10.1002/asna.201913676

Hudec, R. & Hudec, L., Tests of simulated Gaia BP/RP spectra with LDS (Low Dispersion Spectroscopy) photographic sky surveys. 2011, in *Journal of Physics Conference Series*, Vol. **328**, *Journal of Physics Conference Series*, 012018

Hudec, R. & Hudec, L., Finding Hidden Treasures: Investigations in US Astronomical Plate Archives. 2013, *Acta Polytechnica*, **53**, 23

Hudec, R. & Šimon, V., ESA Gaia, ultra-low dispersion spectroscopy and GRBs. 2012, *Memorie della Societa Astronomica Italiana Supplementi*, **21**, 186



Figure 6. Southern Ha Mt Wilson Michigan Survey Plate extensively analyzed by K. Henize. 20 000 spectra were investigated by eye on every plate. 290 high-quality plates 15 x 15 inches were taken in 1950-1952 in South Africa by a dedicated telescope by Karl Henize (for his Dissertation). Taken by telescope D25 cm, 45 nm/mm at Halpha.



Figure 7. Example of prominent emission spectral features found by K. Henize in objective spectrum sky survey (Rate 1: 10 000), Michigan-Mt Wilson Southern Halpha Survey. There are hints that at least some of these strong emissions are variable. Taken by telescope D25 cm, 45 nm/mm at Halpha.



Figure 8. Example of prominent emission spectral features found by K. Henize in objective spectrum sky survey (Rate 1: 10 000), Michigan-Mt Wilson Southern Halpha Survey. There are hints that at least some of these strong emissions are variable. Taken by telescope D25 cm, 45 nm/mm at Halpha.

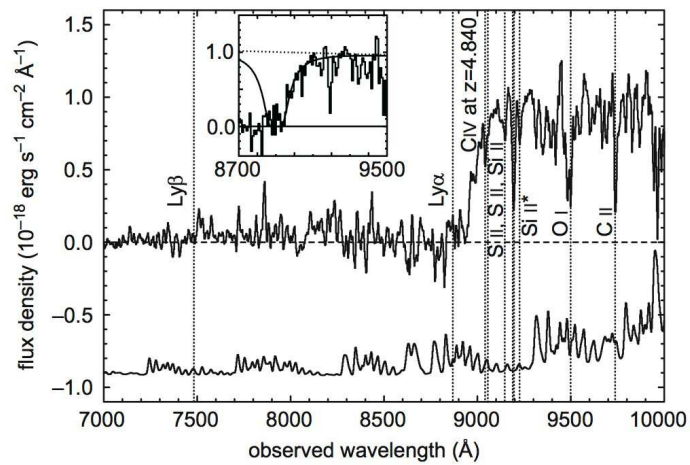


Figure 9. GRB 050904 at $z=6.29$. The target is visible only in very red. [Kawai et al. \(2005\)](#)

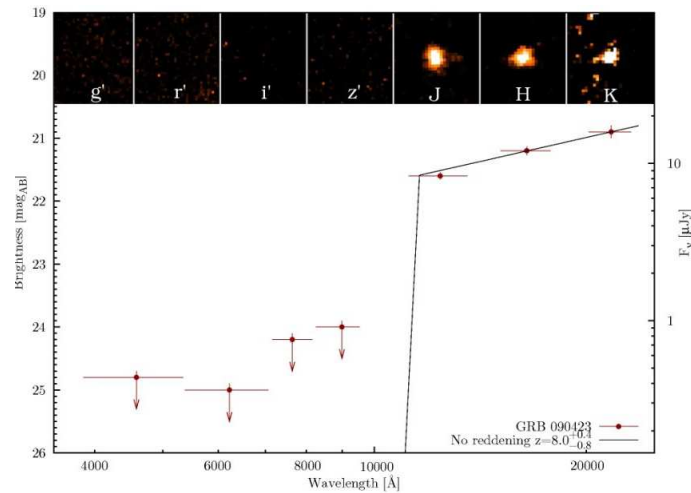


Figure 10. GRB 090423 at redshift 8, GROND observation (<https://www.mpe.mpg.de/jcg/GROND/grb090423.html>) Confirmation that even very low resolution spectrum can provide valuable results for GRBs science. Analogous results can be expected from Gaia BP/RP but the limit will be 1 micron (due to RP energy range) hence redshifts up to 7 are feasible.

Hudec, R., Šimon, V., Hudec, L., & Hudcová, V., ESA Gaia & the multifrequency behavior of high-energy sources with ultra-low dispersion spectroscopy. 2012, *Mem. Societa Astronomica Italiana*, **83**, 342

Kawai, N., Kosugi, G., Aoki, K., et al., Afterglow spectrum of a gamma-ray burst with the highest known redshift $z=6.295$. 2005, *arXiv e-prints*, astro, DOI: 10.48550/arXiv.astro-ph/0512052

Montegriffo, P., De Angeli, F., Andrae, R., et al., Gaia Data Release 3. External calibration of BP/RP low-resolution spectroscopic data. 2023, *Astronomy and Astrophysics*, **674**, A3, DOI: 10.1051/0004-6361/202243880

Witten, C. E. C., Aguado, D. S., Sanders, J. L., et al., Information content of BP/RP spectra in Gaia DR3. 2022, *Monthly Notices of the RAS*, **516**, 3254, DOI: 10.1093/mnras/stac2273

Zhang, X., Green, G. M., & Rix, H.-W., Parameters of 220 million stars from Gaia BP/RP spectra. 2023, *arXiv e-prints*, arXiv:2303.03420, DOI: 10.48550/arXiv.2303.03420

Investigating star formation in Illustris TNG galaxy mergers

B. Koncz¹, A.P. Joó¹ and S. Pintér²

¹ *Dept. of Astronomy, Eötvös Loránd University*

² *Dept. of Natural Science, University of Public Service, Hungary*

Received: June 30, 2023; Accepted: October 24, 2023

Abstract. Dwarf galaxies are the probable sources of the hot intra-cluster medium, a subject of a series of recent X-ray discoveries. Galaxy interaction trigger may lead to high star formation rates in these galaxies, that can lead to multiple core collapse supernovae and hot gas ejection. We studied the star formation rate history of merging galaxies in the IllustrisTNG 100-1, cosmological, magneto-hydrodynamic simulation focusing on mergers where one of the galaxies is a dwarf. We investigated the star formation rate and mass evolution of galaxies (progenitor), their dwarf merger companions (next progenitor) and their descendants at cosmological timescales with the use of the simulation's merger trees. We processed different merger trees testing the robustness of our method and found that the results are consistent. Our results show that properties of galaxies in the compared merger trees are identical, only small differences occur. We will present our methodology and the comparison of three different merger trees, including the mass and star formation rate history of the merging galaxies.

Key words: galaxies: evolution – galaxies: star formation – galaxies: interactions – methods: numerical

1. Introduction

One of the most accepted ideas about the Universe is that it is homogeneous and isotropic on a sufficiently large scale. But the question of the scale on which this can be stated arises more and more often (Paal et al., 1992; Balázs et al., 1999, 2015; Mészáros et al., 2000; Bagoly et al., 2003; Vavrek et al., 2008; Horváth et al., 2015; Horvath et al., 2020, 2022). IllustrisTNG (Nelson et al. (2017), Marinacci et al. (2018), Pillepich et al. (2017), Springel et al. (2017), Naiman et al. (2018)) is a suite of large volume, cosmological, gravo-magneto-hydrodynamic simulations including a comprehensive model for galaxy formation. Each TNG simulation self-consistently solves for the coupled evolution of dark matter, cosmic gas, luminous stars, and supermassive black holes from redshift $z = 127$ to 0 and generates 100 resulting snapshots from $z = 20$ to 0. We used the TNG100 run for analysis, the main high-resolution run including the full TNG physics model, which has the size of 110.73 Mpc^3 and contains more than 10 billion

resolution elements.

The recent X-ray discoveries show that dwarf galaxies are probable sources of the hot intra-cluster medium [Nath & Chiba \(1995\)](#). Galaxy interactions can trigger the star formation rate (SFR) in the merger companions [Shah et al. \(2022\)](#). These events can lead to energetic events like multiple core collapse supernovae. A series of proper observational census of star forming galaxies and their SFR led us to derive the star forming rate density (see eg. [Stickel et al. \(1998\)](#), [Tóth et al. \(2000\)](#), [Héraudeau et al. \(2004\)](#), [Madau & Dickinson \(2014\)](#)). Previous works investigating galaxy mergers SFR with IllustrisTNG: [Hani et al. \(2020\)](#) made a post-merger sample with about 28.000 galaxy between redshifts 0 and 1. They found no dependency on redshifts, but there is anti-correlation with stellar mass, and SFR is correlated with the gas fraction of the progenitors. Here we note that observational results on SFR should also consider geometrical effects, i.e. the attenuation of UV radiation depends also on the inclination of the disk of star forming galaxies (see eg. [Suleiman et al. \(2022\)](#)). [Patton et al. \(2020\)](#) analyzed the massive galaxies dependence on the closest companions, they found that the specific SFR is boosted by 14.5%. [Brown et al. \(2023\)](#) examined the sSFR at $z < 0.2$ as a function of the separation from the closest companion galaxy. They found that star forming galaxies show enhanced sSFR regardless of the companions' type and if there is a close passive companion, the main galaxy is likely to be a passive galaxy as well. Using the IllustrisTNG simulation other aspects of galaxy mergers were examined, e.g. supermassive black hole accretion rates in post-merger galaxies [Byrne-Mamahit et al. \(2022\)](#) and quenching in post-merger galaxies [Quai et al. \(2021\)](#).

Our goal is to estimate the differences of the galaxies average mass and SFR between the merger trees in the IllustrisTNG simulation compared to the predictions of observational uncertainties. [D'Silva et al. \(2023\)](#) used two galaxy formation simulations, Flares [Lovell et al. \(2021\)](#), [Vijayan et al. \(2021\)](#) and Shark [Lagos et al. \(2018\)](#) to explore how well the James Webb Space Telescope (JWST) [Gardner et al. \(2006\)](#) will be able to uncover the existence and parameters of galaxies at $5 < z < 10$. They found that the 1σ uncertainties by Flares are growing with z , by SFR from 0.71 to 0.98 by mass from 0.72 to 1.49 on logarithmic scale. With Shark these values are respectively between 0.32-1.03 and 0.4-1.38.

2. Method

We used the IllustrisTNG 100-1 merger tree, which is a data structure of the galaxies evolution. It uses the Sublink algorithm [Rodriguez-Gomez et al. \(2015\)](#) for the descendants search with the following steps: first the it identifies the candidates for every subhalo, it searches for galaxies in the following snapshot with common particles of the chosen galaxy. The second step is scoring of the candidates based on a merit function, which calculates the binding energy rank of each particle in the galaxies. The last step is the identification of the unique

descendant, which will be the subhalo with the highest score. To build up the merger tree, a linked-list structure was created by [Springel et al. \(2005\)](#), so that each subhalo is assigned pointers to 'key' subhalos. The 'descendant' is the unique descendant of the subhalo in question. The 'next progenitor' is the subhalo, which shares the same descendant as the subhalo in question, and which has the next largest 'mass history' behind the progenitor. In our case the progenitor galaxies are those subhalos for which the descendants and next progenitors were sorted out.

In general the progenitor galaxies are in the same snapshot, the descendants are in the following. But there are some cases, when the descendant galaxy is skipping a snapshot, or the next progenitor and the progenitor galaxies are in different snapshots. These connections between the galaxies build up the merger trees, which are completely independent from each other. Because of this independency we compared three merger trees to find out if there is any difference between them.

For analysing the data of the merger trees we downloaded the sublink tree files, which are in 20 independent files, and each of them contains about 25 million galaxies. We made a galaxy sample with star formation rates greater than 0 to reduce our sample only on those galaxies which are connected to the star formation. After making this sample we searched for the progenitor and next progenitor galaxies which have the same descendant. Since the next progenitor galaxies are less massive galaxies than the progenitors we can identify them as dwarf galaxies, in the next section at the investigation of their mass we can conclude that this assumption was correct. After that we sorted them for every redshift for $z < 15$. We didn't take into account the galaxies at higher redshift, because there were only a few of them. To avoid the problem with the snapshot skipping galaxies and those progenitors which are at different snapshots we made simplifications. Our goal is to examine the average values of large number of galaxies, therefore we simplified the galaxies snapshot numbers. We calculated the average values as if the two progenitors were in the same snapshot and their descendants in the following. We focused on two parameters of the galaxies: SFR and mass. We calculated the mean values for every snapshot ($z < 15$) for progenitors, next progenitors and descendants. We made this process for three different merger trees, the 0th, 5th and 6th, which we chose randomly from the 20 possible files.

3. Results

3.1. Mass

We first investigate the mass of the progenitor, next progenitor and descendant galaxies in a single merger tree. Fig.1 shows the average mass of the galaxies on logarithmic scale in $10^{10}M_{\odot}/h$ values, where h is the reduced hubble constant ($h = 0.6774$), at every redshift lower than 15. Each point represents the average values of the galaxies, 'X' shows the descendants, triangles the selected progenitors and squares the next progenitors. The mean mass of the descendant galaxies shows large increase especially at $z < 2$. The descendant galaxies mass are 2 order of magnitude higher at $z = 0$ than the progenitors. In general the average values of the next progenitor galaxies are lower than $10^9M_{\odot}/h$, which means that these are dwarf galaxies.

The merger tree in the IllustrisTNG 100-1 simulation contains 20 different merger trees, which are numbered from 0 to 19. We investigated three merger trees, Fig. 2 shows the comparison of these trees descendant galaxies average mass at different redshifts below 15. We examined the 0. marked with 'X', 5. 'square' and 6. 'triangle' merger tree. As the results are showing, there is no significant difference between the individual merger trees. Fig. 3 shows the logarithmic difference of the descendant galaxies average mass between the merger trees. The values are compared to the 5th merger tree's results therefore the 5th mergers values are equal to 0. There is only a slight difference (smaller than 0.1) between the trees at high redshifts $z > 2$. After $z = 2$ these differences are getting higher, especially as $z < 1$, where the 0th tree has values over 0.9 and the 6th tree about 0.6. This shows that at high redshifts the results are similar, but at $z < 2$ the dispersion is higher.

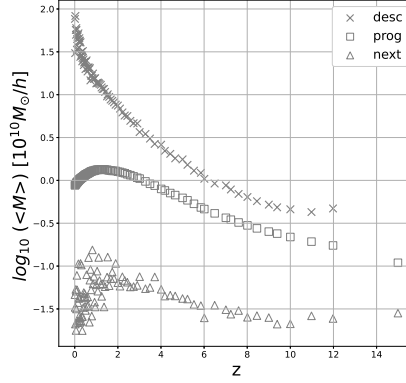


Figure 1. Merger galaxies mean mass ($\langle M \rangle$) versus redshift (z). Each dot shows the average mass versus redshift at a given Snapshot. We represented the selected progenitor galaxies with squares, next progenitors 'next' galaxies with triangles and the descendant 'desc' galaxies with 'X' markers. The progenitors and next progenitors average mass are 2-3 order of magnitude smaller than the Descendant galaxies average mass.

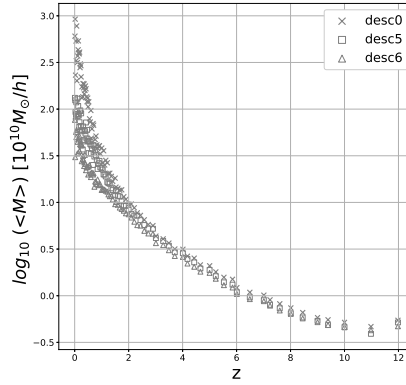


Figure 2. Comparing three merger trees descendant galaxies average mass. No significant difference can be seen between the individual merger trees, which are marked with 'X', triangle and square.

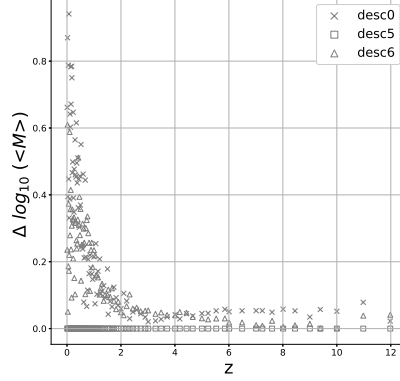


Figure 3. Logarithmic difference ($\Delta \log_{10}(\langle M \rangle)$) versus redshift (z) between the three merger trees descendant galaxies average mass. The individual trees are marked with 'X' (0th tree), square (5th tree) and triangle (6th tree). The differences are below 0.1 at $z > 2$, at lower redshifts the values are getting higher.

3.2. Star formation rate

After the masses we investigated the SFR values of the galaxies. Fig. 4 illustrates the average SFR of the galaxies in the 6. merger tree on logarithmic scale in M_{\odot}/yr values at every redshift lower than 15. Each point represents the average values of the galaxies, 'X' shows the descendants, triangles the selected progenitors and squares the next progenitors. A significant increase can be seen for every redshift between the progenitors and the descendants. Fig. 5 shows the comparing of the descendant galaxies SFR from the examined merger trees. The markers are similar to Fig. 2. The results from the trees are similar, Fig. 6 shows the logarithmic difference between them. Most of the values are below 0.4, only at $z < 1$ are some points with higher differences. Compared to the masses, the differences are in general higher ($z > 1$) and inconsistent, there is a peak at around $z = 6$ with $\Delta = 0.4$ but at $z = 2$ they are smaller than 0.2.

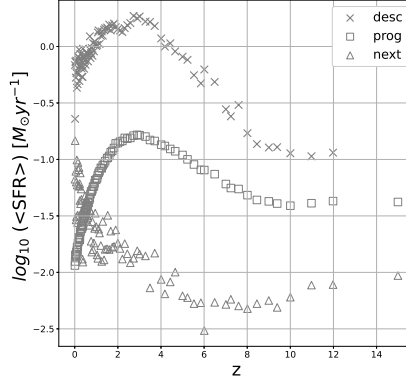


Figure 4. Merger galaxies average star formation rate ($\langle SFR \rangle$) on logarithmic scale versus redshift (z). Each point represents the average SFR of the galaxies at a given snapshot. 'X' shows the descendants, triangles the selected progenitors and squares the next progenitors. The descendant galaxies SFR is significantly higher for the whole timescale than the progenitor galaxies.

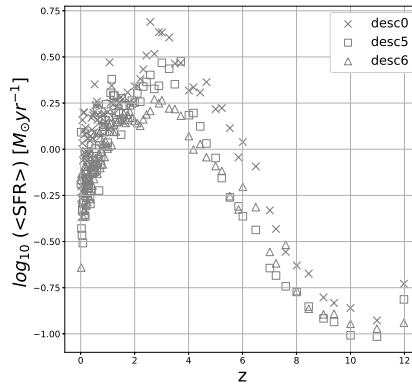


Figure 5. Comparing three merger trees descendant galaxies average SFR. No significant difference can be seen between the individual merger trees. Each mark represents the average SFR of the galaxies at a given snapshot. 'X', triangles and squares are showing an individual merger tree.

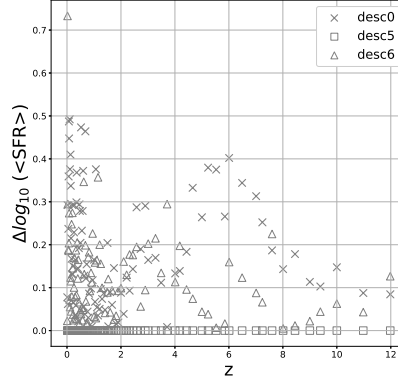


Figure 6. Logarithmic difference ($\Delta \log_{10}(\langle SFR \rangle)$) versus redshift (z) between the three merger trees descendant galaxies average SFR. The individual trees are marked with 'X' (0th tree), square (5th tree) and triangle (6th tree). Excluding one point the differences are lower than 0.5 order of magnitude at all redshifts.

4. Summary and Discussion

We investigated SFR and mass history of the merger galaxies in the IllustrisTNG simulation. We compared the average masses and star formation rates versus redshift in three individual merger tree in the simulation. We found that the descendant galaxies masses are similar at high redshifts: the logarithmic differences (Δ) are below 0.1 at $z > 2$, at lower redshifts $z < 2$ the values are getting higher $\Delta < 1$. The difference of the star formation rates are inconsistent with the redshifts. In general the values at higher redshifts are higher than by the masses (up to 0.4), but the difference at lower redshifts is smaller (up to 0.5). Compared to the simulated JWST observational data from $z = 5$ to $z = 10$, most of the uncertainties are higher than the differences between the merger trees, from which we can conclude that the individual merger trees are precise enough to examine the average properties of the galaxies at high redshifts.

To sum up, we found that there is no significant difference between the individual merger trees at higher redshifts, larger differences can occur at $z < 1$.

Acknowledgements.

We are grateful to L. Viktor Tóth for his supervision of this work and to the High Energy Astronomy Research Team (HEART - https://physics.elte.hu/KRFT_heart) for their support and thoughtful feedback.

The IBWS conference participation of B Koncz was subsidized by the Talent Support Council of ELTE Eötvös Loránd University, Budapest.

The authors thank the Hungarian TKP2021-NVA-16 and OTKA K-146092 program for their support.

References

- Bagoly, Z., Csabai, I., Mészáros, A., et al., Gamma photometric redshifts for long gamma-ray bursts. 2003, *Astronomy and Astrophysics*, **398**, 919, DOI: 10.1051/0004-6361:20021724
- Balázs, L. G., Bagoly, Z., Hakkila, J. E., et al., A giant ring-like structure at $0.78 < z < 0.86$ displayed by GRBs. 2015, *Monthly Notices of the RAS*, **452**, 2236, DOI: 10.1093/mnras/stv1421
- Balázs, L. G., Mészáros, A., Horváth, I., & Vavrek, R., An intrinsic anisotropy in the angular distribution of gamma-ray bursts. 1999, *Astronomy and Astrophysics, Supplement*, **138**, 417, DOI: 10.1051/aas:1999290
- Brown, W., Patton, D. R., Ellison, S. L., & Faria, L., Interacting galaxies in the IllustrisTNG simulations – V. Comparing the influence of star-forming versus passive companions. 2023, *Monthly Notices of the Royal Astronomical Society*, **522**, 5107, DOI: 10.1093/mnras/stad1314
- Byrne-Mamahit, S., Hani, M. H., Ellison, S. L., Quai, S., & Patton, D. R., Interacting galaxies in the IllustrisTNG simulations - IV: enhanced supermassive black hole accretion rates in post-merger galaxies. 2022, *Monthly Notices of the Royal Astronomical Society*, **519**, 4966, DOI: 10.1093/mnras/stac3674
- D’Silva, J. C. J., Lagos, C. D. P., Davies, L. J. M., Lovell, C. C., & Vijayan, A. P., Unveiling the main sequence of galaxies at $z \geq 5$ with the JWST: predictions from simulations. 2023, *Monthly Notices of the RAS*, **518**, 456, DOI: 10.1093/mnras/stac2878
- Gardner, J. P., Mather, J. C., Clampin, M., et al., The James Webb Space Telescope. 2006, *Space Science Reviews*, **123**, 485, DOI: 10.1007/s11214-006-8315-7
- Hani, M. H., Gosain, H., Ellison, S. L., Patton, D. R., & Torrey, P., Interacting galaxies in the IllustrisTNG simulations – II: star formation in the post-merger stage. 2020, *Monthly Notices of the Royal Astronomical Society*, **493**, 3716, DOI: 10.1093/mnras/staa459
- Héraudeau, P., Oliver, S., del Burgo, C., et al., The European Large Area ISO Survey - VIII. 90- μm final analysis and source counts. 2004, *Monthly Notices of the RAS*, **354**, 924, DOI: 10.1111/j.1365-2966.2004.08259.x
- Horváth, I., Bagoly, Z., Hakkila, J., & Tóth, L. V., New data support the existence of the Hercules-Corona Borealis Great Wall. 2015, *Astronomy and Astrophysics*, **584**, A48, DOI: 10.1051/0004-6361/201424829

- Horvath, I., Racz, I. I., Bagoly, Z., Balázs, L. G., & Pinter, S., Does the GRB Duration Depend on Redshift? 2022, *Universe*, **8**, 221, DOI: 10.3390/universe8040221
- Horvath, I., Szécsi, D., Hakkila, J., et al., The clustering of gamma-ray bursts in the Hercules-Corona Borealis Great Wall: the largest structure in the Universe? 2020, *Monthly Notices of the RAS*, **498**, 2544, DOI: 10.1093/mnras/staa2460
- Lagos, C. d. P., Tobar, R. J., Robotham, A. S. G., et al., Shark: introducing an open source, free, and flexible semi-analytic model of galaxy formation. 2018, *Monthly Notices of the RAS*, **481**, 3573, DOI: 10.1093/mnras/sty2440
- Lovell, C. C., Vijayan, A. P., Thomas, P. A., et al., First Light And Reionization Epoch Simulations (FLARES) - I. Environmental dependence of high-redshift galaxy evolution. 2021, *Monthly Notices of the RAS*, **500**, 2127, DOI: 10.1093/mnras/staa3360
- Madau, P. & Dickinson, M., Cosmic Star-Formation History. 2014, *Annual Review of Astron and Astrophys*, **52**, 415, DOI: 10.1146/annurev-astro-081811-125615
- Marinacci, F., Vogelsberger, M., Pakmor, R., et al., First results from the IllustrisTNG simulations: radio haloes and magnetic fields. 2018, *Monthly Notices of the Royal Astronomical Society*, DOI: 10.1093/mnras/sty2206
- Mészáros, A., Bagoly, Z., & Vavrek, R., On the existence of the intrinsic anisotropies in the angular distributions of gamma-ray bursts. 2000, *Astronomy and Astrophysics*, **354**, 1
- Naiman, J. P., Pillepich, A., Springel, V., et al., First results from the IllustrisTNG simulations: a tale of two elements – chemical evolution of magnesium and europium. 2018, *Monthly Notices of the Royal Astronomical Society*, **477**, 1206, DOI: 10.1093/mnras/sty618
- Nath, B. B. & Chiba, M., Dwarf Galaxies and the Origin of the Intracluster Medium. 1995, *Astrophysical Journal*, **454**, 604, DOI: 10.1086/176514
- Nelson, D., Pillepich, A., Springel, V., et al., First results from the IllustrisTNG simulations: the galaxy colour bimodality. 2017, *Monthly Notices of the Royal Astronomical Society*, **475**, 624, DOI: 10.1093/mnras/stx3040
- Paal, G., Horvath, I., & Lukacs, B., Inflation and compactification from galaxy redshifts? 1992, *Astrophysics and Space Science*, **191**, 107, DOI: 10.1007/BF00644200
- Patton, D. R., Wilson, K. D., Metrow, C. J., et al., Interacting galaxies in the IllustrisTNG simulations - I: Triggered star formation in a cosmological context. 2020, *Monthly Notices of the Royal Astronomical Society*, **494**, 4969, DOI: 10.1093/mnras/staa913
- Pillepich, A., Nelson, D., Hernquist, L., et al., First results from the IllustrisTNG simulations: the stellar mass content of groups and clusters of galaxies. 2017, *Monthly Notices of the Royal Astronomical Society*, **475**, 648, DOI: 10.1093/mnras/stx3112
- Quai, S., Hani, M. H., Ellison, S. L., Patton, D. R., & Woo, J., Interacting galaxies in the IllustrisTNG simulations – III. (The rarity of) quenching in post-merger galaxies. 2021, *Monthly Notices of the Royal Astronomical Society*, **504**, 1888, DOI: 10.1093/mnras/stab988

- Rodriguez-Gomez, V., Genel, S., Vogelsberger, M., et al., The merger rate of galaxies in the Illustris simulation: a comparison with observations and semi-empirical models. 2015, *Monthly Notices of the RAS*, **449**, 49, DOI: 10.1093/mnras/stv264
- Shah, E. A., Kartaltepe, J. S., Magagnoli, C. T., et al., Investigating the Effect of Galaxy Interactions on Star Formation at $0.5 < z < 3.0$. 2022, *The Astrophysical Journal*, **940**, 4, DOI: 10.3847/1538-4357/ac96eb
- Springel, V., Pakmor, R., Pillepich, A., et al., First results from the IllustrisTNG simulations: matter and galaxy clustering. 2017, *Monthly Notices of the Royal Astronomical Society*, **475**, 676, DOI: 10.1093/mnras/stx3304
- Springel, V., White, S. D. M., Jenkins, A., et al., Simulations of the formation, evolution and clustering of galaxies and quasars. 2005, *Nature*, **435**, 629, DOI: 10.1038/nature03597
- Stickel, M., Bogun, S., Lemke, D., et al., The ISOPHOT far-infrared serendipity north ecliptic pole minisurvey. 1998, *Astronomy and Astrophysics*, **336**, 116
- Suleiman, N., Noboriguchi, A., Toba, Y., et al., The statistical properties of 28 IR-bright dust-obscured galaxies and SED modelling using CIGALE. 2022, *Publications of the ASJ*, **74**, 1157, DOI: 10.1093/pasj/psac061
- Tóth, L. V., Hotzel, S., Krause, O., et al., ISOPHOT Serendipity Survey observations of interstellar clouds I. Detection of the Coldest Cores in Chamaeleon. 2000, *Astronomy and Astrophysics*, **364**, 769
- Vavrek, R., Balázs, L. G., Mészáros, A., Horváth, I., & Bagoly, Z., Testing the randomness in the sky-distribution of gamma-ray bursts. 2008, *Monthly Notices of the RAS*, **391**, 1741, DOI: 10.1111/j.1365-2966.2008.13635.x
- Vijayan, A. P., Lovell, C. C., Wilkins, S. M., et al., First Light And Reionization Epoch Simulations (FLARES) - II: The photometric properties of high-redshift galaxies. 2021, *Monthly Notices of the RAS*, **501**, 3289, DOI: 10.1093/mnras/staa3715

Investigating star formation in nearby interacting galaxies

A.P. Joó, B. Koncz and E. Pichler

Eötvös Loránd University, Hungary

Received: June 30, 2023; Accepted: October 10, 2023

Abstract. We are investigating how the interaction between galaxies in the local Universe triggers star formation, both globally and in different regions of the galaxies. We highlight two examples where one of the interacting galaxies is significantly smaller. We look at combined spectrographic and multi-wavelength photometric data to look for tracers of intense star formation and obtain metallicities. Comparing the calculated star formation surface densities and metallicities to isolated galaxies gives us a hint at how star formation and the composition of the interstellar material evolved through the interaction. Resolving the nearby galaxies shows how differently the two galaxies change due to the interaction, and at the same time, it makes it possible to identify local star-forming regions with different characteristics.

Key words: Galaxies: interactions – Galaxies: ISM – Galaxies: star formation

1. Introduction

Star formation plays a key role in the chemical evolution of galaxies, and through that, primarily influences the chemical composition of the Universe. High-mass star formation contributes to this process most significantly, as most of the chemical elements are only produced in supernovae (SN) explosions at the end of high-mass stars' evolution.

The environment suitable for high-mass star formation has to contain a high amount of cold interstellar material (ISM) in a compact region of space, in the form of a gravitationally bound giant molecular cloud (GMC) containing (mostly Hydrogen-) gas and dust with a mass of at least $10^4 M_{\text{Sun}}$. As a consequence, star formation and high-mass star formation, in particular, occurs in regions partly or fully obscured by dust, in some cases hiding the entire galaxy, see eg. the so-called dust-obscured galaxies (Suleiman et al., 2022).

Usually, only large spiral galaxies contain a large number of GMCs that can fuel a high rate of star formation or even a starburst episode in the galaxy. Merger events, however, provide a possibility for smaller galaxies to acquire enough material to be able to host high-mass star formation. In these cases, the material gain is usually localized in the interacting region between the galaxies, and limited to the time of the interaction. To study these cases, the observation

of nearby, resolved galaxy interactions is required. Nearby galaxies are also of great interest in multimessenger gravitational wave - gamma-ray burst (GW-GRB) detections which are also connected to high-mass star formation (see e.g. the first multimessenger GW-GRB detections [Abbott et al. \(2017\)](#), [Goldstein et al. \(2017\)](#), [Bagoly et al. \(2016\)](#), [Horváth et al. \(2018\)](#), [Tóth et al. \(2019\)](#)).

We investigated two nearby galaxy interactions: M51 and Arp 84 using archival and literature data. We focused on the star formation rate and the chemical composition of different regions of the galaxy pairs. A typical method to estimate the physical parameters of the star-forming cold ISM in galaxies up to large distances is observing CO lines (see eg. [Hatsukade et al. \(2019\)](#)). Star formation may also be traced by PAH emission (see eg. [Kovács et al. \(2019\)](#)). A linear relationship was found by eg. [Liu et al. \(2016\)](#) between star formation rate and dust continuum emission for both Galactic clumps and the high redshift ($z > 1$) star-forming galaxies, indicating a constant gas depletion time of 100 Myr for molecular gas. Therefore we used $H\alpha$ intensity maps and spectral data with star formation tracing line ratios as star formation rate indicators, CO line maps for mapping molecular clouds, and X-ray intensity maps as indicators for high-mass star formation.

The layout of this paper is as follows: in Section 2 and 3 we show our analysis of the two galaxy interactions, then we sum up our findings in Section 4.

2. M51

M51 (Fig. 1) is an interacting galaxy pair consisting of a larger spiral NGC 5194 (M51a) and a smaller, dusty spheroid NGC 5195 (M51b), in the constellation

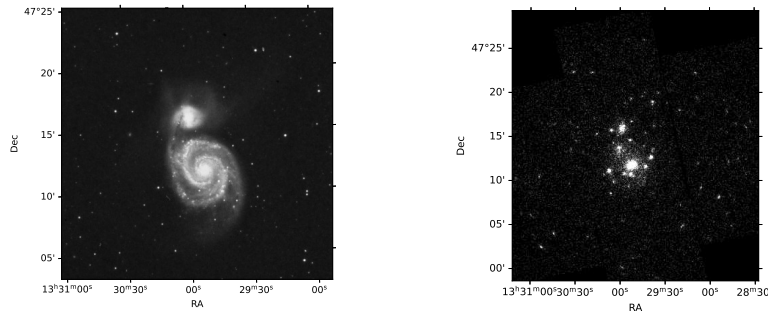


Figure 1. M51 Galaxy pair: NGC 5194 (M51a) spiral galaxy and its dusty spheroid companion NGC 5195 (M51b). **a)** Left: Palomar Observatory optical image, 48-inch Schmidt Telescope, 645 nanometer, **b)** Right: XMM Newton X-ray image, EPIC MOS camera, 0.15 - 15 keV

Canes Venatici, at a distance of 7.9 Mpc according to [Wei et al. \(2020\)](#).

Previous works report a roughly Solar metallicity for NGC 5194 ([Bresolin et al. 2004](#), [Walter et al. 2008](#)) with a relatively flat gradient ([Bresolin et al., 2004](#)). [Walter et al. \(2008\)](#) calculated a star formation rate of $6.05 M_{\text{Sun}}/\text{yr}$ for NGC 5194, and [Lee et al. \(2011\)](#) and [Lee et al. \(2012\)](#) found that the two galaxies have very different star formation rates. The larger spiral NGC 5194 is gas-rich, while its companion is gas-poor ([Watkins et al. 2015](#)).

We are interested in the distribution and chemical composition of the star-forming regions in M51. We are focusing on the interacting region between the two galaxies, in order to see how it affects star formation activity and chemical composition.

The spiral arm of NGC 5194 between the two galaxy centers seems to contain mostly sub-solar metallicity areas, some with high star-formation rate surface density ([Wei et al., 2020](#)). We analyzed the metallicity (Oxygen abundance) and the star formation rate surface density (Σ_{SFR}) of 113 regions observed by [Wei et al. \(2020\)](#), each with a diameter of about 75 pc. In particular, we were interested in finding correlations of the parameters, as well as any clustering of the data points.

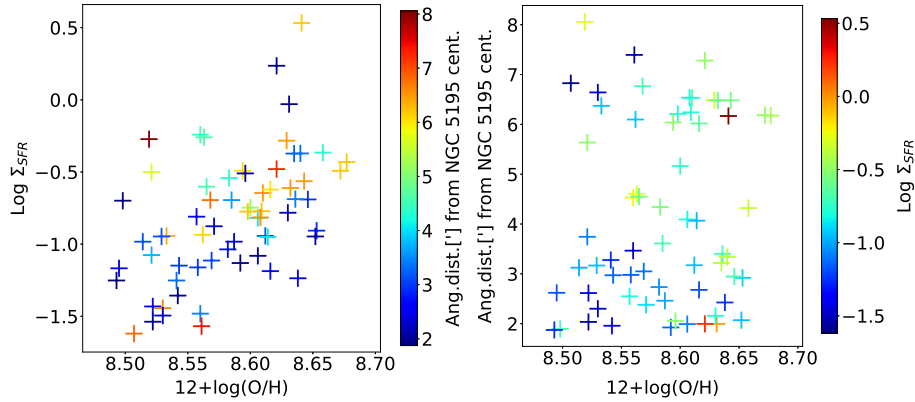


Figure 2. Properties of selected 75 pc diameter areas in M51 from [Wei et al. \(2020\)](#). **a)** Left: Σ_{SFR} with respect to metallicity. The color scale shows the distance from the center of NGC 5195. A linear correlation can be seen between star formation and metallicity with a coefficient of 0.51. **b)** Right: Angular distance with respect to metallicity. The color scale shows the Σ_{SFR} of the areas. A higher fraction of areas with lower star formation rates can be seen closer to the center of NGC 5195.

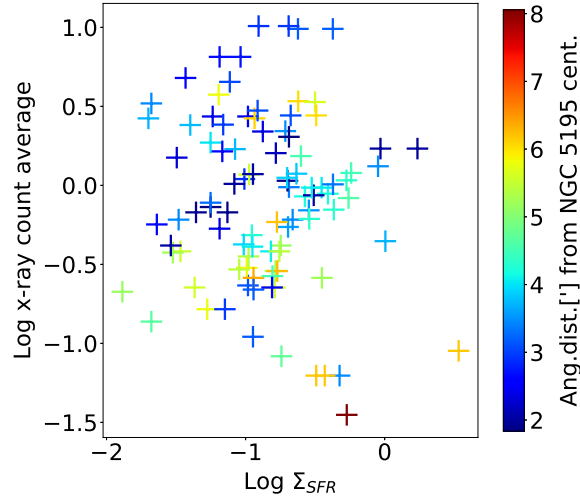


Figure 3. The average X-ray instrumental flux of 75 pc diameter areas in M51 with respect to the Σ_{SFR} . The color scale shows the angular distance from the center of NGC 5195. A slight correlation between the X-ray flux and the Σ_{SFR} can be seen with $PCC = 0.11$, and two groups are separatable by the distance from the center of NGC 5194.

Fig. 2a) shows the Σ_{SFR} with respect to the metallicity, with the color scale showing the distance from the center of NGC 5195, the smaller, spherical galaxy. We found a linear correlation between the metallicity and the Σ_{SFR} with Pearson correlation coefficient $PCC = 0.51$. The interacting region is between 2-3 arcminutes in distance, areas here show diversity, while areas further away tend to group around higher metallicities with a few exceptions.

Fig. 2b) displays the distance from the center of NGC 5195 with respect to the metallicity, with the colors showing Σ_{SFR} this time. The scarce region between 4 and 6 arcmin distance corresponds to the gap between the inner and outer arm of NGC 5194 in the south-eastern direction. We see a higher fraction of areas with lower star formation rates closer to the center of NGC 5195.

Both plots reinforce the basic concept of the larger spiral galaxy having higher star formation activity, which leads to higher metallicities, but at the same time, a notable amount of areas can be found in the interacting region with high star formation activity and corresponding high metallicities, the formation of which could most probably be attributed to the interaction between the two galaxies.

As there is an established connection between the star formation rate and the X-ray flux (for example Grimm et al. (2003), Mineo et al. (2012)), of which

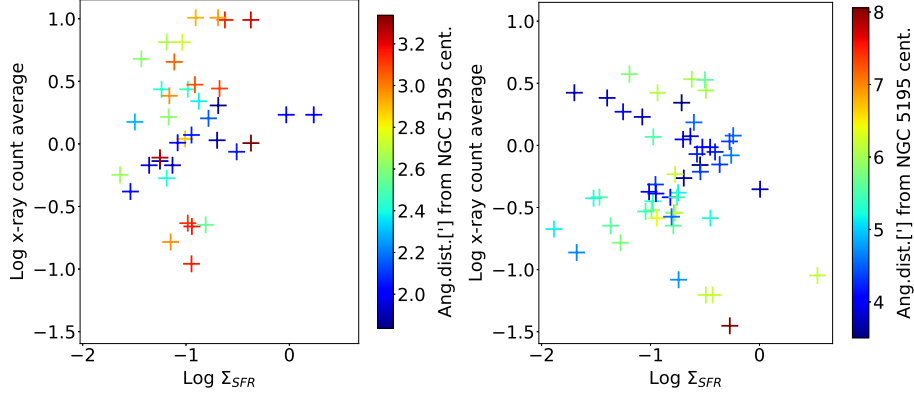


Figure 4. The average X-ray instrumental flux of 75 pc diameter areas in M51 with respect to the Σ_{SFR} . The color scale shows the angular distance from the center of NGC 5195. The two plots show two groups separated by the distance from the center of NGC 5195. Left: areas closer to the center of NGC 5195, mostly in the interacting region. Right: areas mostly outside the interacting region in NGC 5194. Please note, that the same color scale shows different values in the two plots. Areas in the interacting region have higher X-ray fluxes in general.

about 66% comes from X-ray binaries and the rest mostly from hot ISM (Mineo et al., 2013), we used the X-ray flux as a traces for high-mass star formation and looked at its the distribution in M51.

For calculating X-ray flux we used an XMM Newton X-ray image taken with the EPIC MOS camera in the energy range from 0.15 to 15 keV. We calculated average instrumental fluxes for the areas measured by Wei et al. (2020) with the background noise subtracted. We then compared the X-ray fluxes to the Σ_{SFR} and metallicity of the measured areas to see correlations.

You can see our comparison in Fig. 3. There is a slight overall correlation between the X-ray flux and the Σ_{SFR} with $PCC = 0.11$, and two groups can be separated by distance from the center of NGC 5195, which we show in Fig. 4.

The areas closer to the center of NGC 5195 (up to a distance of ≈ 3.5 arcminutes) are mostly in the interacting region, while the other areas are mostly outside of the interacting region in NGC 5194. The closer areas have higher X-ray flux on average, however, the dispersion is significant, which we attribute to the turbulent nature of the interaction. These findings support the hypothesis of the interacting region having a higher rate of high-mass star formation, which

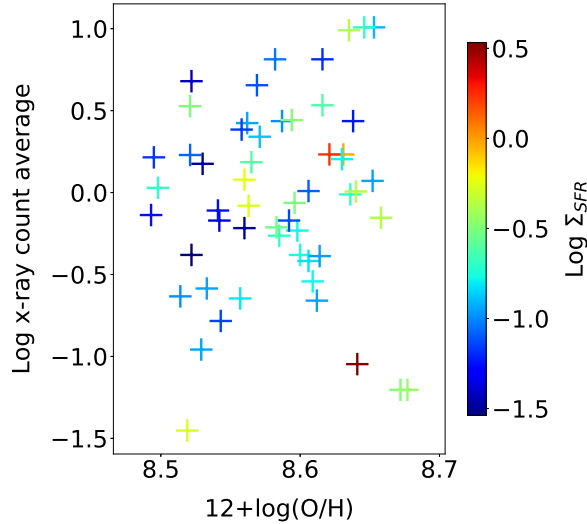


Figure 5. X-ray instrumental flux of 75 pc diameter areas in M51 with respect to the metallicity. The color scale shows the Σ_{SFR} . No correlation can be seen with $PCC = -0.07$.

could be the cause of the higher density and pressure of colliding interstellar material in this region.

We also looked at how the X-ray flux changes with respect to the metallicity, as seen in Fig. 5, which shows no correlation ($PCC = -0.07$).

3. Arp84

Arp 84 is a strongly interacting galaxy pair also in the constellation of Canis Venatici at a distance of 50 Mpc (Smith et al., 2007) consisting of a larger spiral NGC 5395 and a smaller spiral NGC 5394 (see Fig. 6).

Examining the CALIFA¹ spectroscopic data for NGC 5394, the smaller galaxy of the pair, Roche et al. (2015) calculated a star formation rate of $3.39 M_{Sun}/yr$, and an oxygen abundance $\log(O/H) + 12 \approx 8.6$ which corresponds to 0.76 Solar metallicity.

The Arp 84 galaxy pair is significantly less resolved than M51, but still suitable for the purpose of our analysis of the distribution of star-forming regions and their chemical composition.

¹Calar Alto Legacy Integral Field Area survey, optical integral-field spectroscopy (Sánchez, S. F. et al., 2012)

Roche et al. (2015) found that most of the star-forming activity is concentrated at the nucleus (75% in the central $r < 1$ kpc) which is most probably driven by AGN activity. Additional star-forming regions can be found in the interacting region, the SW part of the disk, and in two hot spots on the northern tidal arm. Furthermore, the outer tidal arms have a post-starburst spectrum, evidence of a more intensive star formation episode a few $\cdot 10^8$ years ago. The CALIFA data also show an annular region at radii 2.25 - 4 kpc from the nucleus, with elevated ratios of [NII], [OI]6300 to the Balmer lines - this is evidence of shock excitation, which might be the result of interaction-triggered gas inflow.

Kaufman et al. (1999) also notes that while NGC 5394's CO emission mostly comes from the central starburst region, it has a lopsided gas distribution in the disk with more CO, $H\alpha$, and HI emission from the western or southwestern side.

These findings support the presence of elevated star formation activity in the interacting region with a generally subsolar metallicity. In order to further test this, we analyzed Herschel PACS² 70-micron infrared data from the Herschel Science Archive.

We determined the positions of clumps on the Arp 84 70 micron infrared image (see Fig. 7) and calculated their distances from the center of NGC 5394, the smaller galaxy of the interacting pair. We then calculated the average intensities for the selected areas and subtracted the RMS noise measured on the image backgrounds. For the diameter of the areas, we used a diameter of 30 arcseconds, corresponding to ~ 7 kpc.

In the resulting Fig. 8, we see a strong correlation between the optical and the 70-micron instrumental flux with a coefficient of $PCC = 0.87$. The correlation is evident on the clumps with the closest (blue crosses) and farthest (red and

²Photodetector Array Camera and Spectrometer, one of the three science instruments on ESA's far infrared and submillimeter observatory. (Poglitsch, A. et al., 2010)

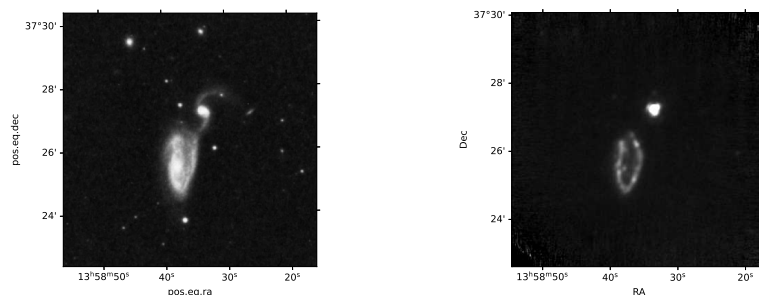


Figure 6. The Arp 84 interacting galaxy pair: NGC 5395 (the larger one) and NGC 5394. **a)** Left: Palomar Observatory optical image, 48-inch Schmidt Telescope, 645 nm. **b)** Right: Herschel PACS 70 micron image.

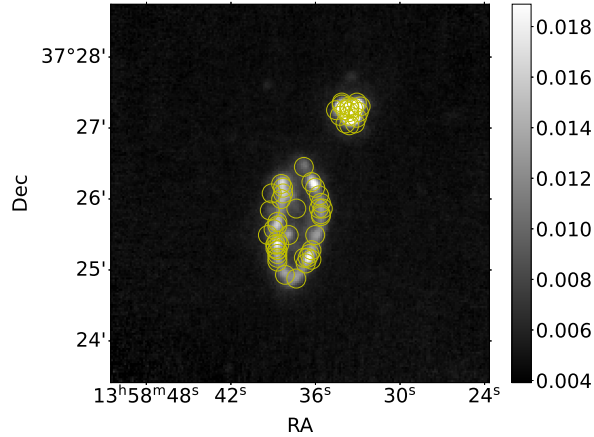


Figure 7. Selected areas of interest in Arp 84 on the Herschel PACS 70 micron image.

orange crosses) angular distance from the small galaxy’s center. A few areas, however, between the distance of about 1 - 2 arcminutes (cyan crosses) seem to deviate to some extent from the trend. From these, the most interesting are the ones at around 1 arcminute distance from the lower mass galaxy, NGC5394. Those areas correspond to the interacting region, and apparently bright both in optical and FIR, with higher relative 70 micron fluxes, which could be a sign of (partly dust obscured) elevated star formation activity.

4. Summary

We analyzed the distribution and chemical composition of star formation regions in the two interacting galaxy pairs M51 and Arp 84. We found higher star formation rates in the interacting galaxies compared to field galaxies and a sub-solar average metallicity in the smaller galaxies. Tracers of star formation show areas in the interacting regions with elevated star formation activity, in some cases even starburst events. These findings present examples of the possibility, that galaxies with lower general metallicity can have areas with high star formation rates or even starburst episodes in merger events, which induces high-mass star formation as well.

Acknowledgements.

We are grateful to L. Viktor Tóth for his supervision of this work and to the High Energy Astronomy Research Team (HEART - https://physics.elte.hu/KRFT_heart) for their support and thoughtful feedback. We thank the anonymous referee for the careful reading of our manuscript and the valuable comments and suggestions.

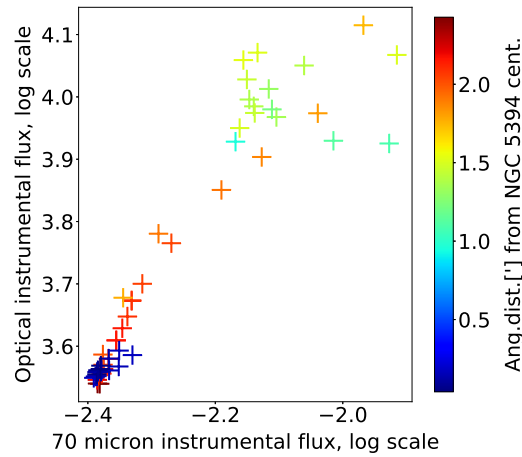


Figure 8. The average 70 micron instrumental flux of selected areas of interest in Arp 84 with respect to the average optical instrumental flux. The color scale shows the angular distance from the center of NGC 5394 (the smaller interacting galaxy). There is a strong correlation with a coefficient of $PCC = 0.87$.

The IBWS conference participation of B. Koncz was subsidized by the Talent Support Council of ELTE Eötvös Loránd University, Budapest. The authors thank for the Hungarian OTKA K-146092 grant.











References

- Abbott, B. P., Abbott, R., Abbott, T. D., et al., GW170814: A Three-Detector Observation of Gravitational Waves from a Binary Black Hole Coalescence. 2017, *Physical Review Letters*, **119**, 141101, DOI: 10.1103/PhysRevLett.119.141101
- Bagoly, Z., Szécsi, D., Balázs, L. G., et al., Searching for electromagnetic counterpart of LIGO gravitational waves in the Fermi GBM data with ADWO. 2016, *Astronomy and Astrophysics*, **593**, L10, DOI: 10.1051/0004-6361/201628569
- Bresolin, F., Garnett, D. R., & Robert C. Kennicutt, J., Abundances of Metal-rich H ii Regions in M51*. 2004, *Astronomical Journal*, **615**, 228, DOI: 10.1086/424377
- Goldstein, A., Veres, P., Burns, E., et al., An Ordinary Short Gamma-Ray Burst with Extraordinary Implications: Fermi-GBM Detection of GRB 170817A. 2017, *Astrophysical Journal, Letters*, **848**, L14, DOI: 10.3847/2041-8213/aa8f41
- Grimm, H.-J., Gilfanov, M., & Sunyaev, R., High-mass X-ray binaries as a star formation rate indicator in distant galaxies. 2003, *Monthly Notices of the RAS*, **339**, 793, DOI: 10.1046/j.1365-8711.2003.06224.x

- Hatsukade, B., Hashimoto, T., Kohno, K., et al., Molecular Gas Properties in the Host Galaxy of GRB 080207. 2019, *Astrophysical Journal*, **876**, 91, DOI: 10.3847/1538-4357/ab1649
- Horváth, I., Tóth, B. G., Hakkila, J., et al., Classifying GRB 170817A/GW170817 in a Fermi duration-hardness plane. 2018, *Astrophysics and Space Science*, **363**, 53, DOI: 10.1007/s10509-018-3274-5
- Kaufman, M., Brinks, E., Elmegreen, B. G., et al., The Interacting Galaxies NGC 5394/5395: A Post-Ocular Galaxy and Its Ring/Spiral Companion. 1999, *Astronomical Journal*, **118**, 1577, DOI: 10.1086/301030
- Kovács, T. O., Burgarella, D., Kaneda, H., et al., Star formation and polycyclic aromatic hydrocarbons in ELAIS N1 galaxies as seen by AKARI. 2019, *Publications of the ASJ*, **71**, 27, DOI: 10.1093/pasj/psy145
- Lee, J. H., Kim, S. C., Park, H. S., et al., HUBBLE SPACE TELESCOPE PIXEL ANALYSIS OF THE INTERACTING FACE-ON SPIRAL GALAXY NGC 5194 (M51A). 2011, *The Astrophysical Journal*, **740**, 42, DOI: 10.1088/0004-637X/740/1/42
- Lee, J. H., Kim, S. C., Ree, C. H., et al., HUBBLE SPACE TELESCOPE PIXEL ANALYSIS OF THE INTERACTING S0 GALAXY NGC 5195 (M51B). 2012, *The Astrophysical Journal*, **754**, 80, DOI: 10.1088/0004-637X/754/2/80
- Liu, T., Kim, K.-T., Yoo, H., et al., Star Formation Laws in Both Galactic Massive Clumps and External Galaxies: Extensive Study with Dust Continuum, HCN (4-3), and CS (7-6). 2016, *Astrophysical Journal*, **829**, 59, DOI: 10.3847/0004-637X/829/2/59
- Mineo, S., Gilfanov, M., Lehmer, B. D., Morrison, G. E., & Sunyaev, R., X-ray emission from star-forming galaxies – III. Calibration of the LX-SFR relation up to redshift $z \approx 1.3$. 2013, *Monthly Notices of the RAS*, **437**, 1698, DOI: 10.1093/mnras/stt1999
- Mineo, S., Gilfanov, M., & Sunyaev, R., X-ray emission from star-forming galaxies – I. High-mass X-ray binaries. 2012, *Monthly Notices of the RAS*, **419**, 2095, DOI: 10.1111/j.1365-2966.2011.19862.x
- Poglitsch, A., Waelkens, C., Geis, N., et al., The Photodetector Array Camera and Spectrometer (PACS) on the Herschel Space Observatory*. 2010, *A&A*, **518**, L2, DOI: 10.1051/0004-6361/201014535
- Roche, N., Humphrey, A., Gomes, J. M., et al., CALIFA spectroscopy of the interacting galaxy NGC 5394 (Arp 84): starbursts, enhanced [N ii] λ 6584 and signs of outflows and shocks. 2015, *Monthly Notices of the RAS*, **453**, 2349, DOI: 10.1093/mnras/stv1669
- Sánchez, S. F., Kennicutt, R. C., Gil de Paz, A., et al., CALIFA, the Calar Alto Legacy Integral Field Area survey - I. Survey presentation. 2012, *A&A*, **538**, A8, DOI: 10.1051/0004-6361/201117353
- Smith, B. J., Struck, C., Hancock, M., et al., The Spitzer Spirals, Bridges, and Tails Interacting Galaxy Survey: Interaction-Induced Star Formation in the Mid-Infrared. 2007, *Astronomical Journal*, **133**, 791, DOI: 10.1086/510350

- Suleiman, N., Noboriguchi, A., Toba, Y., et al., The statistical properties of 28 IR-bright dust-obscured galaxies and SED modelling using CIGALE. 2022, *Publications of the ASJ*, **74**, 1157, DOI: 10.1093/pasj/psac061
- Tóth, B. G., Rácz, I. I., & Horváth, I., Gaussian-mixture-model-based cluster analysis of gamma-ray bursts in the BATSE catalog. 2019, *Monthly Notices of the RAS*, **486**, 4823, DOI: 10.1093/mnras/stz1188
- Walter, F., Brinks, E., de Blok, W. J. G., et al., THINGS: The H I Nearby Galaxy Survey. 2008, *Astronomical Journal*, **136**, 2563, DOI: 10.1088/0004-6256/136/6/2563
- Watkins, A. E., Mihos, J. C., & Harding, P., Deep Imaging of M51: A New View of The Whirlpool's Extended Tidal Debris. 2015, *Astrophysical Journal, Letters*, **800**, L3, DOI: 10.1088/2041-8205/800/1/L3
- Wei, P., Zou, H., Kong, X., et al., Physical Properties of H ii Regions in M51 from Spectroscopic Observations. 2020, *Publications of the ASP*, **132**, 094101, DOI: 10.1088/1538-3873/ab9d92

Timing of accreting neutron stars with future X-ray instruments: towards new constraints on dense matter equation of state

V. Karas¹, K. Klimovičová², D. Lančová², M. Štolc^{1,3},
J. Svoboda¹, G. Török², M. Matuszková², E. Šrámková²,
R. Šprňa² and M. Urbanec²

¹ *Astronomical Institute of the Czech Academy of Sciences, Boční II 1401, CZ-14100 Prague, Czech Republic (E-mail: vladimir.karas@asu.cas.cz)*

² *Research Centre for Computational Physics and Data Processing, Institute of Physics, Silesian University in Opava, Bezručovo nám. 13, CZ-74601 Opava, Czech Republic*

³ *Faculty of Mathematics and Physics, Charles University, V Holešovičkách 2, CZ-18000 Prague, Czech Republic*

Received: July 18, 2023; Accepted: September 28, 2023

Abstract. The Enhanced X-ray Timing and Polarimetry (eXTP) mission is a space mission to be launched in the late 2020s that is currently in development led by China in international collaboration with European partners. Here we provide a progress report on the Czech contribution to the eXTP science. We report on our simulation results performed in Opava (Institute of Physics of the Silesian University in Opava) and Prague (Astronomical Institute of the Czech Academy of Sciences), where the advanced timing capabilities of the satellite have been assessed for bright X-ray binaries that contain an accreting neutron star (NS) and exhibit the quasi-periodic oscillations. Both stellar-mass, supermassive, and tentative intermediate-mass black holes can be included in the program portfolio.

Measurements of X-ray variability originating in oscillations of fluid in the innermost parts of the accretion region determined by general relativity, such as the radial or Lense-Thirring precession, can serve for sensitive tests enabling us to distinguish between the signatures of different viable dense matter equations of state. We have developed formulae describing non-geodesic oscillations of accreted fluid and their simplified practical forms that allow for an expeditious application of the universal relations determining the NS properties. These relations, along with our software tools for studying the propagation of light in strong gravity and neutron star models, can be used for precise modeling of the X-ray variability while focusing on properties of the intended Large Area Detector (LAD).

We update the status of our program and set up an electronic repository that will provide simulation results and gradual updates as the mission specifications progress toward their final formulation.

Key words: stars: black holes – stars: neutron – X-rays: binaries – polarimetry

1. Introduction

The Enhanced X-ray Timing and Polarimetry (eXTP) project is an international project led by China with European contribution (Zhang et al., 2019). eXTP will be a science mission designed to study the state of matter under extreme conditions of density, gravity, and magnetism (in't Zand et al., 2019; Watts et al., 2019; Santangelo et al., 2019). It aims to address three scientific questions in fundamental physics.

Among the primary goals are the long-standing problems of determining the Equation of State (EoS) of matter at supra-nuclear density, the study of accretion in the strong-field regime of gravity, and the measurement of quantum-electrodynamic (QED) effects in highly magnetized stars (Baym et al., 1971; Uzdensky et al., 2019). Primary targets include compact objects: isolated NS as well as those in binary systems, cosmic objects with strong magnetic fields such as magnetars, and stellar-mass, supermassive and tentative intermediate-mass black holes (De Rosa et al., 2019). eXTP will provide a significant enhancement of sensitivity and scheduling flexibility of the parametric measurements, which will build on the exciting results of the currently active IXPE (Weisskopf et al., 2023; Soffitta et al., 2021). Indeed, the magnetic intensity in these objects can reach almost a billion times higher magnitude than what is achievable on Earth.

Almost exactly a decade ago at this conference (10th INTEGRAL/BART Workshop in Karlovy Vary, 22-25 April 2013), we explored the appearance of X-ray signal generated by hot spots moving along quasi-elliptic trajectories close to the innermost stable circular orbit in the Schwarzschild spacetime. The aim of our investigation was to reveal whether the observable characteristics of the Fourier power-spectral density can distinguish between the competing models (Karas et al., 2014). In the present contribution, we elaborate on the approach of X-ray lightcurve timing analysis to constrain the NS EoS. In particular, we are interested in the prospects of the upcoming space-borne technology that has been meanwhile developed.

eXTP is an enhanced proposal based on its predecessor, the XTP mission concept, that has been selected and funded as one of the so-called background missions in the Strategic Priority Space Science Program of the Chinese Academy of Sciences since 2011. The strong European participation has significantly enhanced the scientific capabilities of eXTP (Feroce et al., 2022). Likewise, the Italy-led development of the Large Area Detector is based on the prior LOFT proposal for a mission of the European Space Agency (Feroce et al., 2012,

2016; Costa et al., 2001). In January 2017, the Chinese National Space Agency accepted the eXTP mission as a flagship space science mission, initiated and led by China in an international collaboration (Zhang et al., 2016). The planned launch date of the mission is in the late 2020s. The science observations are planned for at least eight years with the possibility of further extensions.

The mission carries a unique and unprecedented suite of state-of-the-art scientific instruments enabling for the first time ever the simultaneous spectral-timing-polarimetry studies of cosmic sources in the energy range from 0.5–30 keV (and beyond).

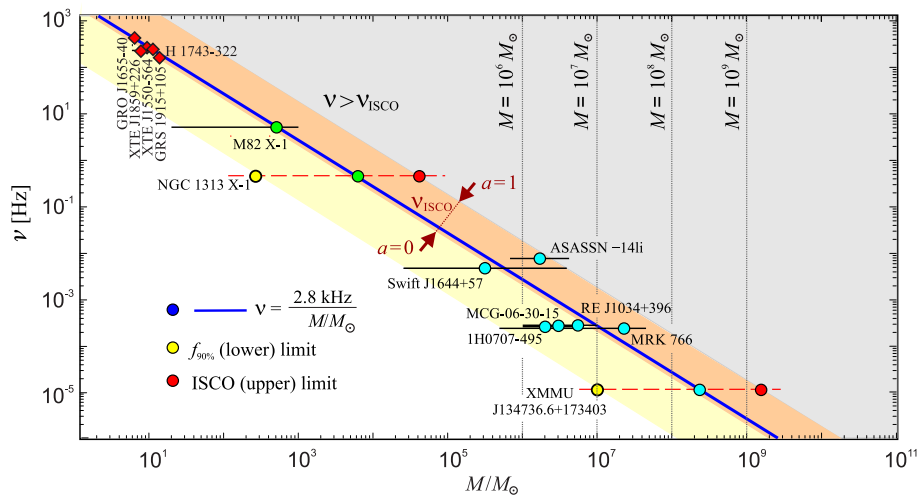


Figure 1. Quasi-Periodic Oscillations from accreting black holes across a wide range of mass. Enhanced sensitivity and a multitude of instruments will make eXTP an ideal mission to explore accretion flow oscillations from a variety of black holes over the range of mass. Whereas the upper left section of the plot corresponds to stellar-mass black holes in microquasars observed in the Milky Way, the lower right section is populated by supermassive black holes in cores of active galaxies. The orange stripe indicates the uncertainty range corresponding to the spin parameter in the range from a non-rotating black hole ($a = 0$) up to maximum rotation ($a = 1$). The yellow stripe gives the uncertainty corresponding to the luminosity distribution from the inner part of the standard (Keplerian) accretion disk, where more than 90% of the entire disk luminosity is produced.

In a brief contribution, we discuss promising scenarios regarding the detection and analysis of quasi-periodic phenomena in the context of eXTP, where its large collection area in the most relevant keV range and advanced timing capabilities offer a leap in our understanding of the puzzling sources. Our re-

search collaboration at the Astronomical Institute of the Czech Academy of Sciences in Prague and the Institute of Physics of the Silesian University in Opava takes part in the work on data simulations and detector performances related to study of accreting NS and the electromagnetic signatures of the internal structure via high-frequency quasi-periodic oscillations (HF QPOs) (e.g. Karas, 1999; Bakala et al., 2014; Karas et al., 2014; Šrámková et al., 2015; Török et al., 2019; Kotrlová et al., 2020; Török et al., 2022, and further references cited therein). An updated overview has been given in a recent Thesis (Lančová, 2023).

2. Rapid variability of accreting black holes and neutron stars

Accreting black holes (both stellar mass and supermassive) and NSs exhibit extraordinarily complex phenomenology of X-ray variability patterns on various timescales, including the shortest ones of millisecond periods (van der Klis, 1998; McClintock & Remillard, 2006; Motta, 2016, and more references cited therein). Here we focus on the widely discussed twin kHz peaks that have been detected in the Fourier power spectra of a few dozen of X-ray binaries, and also in several AGN and the Galactic centre supermassive black hole Sgr A* with correspondingly down-scaled frequency (Abramowicz et al., 2003; Bursa et al., 2004; Török, 2005; Goluchová et al., 2019). The position of the two peaks, and of the third (burst oscillation) one, as well as their significant coherence, limit the variety of potential models of the geometry of the system. Figure 1 shows the scaling relation of selected HF QPO sources in the QPO frequency vs. black hole mass diagram; see also a detailed caption in recent updates and analyses in Šrámková et al. (2021, 2023). The figure has been amended from the original work of Goluchová et al. (2019) by revising data points for several objects and including additional sources (XTE J1859+226, H 1743-322, ASASSN-14li).¹

Very recently, a novel phenomenon of quasi-periodic eruptions (QPE) and outflows (QPOouts) has been diagnosed in a growing number of nuclei of external galaxies (Pasham et al., 2019); the latter events have been tentatively associated with Tidal Disruption Events (TDE) (Gezari, 2021). The effects of general relativity cannot be ignored in modeling systems where the signal is emerging from the immediate vicinity of the inner accretion region near a compact body (Stella & Vietri, 1999; Stella et al., 1999; Ingram & Motta, 2019). It has been argued that the oscillation frequencies can be employed to constrain the viable EoS of the NS matter (Lattimer & Prakash, 2007) and to test the

¹References to individual sources: Greene et al. (2001); Strohmayer (2001); Orosz et al. (2002); Remillard et al. (2002); Greiner et al. (2001); Remillard et al. (2004); Pasham et al. (2014, 2015); Miller & Gültekin (2011); Reis et al. (2012); Czerny et al. (2016); Gierliński et al. (2008); Bentz et al. (2016); Gupta et al. (2018); Hu et al. (2016); Bian & Zhao (2003); Pan et al. (2016); Turner et al. (2006); Zhang et al. (2017); Carpano & Jin (2018); Yanes-Rizo et al. (2022); Motta et al. (2022); Wevers et al. (2017); Pasham et al. (2019); Molla et al. (2017); Zhou et al. (2015).

TDE mechanism and even the validity of the no-hair theorem in the case of black holes space-times.

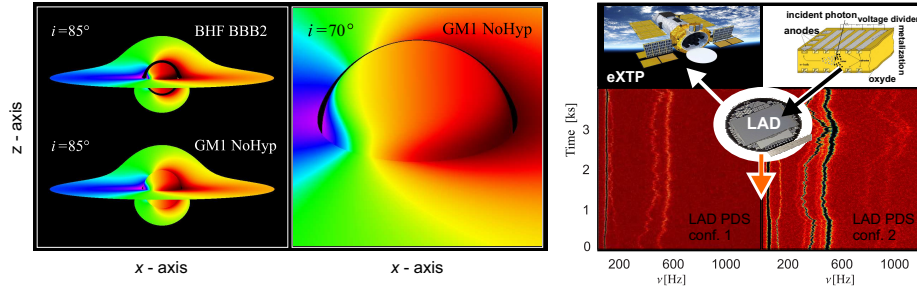


Figure 2. Left: Images illustrating Doppler shifts effects for Keplerian disks around a rotating NS calculated assuming the same NS mass and spin frequency but two different EoS. An emphasized view shows the spreading layer where matter from the disks enters the rotating NS surface. Illustration based on the work of Šprňa et al. (in preparation). Right: The LAD detector on board of the eXTP satellite (isdc.unige.ch/extp) and examples of simulated time evolution of the X-ray variability of NS accretion disk as predicted for the LAD detector (Bakala et al., 2014; Zhang et al., 2016; De Rosa et al., 2019; Feroci et al., 2022).

Here, we concentrate on predictions regarding suitable targets with respect to the low-mass X-ray binaries (LMXBs; Török et al., 2016), and we extend the range over the entire mass scale up to supermassive black holes. In the stellar close-binary systems, the mass is transferred from the companion star by overflowing the Roche lobe and forming an accretion disk or a torus that surrounds the NS. The accretion flow forms the main component that contributes to the high X-ray luminosity of these objects; most of the radiation arises from its inner region and the boundary layer adjacent to the surface. Oscillation properties of the flow should thus reflect the presence of the central body and they could help us to constrain its internal EoS. Particular attention has been attracted to the kilohertz QPOs. In the case of LMXBs, these oscillations occur in the range of 100–1000 Hz; their intrinsic frequencies are thus comparable to the orbital timescale near the surface of the NS. This coincidence suggests that the emerging signal originates in the innermost region of the accretion flow close to the NS surface. As their name suggests, twin kHz QPOs are frequently observed in pairs; correlations between the two peaks can be used to test the viability of different models.

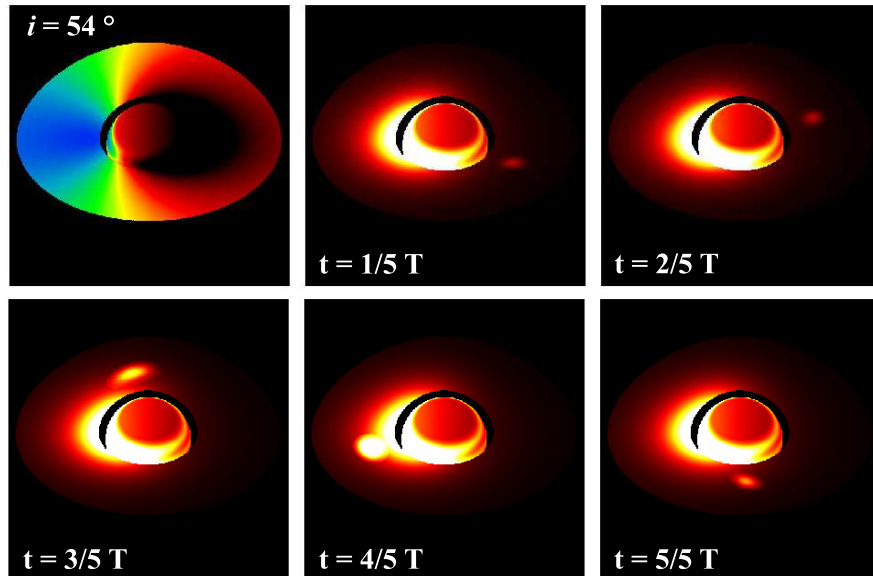


Figure 3. The technique of image mapping shows the Doppler shift effects, here in the case of a Keplerian disk containing an orbiting hot spot (blue-green-red color scale). Consecutive snapshots display the corresponding bolometric intensity of the observed radiation in different parts of the orbital period (red-to-yellow color scale).

3. Results

We have developed a set of flexible simulation tools that are aimed at exploring suitable observational strategies and identifying the characteristics of promising targets for upcoming space programs. The focus has been set on recurrent quasi-periodic events. These allow for an expeditious application of various physical processes and searching for their observable signatures using the LAD detector; see Figure 2 for an illustration of various aspects of the adopted methodology. Efficient ray-tracing computations with all General Relativity effects taken into account are essential to account for the flux variations as well as spectral, timing, and temporal characteristics (Karas et al., 1992; Dovčiak et al., 2004; Bakala et al., 2005; Dovčiak et al., 2008; Bakala et al., 2014, 2015; Karas et al., 2014). Hereafter, we show the setup and the main parameters that govern our simulations.²

²Our simulation results are available together with a more detailed description in an electronic form at astrocomp.physics.cz/simulator/. Access to the data is open to all researchers; we ask for this article to be acknowledged if the data are used in any follow-up publications.

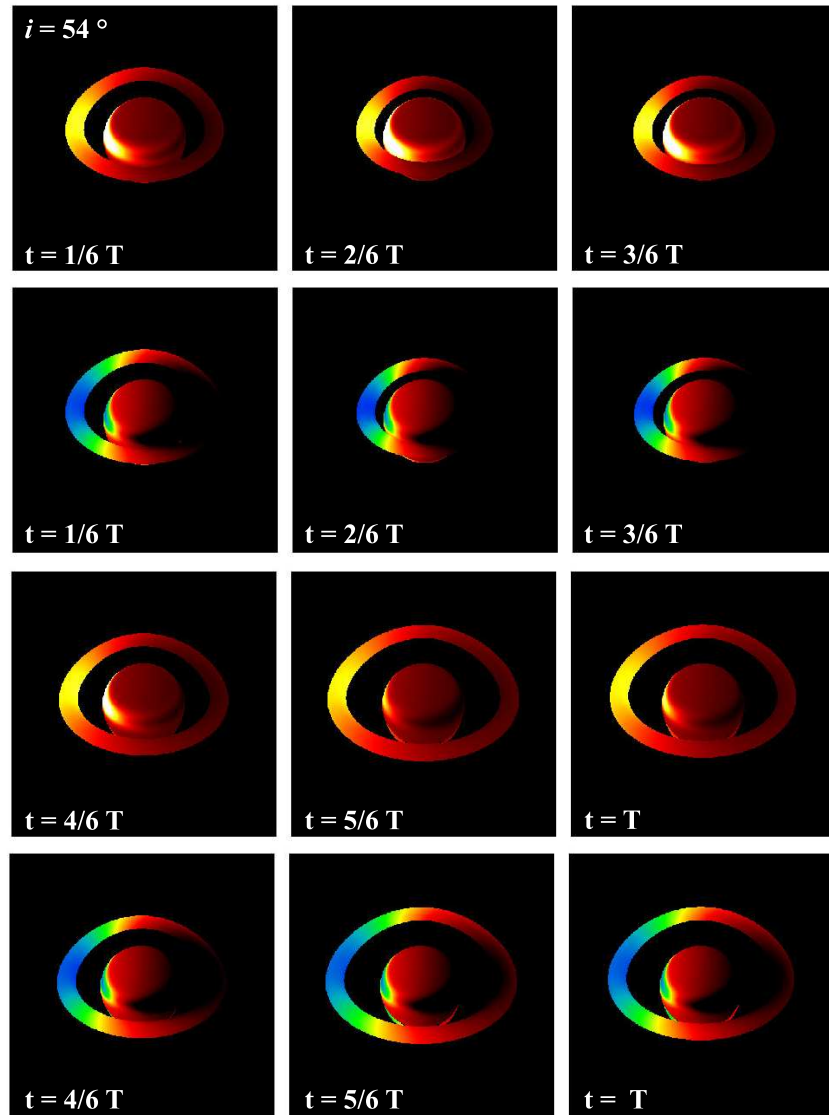


Figure 4. In analogy with the preceding figure, we show snapshots that map the Doppler energy shift effects for axisymmetric radial oscillations of an inner accretion torus (blue-green-red color scale) and the corresponding snapshots displaying the bolometric intensity of the observed radiation in different parts of the disk oscillation period (red-to-yellow color scale).

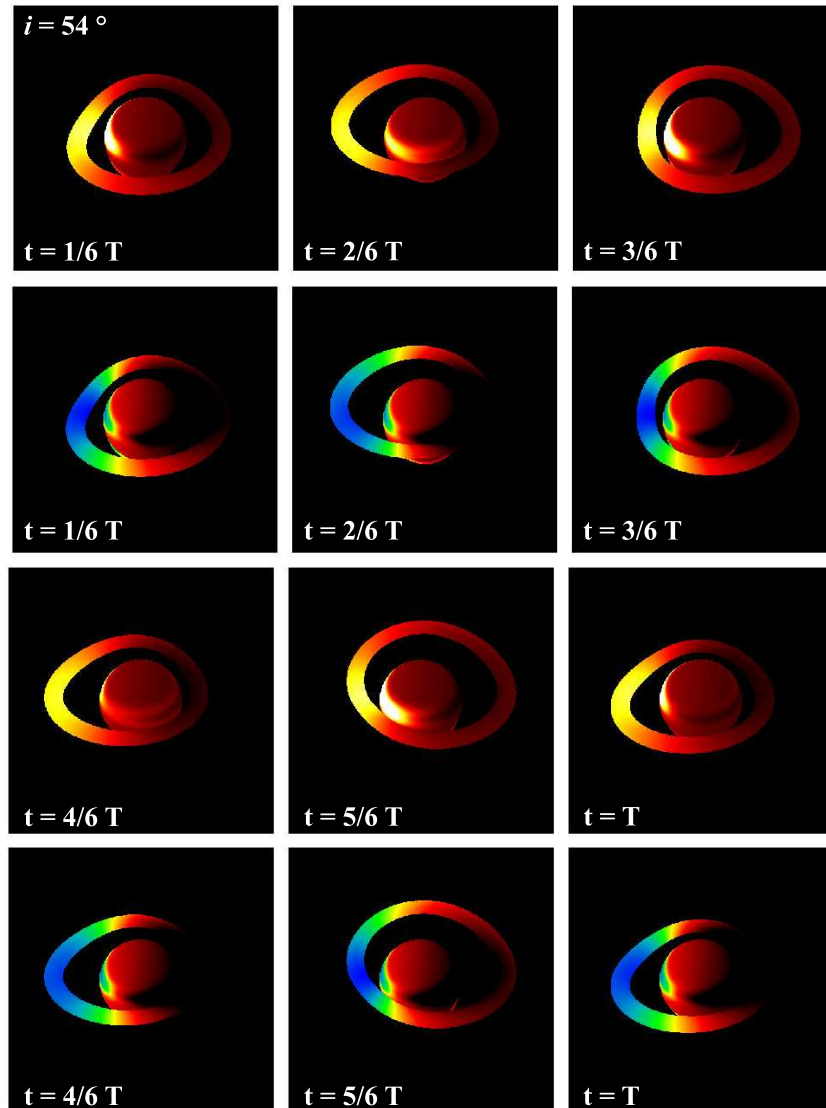


Figure 5. A sequence of snapshots mapping Doppler shift effects in the case of the radial precession (non-axisymmetric oscillations) of an inner accretion torus (blue–green–red scale) and the corresponding snapshots showing the bolometric intensity of the observed radiation in different parts of the disk oscillation period (red-to-yellow scale).

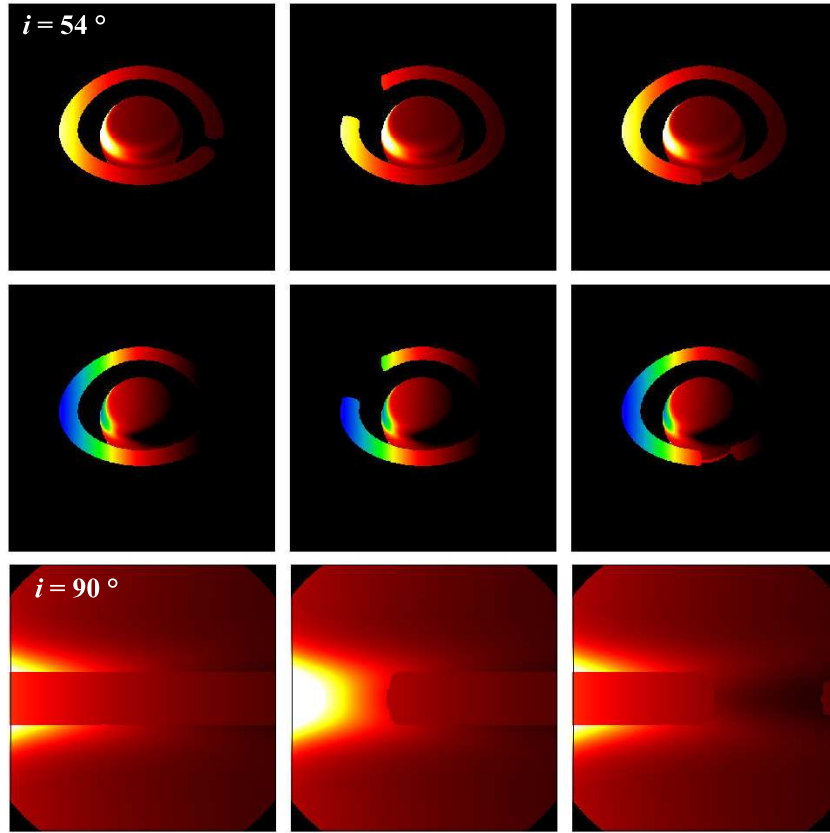


Figure 6. The snapshots displaying the bolometric intensity of the observed radiation in three different parts of the Keplerian period of a rotating product of torus instability (red-to-yellow color scale) along with the corresponding snapshots mapping the Doppler energy shift effects. The bottom row contains three images calculated for a near-equatorial view and very closely following parts of the Keplerian period, illustrating the strong variability of such a configuration. General Relativity effects are all taken into account in the ray-tracing computations.

3.1. Frequencies of QPOs: model predictions

Comparison between the observed and expected QPO frequencies can help reveal the NS mass and angular momentum (Urbanec et al., 2010; Török et al., 2022). To this end, sufficient sensitivity in the kiloelectronvolt band, as well as fine temporal and spectral resolution, are required. In Török et al. (2012, 2016), we studied within the framework of general relativity the mass–angular-momentum relations implied by a number of QPO models.

In the above-quoted papers, we showed that the degeneracy between the mass and angular momentum constraints can be removed when the NS spin frequency is determined in an independent way. Furthermore, in [Török et al. \(2016, 2022\)](#), we extended our results to a large set of EoS and explored effects related to the NS quadrupole moment and its rotationally induced oblateness. Remarkably, we found that strong restrictions to the QPO model and the implied NS mass could be obtained when the low-frequency QPOs or X-ray burst measurements were taken into account.

3.2. Examining full synthetic data, and beyond

While calculations of the QPO frequencies enable comparisons between the observed and synthetic data offering fruitful outputs, a complete comparison of lightcurves that would include consideration of the QPO amplitudes, coherence times, and spectral properties is even more promising.

In the present contribution, we reported on an extended set of model simulations, where we take into account the expected specifications of eXTP detectors, namely, their collecting area and energy and timing resolution.

The current work highly benefits from using our software package, which is based on the consideration of NS models on the background of the Hartle-Thorne geometry ([HTstar](#), [Urbanec et al., 2013](#); [Urbancová et al., 2019](#)) along with the key outputs of the LSD code core ([Lensing Simulation Device](#), [Bakala et al., 2007, 2014, 2015](#)). Within the context of the QPO models, we assume various configurations of oscillating radiating accreted fluid (disks, tori, spots, spiral waves, etc.) along with a rotating NS that exhibits a hot spreading layer of enhanced X-ray emission. Example images of such configurations are given in [Figures 3–6](#).

4. Conclusions

The enhanced X-ray Timing and Polarimetry (eXTP) mission has been developed by a consortium led by the Institute of High-Energy Physics of the Chinese Academy of Sciences and is envisaged to launch in the later-2020s. It is currently considered to be a priority of the upcoming astrophysics program. The Czech contribution is a part of the consortium of several European groups led by the Italian INAF (Istituto Nazionale di Astrofisica). eXTP will carry four instrument packages for the X-ray 0.5–50 keV bandpass, with the primary purpose to explore matter under extreme density, strong-gravity effects on spectra and polarization, and cosmic magnetism in and around compact objects.

The scientific part of our contribution consists mainly of the performance analysis of the instrument to achieve the required scientific goals of the eXTP mission concerning various hardware configurations and different targets. In the present paper, we focused our attention on the dominant program of X-ray timing of accreting NSs. So far, commonly to several promising QPO models, even

the QPO modulation mechanism remains unexplained. Using our simulations we can show that a sufficiently strong modulation of the observed radiation arises when we consider modulation of accretion rate, which provides variable luminosity of the NS boundary layer and is combined with obscuration of the radiation by structures present in the innermost accretion region (see Figure 6 for an illustration).

QPOs offer an independent measurement of black hole mass and spin via modeling the low and high (kilohertz) frequency QPOs observed in the intermediate states of X-ray binaries. Low-frequency QPOs seen in the hard and intermediate states are thought to be produced by the Lense-Thirring precession of the inner hot flow. In this case, modeling the geometry of the precessing flow using tomography and polarimetry will give a direct measure of the offset between the black hole spin and disk angular momentum. This will allow us to explore the accretion flows down to ISCO. An analogy will be explored in the case of accreting supermassive black holes that exhibit the corresponding quasi-periodicities.

Data availability. The synthetic data underlying this article will be shared upon reasonable request. Simulation results and tools will be further added to the above-cited repository (cf. footnote #2), and they will be updated once new mission specifications become available.

Acknowledgements. Our research has been carried out in the context of Czech participation to the upcoming eXTP satellite mission. We acknowledge a continued support from European Space Agency PRODEX program titled “Hardware contribution to the Chinese X-ray mission eXTP” (ref. 4000132152), and from the Czech Science Foundation EXPRO project on “Accreting black holes in the new era of X-ray polarimetry missions” (ref. 21-06825X). We further acknowledge an internal grant of the Silesian University, SGS/31/2023, and the Astronomical Institute’s institutional support, RVO 67985815.

References

- Abramowicz, M. A., Karas, V., Kluzniak, W., Lee, W. H., & Rebusco, P., Non-Linear Resonance in Nearly Geodesic Motion in Low-Mass X-Ray Binaries. 2003, *Publications of the ASJ*, **55**, 467, DOI: 10.1093/pasj/55.2.467
- Bakala, P., Goluchová, K., Török, G., et al., Twin peak high-frequency quasi-periodic oscillations as a spectral imprint of dual oscillation modes of accretion tori. 2015, *Astronomy and Astrophysics*, **581**, A35, DOI: 10.1051/0004-6361/201525867
- Bakala, P., Török, G., Karas, V., et al., Power density spectra of modes of orbital motion in strongly curved space-time: obtaining the observable signal. 2014, *Monthly Notices of the RAS*, **439**, 1933, DOI: 10.1093/mnras/stu076
- Bakala, P., Čermák, P., Hledík, S., Stuchlík, Z., & Truparová, K., Extreme gravitational lensing in vicinity of Schwarzschild-de Sitter black holes. 2007, *Central European Journal of Physics*, **5**, 599, DOI: 10.2478/s11534-007-0033-6

- Bakala, P., Čermák, P., Hledík, S., Stuchlík, Z., & Truparová Plšková, K., A virtual trip to the Schwarzschild-de Sitter black hole: Computer simulation of extreme gravitational lensing in Schwarzschild-de Sitter spacetimes. 2005, in *RAGtime 6/7: Workshops on black holes and neutron stars*, ed. S. Hledík & Z. Stuchlík, 11–28
- Baym, G., Bethe, H. A., & Pethick, C. J., Neutron star matter. 1971, *Nuclear Physics A*, **175**, 225, DOI: 10.1016/0375-9474(71)90281-8
- Bentz, M. C., Cackett, E. M., Crenshaw, D. M., et al., A Reverberation-based Black Hole Mass for MCG-06-30-15. 2016, *Astrophysical Journal*, **830**, 136, DOI: 10.3847/0004-637X/830/2/136
- Bian, W. & Zhao, Y., On X-ray variability in narrow-line and broad-line active galactic nuclei. 2003, *Monthly Notices of the RAS*, **343**, 164, DOI: 10.1046/j.1365-8711.2003.06650.x
- Bursa, M., Abramowicz, M. A., Karas, V., & Kluźniak, W., The Upper Kilohertz Quasi-periodic Oscillation: A Gravitationally Lensed Vertical Oscillation. 2004, *Astrophysical Journal, Letters*, **617**, L45, DOI: 10.1086/427167
- Carpano, S. & Jin, C., Discovery of a 23.8 h QPO in the Swift light curve of XMMU J134736.6+173403. 2018, *Monthly Notices of the RAS*, **477**, 3178, DOI: 10.1093/mnras/sty841
- Costa, E., Soffitta, P., Bellazzini, R., et al., An efficient photoelectric X-ray polarimeter for the study of black holes and neutron stars. 2001, *Nature*, **411**, 662, DOI: 10.1038/35079508
- Czerny, B., You, B., Kurcz, A., et al., The mass of the black hole in RE J1034+396. 2016, *Astronomy and Astrophysics*, **594**, A102, DOI: 10.1051/0004-6361/201628103
- De Rosa, A., Uttley, P., Gou, L., et al., Accretion in strong field gravity with eXTP. 2019, *Science China Physics, Mechanics, and Astronomy*, **62**, 29504, DOI: 10.1007/s11433-018-9297-0
- Dovčiak, M., Karas, V., Matt, G., & Goosmann, R. W., Variation in the primary and reprocessed radiation from an orbiting spot around a black hole. 2008, *Monthly Notices of the RAS*, **384**, 361, DOI: 10.1111/j.1365-2966.2007.12713.x
- Dovčiak, M., Karas, V., & Yaqoob, T., An Extended Scheme for Fitting X-Ray Data with Accretion Disk Spectra in the Strong Gravity Regime. 2004, *Astrophysical Journal, Supplement*, **153**, 205, DOI: 10.1086/421115
- Feroci, M., Ambrosi, G., Ambrosino, F., et al., The large area detector onboard the eXTP mission. 2022, in Society of Photo-Optical Instrumentation Engineers (SPIE) Conference Series, Vol. **12181**, *Space Telescopes and Instrumentation 2022: Ultraviolet to Gamma Ray*, ed. J.-W. A. den Herder, S. Nikzad, & K. Nakazawa, 121811X
- Feroci, M., Bozzo, E., Brandt, S., et al., The LOFT mission concept: a status update. 2016, in Society of Photo-Optical Instrumentation Engineers (SPIE) Conference Series, Vol. **9905**, *Space Telescopes and Instrumentation 2016: Ultraviolet to Gamma Ray*, ed. J.-W. A. den Herder, T. Takahashi, & M. Bautz, 99051R
- Feroci, M., Stella, L., van der Klis, M., et al., The Large Observatory for X-ray Timing (LOFT). 2012, *Experimental Astronomy*, **34**, 415, DOI: 10.1007/s10686-011-9237-2

- Gezari, S., Tidal Disruption Events. 2021, *Annual Review of Astron and Astrophys*, **59**, 21, DOI: 10.1146/annurev-astro-111720-030029
- Gierliński, M., Middleton, M., Ward, M., & Done, C., A periodicity of ~1hour in X-ray emission from the active galaxy RE J1034+396. 2008, *Nature*, **455**, 369, DOI: 10.1038/nature07277
- Goluchová, K., Török, G., Šrámková, E., et al., Mass of the active galactic nucleus black hole XMMUJ134736.6+173403. 2019, *Astronomy and Astrophysics*, **622**, L8, DOI: 10.1051/0004-6361/201834774
- Greene, J., Bailyn, C. D., & Orosz, J. A., Optical and Infrared Photometry of the Microquasar GRO J1655-40 in Quiescence. 2001, *Astrophysical Journal*, **554**, 1290, DOI: 10.1086/321411
- Greiner, J., Cuby, J. G., & McCaughrean, M. J., An unusually massive stellar black hole in the Galaxy. 2001, *Nature*, **414**, 522, DOI: 10.1038/35107019
- Gupta, A. C., Tripathi, A., Wiita, P. J., et al., Possible 1 hour quasi-periodic oscillation in narrow-line Seyfert 1 galaxy MCG-06-30-15. 2018, *Astronomy and Astrophysics*, **616**, L6, DOI: 10.1051/0004-6361/201833629
- Hu, C., Wang, J.-M., Ho, L. C., et al., Improving the Flux Calibration in Reverberation Mapping by Spectral Fitting: Application to the Seyfert Galaxy MCG-6-30-15. 2016, *Astrophysical Journal*, **832**, 197, DOI: 10.3847/0004-637X/832/2/197
- Ingram, A. R. & Motta, S. E., A review of quasi-periodic oscillations from black hole X-ray binaries: Observation and theory. 2019, *New Astronomy Review*, **85**, 101524, DOI: 10.1016/j.newar.2020.101524
- in't Zand, J. J. M., Bozzo, E., Qu, J., et al., Observatory science with eXTP. 2019, *Science China Physics, Mechanics, and Astronomy*, **62**, 29506, DOI: 10.1007/s11433-017-9186-1
- Karas, V., Twin Peak Separation in Sources with Kilohertz Quasi-periodic Oscillations Caused by Orbital Motion. 1999, *Astrophysical Journal*, **526**, 953, DOI: 10.1086/308015
- Karas, V., Bakala, P., Torok, G., et al., Distinguishing between Spot and Torus Models of High-Frequency Quasiperiodic Oscillations. 2014, *Acta Polytechnica*, **54**, 191, DOI: 10.14311/AP.2014.54.0191
- Karas, V., Vokrouhlický, D., & Polnarev, A. G., In the vicinity of a rotating black hole: a fast numerical code for computing observational effects. 1992, *Monthly Notices of the RAS*, **259**, 569, DOI: 10.1093/mnras/259.3.569
- Kotrlová, A., Šrámková, E., Török, G., et al., Models of high-frequency quasi-periodic oscillations and black hole spin estimates in Galactic microquasars. 2020, *Astronomy and Astrophysics*, **643**, A31, DOI: 10.1051/0004-6361/201937097
- Lančová, D., Computer modelling of accretion processes in binary systems with black holes and neutron stars. 2023, *Ph.D. Thesis*, Institute of Physics (Silesian University in Opava), viii+201 pp.

- Lattimer, J. M. & Prakash, M., Neutron star observations: Prognosis for equation of state constraints. 2007, *Physics Reports*, **442**, 109, DOI: 10.1016/j.physrep.2007.02.003
- McClintock, J. E. & Remillard, R. A., Black hole binaries. 2006, in *Compact Stellar X-ray Sources*, **39**, 157, DOI: 10.48550/arXiv.astro-ph/0306213
- Miller, J. M. & Gültekin, K., X-Ray and Radio Constraints on the Mass of the Black Hole in Swift J164449.3+573451. 2011, *Astrophysical Journal, Letters*, **738**, L13, DOI: 10.1088/2041-8205/738/1/L13
- Molla, A. A., Chakrabarti, S. K., Debnath, D., & Mondal, S., Estimation of Mass of Compact Object in H 1743-322 from 2010 and 2011 Outbursts using TCAF Solution and Spectral Index-QPO Frequency Correlation. 2017, *Astrophysical Journal*, **834**, 88, DOI: 10.3847/1538-4357/834/1/88
- Motta, S. E., Quasi periodic oscillations in black hole binaries. 2016, *Astronomische Nachrichten*, **337**, 398, DOI: 10.1002/asna.201612320
- Motta, S. E., Belloni, T., Stella, L., et al., Black hole mass and spin measurements through the relativistic precession model: XTE J1859+226. 2022, *Monthly Notices of the RAS*, **517**, 1469, DOI: 10.1093/mnras/stac2142
- Orosz, J. A., Groot, P. J., van der Klis, M., et al., Dynamical Evidence for a Black Hole in the Microquasar XTE J1550-564. 2002, *Astrophysical Journal*, **568**, 845, DOI: 10.1086/338984
- Pan, H.-W., Yuan, W., Yao, S., et al., Detection of a Possible X-Ray Quasi-periodic Oscillation in the Active Galactic Nucleus 1H 0707-495. 2016, *Astrophysical Journal, Letters*, **819**, L19, DOI: 10.3847/2041-8205/819/2/L19
- Pasham, D. R., Cenko, S. B., Zoghbi, A., et al., Evidence for High-frequency QPOs with a 3:2 Frequency Ratio from a 5000 Solar Mass Black Hole. 2015, *Astrophysical Journal, Letters*, **811**, L11, DOI: 10.1088/2041-8205/811/1/L11
- Pasham, D. R., Remillard, R. A., Fragile, P. C., et al., A loud quasi-periodic oscillation after a star is disrupted by a massive black hole. 2019, *Science*, **363**, 531, DOI: 10.1126/science.aar7480
- Pasham, D. R., Strohmayer, T. E., & Mushotzky, R. F., A 400-solar-mass black hole in the galaxy M82. 2014, *Nature*, **513**, 74, DOI: 10.1038/nature13710
- Reis, R. C., Miller, J. M., Reynolds, M. T., et al., A 200-Second Quasi-Periodicity After the Tidal Disruption of a Star by a Dormant Black Hole. 2012, *Science*, **337**, 949, DOI: 10.1126/science.1223940
- Remillard, R. A., Gazak, J. Z., Lin, D., Morgan, E. H., & Pooley, G. G., The 67 Hz QPO and Other High-Frequency Oscillations from the Black Hole Binary GRS1915+105. 2004, in American Astronomical Society Meeting Abstracts, Vol. **205**, *American Astronomical Society Meeting Abstracts*, 104.05
- Remillard, R. A., Munro, M. P., McClintock, J. E., & Orosz, J. A., Evidence for Harmonic Relationships in the High-Frequency Quasi-periodic Oscillations of XTE J1550-564 and GRO J1655-40. 2002, *Astrophysical Journal*, **580**, 1030, DOI: 10.1086/343791

- Santangelo, A., Zane, S., Feng, H., et al., Physics and astrophysics of strong magnetic field systems with eXTP. 2019, *Science China Physics, Mechanics, and Astronomy*, **62**, 29505, DOI: 10.1007/s11433-018-9234-3
- Soffitta, P., Baldini, L., Bellazzini, R., et al., The Instrument of the Imaging X-Ray Polarimetry Explorer. 2021, *Astronomical Journal*, **162**, 208, DOI: 10.3847/1538-3881/ac19b0
- Stella, L. & Vietri, M., kHz Quasiperiodic Oscillations in Low-Mass X-Ray Binaries as Probes of General Relativity in the Strong-Field Regime. 1999, *Physical Review Letters*, **82**, 17, DOI: 10.1103/PhysRevLett.82.17
- Stella, L., Vietri, M., & Morsink, S. M., Correlations in the Quasi-periodic Oscillation Frequencies of Low-Mass X-Ray Binaries and the Relativistic Precession Model. 1999, *Astrophysical Journal, Letters*, **524**, L63, DOI: 10.1086/312291
- Strohmayer, T. E., Discovery of a 450 HZ Quasi-periodic Oscillation from the Microquasar GRO J1655-40 with the Rossi X-Ray Timing Explorer. 2001, *Astrophysical Journal, Letters*, **552**, L49, DOI: 10.1086/320258
- Török, G., QPOs in microquasars and Sgr A* measuring the black hole spin. 2005, *Astronomische Nachrichten*, **326**, 856, DOI: 10.1002/asna.200510427
- Török, G., Bakala, P., Šrámková, E., et al., Mass-Angular-momentum Relations Implied by Models of Twin Peak Quasi-periodic Oscillations. 2012, *Astrophysical Journal*, **760**, 138, DOI: 10.1088/0004-637X/760/2/138
- Török, G., Goluchová, K., Urbanec, M., et al., Constraining Models of Twin-Peak Quasi-periodic Oscillations with Realistic Neutron Star Equations of State. 2016, *Astrophysical Journal*, **833**, 273, DOI: 10.3847/1538-4357/833/2/273
- Török, G., Goluchová, K., Šrámková, E., Urbanec, M., & Straub, O., Time-scale of twin-peak quasi-periodic oscillations and mass of accreting neutron stars. 2019, *Monthly Notices of the RAS*, **488**, 3896, DOI: 10.1093/mnras/stz1929
- Török, G., Kotrlová, A., Matuszková, M., et al., Simple Analytic Formula Relating the Mass and Spin of Accreting Compact Objects to Their Rapid X-Ray Variability. 2022, *Astrophysical Journal*, **929**, 28, DOI: 10.3847/1538-4357/ac5ab6
- Turner, T. J., Miller, L., George, I. M., & Reeves, J. N., Evidence for orbital motion of material close to the central black hole of Mrk 766. 2006, *Astronomy and Astrophysics*, **445**, 59, DOI: 10.1051/0004-6361:20053042
- Urbanecová, G., Urbanec, M., Török, G., et al., Epicyclic Oscillations in the Hartle-Thorne External Geometry. 2019, *Astrophysical Journal*, **877**, 66, DOI: 10.3847/1538-4357/ab1b4c
- Urbanec, M., Beták, E., & Stuchlík, Z., Observational Tests of Neutron Star Relativistic Mean Field Equations of State. 2010, *Acta Astronomica*, **60**, 149, DOI: 10.48550/arXiv.1007.3446
- Urbanec, M., Miller, J. C., & Stuchlík, Z., Quadrupole moments of rotating neutron stars and strange stars. 2013, *Monthly Notices of the RAS*, **433**, 1903, DOI: 10.1093/mnras/stt858

- Uzdensky, D., Begelman, M., Beloborodov, A., et al., Extreme Plasma Astrophysics. 2019, *Bulletin of the AAS*, **51**, 362, DOI: 10.48550/arXiv.1903.05328
- van der Klis, M., Kilohertz quasi-periodic oscillations in low-mass x-ray binaries. 1998, *Advances in Space Research*, **22**, 925, DOI: 10.1016/S0273-1177(98)00125-2
- Šrámková, E., Goluchová, K., Török, G., et al., Exploring the X-ray universe via timing: mass of the active galactic nucleus black hole XMMUJ134736.6+173403. 2021, in *Nuclear Activity in Galaxies Across Cosmic Time*, **356**, 348, DOI: 10.1017/S1743921320003312
- Šrámková, E., Matuszková, M., Klimovičová, K., et al., Oscillations of fluid tori around neutron stars. 2023, *Astronomische Nachrichten*, **344**, easna.20220114, DOI: 10.1002/asna.20220114
- Šrámková, E., Török, G., Kotrlová, A., et al., Black hole spin inferred from 3:2 epicyclic resonance model of high-frequency quasi-periodic oscillations. 2015, *Astronomy and Astrophysics*, **578**, A90, DOI: 10.1051/0004-6361/201425241
- Watts, A. L., Yu, W., Poutanen, J., et al., Dense matter with eXTP. 2019, *Science China Physics, Mechanics, and Astronomy*, **62**, 29503, DOI: 10.1007/s11433-017-9188-4
- Weisskopf, M. C., Soffitta, P., Ramsey, B. D., et al., A space-borne X-ray imaging polarimeter. 2023, *Nature Astronomy*, **7**, 635, DOI: 10.1038/s41550-023-01950-w
- Wevers, T., van Velzen, S., Jonker, P. G., et al., Black hole masses of tidal disruption event host galaxies. 2017, *Monthly Notices of the RAS*, **471**, 1694, DOI: 10.1093/mnras/stx1703
- Yanes-Rizo, I. V., Torres, M. A. P., Casares, J., et al., A refined dynamical mass for the black hole in the X-ray transient XTE J1859+226. 2022, *Monthly Notices of the RAS*, **517**, 1476, DOI: 10.1093/mnras/stac2719
- Zhang, P., Zhang, P.-f., Yan, J.-z., Fan, Y.-z., & Liu, Q.-z., An X-Ray Periodicity of ~ 1.8 hr in Narrow-line Seyfert 1 Galaxy Mrk 766. 2017, *Astrophysical Journal*, **849**, 9, DOI: 10.3847/1538-4357/aa8d6e
- Zhang, S., Santangelo, A., Feroci, M., et al., The enhanced X-ray Timing and Polarimetry mission—eXTP. 2019, *Science China Physics, Mechanics, and Astronomy*, **62**, 29502, DOI: 10.1007/s11433-018-9309-2
- Zhang, S. N., Feroci, M., Santangelo, A., et al., eXTP: Enhanced X-ray Timing and Polarization mission. 2016, in Society of Photo-Optical Instrumentation Engineers (SPIE) Conference Series, Vol. **9905**, *Space Telescopes and Instrumentation 2016: Ultraviolet to Gamma Ray*, ed. J.-W. A. den Herder, T. Takahashi, & M. Bautz, 99051Q
- Zhou, X.-L., Yuan, W., Pan, H.-W., & Liu, Z., Universal Scaling of the 3:2 Twin-peak Quasi-periodic Oscillation Frequencies With Black Hole Mass and Spin Revisited. 2015, *Astrophysical Journal, Letters*, **798**, L5, DOI: 10.1088/2041-8205/798/1/L5

Development of an operation plan for observing the Galactic center region with the lobster-eye monitor

V. Šimon^{1,2} and R. Hudec^{2,1}

¹ *Astronomical Institute, The Czech Academy of Sciences, 25165 Ondřejov, Czech Republic (E-mail: simon@asu.cas.cz)*

² *Czech Technical University in Prague, Technická 2, 16627 Prague, Czech Republic (E-mail: rene.hudec@gmail.com)*

Received: June 30, 2023; Accepted: September 20, 2023

Abstract. Using a CubeSat-like satellite, we show the lobster-eye (LE) monitor’s perspectives and development of an observing plan. This instrument is important because it is able to provide wide-field X-ray imaging. We present the possibilities of monitoring the Galactic center region in the soft X-ray energy (a few keV) bands. The reason is that many X-ray binaries concentrate in the bulge surrounding the center of our Galaxy. Several such binaries are expected to be present in the monitor’s field of view (typically a square of about 5×5 degrees or more) at the same time. We used the planned LE telescope’s 3–6 keV and 6–9 keV band flux. To compare the expected results, we used the data obtained by MAXI/*ISS* and accommodated these energy bands to assess the object types and their light curves expected to be detected by this LE. We show how such data of GX 5–1 can contribute to this branch.

Key words: X-rays: binaries – Radiation mechanisms: general – Astronomical instrumentation – Methods: observational

1. Introduction

X-ray binaries are systems that contain a neutron star (NS) or a black hole (BH), accreting matter from their companions (donors). The donor can be either a low-mass star in a low-mass X-ray binary (LMXB) or an early-type high-mass star in a high-mass X-ray binary (HMXB). This mass accretion produces X-ray emissions that are highly variable on various timescales. Reviews of these systems can be found, e.g., in [Lewin et al. \(1995\)](#) and [Lewin & van der Klis \(2006\)](#).

X-ray monitoring enables observing various states of activity, particularly often unpredictable events of an object. It helps place these events in the framework of activities of various types of X-ray sources. This approach also enables making a representative ensemble of events in such objects.

The recent progress in CubeSat-related techniques and technologies allows missions with small scientific payloads like novel lobster-eye (LE) telescopes to

be considered (Hudec et al., 2010; Tichý et al., 2015; Hudec, 2017; Hudec et al., 2018; Hudec, 2019a; Tichý et al., 2019; Hudec, 2019b; Dániel et al., 2022).

The CubeSat unit is a cube of $10\text{ cm} \times 10\text{ cm} \times 10\text{ cm}$. These cubes can be assembled into multiples to accommodate the equipment of larger satellites. If we use the miniature LE telescope with the necessary equipment, a small resulting cubesat could consist of at least two cubes, analogously to VZLUSAT1 minisatellite (Daniel et al., 2019). Typically, one LE module provides a field-of-view (FOV) of 5×5 deg, so if one needs a larger FOV, several such modules are necessary. In addition, more units (more than four) are necessary for pointed mode because the satellite must also accommodate an altitude control system.

We note that CubeSats are able to accommodate miniature LE systems covering a reasonable FOV, as mentioned above. Although achieving remarkably large FOVs is possible by modular concept with more LE modules, we note that even a single module can provide valuable scientific results with a sophisticated observing strategy.

2. MAXI observations for comparison with LE

We already described in our previous paper (Šimon & Hudec, 2022) that we used the data obtained by MAXI/*ISS* (Matsuoka et al., 2009) to assess the light curves of various objects that are expected to be detected by simple LE monitor in X-rays with energy of a few keV. We mainly used the 3–6 keV and the 6–9 keV MAXI data. These energies are close to the expected bands of the LE telescope and its available detector.

The flux in the 1-day mean of observations is abbreviated as I_M in Fig. 1. We set the time of each such 1 day-bin to the beginning of each day’s monitoring. The integration time of one MAXI scan was about 60 s, which comes in every 92 minutes. Therefore, the total exposure time of a given celestial object is about 15 minutes per day. We show an example of what features of the X-ray light curve can be observed with such exposure time. The light curves of all observations are available at ¹ and ².

2.1. Example of activity of GX 5–1 in the LE observing plan

Figure 1 shows an example of the activity of the LMXB GX 5–1 in the 3–6 keV and 6–9 keV bands (one-day means of data). It is a Z-source (Hasinger & van der Klis, 1989; Jackson et al., 2009). The X-ray spectral changes from flaring branch to normal branch and horizontal branch can occur for several hours.

GX 5–1 is a bright X-ray source. Besides studies of its X-ray activity, it is also helpful for the testing flight of the LE monitor. MAXI observes it in a

¹<http://maxi.riken.jp/top/lc.html>

²<http://maxi.riken.jp/mxondem/>

typical I_M of ~ 1.8 photons $\text{cm}^{-2} \text{s}^{-1}$ in the 3–6 keV band. For comparison, the 3–6 keV I_M of Crab nebula observed by MAXI is ~ 1.4 photons $\text{cm}^{-2} \text{s}^{-1}$.

Figure 1 shows that the 3–6 keV and 6–9 keV band fluxes (1-day means) of GX 5–1 significantly vary on the timescale of days. The relatively recent segment of observations, spanning about 200 days, was selected to show the current activity state. Most observations accumulate in a broad, gradually winding belt, suggesting the flux changing on various timescales detected by the 1-day means.

Figure 1 shows that the light curve of the 3–6 keV data is significantly different from that for the 6–9 keV band. A series of short drops (about weeks) of flux contributes only to the softer band.

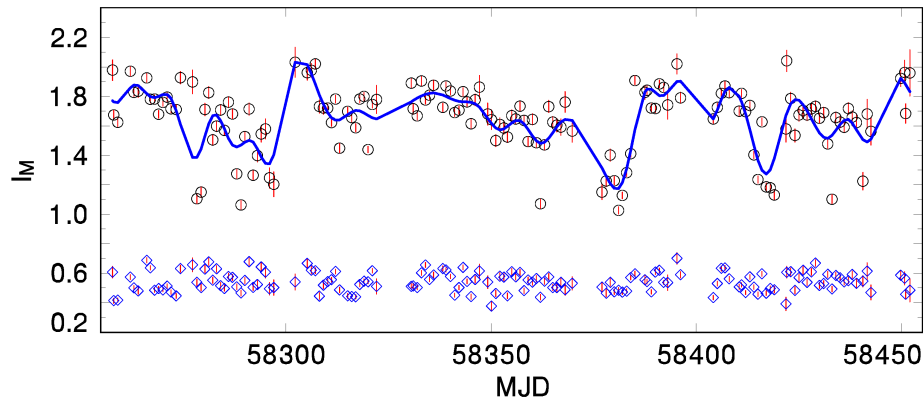


Figure 1. Example of activity of the Z-source GX 5–1 in the 3–6 keV and 6–9 keV bands. Empty circles denote the 1-day means of the MAXI 3–6 keV data. Empty diamonds represent the 6–9 keV data. Their error bars are included in the diagram; some sizes are comparable to the sizes of the symbols. The line represents a HEC13 fit with $\epsilon = 1$ and $\Delta T = 5$ d to the 3–6 keV band observations. A fit runs through a broad belt of observations with significant rapid (day-to-day) flux variations.

To separate the long-term evolution of GX 5–1 from its shorter-term activity, the light curve consisting of the 1-day means was smoothed by the code HEC13, written by Prof. P. Harmanec³, and based on the method of Vondrák (1969). Regardless of their profile, it can fit a smooth curve to the non-equidistant data. A full description can be found in Vondrák (1969). HEC13 uses two input parameters, ϵ (in dimensionless units) and ΔT (in days in our case). We found that a HEC13 fit with $\epsilon = 1$ and $\Delta T = 5$ d represents the 1-day data running through the belt caused by the day-to-day changes (the thick line in Fig. 1). A single deviating 1-day mean with the error bar considerably lower than the amplitude

³<http://astro.troja.mff.cuni.cz/ftp/hec/HEC13/>

of this difference only slightly influences this fit. Only groups of several points are essential.

This fit shows significant flux modulations on the timescale of weeks. The fitted flux repeatedly decreases and subsequently returns to roughly the same value, thus forming a series of undulations. We show that even a 1-day binning that may be used in the testing LE is able to investigate the long-term activity of GX 5–1.

A data fitting emphasizes the light curve’s features on long timescales like weeks and months. The observing noise, flares, dips, and possible features of the orbital modulation of GX 5–1 are suppressed by this fitting. Because [Jackson et al. \(2009\)](#) shows that the X-ray spectral changes among the branches of this Z-source can occur during several hours, they cannot cause the waves shown by the HEC13 fit in Fig. 1. Interpreting the fit to the data in Fig. 1 requires contributing another mechanism. The reason is the discrepant timescale. The shifts across the Z-branch could contribute to forming the winding belt. In principle, the fits to the light curves for the different energy bands differ.

The histograms of I_M in Fig. 2 show discrepant profiles of X-ray flux for different energy bands. While the 1-day data means of the 6–9 keV band flux create a single roughly symmetric bump without remarkable wings, the 3–6 keV band I_M gives significant broad wings with a long tail toward low flux. The occasional 3–6 keV flux depressions are reflected in the tail in the histogram in Fig. 2. A comparison of the histograms for the 1-day means of I_M and the fits by HEC13 shows that rapid changes like observing noise, flares, dips, and possible orbital modulation are suppressed by this fitting.

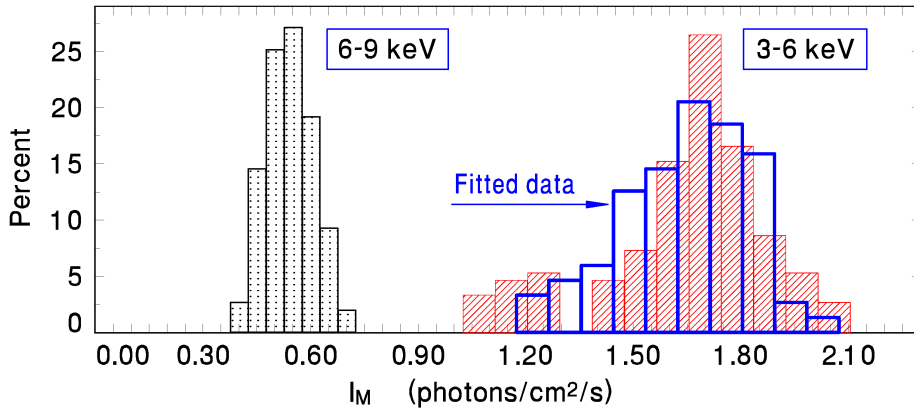


Figure 2. Histograms of I_M of GX 5–1 in the 3–6 keV and 6–9 keV bands (both for the 1-day means of the data (hatched bars) and the HEC13 fit (empty bars)).

The luminosity of GX 5–1 is close to the Eddington luminosity ($\sim 7 \cdot 10^{38} \text{ erg s}^{-1}$)

in the 1–30 keV band) (Jackson et al., 2009), so it is reasonable to suppose that the accretion disk is always in the ionized state. Therefore, we ascribe these fluctuations of I_M to the variations of the mass transfer rate from the companion. Phillips & Podsiadlowski (2002) showed that the radiation pressure of strong external irradiation close to the Eddington limit causes a non-axisymmetric deformation of the donor’s surface.

Furthermore, Phillips & Podsiadlowski (2002) showed that if the accretion disk shadows the inner Lagrangian point from strong external irradiation, the radiation pressure further modifies the donor’s surface deformation. The transferring matter (e.g., a bulge in the impact stream region on the outer disk rim (Livio et al., 1986)) between the irradiating light source and the donor star can modify the irradiation of this star. We ascribe the undulations of I_M on the timescale of weeks to the effects of the pressure on the irradiated donor. The observed recurrent changes of I_M on the timescale of weeks can be caused by the changes in the geometric configuration of the irradiated donor with time. E.g., increasing the size of the bulge in the impact of the stream onto the disk gives rise to screening of irradiating flux; it leads to a change in the shape of the irradiated donor, hence a decrease of the mass outflow through the stream. Modeling time variations of the impact disk region and their influence on blocking the donor’s irradiation is essential.

The LE dense (typically about 10 min time resolution in pointed mode) monitoring can enable tracking of the long-term I_M variations of GX 5–1 even when the observations are grouped into the 1-day bins. Separating into several energy bands can show a dependence of amplitude on energy. Resolution of the structure of the winding belt of I_M and the relation of this structure to the undulations occurring on the timescale of weeks will be essential. They will be in the possibility of an LE monitor in a CubeSat-type satellite.

3. Conclusions

We show progress in preparing the observing plan and an observational strategy of a small LE telescope in a pointed mode in a small (CubeSat-like) satellite. This telescope is able to provide wide-field X-ray imaging and monitoring. We present the possibility of monitoring the Galactic center region in the relatively soft X-ray energy band (which is constrained by the optics and the available detector).

The reason for selecting this region is that many X-ray binaries (especially those with a low-mass lobe-filling secondary and mostly the NS accretor) concentrate in the bulge surrounding the center of our Galaxy.

Several X-ray binaries are expected to be present in the monitor’s FOV (a square of about 5×5 degrees). It will enable obtaining the light curves of several objects without apriori information of their state of activity. Also, early phases of outbursts of yet-unknown transients can be observed. X-ray binaries’ long-

term activity in this region can be reliably observed even with sufficiently long exposure times (e.g., about 1 day). Observing in the soft X-ray band is the most promising because the X-ray intensity of these objects is the highest in this band.

Such LE monitor can reliably observe the typical features of such objects' long-term X-ray activity (e.g., outbursts and state transitions). The observed data will be essential and valuable for scientific analyses.

We show that fitting the X-ray light curve with HEC13 enables us to track the profile of the long-term flux variations that may be hidden in relatively rapid (day-to-day) changes. Separating the energy band into several sub-bands wide enough to allow for the detection of cosmic objects by a CubeSat LE, at least in the case of the relatively bright objects, can enable analysis of the differences in the light curves and histograms of I_M .




Acknowledgements. The research leading to these results has received funding from the European Union's Horizon 2020 Programme under the AHEAD2020 project (grant agreement n. 871158). Also, support by the project RVO:67985815 is acknowledged. This work was also supported by the Grant Agency of the Czech Technical University in Prague, grant No. SGS21/120/OHK3/2T/13. This research has made use of MAXI data provided by RIKEN, JAXA and the MAXI team. We also thank Prof. Petr Harmanec for providing us with the code HEC13. The Fortran source version, compiled version, and brief instructions on how to use the program can be obtained at <http://astro.troja.mff.cuni.cz/ftp/hec/HEC13/>

References

- Daniel, V., Inneman, A., Vertat, I., et al., In-Orbit Commissioning of Czech Nanosatellite VZLUSAT-1 for the QB50 Mission with a Demonstrator of a Miniaturised Lobster-Eye X-Ray Telescope and Radiation Shielding Composite Materials. 2019, *Space Science Reviews*, **215**, 40, DOI: 10.1007/s11214-019-0589-7
- Dániel, V., Maršíková, V., Hudec, R., et al., Small Spacecraft Payload Study for X-ray Astrophysics including GRB Science. 2022, *Universe*, **8**, 144, DOI: 10.3390/universe8030144
- Hasinger, G. & van der Klis, M., Two patterns of correlated X-ray timing and spectral behaviour in low-mass X-ray binaries. 1989, *A&A*, **225**, 79
- Hudec, R., Astrophysical payloads for picosatellites. 2017, *CoSka*, **47**, 143, DOI: <https://articles.adsabs.harvard.edu/pdf/2017CoSka..47..143H>
- Hudec, R., Micro-Nano-Pico-satellites: Complementary Tools for Big Astrophysics. 2019a, in *Frontier Research in Astrophysics - III. 28 May - 2 June 2018. Mondello (Palermo)*, 77
- Hudec, R., X/EUV and UV optics for miniature cubesats payloads. 2019b, in Society of Photo-Optical Instrumentation Engineers (SPIE) Conference Series, Vol. **11032**, *EUV and X-ray Optics: Synergy between Laboratory and Space VI*, 1103204

- Hudec, R., Pina, L., Marsikova, V., & Inneman, A., Lobster-Eye X-Ray Astronomy. 2010, *X-RAY ASTRONOMY 2009: PRESENT STATUS, MULTI-WAVELENGTH APPROACH AND FUTURE PERSPECTIVES: Proceedings of the International Conference. AIP Conference Proceedings*, **1248**, 585, DOI: 10.1063/1.3475346
- Hudec, R., Pina, L., Marsikova, V., et al., Lobster Eye X-ray optics for astrophysics: Recent status. 2018, *Contributions of the Astronomical Observatory Skalnaté Pleso*, **48**, 456
- Jackson, N. K., Church, M. J., & Bałucińska-Church, M., A model for the Z-track phenomenon in GX 5-1 and observational evidence for the physical origins of the kHz QPO. 2009, *A&A*, **494**, 1059, DOI: 10.1051/0004-6361:20079234
- Lewin, W. H. G. & van der Klis, M. 2006, *Compact Stellar X-ray Sources*
- Lewin, W. H. G., van Paradijs, J., & van den Heuvel, E. P. J., X-ray binaries. 1995
- Livio, M., Soker, N., & Dgani, R., On the Stream-Disk Interaction in Accreting Compact Objects. 1986, *ApJ*, **305**, 267, DOI: 10.1086/164247
- Matsuoka, M., Kawasaki, K., Ueno, S., et al., The MAXI Mission on the ISS: Science and Instruments for Monitoring All-Sky X-Ray Images. 2009, *PASJ*, **61**, 999, DOI: 10.1093/pasj/61.5.999
- Phillips, S. N. & Podsiadlowski, P., Irradiation pressure effects in close binary systems. 2002, *MNRAS*, **337**, 431, DOI: 10.1046/j.1365-8711.2002.05886.x
- Tichý, V., Barbera, M., Hudec, R., & Willingale, R., Effective collecting area of lobster eye optics and optimal value of effective angle. 2019, *Experimental Astronomy*, **47**, 161, DOI: 10.1007/s10686-019-09622-2
- Tichý, V., Burrows, D. N., Prieskorn, Z., & Hudec, R., Optics for nano-satellite X-ray monitor. 2015, *Baltic Astronomy*, **24**, 242, DOI: 10.1515/astro-2017-0225
- Vondrák, J., A contribution to the problem of smoothing observational data. 1969, *Bulletin of the Astronomical Institute of Czechoslovakia*, **20**, 349
- Šimon, V. & Hudec, R., Perspectives of the LOBSTER-EYE monitor in the soft X-ray observing the Galactic center region. 2022, *JHEAp*, **35**, 69, DOI: 10.1016/j.jheap.2022.06.001

Preliminary optical tests of lobster eye X-ray optics prototype for nano-satellite missions based on new technology

V. Tichý¹ , M. Míka²  and R. Hudec¹ 

¹ *Czech Technical University in Prague, Faculty of Electrical Engineering, Technická 2, 166 27 Prague, Czech Republic (E-mail: vladimir-tichy@email.cz)*

² *University of Chemistry and Technology Prague Technická 5, 166 28 Prague, Czech Republic*

Received: July 4, 2023; Accepted: October 9, 2023

Abstract. This paper presents preliminary results of optical tests of Schmidt lobster eye module based on a new technology. The module was tested using visible light, which is possible because glass plates coated with gold are used as mirrors. The results show good accordance with simulations. It means that the technological concept offers precise assembly of optical mirrors, which is the key aspect to obtain sharp focal image.

Key words: lobster eye – multi-foil optics – reflective optics – grazing incidence optics – x-ray optics

1. Introduction

The Schmidt lobster eye (Schmidt, 1975) is composed of flat rectangular mirrors. These mirrors form an uniform pattern around a virtual cylinder with the centre **C** and radius r , see Fig. 1. This set of mirrors is called stack. In a real case, grazing angles are much smaller and mirrors are closer one to each. The point **F** represents the focus of the system. The lobster eye optics is intended mainly for X-rays. Its main advantage is wide field of view, therefore the lobster eye optics is suitable mainly for space X-ray monitors (Dániel et al., 2022; Hudec & Feldman, 2022; Hudec et al., 2018, 2017b,a,c,e,d)

Schmidt lobster eye geometry is defined by these parameters:

- r radius of the system
- a mirror spacing
- t mirrors thickness
- h mirrors depth

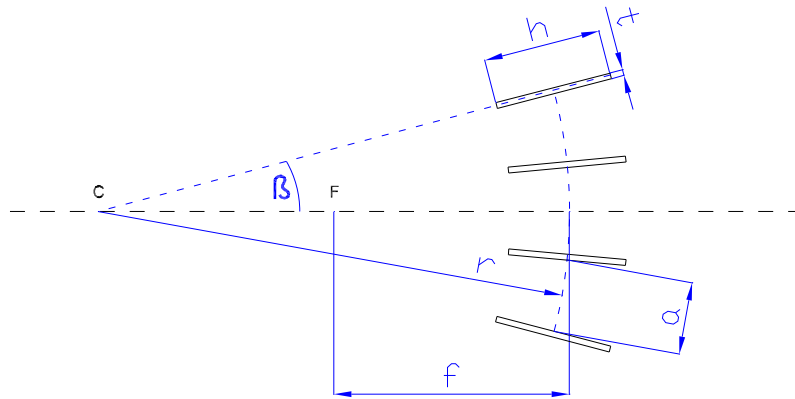


Figure 1. Arrangement of mirrors of one-dimensional Schmidt lobster eye

- N number of mirrors
- β represents angle position of a mirror

Operation of a single stack is similar to a cylindric lens.

Two orthogonally arranged stacks form a double-reflecting device, see Fig. 2. Note that there exists another concept of lobster eye based on square pores ([Angel, 1979](#)).

The main manufacturing problem of Schmidt lobster eye is to achieve exact positioning of each mirror. Therefore a new technological concept has been proposed and registered as utility model ([Tichý, 2022b](#)) and patent application ([Tichý, 2022a](#)).

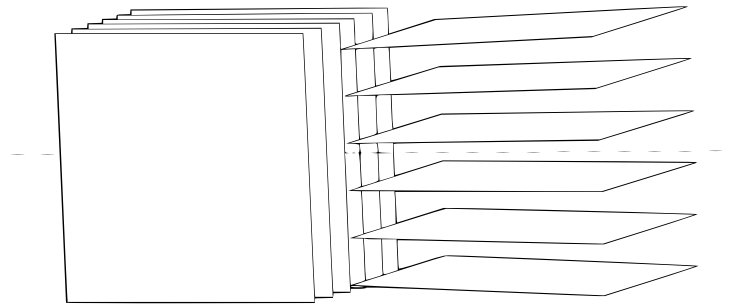


Figure 2. Arrangement of stacks of two-dimensional Schmidt lobster eye.

2. Prototype one-dimensional Schmidt lobster eye optics module LNA-215

To prove the technological concept, prototype one-dimensional Schmidt lobster eye optics module LNA-215 was manufactured, see Fig. 3.

The module LNA-215 has following parameters:

- Focal length $f = 215\text{mm}$
- Input aperture $84\times 84\text{mm}$
- Composed of $N=66$ glass mirrors of depth $h=24\text{mm}$ and thickness $t=0.28\text{mm}$ coated with gold
- Mirror spacing $a = 1.05\text{mm}$
- Outer dimensions $95.8\times 95.8\times 26\text{mm}$ without external housing
- Intended for X-ray energy 1keV
- Calculated field of view 22° .

CubeSat satellites represent a common platform to test new space devices. Therefore, the focal length and the input aperture of the optics were chosen so that the optics together with a focussed detector would fit three units of a CubeSat satellite.

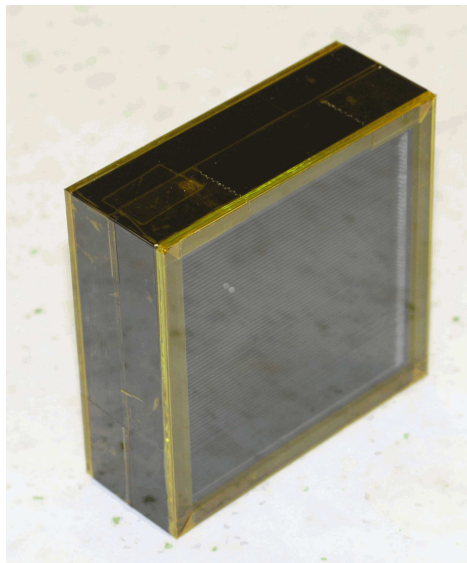


Figure 3. Prototype of one-dimensional Schmidt lobster eye optics module LNA-215.

3. Experimental setup

As the mirrors are made of glass coated with gold, they reflect visible light, too. It allows to use visible light to perform the preliminary experiment, which proves the technological concept. This experiment was performed in laboratories of the University of Chemistry and Technology in Prague.

The experimental setup is shown in Fig. 3. A white high-power light emitting diode was used as the light source. The source was equipped by aperture of diameter ca. 0.1mm made of aluminium foil. A plano-convex lens of focal length 130mm was used as collimator. Distance between the planar side of collimator and the center of the optics was 850mm. The image was taken by a camera Canon EOS 50D. This camera has a sensor of size 22.3 x 14.9mm and resolution of 4752 x 3168 pixels.

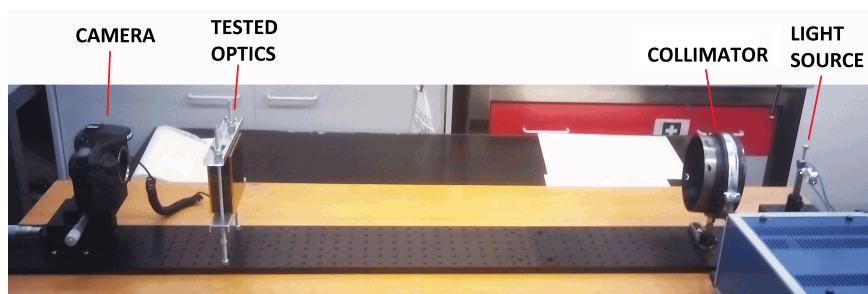


Figure 4. Experimental setup

4. Results

The image acquired by camera is shown in Fig. 5(a). Red color channel was used. The image is in negative colors and with enhanced contrast. The focal line does not have an observable skew error contrary to results with previous prototype presented in (Tichý et al., 2018).

Simulations were done using LOPSIMUL software (Tichý, 2023) by the simplified ray-tracing algorithm (Tichý et al., 2016; Tichý, 2013; Tichý et al., 2011). Perfectly flat mirrors of 100% reflectivity were considered for the simulations. Resulting image of the simulation for aligned optics is seen in Fig. 5(b).

It is seen that the central focal line in images Fig. 5(a) and Fig. 5(b) has different position relative to positions of shadows of mirrors. This is because the entire lobster optics module was tilted a little relative to direction of incoming rays. However, the setup did not allow perfect alignment.

Therefore, the tilt angle was included in next simulations and the tilt value was manually found by comparison of the experimental image to the result of

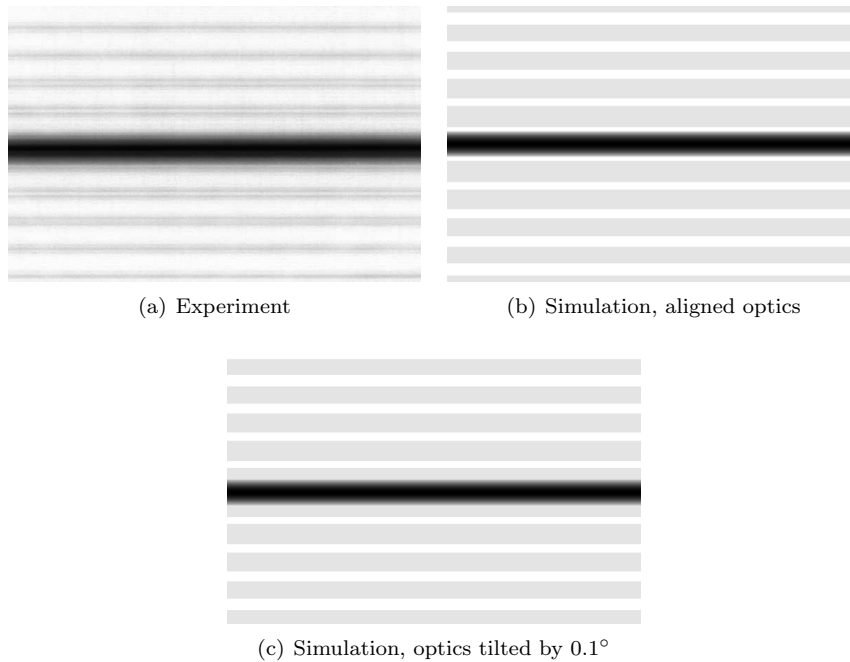


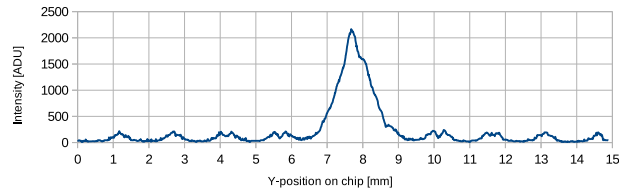
Figure 5. Focal images

the simulations. It was found that tilt value of 0.1° gives the good accordance between experimental image (Fig. 5(a)) and result of the simulation including the tilt angle (Fig. 5(c)). The experimental image with visible light is affected by diffraction effects.

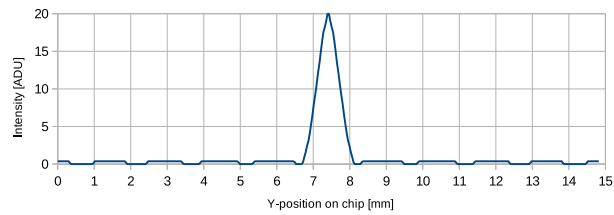
Graphs of intensity along vertical axis are shown in Fig. 6. FWHM of the peak of the experimental image (Fig. 6(a)) is 0.96mm while FWHM of the peaks of both simulated images (Fig. 6(b), Fig. 6(c)) reaches 0.71mm. The experimental value is slightly worse compared to the result of simulation due to diffraction effects and due the fact that the diameter of aperture was not small enough.

5. Conclusions

The experiment with visible light proves that the prototype optics is functioning and the technological concept is promising. FWHM of the experimental image is slightly worse than the result of the simulation, which is due to diffraction effects and due to the small divergence of rays. The focal line does not have the skew error.



(a) Experiment



(b) Simulation, aligned optics

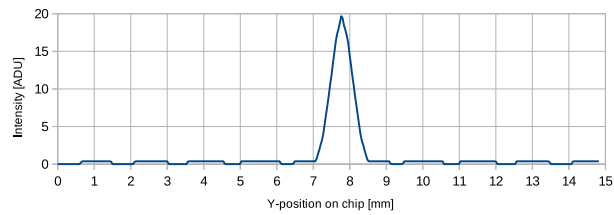
(c) Simulation, optics tilted by 0.1°

Figure 6. Intensity along vertical axis. Vertical scales of experimental and simulated images are not comparable.

The authors expect that experiment in X-ray tunnel at designed energy around 1keV will give result that will be in perfect accordance with the simulation.

Acknowledgements. We would like to thank Mr. Pavel Maun for machining works. Thanks for funding from the European Union's Horizon 2020 Programme under the AHEAD2020 project (grant agreement n. 871158). We also acknowledge CVUT FEL grant No. SGS21/120/OHK3/2T/13.

References

Angel, J. R. P., Lobster eyes as X-ray telescopes. 1979, *Astrophysical Journal*, **233**,

364, DOI: 10.1086/157397

- Dániel, V., Maršíková, V., Hudec, R., et al., Small Spacecraft Payload Study for X-ray Astrophysics including GRB Science. 2022, *Universe*, **8**, 144, DOI: 10.3390/universe8030144
- Hudec, R. & Feldman, C., Lobster Eye X-ray Optics. 2022, in *Handbook of X-ray and Gamma-ray Astrophysics*, 45
- Hudec, R., Inneman, A., Pina, L., et al., Innovative space x-ray telescopes. 2017a, in Society of Photo-Optical Instrumentation Engineers (SPIE) Conference Series, Vol. **10568**, *Society of Photo-Optical Instrumentation Engineers (SPIE) Conference Series*, 105681D
- Hudec, R., Pina, L., & Inneman, A., Novel wide-field x-ray optics for space. 2017b, in Society of Photo-Optical Instrumentation Engineers (SPIE) Conference Series, Vol. **10569**, *Society of Photo-Optical Instrumentation Engineers (SPIE) Conference Series*, 105692F
- Hudec, R., Pina, L., Marsikova, V., et al., Lobster Eye X-ray optics for astrophysics: Recent status. 2018, *Contributions of the Astronomical Observatory Skalnaté Pleso*, **48**, 456
- Hudec, R., Pina, L., Semencova, V., et al., Novel technologies for space x-ray optics. 2017c, in Society of Photo-Optical Instrumentation Engineers (SPIE) Conference Series, Vol. **10567**, *Society of Photo-Optical Instrumentation Engineers (SPIE) Conference Series*, 105673L
- Hudec, R., Semencova, V., Inneman, A., et al., Space optics with silicon wafers and slumped glass. 2017d, in Society of Photo-Optical Instrumentation Engineers (SPIE) Conference Series, Vol. **10566**, *Society of Photo-Optical Instrumentation Engineers (SPIE) Conference Series*, 105660Q
- Hudec, R., Sveda, L., Pina, L., et al., LOBSTER: new space x-ray telescopes. 2017e, in Society of Photo-Optical Instrumentation Engineers (SPIE) Conference Series, Vol. **10567**, *Society of Photo-Optical Instrumentation Engineers (SPIE) Conference Series*, 1056719
- Schmidt, W. K. H., A proposed X-ray focusing device with wide field of view for use in X-ray astronomy. 1975, *Nuclear Instruments and Methods*, **127**, 285, DOI: 10.1016/0029-554X(75)90501-7
- Tichý, V., Simple and fast algorithm for computer simulations of reflective optical systems. 2013, in Society of Photo-Optical Instrumentation Engineers (SPIE) Conference Series, Vol. **8777**, *Damage to VUV, EUV, and X-ray Optics IV; and EUV and X-ray Optics: Synergy between Laboratory and Space III*, ed. L. Juha, R. Hudec, L. Pina, S. Bajt, & R. London, 877710
- Tichý, V. 2022a, Patent, CZ PV 2022-511
- Tichý, V. 2022b, Utility Model, CZ UV 36 961
- Tichý, V. 2023, LOPSIMUL simulator, available for download at www.lopsimul.eu

- Tichý, V., Barbera, M., Butcher, G. I., et al., Effects of manufacturing inaccuracies on spatial resolution of lobster eye optics. 2018, *Contributions of the Astronomical Observatory Skalnaté Pleso*, **48**, 405
- Tichý, V., Barbera, M., Collura, A., et al., Lobster eye optics for nano-satellite x-ray monitor. 2011, in Society of Photo-Optical Instrumentation Engineers (SPIE) Conference Series, Vol. **8076**, *EUV and X-Ray Optics: Synergy between Laboratory and Space II*, ed. R. Hudec & L. Pina, 80760C
- Tichý, V., Hudec, R., & Němcová, Š., Effective algorithm for ray-tracing simulations of lobster eye and similar reflective optical systems. 2016, *Experimental Astronomy*, **41**, 377, DOI: 10.1007/s10686-016-9493-2

Overview of LOPSIMUL software, quick ray-tracing simulator of multi-foil reflective optical system

V. Tichý[✉] and R. Hudec[✉]

Czech Technical University in Prague, Faculty of Electrical Engineering, Technická 2, 166 27 Prague, Czech Republic (E-mail: vladimir-tichy@email.cz)

Received: July 15, 2023; Accepted: October 29, 2023

Abstract. This paper presents description of LOPSIMUL ray-tracing simulation software that offers extremely high computational rate. LOPSIMUL has not a specific requirements for computer hardware and the computing time is less than one second or few seconds on a common personal computer. The software is optimized for lobster eye reflective optics (Angel as well as Schmidt variants) and various types of multi-foil optics. These systems are commonly used for X-rays. As the optimization supposes a specific optics design, the software cannot be used for a generic optics. Lopsimul draws focal image and x and y profiles. LOPSIMUL calculates FWHM, effective collecting area and other principal results.

Key words: multi-foil optics – lobster eye – ray-tracing – simulations – reflective optics – grazing incidence optics – x-ray optics

1. INTRODUCTION

The main motivation was to develop the quick algorithm and consequently the software for Schmidt (Schmidt, 1975) and Angel (Angel, 1979) lobster eye wide field of view reflective optics. These optics are intended mainly for X-rays, particularly X-ray astronomy and astrophysics. Contrary to general ray-tracing algorithm (e.g. Spencer & Murty 1962), the usage is limited to some types of optics but the computational rate is extremely high. The software works on a common personal computer and the computing time is usually few seconds or less than one second.

The research resulted to simplified ray-tracing algorithm that was published in papers Tichý et al. (2016, 2011); Tichý (2013). Limitations for the optics come from this algorithm. The usage is generalised to any multi-foil optical system consisting of one or two orthogonally arranged stacks of flat mirrors. It is e.g. a case of optics that is similar to Schmidt lobster eye but spaces between mirrors are not equal.

Kirkpatrick-Baez reflective optical system (Kirkpatrick & Baez, 1948) can be simulated in an approximation when curved mirrors are replaced by set of

flat surfaces. It is known that any continuous curve can be approximated by set of line segments. The approximation can be done with any given precision.

Users of the software are encourage to understand the algorithm presented in named papers to understand what the limitations for the optics are exactly and what LOPSIMUL does "inside".

This paper gives summary of the LOPSIMUL functionality in more details than the paper of [Tichý & Hudec \(2023\)](#) but none of these papers does not represent a user manual.

LOPSIMUL is intended for Microsoft® Windows™ 64-bit operating systems.

2. LOPSIMUL overview

LOPSIMUL consist of four windows, see Fig. 1.

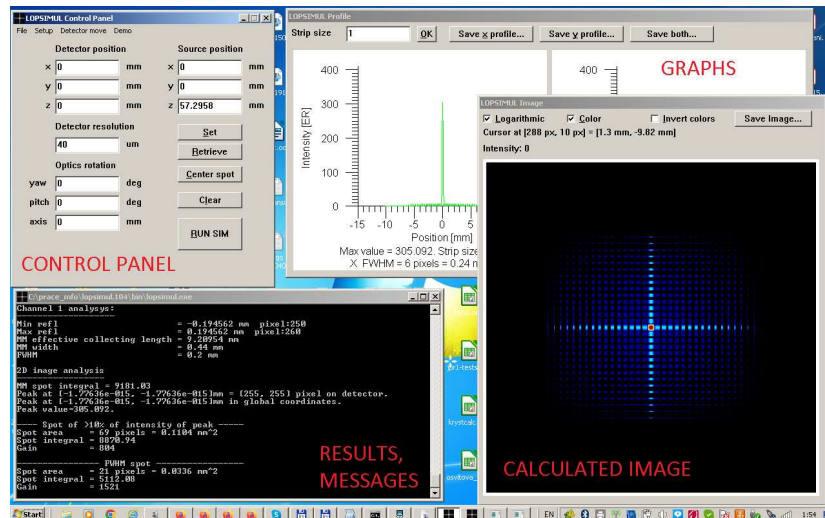


Figure 1. LOPSIMUL overview

The control panel represents the simulation input interface. The optics geometry, source type and all other parameters are entered through the control panel.

Other windows shows the simulation output. The console window shows simulation progress and numerical outputs. The image window shows the calculated image. The profile window shows graphs of profiles in x (horizontal) and y (vertical) axes.

2.1. Control panel

The control panel, see Fig. 2 is used for entering of all simulation inputs.

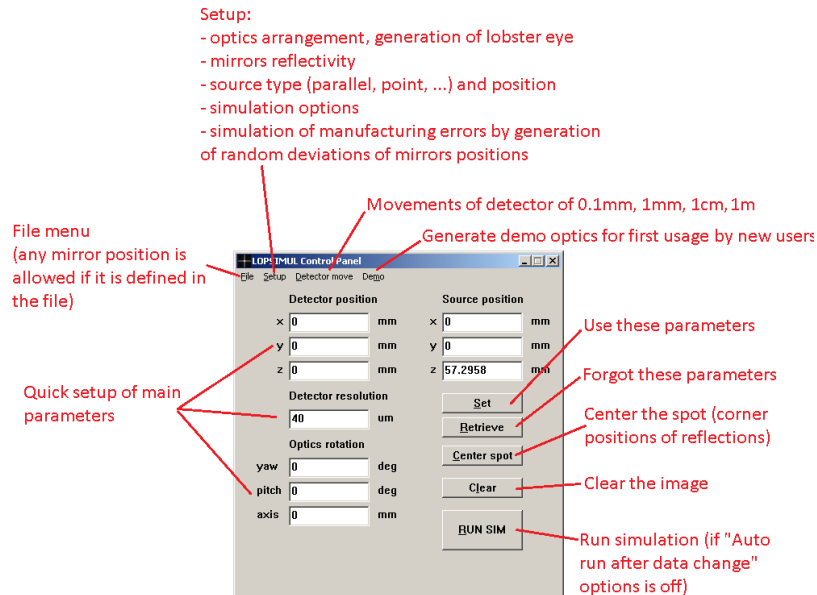


Figure 2. LOPSIMUL control panel

For the first usage, there are two built-in optics available in the "Demo" menu.

Main parameters are directly available in the control panel window. As default, the source is of parallel beam type and the coordinates in the control panel represent the source direction vector. For point source (and other sources that are available in the "Setup" menu), these coordinates represent the source position (or position of its center) in 3-D space.

Other parameters are clear to understand.

2.1.1. Optics set-up

For reasons explained in the Introduction, the optics set-up must be defined in terms of stacks. The term "stack" stands for set of mirrors. The stack must operate in one plane only and therefore it must be possible to simulate it in two-dimensional cross-section. The stacks are possible to generate in "Setup → Optical stacks list" submenu

The stacks are defined by following parameters: radius of the stack, pitch of mirrors, number of mirrors, mirror depth and thickness. Vertical or horizontal orientation of the stack can be set. Two stacks of different radii and different orientations form a Schmidt lobster eye system. Two stacks of the same radii and different orientation form an Angel lobster eye system.

More general system can be entered to the program via data-file. The data-file can be imported or exported via functions in "File" menu. In the input file, each mirror is defined as a set of four vertices of planar cross-section of the mirror. Mirrors are usually represented by rectangular cuboids (rectangles if the thickness is neglected). If opposite mirroring planes of mirrors are not parallel, mirrors can be represented by prisms of convex quadrilateral base.

2.1.2. Radiation source set-up

The radiation source can be set in "Setup → Source" submenu. Although LOPSIMUL is intended mainly for X-ray optics, it can be used for other type of radiation if the proper model of reflectivity is set. LOPSIMUL can operate with parallel beam source, point source, line source and "flower 7" source. "Flower 7" source represents an approximation of disc source, where 7 point sources are used. One of point sources lays in the centre of the disc and 6 sources lays around the center. This arrangement looks like a flower. The source can be also defined in the input file.

2.1.3. Mirrors reflectivity set-up

Submenu "setup → material" allows to set-up reflectivity of mirrors.

LOPSIMUL contains few models of reflectivity: ideal mirror, constant reflectivity, linear model and two "trapezoid" models.

The linear model assumes that reflectivity \mathbb{R} at grazing angle θ in radians equals

$$\mathbb{R}(\theta) = \begin{cases} Q \left(1 - \frac{\theta}{k}\right) & \forall 0 \leq \theta \leq k \\ 0 & \forall \theta \geq k \end{cases} \quad (1)$$

Constants Q and k are defined by the user.

The horizontal trapezoid model assumes that

$$\mathbb{R}(\theta) = \begin{cases} Q & \forall 0 \leq \theta \leq r \\ Q \frac{k-\theta}{k-r} & \forall r \leq \theta \leq k \\ 0 & \forall \theta \geq k \end{cases} \quad (2)$$

Constants Q , k and r are defined by the user.

The vertical trapezoid model assumes that

$$\mathbb{R}(\theta) = \begin{cases} Q \left(1 - \frac{\theta}{r}\right) & \forall 0 \leq \theta \leq k \\ 0 & \forall \theta \geq k \end{cases} \quad (3)$$

Constants Q , k and r are defined by the user.

Any model of reflectivity can be imported to the program in the form of table. Table generated at on-line calculator (Henke, 2023) can be directly imported to LOPSIMUL. Up to 10 of these tables can be imported to LOPSIMUL this way.

2.2. Image window

The image window shows the simulated resulting image, see Fig. 3. Black-and-white or false color view is available. Color scale can be inverted. Linear or logarithmic scale can be chosen. It is possible to save the image in .png or .bmp format. The image can be exported as text table for consequent processing in other software. If the mouse cursor is placed over the image, coordinates in image pixels and position in millimeters are shown together with intensity of the image at the corresponding point.

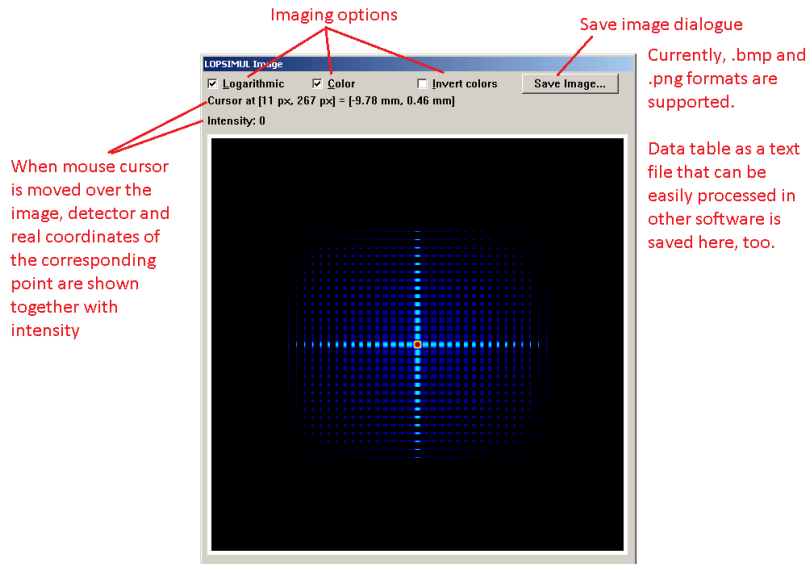


Figure 3. LOPSIMUL image window

2.3. Profiles window

Profiles window shows x and y cross-section graph of the image, see Fig. 4. The intensity is averaged over a strip of set size. The cross section is done through

center of image that may not be the same as the spot position. If you would like to move the image to get the spot centered, use "Center spot" button of the Control Panel. Any of the profiles can be saved as image or both profiles can be saved in one image. Currently, .png and .bmp. image formats are available. Any of profiles can be exported as text table to be consequently processed in other software.

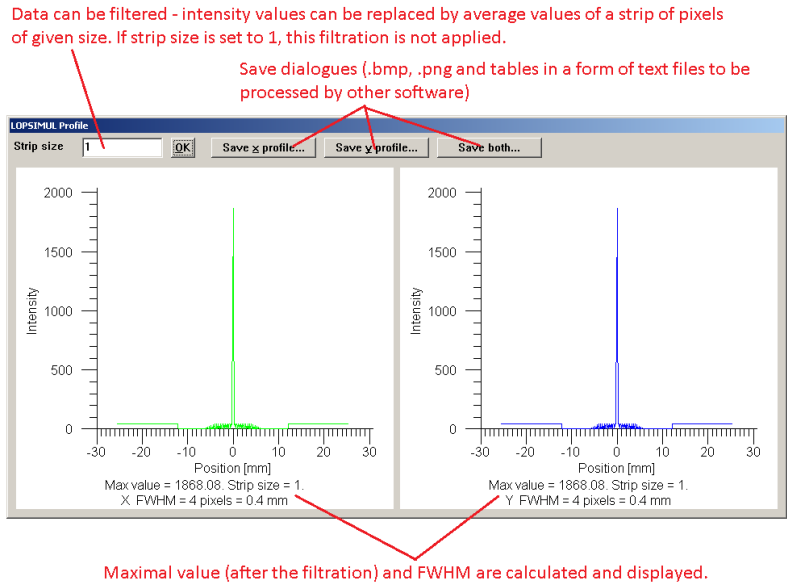


Figure 4. LOPSIMUL profiles window

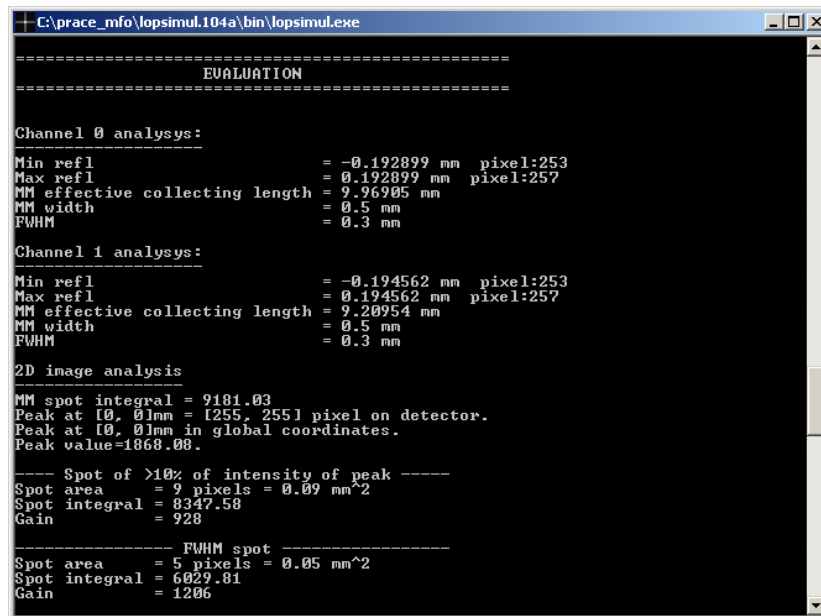
If a simulation is finished but one or both graphs of profiles is (are) missing, the focal spot might not be centered. In this situation, try to press "Center spot" button in the control panel.

2.4. Console window

Console window shows progress of calculation during the simulations. When the simulation is finished, evaluation is listed in the console window, see Fig. 5.

For each of the channels (vertical and horizontal), the following values are calculated:

- Min refl, Max refl = border position of all reflections.



```

C:\prace_mfo\lopsimul.104a\bin\lopsimul.exe
=====
EVALUATION
=====
Channel 0 analysys:
-----
Min refl          = -0.192899 mm  pixel:253
Max refl          =  0.192899 mm  pixel:257
MM effective collecting length = 9.96905 mm
MM width          =  0.5 mm
FWHM              =  0.3 mm

Channel 1 analysys:
-----
Min refl          = -0.194562 mm  pixel:253
Max refl          =  0.194562 mm  pixel:257
MM effective collecting length = 9.20954 mm
MM width          =  0.5 mm
FWHM              =  0.3 mm

2D image analysis
-----
MM spot integral = 9181.03
Peak at [0, 0]mm = [255, 255] pixel on detector.
Peak at [0, 0]mm in global coordinates.
Peak value=1868.08.
---- Spot of >10% of intensity of peak ----
Spot area        = 9 pixels = 0.09 mm^2
Spot integral    = 8347.58
Gain             = 928

----- FWHM spot -----
Spot area        = 5 pixels = 0.05 mm^2
Spot integral    = 6029.81
Gain             = 1206

```

Figure 5. LOPSIMUL console window

- MM effective collecting length = effective collecting length related to the area bordered by Min rel and Max refl, i.e. by border rays that are reflected.
- MM width = width of focal image bordered by Min refl and max refl. It is not exactly equal to difference of Min refl and Max refl because of non-zero pixel size.
- FWHM = full width at half maximum of focal image.

The analysis of full 2-D image gives:

- MM spot integral = sum of intensities of all pixels laying within area bordered by Min refl and Max refl. I. e. it is total intensity in a rectangular box bordered by all double-reflected rays.
- Peak position in pixel coordinates.
- Peak position in millimeters related to global coordinate system.
- Intesity of the peak.

For area defined by FWHM and 10% rule, following values are calculated:

- Size of the area in pixels and square millimeters.
- Spot integral = sum of intensities of all pixels laying within this area.
- Gain

3. Conclusions

LOPSIMUL is optimized for some types of multi-foil reflective of optics, particularly for Schmidt and Angel lobster eye optics. These optics are used mainly for X-rays. LOPSIMUL offers extremely high computational rate but works only for particular optics types described above.

The code can be used e.g. for design and simulations of X-ray monitors based on Lobster Eye wide field optics.

LOPSIMUL can be downloaded and used by anybody for any purpose free of charge. LOPSIMUL is available for download (Tichý, 2023).

However, if results obtained by this program are published anywhere (e.g. in article, paper, thesis, report, etc.), users are asked to mention there that this program was used and cite at least one paper related to LOPSIMUL, e.g. this one or the paper that presents the simplified ray-tracing algorithm (Tichý et al., 2016). Citations of other papers are welcomed, too.

LOPSIMUL and any of its parts can be distributed by its author only. LOPSIMUL and any of its parts can be modified by the author only.

Acknowledgements. Thanks for funding from the European Union’s Horizon 2020 Programme under the AHEAD2020 project (grant agreement n. 871158). We also acknowledge CVUT FEL grant No. SGS21/120/OHK3/2T/13.

References

- Angel, J. R. P., Lobster eyes as X-ray telescopes. 1979, *Astrophysical Journal*, **233**, 364, DOI: 10.1086/157397
- Henke. 2023, Optical constants, <http://henke.lbl.gov/optical.constants/>
- Kirkpatrick, P. & Baez, A. V., Formation of optical images by X-rays. 1948, *Journal of the Optical Society of America*, **38** 9, 766
- Schmidt, W. K. H., A proposed X-ray focusing device with wide field of view for use in X-ray astronomy. 1975, *Nuclear Instruments and Methods*, **127**, 285, DOI: 10.1016/0029-554X(75)90501-7
- Spencer, G. H. & Murty, M. V., General ray-tracing procedure. 1962, *Journal of the Optical Society of America*, **52**, 672
- Tichý, V., Simple and fast algorithm for computer simulations of reflective optical systems. 2013, in Society of Photo-Optical Instrumentation Engineers (SPIE) Conference Series, Vol. **8777**, *Damage to VUV, EUV, and X-ray Optics IV; and EUV*

and X-ray Optics: Synergy between Laboratory and Space III, ed. L. Juha, R. Hudec, L. Pina, S. Bajt, & R. London, 877710

Tichý, V. 2023, LOPSIMUL simulator, available for download at www.lopsimul.eu

Tichý, V., Barbera, M., Collura, A., et al., Lobster eye optics for nano-satellite x-ray monitor. 2011, in Society of Photo-Optical Instrumentation Engineers (SPIE) Conference Series, Vol. **8076**, *EUV and X-Ray Optics: Synergy between Laboratory and Space II*, ed. R. Hudec & L. Pina, 80760C

Tichý, V. & Hudec, R., LOPSIMUL: quick numerical simulator of multi-foil reflective optical system. in , *EUV and X-ray Optics: Synergy between Laboratory and Space VIII*, ed. R. Hudec & L. Pina, Vol. **12576**, International Society for Optics and Photonics (SPIE), 1257609

Tichý, V., Hudec, R., & Němcová, Š., Effective algorithm for ray-tracing simulations of lobster eye and similar reflective optical systems. 2016, *Experimental Astronomy*, **41**, 377, DOI: 10.1007/s10686-016-9493-2

PRÁCE ASTRONOMICKÉHO OBSERVATÓRIA
NA SKALNATOM PLESE
LIII, číslo 4

Zostavovatelia:	Mgr. Martin Jelínek, PhD. Bc. Marianna Dafčíková
Výkonný redaktor:	RNDr. Richard Komžík, CSc.
Vedecký redaktor:	RNDr. Augustín Skopal, DrSc.
Vydal:	Astronomický ústav SAV, Tatranská Lomnica
IČO vydavateľa:	00 166 529
Periodicita:	3-krát ročne
ISSN (on-line verzia):	1336-0337
CODEN:	CAOPF8
Rok vydania:	2023
Počet strán:	216

Contributions of the Astronomical Observatory Skalnaté Pleso are processed using
L^AT_EX 2_ε CAOSP DocumentClass file 3.09 ver. 2021.